PROCEEDINGS

OF THE

INTERNATIONAL COLLOQUIUM

ON

DROPS AND BUBBLES

THEIR SCIENCE AND THE SYSTEMS THEY MODEL

California Institute of Technology
and
Jet Propulsion Laboratory

28-30 August, 1974

Volume I

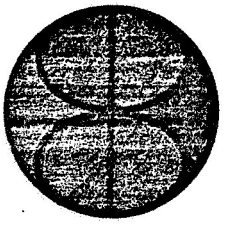

330.

PROCEEDINGS
OF THE
INTERNATIONAL COLLOQUIUM
ON
DROPS AND BUBBLES

THEIR SCIENCE AND THE SYSTEMS THEY MODEL

California Institute of Technology
and
Jet Propulsion Laboratory

28-30 August, 1974

Volume I

Editors

D. J. COLLINS
M. S. PLESSET
M. M. SAFFREN

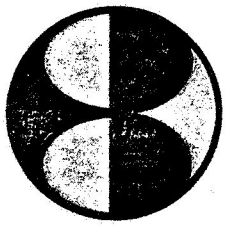

CHAIRMAN

M. S. Plesset —*Caltech*

STEERING COMMITTEE

M. M. Saffren
Chairman —*Jet Propulsion Lab.*

F. H. Busse —*UCLA*

J. R. Carruthers —*Bell Laboratories*

R. J. Donnelly —*University of Oregon*

D. D. Elleman —*Jet Propulsion Lab.*

D. W. Moore —*Imperial College-London*

M. Neiburger — *UCLA*

M. S. Plesset —*Caltech*

L. E. Scriven —*University of Minnesota*

EXECUTIVE SECRETARY

D. J. Collins

M/S 183-601

Jet Propulsion Laboratory

4800 Oak Grove Dr.

Pasadena, CA 91103

PREFACE

These Proceedings have been organized with papers given in the order in which they were presented in the Colloquium. Those papers representing contributions to the evening film sessions have been placed following the full length papers because of the somewhat different format involved. In several of these shorter papers are to be found some of the most stimulating presentations of the Colloquium, and the organizers are indeed grateful that the authors of these film discussions have been willing to participate by contributing what have in many cases been examples from unfinished and ongoing research.

The presentations of the Introductory Session have not been included in these Proceedings. In this Session, chaired by Dr. R. J. Mackin, Jr., Dr. W. H. Pickering greeted the participants, Dr. F. E. Goddard explained the Research and Advanced Developments Program at JPL, and Dr. M. M. Saffren gave the Introduction to the Colloquium.

The Editors

ACKNOWLEDGMENTS

In organizing and carrying out a colloquium of this scope and magnitude it is essential that myriad details be anticipated and attended to in order to ensure smooth functioning of colloquium activities which, besides the formal and informal sessions, included meals and transportation. The great effort required to accomplish this was borne by the members of the Steering Committee, and in particular by the Colloquium Chairman, Dr. Milton Plesset.

We specially thank Anne Shanahan who, as Colloquium Secretary, provided invaluable help in every phase of the preparation for the Colloquium, the activities of the Colloquium, and the preparation of these Proceedings; Nancy Hopkins for her capable assistance with local arrangements; Alex Irving for his support during the Colloquium in arranging for the facilities and equipment; and Carol Litchfield and Sandi Campbell for conducting tours and helping participants and their guests to feel at home in Pasadena.

We owe special gratitude to the Jet Propulsion Laboratory and the California Institute of Technology for their support of this Colloquium and for the use of the facilities. We also wish to thank the Space Technology Payloads Office of the Office of Aeronautics and Space Technology of NASA under Contract NAS 7-100 for supporting both the activities of the meeting and in part the publication of these Proceedings.

Without these people and organization--and we do not forget the participants themselves--this Colloquium could not have been the success that it was, both technically and as an international gathering of unusual warmth.

Dr. Melvin M. Saffren
Chairman, Steering Committee

TABLE OF CONTENTS

VOLUME I

TABLE OF CONTENTS

	Page
PREFACE	i
ACKNOWLEDGMENTS	ii
TABLE OF CONTENTS	iii
INTRODUCTION	x
TECHNICAL SUMMARY	xii

SESSION I - NON-CONVENTIONAL FLUIDS

INTRODUCTORY PAPERS - M. S. PLESSET, CHAIRMAN

The Fission Theory of Binary Stars N. R. Lebovitz	1
Rotating Stars D. O. Gough	11

INVITED PAPERS - R. J. DONNELLY, CHAIRMAN

The Electron Bubble in Liquid Helium P. H. Roberts	35

SESSION II - CHARGED DROPS AND LIQUID DROP MODEL OF THE ATOMIC NUCLEUS

INTRODUCTORY PAPERS - M. S. PLESSET, CHAIRMAN

The Rotating, Charged or Gravitating Liquid Drop, and Problems in Nuclear Physics and Astronomy W. J. Swiatecki	52

INVITED PAPERS - W. J. SWIATECKI, CHAIRMAN

Vibrational Frequency of a Non-Conducting Charged Liquid Drop C. Y. Wong and H. H. K. Tang	79
Similarities and Differences Between Volume-Charged (Nuclear) Drops and Charged Conducting (Rain) Drops C. F. Tsang	85

The Roles of Electrohydrodynamic Phenomena in the Motion of Drops and Bubbles
R. B. Spertell and D. A. Saville 106

Duality Between Surface Coupled Interfacial Waves for Electrically Charged and Self-Gravitating Drops
M. Zahn 122

The Dynamics of Colliding and Oscillating Drops
C. T. Alonso 139

SESSION III - SPACE PROCESSING AND ACOUSTIC LEVITATION

INTRODUCTORY PAPERS - M. S. PLESSET, CHAIRMAN

Skylab Fluid Mechanics Demonstrations
E. G. Gibson 158

The Application of Drops and Bubbles to the Science of Space Processing of Materials
J. R. Carruthers 161

INVITED PAPERS - J. R. CARRUTHERS, CHAIRMAN

Thermocapillary Flow in a Cylindrical Liquid Drop at Zero Gravity
C. E. Chang and W. R. Wilcox 194

Steady Thermocapillary Convection Cells in Liquid Drops
A. L. Dragoo 208

Analysis of Liquid Dynamics for M551 and M553 Skylab Space Processing Experiments
M. R. Brashears, S. V. Bourgeois, C. Fan 227

Experiments with Acoustically Levitated Droplets
R. E. Apfel 246

Drop Dynamics in Space
T. G. Wang, M. M. Saffren, D. D. Elleman 266

TABLE OF CONTENTS

VOLUME II

Page

SESSION IV - FLUID MECHANICS I

INTRODUCTORY PAPERS - M. S. PLESSET, CHAIRMAN

The Motion of Bubbles and Drops in Liquids
J. F. Harper 300

INVITED PAPERS - J. F. HARPER, CHAIRMAN

The Pendant Drop: Theory and Experiment
A. A. Kovitz 304

On the Production of Bubbles by Focused Laser Light
W. Lauterborn and H. Bolle 322

Some Aspects on Dynamics of Nonspherical Bubbles and Liquid Drops
D. Y. Hsieh 338

On the Oscillations of Drops and Bubbles in Viscous Liquids
A. Prosperetti 357

Non-Linear Effects on Droplet Deformation
P. G. Simpkins 372

SESSION V - FLUID MECHANICS II

INTRODUCTORY PAPERS - M. S. PLESSET, CHAIRMAN

Deformation and Burst of Single Drops in a Viscous Fluid
A. Acrivos 390

INVITED PAPERS - A. ACRIVOS, CHAIRMAN

Pressure Waves in Bubbly Liquids
L. van Wijngaarden 405

Models of Spherical-Cap Bubbles
R. Collins 414

The Application of Drops and Bubbles to Fluid Flow Measurements
E. F. C. Somerscales 427

Page

The Dynamics of Bubbles and Drops in a Viscoelastic Fluid
E. Zana and L. G. Leal 428

A Study of the Deformation and Breakup of Accelerating Water Droplets
J. M. Reichman and S. Temkin 446

SESSION VI - METEOROLOGY

INTRODUCTORY PAPERS - M. S. PLESSET, CHAIRMAN

The Role of Drop Dynamics in the Physics of Clouds and Rain
M. Neiburger, I. Y. Lee, E. Lobl, L. Rodriguez, Jr. 465

INVITED PAPERS - M. NEIBURGER, CHAIRMAN

Water Drop Interactions
C. P. R. Saunders 487

Nucleation Theory and Its Atmospheric Applications
C. S. Kiang, D. Stauffer, V. A. Mohnen, P. Hamill, G. H. Walker 506

Current Meteorological Theory of Drop Growth by Condensation and Some Comparisons with Experiment
J. C. Carstens and J. M. Carter 529

Growth Mechanisms for Urban Aerosol Particles
S. L. Heisler and S. K. Friedlander 553

Microstructure, Composition and Dynamical Evolution of Scattering Particulates Determined from Optical Data
A. L. Fymat 572

FILM SESSION I

SESSION CHAIRMAN - J. R. CARRUTHERS

Surface Instability of Stationary Air Bubbles
C. J. Remenyik 592

Page

On the Growth and Collapse of Vapor Bubbles at Liquid/Liquid Interfaces
W. E. Kastenberg and Ivan Catton 606

FILM SESSION II

SESSION CHAIRMAN - E. G. GIBSON

An Analysis of Oscillations of a Water Droplet Under Low Gravity Conditions
O. H. Vaughan, R. E. Smith, R. J. Hung, S. T. Wu 617

Liquid Drop Behavior in Weightlessness from Skylab
T. C. Bannister and S. V. Bourgeois. 629

LIST OF PARTICIPANTS 632

GROUP PHOTOGRAPH 637

INTRODUCTION

Interest in the science of liquid drops and bubbles extends beyond those who work in fundamental fluid dynamics. Workers in meteorology, chemical engineering, mechanical engineering, and space processing have an evident and very practical concern with this science. Workers in nuclear physics and in astrophysics use liquid drops and bubbles as models for phenomena in atomic nuclei, and in self-gravitating astronomical systems.

This Colloquium provided an opportunity for workers in these various disciplines to come together, for the first time, to

- assess the present status of the science of liquid drops and bubbles in liquids
- forecast and help determine the future directions of this science
- determine the value to this science of forthcoming opportunities to perform experiments in a weightless environment.

One aim of the Colloquium was to make evident that what might appear at first sight to be a narrow and proscribed science with its best days behind it, was none of these things. A reader of these Proceedings can judge for himself how successfully this aim was met. An excellent technical summary of the Colloquium is provided by Dr. Scriven's paper on page xii.

A second aim was to help establish the future direction of the science of drops and bubbles by looking toward the proper balance of future work in theory, computation, laboratory experiment, and experiments in weightlessness. In retrospect this was too ambitious an aim to be met definitively by a single Colloquium; such a balance will probably emerge only after more conventions of this Colloquium have taken place.

Even so, the presentations do allow some general conclusions to be drawn. Almost without exception, theory is treated in linear approximation and applies to the equilibrium, or at best stationary state. While computation does indeed treat the non-linear dynamics of drops and bubbles it does so only when a high degree of symmetry significantly reduces the computational complexity. In laboratory experiments the fact that there are usually several complicated effects that are taking place simultaneously makes precise analysis difficult. Experiments in weightlessness are relatively new. However the several papers presented on the Skylab demonstrations hint at the potential for remarkable experiments that may allow effects simultaneously present in earth-based experiments to be disentangled.

Here I must confess to the personal prejudice that as this potential is slowly realized in the next few years, when what were demonstrations become carefully controlled experiments, more and more experimenters will be drawn to experiments in weightlessness, and what is learned will greatly stimulate both

theory and computation and even result in new experiments on earth. Presently, NASA KC 135 aircraft flying along a ballistic trajectory afford up to 25 seconds of weightlessness. Soon to be flown as part of the NASA Space Processing Program, sounding rockets will allow experiments times in weightlessness up to 10 minutes. Eventually, in 1980, the NASA Space Shuttle will provide 7 days of weightlessness, and in fact JPL is engaged in a project to result in an experiment module being made available on the Shuttle for drop dynamics experiments. It is expected that future conventions of this Colloquium will be under the auspices of this project which is itself part of the NASA Physics and Chemistry in Space Experiments Program.

Interdisciplinary meetings such as this one are notoriously high risk events. When successful, as this Colloquium was, the presentations stimulate specialist and non-specialist alike, provoking exciting discussions at sessions that spill over into corridors, and irrepressibly into the coffee and mealtime breaks. Hopefully the presentations as recorded in these Proceedings will be just as exciting to read as they were to hear.

Dr. Melvin M. Saffren
Chairman, Steering Committee

COLLOQUIUM SUMMARY

DROPS AND BUBBLES: THEIR SCIENCE AND THE SYSTEMS THEY MODEL

L. E. Scriven
Department of Chemical Engineering and Materials Science
University of Minnesota, Minneapolis, Minnesota 55455

A bubble or a drop is a relatively compact blob — a sphere or its topological equivalent — of one fluid phase surrounded by another. It is contained within a fluid interface which usually resembles a closed mathematical surface and often behaves like a permeable, weakly elastic membrane under tension. By extension the term bubble or drop is also applied to a fluid blob in partial contact with a solid, but otherwise surrounded by a second fluid. In this case the containing surface consists of two types of interface separated by a narrow region which resembles a closed mathematical curve, the line of mutual contact of three phases.

Bubbles and drops of everyday experience are apt subjects of experimental study and mathematical analysis. Their relationship to the sphere, their near symmetry, invites theoretical simplification. They have always been on the thoroughfare of physical science. Two monuments are J. A. F. Plateau's 1873 Statique Expérimentale et Théorique des Liquides soumis aux seules Forces Moléculaires and, a lifetime earlier, P. S. Laplace's 1806 Sur l'Action Capillaire, which appeared as a supplement to Volume 10 of his Mecanique Céleste. Plateau was a blind genius of an experimentalist. Laplace was a sightful mathematician and physicist. Their works still repay study and are available in English, Laplace's in Bowditch's heavily annotated 1839 translation, Celestial Mechanics, which was reprinted by Dover Publications, and Plateau's in the Annual Reports of the Smithsonian Institution for the years 1863-1866.

From the times of Plateau and Laplace everyday bubbles and drops have served as models for physical systems on other scales, from nuclear physics to astrophysics. This colloquium links together, in a way that has not been tried before,

the divergent trails up which science and engineering have carried the study of bubbles, drops and the forces which mold and move them. Those forces are the grid on which can be charted the interrelationships among the papers in this volume.

The science of bubbles and drops can be split into investigations of their formation or disappearance, by mass transfer processes, and of their behavior once formed, which is fluid mechanics first of all. For phenomena of all scales treated in this volume, fluid mechanics is indeed the common denominator, although growth processes are the subject of the papers on atmospheric aerosols and precipitation. The science can also be cut crosswise into systems of a lone bubble or drop, two or not many more globules in some manner of interaction with each other, and swarms of them engaged in collective action as dispersions of one phase in another. The less populous systems are most often the focus in basic disciplines, while the dispersions more frequently command the attention of applied scientists and engineers, as is evident in this volume.

Everywhere in the science the coordinate forces are those of surface tension, gravity (sometimes cast as buoyancy), charges, magnets, radiation fields, pressure and viscous action, and accelerations in disguise as centrifugal and other inertial forces. The following survey of the Colloquium proceedings is laid out along intersections of these forces and ought to provide a perspective of the field of bubbles and drops — and of some possibilities for experiments in a weightless environment.

Static configurations

At equilibrium the only stress field in a fluid is hydrostatic pressure, which is balanced in bulk fluid by volume-distributed force fields and at interfaces by the effect of surface tension in a curved surface. If the former are absent, as in Gibson's free droplets in Skylab, or without effect, as in Plateau's droplets suspended in liquid of equal density, the only isolated form is the sphere. When the bubble or drop makes contact with a solid, the shape depends on the contact line. If that is a circle and around it the contact angle is uniform, the shape is still a segment of sphere, as in the final state of Pogue's Skylab water droplet described by Vaughan et al. [617]. If the drop contacts the solid in two coaxial circles, then the shape may be nodoidal, unduloidal, spherical or cylindrical — Plateau's axisymmetric figures — as in the rest states of the captive drops in the Skylab floating zone experiments discussed by Carruthers and others. If drop-solid contact is other than a single circle or two coaxial circles, its configuration is in general a three-dimensional surface of constant mean curvature, difficult to describe from experiment and non-trivial to compute from theory. Examples are a droplet clinging to, yet incompletely wetting, a cylinder, as in the clamshell forms of dew on a spiderweb, and a drop penetrated off-center by a thread, as in the Skylab handling procedure (when the drop's diameter greatly exceeds the thread's, the departures from sphericity are significant only near the contact lines, however).

When external gravity joins surface tension in the molding of bubbles and drops, the shapes become more complex. The axisymmetric forms known as pendent and sessile drops or bubbles have long been used for measurement of the surface tension of liquids and the interfacial tension between liquids. Because comparison

of experiment with theory depends on tedious numerical integration, only with the advent of efficient electronic computation have pendent and sessile drops become the method of choice for accurate tension determinations, particularly for values less than 1 dyne/cm. Kovitz's [304]careful photography and computation of pendent drops are exemplary, and his study of multiple equilibrium shapes and their stability is representative of recent researches by several groups, including Padday's at Kodak, Ltd., and the writer's at Minnesota. Nitsche [American Mathematical Monthly 81 945-968 (1974)] reviews the many aspects of current mathematical interest to himself, Concus, Fin and others. Questions of configurational stability arise in connection with certain processes of crystal growth and solidification that Carruthers describes in his paper on space processing of materials [161] .

With rotating bubbles and drops the interplay of centrifugal force and surface tension causes more complicated shapes. Spheroidal bubble forms are the basis of the recently perfected spinning 'drop' method of measuring interfacial tension. At higher rates of rotation the static configurations lose axial symmetry; in some cases they take on a dumbbell shape but there are many other forms and the issues of stability and drop fission originally tackled by Plateau are still active research areas.

Since Bohr and Wheeler began modeling atomic nuclei as uniformly charged liquid drops with surface tension, nuclear physics has contributed theoretical analysis and impetus for experimental study. However, to contrive in the laboratory a liquid drop with uniform volume charge is very difficult, as several Colloquium participants remarked. Perhaps a system can be found with enough charge well enough bound throughout the interior to permit experimental modeling of nuclei. Until the challenge is met the only possibility is analysis and calculation of the sorts presented by Tsang in study of volume-charged drops and charged, conducting drops [85], and by Foote [Journal of the Atomospheric Sciences 32 390-402 (1975)] Alonso [139] in their computer

simulations. Unrepresented in the proceedings is the finite-element method, which offers considerable advantages for computing static meniscus configurations that are not axisymmetric.

When internal gravity and surface tension dominate a drop there is a close mathematical analogy with the case of volume charge and surface tension. The energy of self-gravitation shares the inverse-distance dependence of electrostatic energy. Self-gravitating blobs have long been models for stars, and so it is that astrophysics and nuclear physics can be linked through drops. In astrophysics the angular momentum of stellar masses is crucial to their form and stability, as Lebovitz so lucidly brings out [1]. In nuclear physics the effects of large angular momentum on the stability of nuclei is of high interest, as Swiatecki indicates [52]. The difference is that no analog of surface tension is significant in the astrophysical case, whereas the relatively sharp fall-off in nucleon density which defines larger nuclei is quite analogous to the cause of surface tension of everyday liquids.

Swiatecki's masterful survey of the equilibrium configurations of rotating, charged or gravitating, liquid masses with or without surface tension is an outstanding contribution to the science of bubbles and drops [52]. With two dimensionless coordinates, one measuring the ratio of inverse-distance energy to surface energy, the other measuring the ratio of rotational to surface energy, he unifies the gyrostatic configurations from astrophysics, nuclear physics, and virtually everything in between (see his Fig. 6). From Swiatecki's survey and Lebovitz's summary of the fission theory of binary stars it becomes clear that the most intense theoretical studies of drop stability and breakup have come at the ends of the range. However, ordinary pendent drops (in a uniform gravitational field) if they are reflected in their neck planes resemble the nuclear saddle-point shapes known as Bohr-Wheeler dumbbells and so there may be useful link-ups with the laboratory mid-range.

While the quantum underpinnings are suppressed in liquid-drop models of atomic nuclei, the electron bubble in liquid helium treated by Roberts is flagrantly quantum mechanical [35]. Nevertheless a shell of steep density variation gives rise to a surface-excess stress analogous to surface tension, and one has a system that can be partly modeled as a gas bubble. On a larger scale, blobs of liquid suspensions of interacting colloidal particles can be expected to display a weak interfacial tension: yet another sort of system for modeling by drops..

Oscillation and circulation

Motion within a drop or around a bubble brings inertial and viscous forces into play, and these by their action on the interface recruit surface tension as well. Small amplitude oscillations leave the inertial effects nearly linear and so normal-mode analysis has been standard in theory and experiment. Early motion of a deformed drop may be virtually irrotational, but viscosity generates vorticity near the interface and diffuses it eventually throughout the drop. This important transient had escaped analysis before Prosperetti's, which indicates that evolution toward the well-known asymptotic regime of viscous damping is not exponential but algebraic with time [357]. Prosperetti's striking results invite experiments to confirm and extend them, and the Skylab science demonstrations point to one possibility.

Those demonstrations by Gibson, Pogue and Carr include not only free-floating drops but also oscillating sessile drops whose contact lines on the supporting solid appear to remain fixed, according to Vaughan et al. [617]. The same is apparently true of the oscillating and circulating captive drops, or cylindrical floating zones. In these cases experiment leads theoretical analysis, and in the more common circumstance that the contact line moves over the solid (often intermittently and irregularly), theory itself is incomplete because the physics of contact line movement is still unclear.

Observations of bubble oscillations so violent that small 'bubblets' tear off from the surface or the bubble itself disintegrates, as in Remenyik's high-speed cinematography [592], are challenge to analysis. So are the instabilities and microjet formation in collapse of bubbles as photographed by Lauterborn and Bolle [322], although Plesset, Chapman and others have made computational inroads on the phenomena by disregarding local surface tension and viscous effects as well as vapor and liquid compressibilities. Vapor film collapse, or

bubble collapse, and microjet formation are put forward by Kastenberg and co-workers to account for the spectacular, complex events that follow on plunging hot liquid into a cooler, more volatile one [606].

Oscillations of an inviscid liquid drop endowed with surface charge can be altered by the coulombic forces, as pointed out by Wong and Tang [79]. However, the electrical forces are sensitive to charge convection, which in turn can be strongly affected by the viscous effects that are magnified at a charged interface, a point touched on in closing by Zahn and developed by Spertell and Saville[106]. Zahn himself treats small-amplitude oscillation and stability of inviscid, charged drops suspended in a second, charged fluid [122]. He emphasizes the volume-charged, non-conducting drop which, as described above, serves as a model for nuclei and, less accurately, for certain stars. Now electrohydrodynamics needs laboratory studies of the oscillations and break-up of charged, viscous drops, as in Saunders' experiments [487].

The problem on the astrophysical scale is whether a self-gravitating, rotating, non-isothermal, compressible mass can exist in any state of gyrostatic equilibrium. Gough [11] remarks that the surface angular velocity of the sun varies significantly from pole to equator, adduces theoretical grounds for concluding that meridional currents of internal circulation necessarily exist, and goes on to argue that there are no stable steady states. The subject is vast and rapidly recedes from analogies with everyday bubbles and drops.

On the other hand the connections between bubbles and drops and nuclear dynamics are so tight that classical Newtonian hydrodynamics and Maxwellian electrostatics are being used in elaborate computer simulations of nuclear oscillations. A highlight of the Colloquium was Alonso's lucid presentation and SQUISH-generated motion pictures of axisymmetric oscillations and near break-up — fission — of viscous drops with surface tension [139]. The program

is based on Harlow and Amsden's finite difference scheme, the Simplified Marker and Cell Method, and draws on Foote's earlier simulation of droplet collision and oscillation for meteorological application. It may prove useful for antiseptic experiments with a wide variety of deformed bubbles and drops, as well as other transient, viscous flows with free surfaces. Marker and cell methods have a reputation for being extremely demanding of computer memory and time, however. It should be pointed out that experiments with expensive high-energy machines to produce superheavy elements are costly too. So are laboratory experiments with the convenience of zero gravity.

Translation and shear

A bubble or drop usually differs in density from its surroundings. If gravity is present, or any similar force field, the external fluid exerts a net hydrostatic pressure force known as buoyancy force which tends to translate the bubble or drop. In translation its interface ought to be generated at the forward stagnation point, expand freely over the leading hemisphere, contract over the trailing hemisphere, and disappear at the rearward stagnation point. This expectation is rarely met, for reasons discussed by Harper [300] and Acrivos [390].

In the first place a fluid interface is generally not 'clean,' i.e. the interface is a region of variable composition owing to its thermodynamic attraction for many of the contaminants present in trace amounts in bulk. Though an experienced and painstaking surface chemist may be able to remove most of these, water is a notoriously bad actor especially around glass or quartz. K. C. D. Hickman's researches should be well known. We also have Savic's observations of contaminant-saturated rearward caps on rising bubbles.

Harper [300] suggests a new hypothesis that all semi-clean water has the same amount of the same surface-active constituent always in it, and then nominates bicarbonate ions. The test will require more than ordinary hydrodynamic experimentation.

In the second place the translation of a globule excites nonuniform viscous traction over its surface and causes nonuniform dynamic pressure there as well. The result is that surface tension can no longer maintain sphericity, and as out-of-roundness increases the flow field is further altered until steady translation becomes unstable, the motion becoming helical or zig-zag. Many features revealed by experiment are still not satisfactorily explained, as Acrivos [390] and Harper [300] bring out. The subject is one that continues to attract the attention of fluid-mechanicists and applied mathematicians.

Large drops and bubbles in translation take the form known as the spherical-cap bubble, which has been investigated extensively by Collins [414] and others. Interestingly, surface tension force appears to be inconsequential over the surface of a spherical-cap bubble, except around the circumference, where surface curvature is high and the ultimate controls of cap diameter and velocity may reside. Attention has been riveted on the structure of the cap's wake, visualized in the cine film shown by Collins.

Though cap bubbles are important in fluidized beds of catalyst, there is more concern in technology with bubbles and drops suspended in bulk liquid undergoing shearing motion. Acrivos [390] reviews research on the simplest case: a neutrally buoyant drop in a linear shear field (one of many branches of our science in which McGill's experimentalist S. G. Mason and his theoretician co-workers have been leaders). Of greatest consequence are the deformation and burst of the drop. Depending on conditions, the drop may become a greatly elongated filament, or it may deform only moderately before bursting, i.e., fissioning

under the influence of applied surface traction. Acrivos emphasizes the practical importance of understanding the bursting phenomenon.

Somewhat similarly, a drop suddenly bludgeoned by the passage of a shock front may be merely set into oscillation (an outcome that might fit an analysis by Prosperetti or Alonso), or it may be sent into the sequence that leads to 'bag' breakup, or it may be shattered nearly outright. Photographic details are given by Reichman and Temkin [446]. Here too there are ample reasons to try to understand better the phenomena of breakup and shattering.

Surface tension gradients

A surface tension gradient is a shear stress applied by an interface on the adjoining bulk fluid. Viscosity propagates the effect deeper into the bulk. This cause of motion in real bubbles and drops is still too little appreciated. It can also resist movement brought about by other causes. Everyone working in this field should digest the movie made by Trefethen and the National Committee for Fluid Mechanics Films, Surface Tension in Fluid Mechanics, now distributed by Encyclopedia Britannica Educational Corporation.

Surface tension depends on temperature, electrical potential, composition. Thus a gradient of any of these along an interface causes a surface tension gradient and can thereby drive a flow — the so-called Marangoni effect. Moreover, a gradient perpendicular to the interface can in some circumstances be converted by 'Marangoni instability' into more or less steady convection. These are 'thermocapillary,' 'thermoelectric' and 'diffusocapillary' flows. Order of magnitude estimates indicate that the thermocapillary effect can produce more vigorous convection than buoyancy effects do in centimeter-scale systems.

Chang and Wilcox [194] validate these estimates by means of computer solutions of the heat transfer and Navier-Stokes equations for the floating zone

melt technique described by Carruthers [161]. Insofar as crystal growth and solidification are nonisothermal processes, it appears that absence of convection is an unattainable goal for those techniques prominently mentioned for space processing of materials. Dragoo's [208] simulations of spherical drops in non-uniform temperature fields provide additional indications of the importance of surface-tension-driven flow in low gravity environments.

Owing to the ubiquity of surface-active contaminants — whether adventitious or deliberately added, as were soap and Tang, the General Foods breakfast drink, for Skylab demonstrations — surface tension gradients caused by composition variations are the experimentalists' bane. Because fluid motion can cause local changes in surface area and these in turn alter surface composition, the gradient mechanism (reinforcing the effect of viscosity) can damp motion. This is often referred to as the Plateau-Marangoni-Gibbs effect and it can impede translation, dominate oscillation, and modulate breakup. It is itself reduced by diffusion, the fact behind Harper's suggestion that someone searching for experiments impossible on earth might consider a bubble rising with low Péclet number in 'ideal' surfactant solution.

In any event those who actually experiment with bubbles and drops in motion should be aware of tension gradient effects as described in Davies and Rideal's Interfacial Phenomena (1971), Levich's Physicochemical Hydrodynamics (revised edition in preparation), and more recent review articles.

Non-newtonian behavior

The commonest fluids under ordinary conditions display Newtonian viscosity. That is, stress is linear in strain rate and flow is dissipative, irreversibly doing away with mechanical energy. Thus bubbles and drops of Newtonian fluids serve as models for dissipative and radiative stellar and nuclear systems.

In many technologically important liquids there is microstructure giving rise to significant effects of shear thinning, extra normal stresses, and viscoelasticity. This is a large and difficult field, from which Zana and Leal [428] bring to attention some of the bubble and drop phenomena that have been observed. It is interesting that Alonso describes nuclear rheology in terms of the purely linear Kelvin, Maxwell, and Bingham materials.

Multiple bubbles and drops

Lauterborn and Bolle [322] report on interactions between two or more bubbles collapsing near one another. Theirs is a novel technique for producing synchronized cavitation bubbles by focused laser light. A clever extension by means of holography will enable them to study collapse behavior in arrays of many bubbles. Otherwise the hydrodynamic interaction of non-colliding globules is scarcely represented here, although it is a fairly well developed area, still quite active.

Colliding drops are another matter. Collision and coalescence — fusion or capture — are important processes in clouds and rain, as described by Neiburger et al. [465] and Saunders [487], and in models of nuclear fusion, as touched on by Alonso [139]. In both cases it is necessary to account for the actions of electrical charge, which, Saunders explains, are more varied in the meteorological setting owing to the presence of external electric field. The complicated process of coalescence, which requires thinning, nucleation and rupture of the intervening film of fluid, is vitally important in many fields of application of suspensions of bubbles and drops and so deserves greater attention than given it here.

While Acrivos, Leal and Saville all refer to problems of generating dispersions or of describing their rheology, the lone paper on collective behavior

of a swarm is Wijngaarden's [405] on pressure waves in bubbly liquids. Its matchings of experiment with theory, microscopic detail with macroscopic behavior, and, by means of an analogy, bubbly liquids with reactive gas solutions, make the paper a fine representative of its genre.

In cloud physics there are important droplet interactions by mass transfer. They are indirect, through the prevailing degree of saturation, in the growth of droplets on condensation nuclei, as discussed by Neiburger et al.[465] and in detail by Carstens and Carter [529]. The interactions are more direct in the growth of ice crystals at the expense of liquid droplets, the three-phase process described by Neiburger et al. Apart from these papers and those on growth in distributions of aerosol particles, there is little representation here of the mass transfer processes central to bubble and drop behavior in boiling and condensation. The major exception is Apfel's report on superheat experiments with acoustically levitated droplets [246].

External radiation pressure

Three of the most intriguing reports in the Colloquium are of techniques for levitating liquid drops by radiation pressure. Apfel [246] employs an acoustic standing wave field to suspend a droplet in the middle of host liquid. Wang et al. [266] apply the same principle to position a droplet in a gas-filled enclosure. Ashkin and Dziedzic [Applied Physics Letters 24 586-588 (1974), Science 187 1073-1075 (1975)] make use of the stable trapping of a nonabsorbing droplet in the high-intensity core of a laser beam; droplets with diameters in the range 1-40 microns are named. The technique can be used to impel two droplets together in a collision, or to force them slowly together until they coalesce.

The radiation intensity required depends on the difference between gravity and buoyancy forces on the droplet. Both decrease in proportion to the gravitational field and so radiation-pressure positioning is very attractive for low-gravity, containerless handling of liquids. Wang describes an apparatus under development for this purpose. The effects of even low radiation pressure on the dynamics of suspended drops remain to be assessed fully.

Possibilities for a weightless environment

In this observer's view the Colloquium proceedings reveal few unique opportunities for taking advantage of a zero-gravity laboratory to get scientific information that cannot be derived from experiments or simulations at the earth's surface.

One purpose of eliminating gravity might be to guide and to test theories of bubble and drop dynamics and other free surface flows. In such theories gravity can be isolated in a single dimensionless parameter which can equally well be made small by controlling other quantities in it, and thus it may be possible to simulate low gravity conditions experimentally, particularly if the total number of significant dimensionless parameters is small enough that all can be scaled simultaneously. An exception arises when the zero-gravity limit is singular, i.e. the predicted behavior at the limit is qualitatively different from the behavior as the limit is approached. In any case a weightless environment could be a convenience in developing and testing a theory.

A second purpose might be to examine the behavior of a laboratory model of a much larger or much smaller system, when both the prototype and the model are so complicated that numerical simulation is prohibitively expensive or even impossible. When the essence of the prototype's surroundings is the absence of a uniform external field like gravity at the earth's surface, a weightless

environment is certainly desirable. For a model to be successful the equation systems governing it and the essential features of the prototype must be known and must match. The difficulty here is likely to be the control of unwanted side effects in the model system — positioning disturbances and surface-active contamination of bubbles and drops, for examples. But a zero-gravity laboratory could be a great convenience for liquid-drop simulations of the dynamics of nuclear and stellar masses.

A third purpose of eliminating gravity might be to avoid buoyancy forces, which are the effect of gravity on all but perfectly aligned density gradients and density discontinuities. The main reason for avoiding buoyancy forces is to eliminate unwanted buoyancy-driven natural convection in systems with density gradients caused by heat or mass transfer. But wherever the gradients responsible for transfer reach to a fluid interface, surface tension gradients may drive equally undesirable natural convection.

A fourth purpose of eliminating gravity is to facilitate isolating a body of liquid from solid walls or a host liquid, that is, to make 'containerless processing' possible. There is still a problem of positioning and manipulating the liquid in the presence of a residual inertial force field. Radiation pressure may be the answer. Perhaps the most worthwhile possibilty that appears here is Wang's proposal of a low temperature experiment with a drop of super-fluid helium II in order to study the formation of quantized vorticity in the absence of any rigid containing wall.

Regardless of the purpose, the potential value of the result has to be assessed realistically and weighed first against the cost of the experiment in a zero-gravity laboratory and then against the cost of getting the same information

by the most economical means that can be devised — by expert experimental scientists who have substantial experience in the subject area. There will be trade-offs, of course. The choice will be biased if the zero-gravity laboratory is subsidized owing to extra-scientific factors. Such a laboratory appears to be a certainty. Thus the immediate challenge to science is to see that truly worthwhile scientific experiments are performed in the laboratory.

Concluding remark

As a unique opportunity for interdisciplinary exchange in the science of drops and bubbles the Colloquium has met the expectations of its planners and most if not all of its participants. For so uncommonly stimulating an experience all are grateful to the organizers and sponsors at the Jet Propulsion Laboratory and California Institute of Technology. Well done!

THE FISSION THEORY OF BINARY STARS

N. R. Lebovitz

University of Chicago

Abstract

About half the stars in the sky are binary stars. The fission theory, proposed by Poincàré in 1885, tries to explain the occurrence of binary stars by a natural process of evolution of a single star; in virtue of radiating energy, a rotating, axisymmetric liquid mass becomes highly flattened, becomes unstable, and continues its evolution along a series of progressively more elongated ellipsoids. When these become unstable, further evolution is supposed to take place along a series of "pear-shaped" figures, having a constriction in the middle. When this constriction has become deep enough, the figure consists effectively of a pair of detached masses orbiting one another.

Part of this picture lay on firm mathematical grounds; the rest depended on the outcome of a series of mathematical problems. By the 1920's, these problems had been worked out, their solutions were adverse to Poincàré's picture, and the fission theory became dormant. A recent reformulation of the theory, to bring it more nearly in line with newer astrophysical information, promises a different outcome to the analogous series of mathematical problems, and has awakened the fission theory.

INTRODUCTION

About half the stars in the sky are not individual stars at all, but binary stars, i.e., pairs of stars in orbit about a common center of mass. This figure (and the true fraction may be substantially greater than one-half; cf. [1]) is so large that it is not possible to regard the binary star as a freak occurrence without meaning for an understanding of the broad outlines of cosmogony. An explanation must be sought in the general framework of stellar origins and evolution.

Several suggestions as to the origin of binary and multiple systems have been made. Some of these, particularly those requiring two or more nearby points at which the interstellar medium begins the process of star formation, present mathematical

and formulational difficulties so great that it has not as yet proved possible to analyze them even approximately. They must be regarded as speculative at present. Two others have proved more or less tractable mathematically; these are the capture theory and the fission theory. It is widely agreed (1) that the capture theory is not capable of producing binary systems in anything like the large numbers observed.

The subject of this article is the fission theory. Briefly expressed, this theory provides a mechanism whereby a single, rotating star evolves into a pair of stars orbiting one another. The remaining sections are devoted to describing the mechanism in detail, explaining some of the criticisms that have been made against the fission theory during its long history, and how these criticisms are affected by recent theoretical developments. The last section is an assessment of the present status of the fission theory.

ELLIPSOIDAL FLUID MASSES

The model-context in which the fission theory is discussed is that of the Maclaurin spheroids and the Jacobi ellipsoids. We briefly describe these and certain generalizations of them here, referring to (2) for a fuller description and derivations.

An ellipsoidal fluid mass of uniform density ρ, rotating with a uniform angular velocity Ω, having semiaxes $a_1 \geq a_2 \geq a_3$, and subjected only to the force of its own gravitation, is a figure of relative equilibrum if

$$a_2 = a_1 \quad \text{and} \quad \Omega^2 = 2\left(A_1 - \frac{a_3^2}{a_1^2}A_3\right) \tag{1}$$

or if

$$a_1^2 a_2^2 A_{12} = a_3^2 A_3 \quad \text{and} \quad \Omega^2 = 2B_{12}, \tag{2}$$

where

$$A_i = \pi G \rho a_1 a_2 a_3 \int_0^\infty \frac{du}{(a_i^2+u)\{(a_1^2+u)(a_2^2+u)(a_3^2+u)\}^{1/2}} \qquad (i=1,2,3,)$$

and

$$A_{12} = \frac{A_1 - A_2}{a_2^2 - a_1^2}, \quad B_{12} = A_2 - a_1^2 A_{12}.$$

Here G is the universal constant of gravitation.

Equation (1) represents a sequence of spheroids, the Maclaurin spheroids. There is one such equilibrum figure for each value of a_3/a_1 between zero and one (or for each value of the eccentricity e of meridian sections in the same interval). Equation (2) represents a sequence of ellipsoids with unequal axes, the so-called Jacobi ellipsoids. It can be shown that for each value of a_2/a_1 between 0 and 1, there is a unique value of a_3/a_1 satisfying the first of equations (2). This gives the curve in the $(a_2/a_1)(a_3/a_1)$-plane marked $\Lambda = 0$ in Figure 1.

At the point along the Jacobi sequence where $a_2/a_1 = 1$, $a_3/a_1 = 0.5827$ (or $e = 0.8127$) and the two series have a member in common. This is the "point of bifurcation" to which reference will be made later.

These figures of relative equilibruim were shown by Riemann (3) to be special solutions of a much more general system of equations. Riemann considered the problem of finding the most general motions of a self-gravitating fluid of uniform density compatible with the assumption that the free surface remains an ellipsoid. This leads to motions of uniform vorticity relative to the rotating reference frame in which the ellipsoidal surface is at rest. Moreover, there is no requirement that the figures be in a steady-state: a system of ordinary differential equations determining the semiaxes and the parameters of the motion is obtained. These equations can take the form

$$\begin{aligned}
\ddot{a}_1 &= -2a_1A_1 + \frac{2p_c}{\rho a_1} + \frac{2K_1^2}{(a_1-a_2)^3} + \frac{2K_2^2}{(a_1+a_2)^3}, \\
\ddot{a}_2 &= -2a_2A_2 + \frac{2p_c}{\rho a_2} + \frac{2K_1^2}{(a_2-a_1)^3} + \frac{2K_2^2}{(a_1+a_2)^3}, \qquad (3) \\
\ddot{a}_3 &= 2a_3A_3 + \frac{2p_c}{\rho a_3},
\end{aligned}$$

with K_1 and K_2 constants depending on initial conditions. To these equations must be adjoined the equation of mass conservation $a_1a_2a_3\rho = \text{constant}$, and a constitutive equation relating the pressure at center p_c to other variables; if the fluid is incompressible, this relation is $\rho=\text{constant}$ and can be used to eliminate the central pressure from equations (3). We observe, however, that in Riemann's more general formulation, the fluid need not be incom-

pressible, i.e., ρ may be a function of time.

The system (5) allows equilibrium solutions, obtained by setting the time-derivative terms equal to zero. When mapped out in Figure 1, this family of equilibrium figures is found to occupy the horn-shaped region bounded above and below by the curves marked $K_2 = 0$ and $K_1 = 0$, respectively, and on the right by the segment of the Maclaurin series between $e = 0$ and $e = 0.9529$.

RESUMÉ OF THE FISSION THEORY

Although the earliest ideas of the fission hypothesis are attributable to Lord Kelvin (4) the theory only emerged in a complete form with the appearance of a remarkable memoir by Poincaré in 1885 (5). One of the outcomes of Poincaré's work was a description of how a single self-gravitating mass (a star or planet) might become a double system (a binary star or a planet-sattelite system). The mechanism, explained in the model-context of the Maclaurin spheroids and Jacobi ellipsoids, operates as follows.

Imagine a Maclaurin spheroid with an eccentricity e less than 0.8127. Suppose it contracts in virtue of radiating energy away, but so slowly as not to disburb the relative equilibrium. As it contracts, it becomes more flattened in virtue of angular momentum conservation. Ultimately it reaches the point of bifurcation where $e = 0.8127$. Beyond this point, the Maclaurin spheroid is known to be "secularly unstable," i.e., unstable if viscosity is present. Supposing the latter so, further evolution cannot proceed along the Maclaurin sequence, but must proceed along the Jacobi sequence which is known to be secularly stable. Next a further point of bifurcation, where a new, so-called pear-shaped series, branches off the Jacobi series, is attained. Assuming the Jacobi series secularly unstable past the new point of bifurcation and the pear-shaped series secularly stable, further evolution must proceed along the latter series.

In Poincaré"s original memoir, a sketch of the pear-shaped figure was given showing it to have the shape suggested by its name. The two ends of the figure are rather thicker than the central portion, which appears constricted. Poincaré suggested that this constriction narrows as evolution along the pear-shaped sequence continues. When it has narrowed to the extent that the figure consists essentially of a pair of detached masses connected by a narrow neck, the system is a binary system.

This picture that Poincaré painted rested on a basis of solid mathematical reasoning up to and including the computations implying the existence of the pear-shaped sequence that branches off the Jacobi sequence. Two important elements in his description, however, were conjectures as to the outcomes of certain complicated problems left open to subsequent research. One of these

conjectures was that the pear-shaped series is secularly stable. This conjecture was taken up by Darwin (6), Liapounov (7), and Jeans (8). Although Darwin initially concluded stability, the others instability, Jeans further detected a minor error in Darwin's computations which, when corrected, also led to the conclusion of instability.

The other principal conjecture was that the instability along the Jacobi sequence was a secular and not a dynamical instability, implying that the ensuing motions take place on the viscous timescale T_ν rather than on the much shorter dynamical timescale. This requires further explanation.

The instability along the Maclaurin sequence that sets in at $e = 0.8127$ (at the point of bifurcation where the Jacobi sequence branches off) is a secular instability only; i.e., if viscosity is absent, the Maclaurin sequence is stable down to $e = 0.9529$ (where the curve $K_1 = 0$ intersects the Maclaurin line $a_2/a_1 = 1$; cf. Fig. 1). If viscosity is present, the Maclaurin spheroids are unstable for $e > 0.8127$, and the e-folding time is the viscous diffusion time T_ν. Poincaré conjectured that the same situation prevailed along the Jacobi sequence. The reason, or rather, the hope, behind this conjecture was the conviction that, if the instability were dynamical, rapid motions, on the dynamical timescale would ensue, and it would not be possible to infer the subsequent behavior on the basis of equations of equilibrium: the full, dynamical equations would then have to be used. But this conjecture that the instability is secular and not dynamic is also wrong, as Cartan showed in 1924 (9).

CRITICISMS OF THE THEORY

The adverse outcomes to the two problems left open by Poincaré appeared to destroy the theoretical foundations of the fission theory, because the fluid mass no longer has any stable state toward which it can evolve, and its behavior must indeed be dynamical. While the result of this dynamical behavior may yet be a binary system ([10], [11]), the arguments used to infer this are of a highly speculative character. Moreover, there are further criticisms of the theory. It may be useful to list the principal criticisms:

1. The Jacobi sequence is dynamically unstable at the point where the pear-shaped sequence bifurcates.

2. The pear-shaped sequence is unstable.

3. The theory refers to incompressible masses, whereas stars are gaseous.

4. The theory relies on the presence of viscosity, implicitly assuming that the viscous timescale T_v is short compared to the contraction timescale T_c, whereas the opposite is true (12).

This list is by no means complete, but is perhaps sufficient to make one wonder why there remains any interest in the fission theory. One reason, no doubt, is the vague feeling that the adverse conclusions are in some measure due to the unrealistic character of the model, and that the qualitative picture may yet be right. Recent developments support this feeling.

RECENT DEVELOPMENTS

Many of the criticisms of the fission theory can be answered. In this section we concentrate on the four criticisms listed in the preceding section (for a fuller discussion, see ref. [13]).

The first criticism in that list is a criticism only because of the conviction that the occurrence of a dynamical instability requires solving the full, dynamical equations to follow up its consequences. Now, this need not be the case where two timescales are involved (13). Recent work on similar, but mathematically simpler, problems of this kind shows that motion may always take place on the slow timescale, except for a very short time interval during which the evolutionary path shifts from one stable branch of equilibrium solutions to another (14), (15).

Turning to the second criticism in that list, the instability of the pear-shaped sequence, we observe that the question of stability or instability is very sensitive to the change in energy on going from the ellipsoidal to the pear-shaped figure. In a star, an important contribution to the total energy is made by the internal energy. This contribution is suppressed by the assumption (criticism 3) of incompressibility. Hence criticisms 2. and 3. may be closely related, and reformulation of the problem that answers criticism 3. may well yield a conclusion of stability rather than instability for the pear-shaped sequence.

A form of the theory free of the fourth criticism has recently been given (13), (16). It also answers criticism 3. to the extent of allowing for internal energy, as well as gravitational and kinetic energy. It is formulated in the context of the Riemann ellipsoids with ρ a function of time. Instead of evolving along the Maclaurin-Jacobi sequence as in the classical theory, the fluid mass evolves along the Maclaurin series to the point marked O in Figure 1, and thereafter along the series marked $K_1 = 0$. Instability (analogous to that of Jacobi sequence) sets in at the point marked L_1. Hence the evolution is qualitatively similar to that of the classical theory, at least to the point where the ellipsoidal sequence encounters a point

of bifurcation. The dashed line in Figure 1 represents a sample trajectory that starts out almost, but not quite, axisymmetric.

PRESENT STATUS

Insofar as the four criticisms explicitly dealt with are concerned, it would appear that none of them need apply in the reformulated version of the theory referred to in the preceding section, although the question of the stability of the analogue of the pear-shaped sequence has yet to be settled.

Other criticisms can be made, and it may not be possible to answer them all to the critic's satisfaction, so the question whether the fission theory is or is not a viable explanation for the occurrence of binary stars may never have a universally accepted answer. We can, however, say the following: whereas it appeared some years ago that the fission theory may have been incompatible with the laws of dynamics, this no longer appears to be the case.

Further research along the lines of working out, and testing the stability of, the analogue of the pear-shaped sequence should do much to clarify the situation.

REFERENCES

1. A. H. Batten, "Binary and Multiple Systems of Stars," Pergamon Press, Oxford (1973)

2. S. Chandrasekhar, "Ellipsoidal Figures of Equilibrium," Yale University Press, New Haven (1969)

3. H. Poincaré, "Sur l'Equilibre d'une Masse Fluide Animeé d'un Mouvement de Rotation," Acta Mathematica 7, p. 259 (1885)

4. B. Riemann, "Gesammelte Mathematische Werke," Verlag von B. G. Teubner, Leipzig (1892)

5. W. Thomson and P. Tait, " Treatise on Natural Philosophy," Cambridge University Press, Canbridge (1890)

6. G. H. Darwin, "The Stability of the Pear-shaped Figure of Equilibrium of a Rotating Mass of Fluid," Phil. Trans. Roy. Soc. A, 200, p. 251 (1902)

7. A. N. Liapounov, " Sur un Probleme de Tchebychef," Memoires de l'Academie de St. Petersbourg, XVII, 3 (1905)

8. J. H. Jeans, "On the Instability of the Pear-shaped Figure of Equilibrium of a Rotating Mass of Liquid" Phil. Trans. Roy. Soc. A, 217, p. 1 (1918)

9. E. Cartan, "Sur la Stabilité Ordinaire des Ellipsoides de Jacobi," Proc. International Math. Congress, Toronto, 1924, 2, University of Toronto Press, Toronto (1928)

10. J. H. Jeans, "Astronomy and Cosmogony," Cambridge University Press, Cambridge (1928)

11. R. A. Lyttleton, "The Stability of Rotating Liquid Masses," Cambridge University Press, Cambridge (1953)

12. D. Lynden-Bell, "On Large-Scale Instabilities During Gravitational Collapse and the Evolution of Shrinking Maclaurin Spheroids," Astroph. J., 139, p 1195 (1964)

13. N. R. Lebovitz, "On the Fission Theory of Binary Stars," Astroph. J. 175, p 171 (1972)

14. R. J. Schaar, "The Singularly Perturbed Initial-Value Problem when the Reduced Path Encounters a Point of Bifurcation," Doctoral thesis, University of Chicago (June 1974)

15. N. R. Lebovitz and R. J. Schaar, "Exchange of Stabilities in Autonomous Systems," in preparation

16. N. R. Lebovitz, "The Fission Theory of Binary Stars. II. Stability to Third-Harmonics Disturbances," Astroph. J., 190, p. 121 (1974)

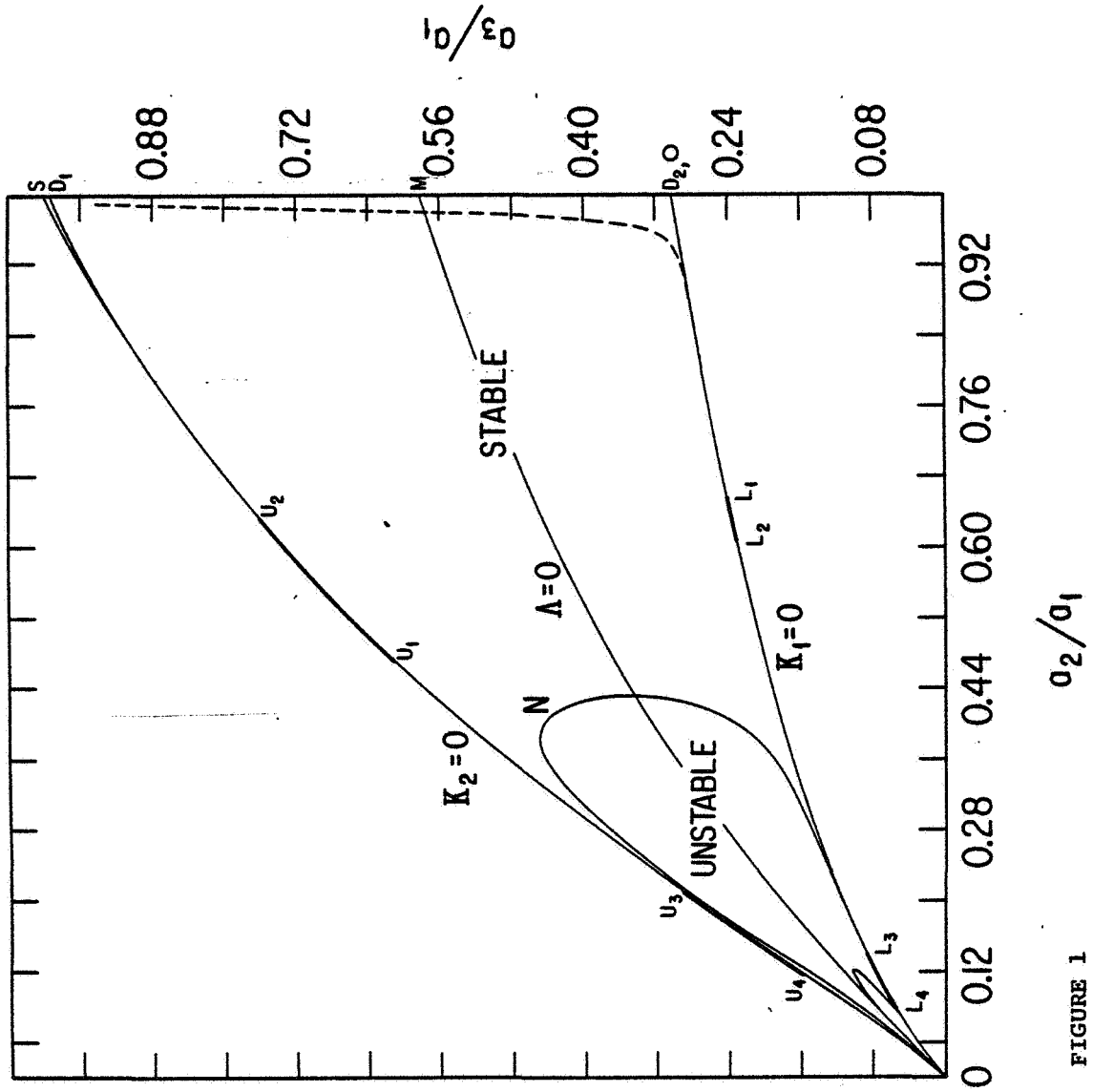
a_3/a_1
0.88
0.72
0.56
0.40
0.24
0.08
S
D_1
M
D_2, O
U_2
U_1
$K_2=0$
STABLE
$\Lambda=0$
N
UNSTABLE
U_3
U_4
L_3
L_4
L_2 L_1
$K_1=0$
0
0.12
0.28
0.44
0.60
0.76
0.92
a_2/a_1

FIGURE 1

D2

ROTATING STARS

D.O. Gough

Institute of Astronomy & Department of Applied Mathematics
and Theoretical Physics, University of Cambridge,
& National Center for Atmospheric Research, Boulder, Colorado

ABSTRACT

A normal star is a mass of compressible gas of low Prandtl number, held together by its own gravitational force. It generates energy principally in its central regions, either by very slow gravitational contraction or, more commonly, by thermonuclear reactions; this energy is subsequently transported to the surface down a temperature gradient by radiative diffusion or convection.

If the star has no angular momentum the equations governing its motion admit spherically symmetric stationary solutions. But if the star is rotating it is not possible in general for it to exist in a state with no motion other than its rotation; meridional currents are set up which advect angular momentum through the star. The details of this process are not well understood. Stability calculations seem to imply that no stable steady solutions exist.

The distribution of angular momentum in a star depends on a balance between transport by the large scale meridional motions and by the Reynolds stresses of turbulence. Neither theory nor observation is yet sufficiently refined to deduce what that distribution is even in the sun.

INTRODUCTION

The structure and evolution of the majority of stars for most of their life seem to be well represented by theoretical models that ignore the fact that they rotate. This is because the ratio of the centrifugal to gravitational forces, or rotational Froude number, is low, and for many purposes the dynamical effects of rotation produce only a small perturbation from a nonrotating configuration. Nevertheless rotation presents some very interesting fluid dynamical problems which are the subject of this review.

The astrophysical consequences of rotation in stars are not without interest. Rotation affects the spectra of the emitted radiation from which conditions in stellar atmospheres are deduced, and the possibility of rotationally induced mixing, which is discussed below, has important implications concerning the nuclear transmutations that occur in stellar cores. In addition, there are stars which appear to be rotating so rapidly that the dynamical effects of the centrifugal force have a significant influence on their evolution. These matters are not discussed

here; instead the reader is referred to the reviews by Strittmatter [1] and Fricke and Kippenham [2], and the IAU colloquium proceedings edited by Slettebak [3].

Stars condense from the interstellar medium and at some point attain a state of hydrostatic equilibrium. They are opaque and hot in the centre, the stored heat maintaining a pressure gradient which balances gravity. Their structure is such that the balance

$$2T + V = 0 \tag{1.1}$$

is satisfied, where V is the gravitational potential energy of the star and T the total kinetic energy, both macroscopic and microscopic [4]. This is the virial theorem of Poincaré and Eddington, and assumes that no body force other than gravity is exerted on the star. Normal stellar material is gaseous and can be assumed to satisfy the usual equations of fluid dynamics. The perfect gas law

$$p = \frac{R\rho T}{\mu} \tag{1.2}$$

is approximately satisfied, where p, ρ and T are pressure, density and temperature, R is the gas constant and μ is the mean molecular weight of the gas (mean mass per particle measured in units of the hydrogen atomic mass) which depends upon the chemical composition and the state of ionization. Radiation pressure is usually comparatively small and will be ignored in this discussion.

If all the kinetic energy of the stellar material is in microscopic particle motions (so there is no fluid motion) equation (1.1) may be written

$$3(\gamma - 1)U + V = 0, \tag{1.3}$$

where U is the total internal energy of the gas and γ an appropriate mean ratio of principal specific heats. The total energy of the star is

$$E = U + V = -(3\gamma - 4)U. \tag{1.4}$$

It can be shown that for the star to be dynamically stable γ must exceed 4/3. Thus as energy is lost by radiation from the stellar surface, E decreases and U increases. The star contracts slowly, liberating gravitational energy which is partly radiated away and partly stored in the compressed heated gas. This process, first discussed by Kelvin and Helmholtz, is controlled by the rate radiation can escape by diffusion from the star. It continues until the centre becomes so hot that nuclear reactions begin to take place. Contraction halts; the star has reached the main sequence, the total energy output, or luminosity, at the surface being supplied entirely by the thermonuclear reactions. Its gross structure now depends primarily on just its mass. On the main sequence stars convert hydrogen, their principal constituent, into helium. This is the longest phase of their evolution, and consequently most of the visible stars in the sky are main sequence stars.

Once hydrogen has been exhausted from the reacting core further gravitational contraction and additional nuclear reactions take place, the details depending on the star's mass and composition, and eventually the star contracts into its final state : a cooling white dwarf supported against gravity by a sea of degenerate electrons, a neutron star of degenerate nuclear matter, or perhaps a black hole.

This review does not attempt to discuss the properties of a star in all stages of its evolution, but concentrates on the main sequence. Magnetic fields, which are undoubtedly important in some stars, are hardly considered; it seems prudent to try to understand first what is probably the simpler dynamics of a nonmagnetic star. Observational techniques are not discussed at all.

If one plots the mean surface rotation rates of main sequence stars as a function of their mass M the most striking feature is an abrupt rise, in the vicinity of 1½ solar masses, from approximately zero to a value corresponding to a Froude number which is an appreciable fraction of unity [5]. Observations of the distribution of angular velocity across the surface have been made only for the sun, which is a typical slowly rotating star. The angular velocity Ω varies by about 20% from pole to equator, the rotational Froude number $R_\odot^3\Omega^2/GM_\odot$ being about 2×10^{-5} [6], where $M_\odot$ and $R_\odot$ are the solar mass and radius and G the gravitational constant. These are the principal main sequence observations a theory of stellar rotation must explain.*

Aside from the astrophysical and fluid dynamical aspects of the solar rotation interest has recently been aroused in connection with gravitation theory. One of the major puzzles of the last century was the discrepancy between the measured precession of the perihelion of the orbit of Mercury and the predictions of Newtonian gravitation theory [7]. One of the proposed explanations was that the sun was oblate, but the observed oblateness [8,9] turned out to be too small to account for the precession [10]. With the advent of General Relativity, however, it was generally agreed that the problem had been resolved, because Einstein's theory predicted the observed result [11]. But more recently Dicke [12] and Roxburgh [13] proposed that the apparent agreement was fortuitous, and that an alternative theory of gravitation [14] based on the scalar-tensor theory of Jordan [15], which predicts a lower precession rate, is correct, the residual precession of Mercury's orbit arising from an assumed oblateness of the sun's figure. Subsequently the shape of the sun's image was remeasured by Dicke and Goldenberg [16, 17]. An oblateness of about the required value was reported, if it is assumed that the oblateness of the image implies a similar oblateness in the shape of the gravitational equipotentials. That this assumption is justified has been argued by Dicke but has not been generally accepted [17,18]. This important issue will be discussed in the concluding section of this review.

---

*Perhaps the most important question of the subject is why stars exist at all, for had they condensed conserving angular momentum to their present size from interstellar material with initial rotation rates typical of the galactic rotation they would not be gravitationally bound. This is a problem in star formation.

In the next section possible steady solutions of the equations governing rotating stars are discussed. Their stability is considered in the subsequent section, and the final section is addressed to how angular momentum is distributed thoughout a star as it evolves. But before that a few remarks about the magnitudes of quantities pertaining to stars are perhaps not out of place.

The sun, which may be considered representative, has a mass $M_\odot = 2 \times 10^{33}$ g, a radius $R_\odot = 7 \times 10^{10}$ cm and a luminosity $L_\odot = 4 \times 10^{33}$ erg sec^{-1}. At a distance of about 0.5 $R_\odot$ from the centre its density is about the same as its mean density which is approximately the density of water, and its temperature is about 3×10^6 °K; the central density and temperature are about 100 g cm^{-3} and 1.5×10^7 °K. At the visible surface, or photosphere, its density and temperature are about 3×10^{-7} g cm^{-3} and 5800 °K. The outer 20% by radius is in a state of turbulent convection and the rest is generally believed to be convectively stable. Qualitatively this is a property of all stars at the low mass end of the main sequence (lower main sequence); the higher mass rapidly rotating stars of the upper main sequence have only thin weak convective regions near the surface, and they also have convective central cores.

Energy is transported through the convectively stable regions of a star principally by radiative diffusion. Except near the surface, the energy flux $\underset{\sim}{F}$ satisfies

$$\underset{\sim}{F} = - K \nabla T , \qquad (1.5)$$

where $K = 4acT^3/3\chi\rho$ is the radiative conductivity; a is the radiation constant, χ the opacity of the gas and c the velocity of light. At a median point in the sun its value is about 10^{15} erg cm^{-1} sec^{-1} $°K^{-1}$. The kinematic shear viscosity arising from photon momentum transport is $\nu_r = 4aT^4/15\ \chi\rho^2 c \simeq 1$ cm^2 sec^{-1} at a radius r of 0.5 $R_\odot$ and increases with r nearly everywhere. Viscosity due to microscopic particle ion motions ν_i is of order $m_p^{\frac{1}{2}}(kT)^{5/2}/(e^4\rho\ \ln A)$ where $A = (m_p/\rho)(kT/e^2)^3$, m_p and e are the proton mass and charge and k is the Boltzmann's constant; this is about 10 cm^2 sec^{-1} at $r = 0.5\ R_\odot$ and increases slowly with r.

From these values can be calculated a timescale characteristic of large scale dynamical motions : the time for free fall under gravity from surface to centre. In view of the balance (1.1) this is of the same order as the sound travel time τ_p and is about 1 hr. The thermal diffusion time across a distance $R_\odot$ is equal to the Kelvin-Helmholtz gravitational contraction time $\tau_{KH} \simeq 10^7$ yr and is short compared with the nuclear time $\tau_n \simeq 10^{10}$ yr to convert say 10% of all the hydrogen to helium at the current luminosity. The age of the sun $\tau_\odot$ is 5×10^9 yr.

The Reynolds number associated with the smallest velocity that can be of global significance in this time, $R_\odot/\tau_\odot$, is $R_\odot^2/(\nu_r+\nu_i)\tau_\odot = 3000$. In other words, the characteristic viscous diffusion time is much larger than the age of the sun. For flow velocities comparable with the rotation speed (about 2 km sec^{-1} at the equator) the Reynolds number is of order 10^{16} throughout most of the star. Under most circumstances, therefore, viscous forces can be ignored. Only in the extreme outer regions and in boundary layers might this not be so. The Prandtl number $(\nu_r+\nu_i)\rho C_p/K$, where C_p is the specific heat at constant pressure, is about 10^{-6} at a median point.

STEADY ROTATING CONFIGURATIONS

As with most physical systems it is expedient to seek the steady configurations first. They are comparatively simple to analyse and, if stable, are states towards which one might expect stars to evolve.

In most of the published work steady axisymmetric models are constructed in which the only motion is a rotation about the z axis. The momentum equation then reduces

$$-\nabla p + \rho\nabla\Phi + \rho\Omega^2\underset{\sim}{\varpi} = 0, \tag{2.1}$$

where $\underset{\sim}{\varpi}$ is the cylindrical radius vector from the z axis, Ω is the angular velocity and Φ is the gravitational potential which satisfies

$$\nabla^2\Phi = -4\pi G\rho. \tag{2.2}$$

In equation (2.1) viscous forces have been ignored and it has been assumed that no magnetic field is present.

The simplest models to analyse are of white dwarfs. In these stars the electrons are degenerate and a barytropic equation of state is a good approximation. Because the fluid is assumed inviscid the angular velocity distribution is not determined completed by the equations of motion. However, it follows immediately from equation (2.1) that the centrifugal force is derivable from a potential V and that Ω varies only with distance ϖ from the axis of rotation. Accordingly equation (2.1) reduces to

$$\nabla p = \rho\nabla(\Phi + V) \equiv \rho\nabla\Psi, \tag{2.3}$$

from which it follows that p and ρ are constant on surfaces of Ψ , or level surfaces. There remains considerable freedom in the choice of $\Omega(\varpi)$. It can be set by specifying, for example, the angular momentum per unit mass h(m), where m is the mass enclosed in a cylinder ϖ = constant. Then any choice of h(m) leads to a solution. It was pointed out by Ostriker and Mark [19] that $\Omega(\varpi)$ cannot be specified arbitrarily.

An important consequence of rotation concerns the possible masses of white dwarfs. The equation of state of the degenerate white dwarf material is such that in the special case of no rotation there is a maximum mass M_c which can be supported against the self gravity of the star. This was first demonstrated by Chandrasekhar [20] who found

$M_c \approx 1.44\ M_\odot$. The estimate has been revised with the use of a more refined equation of state [e.g. 21], but the principle is unchanged and for a long time it was commonly believed that M_c was an upper limit to the masses of real white dwarfs. However, it was emphasised by Mestel [22], for example, that this limit applies only to nonrotating spherically symmetric configurations, and Ostriker, Bodenheimer and Lynden-Bell [23] suggested that rotating white dwarfs with masses much greater than M_c exist. Because gravitational forces scale with their characteristic length L as L^{-2} and centrifugal forces as L^{-3} for a star whose mass and angular momentum are conserved, a rotating star more massive than M_c would be prevented from collapsing indefinitely by the centrifugal forces. Indeed Ostriker et al. pointed out that were it not for the changes in physics that occur at extremely high densities a strict upper bound to the possible masses of rotating white dwarfs would be removed entirely, whatever the angular momentum.

More interesting from a fluid dynamical point of view are the nondegenerate main sequence stars for which temperature is present in the equation of state. In these stars energy is transported down the temperature gradient from centre to surface. Now configurations in which the only motion is rotation with an associated conservative centrifugal force field do not occur, and much of the wisdom gained from the simple barytropic models is not very useful. In general the energy transport equation does not permit T to be constant on level surfaces. Consequently, in view of equation (1.2), p and ρ cannot both be constant on level surfaces, which implies that the momentum equation (2.3) cannot be accurately satisfied. The unbalanced pressure gradients drive a circulation $\underset{\sim}{u}$ in meridional planes which advects both heat and angular momentum through the star [24-26].

Except in the surface layers of the star the motions induced are so slow that inertial forces are negligible compared with the other terms in the momentum equation so that equation (2.3) is very nearly satisfied. For a given rotation field the circulation velocity can thus be estimated from the energy equation

$$\rho C_p \underset{\sim}{u}.\nabla T - \delta \underset{\sim}{u}.\nabla p = \rho\varepsilon - \operatorname{div} \underset{\sim}{F} \qquad (2.4)$$

simply as that required to transport the requisite amount of heat to maintain p, ρ and T (very nearly) constant on level surfaces. In equation (2.4) $\delta \equiv -\left(\frac{\partial \ln\rho}{\partial \ln T}\right)_p$ and ε is the thermonuclear energy generation rate per unit mass. Thus equation (2.5) may be rewritten approximately :

$$\frac{\rho T C_p}{p} (\nabla - \nabla_{ad}) \underset{\sim}{u}.\nabla \Psi = \varepsilon - \frac{1}{\rho} \operatorname{div} \underset{\sim}{F}, \qquad (2.5)$$

where $\nabla = \frac{d\ln T}{d\ln p}$ and $\nabla_{ad} = \left(\frac{\partial \ln T}{\partial \ln p}\right)_s$, the derivative being taken at constant specific entropy s, and

$$\operatorname{div} \underset{\sim}{F} = - f'(\Psi)\left|\nabla\Psi\right|^2 + f(\Psi)\left[\frac{1}{\varpi}\frac{d}{d\varpi}(\varpi^2\Omega^2) - 4\pi G\rho\right], \tag{2.6}$$

where $f(\Psi) = K\frac{dT}{d\Psi}$ and a prime denotes differentiation with respect to the argument. It is immediately clear from (2.5) and (2.6) that $\underset{\sim}{u}$ cannot be zero if Ω is constant, for since all the terms in (2.6) except $\nabla\Psi$ are then constant on level surfaces it would follow that $f'(\Psi) = 0$ and $\epsilon = 2(\Omega^2/\rho - 2\pi G)f$; in general this cannot be satisfied because ϵ depends on nuclear physics, and hence on ρ and T but not on Ω, and in particular is essentially zero in all but a central core of the star [27]. There is no general proof that $\underset{\sim}{u} = \underset{\sim}{0}$ when Ω is a function of ϖ alone, though it has been shown to be the case if $\frac{1}{\varpi}\frac{d}{d\varpi}(\varpi^2\Omega^2) - 4\pi G\rho$ vanishes in a region in which $\epsilon = 0$ [28]. Detailed calculations of the meridional flow were first performed by Sweet [29] who assumed slow uniform rotation.

The magnitude of this meridional Eddington-Sweet circulation velocity u can be estimated from equations (2.5) and (2.6) to be [30]

$$u \sim \lambda \frac{L}{Mg}\left(\frac{1}{\nabla - \nabla_{ad}}\right)\frac{\bar{\rho}}{\rho}, \tag{2.7}$$

where M, L and $\bar{\rho}$ are the mass, luminosity and mean density of the star, g is gravitational acceleration and $\lambda = R\Omega^2/g$ is the Froude number. This estimate has been confirmed by detailed computations for certain specified nonuniform rotation laws with λ small [31] by expanding in powers of λ about the nonrotating configuration; the case of uniform rotation is singular but appears to yield similar velocities [29, 32].

So far it has been implicitly assumed that the stellar fluid is chemically homogeneous. Nuclear transmutations in the cores of main sequence stars generate gravitationally stable gradients in the mean molecular weight μ. According to Mestel [33] these prevent the Eddington-Sweet circulation from penetrating the core by deflecting them in a thin viscous boundary layer.

It has been of some concern that the Eddington-Sweet circulation velocity, in the present approximation, diverges at the surface of the star where the density is almost zero. This arises because the heat capacity of the gas per unit volume is too low to transport at low

velocities the flux of heat required to satisfy equations (2.5) and (2.6). Smith [34] pointed out that excessive demands were being made by the diffusion approximation (1.5) near the stellar surface, where it isn't valid, and showed that the situation was alleviated somewhat by using a more careful treatment of radiative transfer for the outer layers [see also ref. 35]. The velocities were still so great near the surface that the assumptions of the procedure, such as the neglect of the inertia terms, are hardly plausible, and Smith concluded that in any case the flow would be liable to shear instabilities.

Smith's analysis, in common with earlier work, assumed an inexorable uniform rotation, a weak poloidal magnetic field having been invoked to preserve it. In the absence of such a field, advection of angular momentum by meridional circulation is inevitable, and a state of nonuniform rotation would rapidly be set up in the surface layers. Osaki [36] argued, without proof, that in that event readjustment of the angular velocity distribution would be such as to reduce the meridional circulation velocity in the stellar atmosphere to zero.

Another place where the circulation is unable to advect heat efficiently is at the edge of a convection zone where $\nabla = \nabla_{ad}$, this time because the slowly rising or falling fluid, which maintains pressure balance with its surroundings, cannot modify the temperature difference between it and its environment. Once again equation (2.5) demands an infinite velocity unless div $\underset{\sim}{F} = \rho\varepsilon$ when $\nabla = \nabla_{ad}$, which is not generally the case for an arbitrarily specified distribution of angular momentum. Osaki [37] pointed out once again that this implies that a steady solution does not exist for the assumed rotation law, and that appropriate readjustments must take place.

From (2.7) can be estimated the timescale for stellar material to traverse a distance comparable with the radius R of the star :

$$\tau_{ES} = \frac{R}{u} \approx \lambda^{-1}\tau_{KH} \approx 2 \times 10^{-3}\left(\frac{M}{M_\odot}\right)\left(\frac{R}{R_\odot}\right)^{-1} \lambda^{-1}\tau_n. \qquad (2.8)$$

For the sun $\tau_{ES} \approx 100\ \tau_n$, if it assumed to rotate with about its surface angular velocity throughout, which suggests that little advection of angular momentum by Eddington-Sweet currents is taking place. This conclusion must be treated with some caution, however, because the estimate (2.8) is very approximate and there is evidence [38] that it overestimates the circulation time somewhat. For the rapidly rotating upper main sequence stars $\tau_{ES} \approx 10^{-2}\ \tau_n$ and considerable readjustment of the rotation field must have occurred.

The advection of angular momentum by meridional currents has not been discussed in great detail, though Sakurai [38] has considered the early stages of evolution of a simplified solar model from a state of rigid rotation. A steady state with circulation must have $\varpi^2\Omega$ constant on streamlines, which implies that Ω is generally greater near the rotation axis. However, Mestel [30] has suggested that a star that conserves its angular momentum will redistribute it in such a way as to choke off completely the meridional flow. Accordingly one might seek (nonconservative) rotation laws which drive no Eddington-Sweet

circulation. Schwarzschild [39], Roxburgh [40,41] and Clement [42] have attempted this, but their models are not entirely consistent. However even if consistent models are obtained, either with or without circulation, it is not at all obvious that a star could actually evolve to such a state. Furthermore, as is discussed in the next section, it seems likely that all steady solutions are unstable.

This discussion has concentrated on the rotation of regions that are stable to convection. In convection zones too meridional currents are likely to arise except for very special distributions of angular momentum [43], but here the dynamics is complicated by the influence of the rotation on the convection. It is common practice to assume the Reynolds stresses act to force rigid rotation [39-42], though other assumptions have been made when discussing the convective envelope of the sun [see final section].

There has been no detailed study of nonaxisymmetric configurations of the type discussed by Lebovitz [44] using an equation of state that is realistic for stars.

STABILITY

The discussion will be limited to instabilities that arise directly from the rotation of the star. Dr Lebovitz has already explained what is known about fission [44] and I shall dwell on it no further. Of the modes of instability that remain the most widely studied have been the axisymmetric ones on a length scale small compared with the characteristic scale of variation of the basic 'equilibrium' state, and which derive from the Rayleigh instability.

Rayleigh [45] argued, by analogy with the instability of a density stratified fluid under gravity and by energy considerations, that a uniform incompressible inviscid fluid, steadily rotating between two coaxial cylinders, is stable to axisymmetric perturbations if

$$\frac{d}{d\varpi}(\varpi^2\Omega)^2 > 0 \qquad (3.1)$$

everywhere in the fluid, and is unstable if (3.1) is violated anywhere. For an inhomogeneous incompressible fluid the criterion is

$$\frac{d}{d\varpi}(\rho\varpi^4\Omega^2) > 0. \qquad (3.2)$$

It is possible to perform a proper perturbation analysis to establish that criterion (3.2) is both necessary and sufficient for stability to axisymmetric perturbations [46]. Generalization to the more complicated flows encountered in stellar models is difficult, however, and one must resort to other arguments. A powerful method which is relatively simply to handle is to use the principle of virtual work : an infinitesimal virtual adiabatic displacement ξ of the fluid is imagined to occur and the energy difference δE between the final and initial states is computed. If $\delta E > 0$ for all possible ξ

there is no energy available in the fluid to drive any disturbance, and the basic state is stable. On the other hand, if displacements $\underset{\sim}{\xi}$ exists for which $\delta E < 0$ instability cannot be deduced (unless ~~$\delta E < 0$ for all $\underset{\sim}{\xi}$) unless it can be demonstrated that~~ δE is negative for a realizable disturbance which satisfies the equations of motion. However, even though instability cannot be strictly proved, in most of the special cases that have been investigated instability has been found. The method has been used by Høiland [47] who used d'Alembert's principle to estimate the frequencies of linearized axisymmetric adiabatic perturbations of a purely rotating flow. The criterion for the stability of such a flow is that the quadratic form in ξ:

$$I \equiv \left[\frac{1}{\varpi^3}\frac{\partial C^2}{\partial \varpi} + g_\varpi \frac{\partial \ln q}{\partial \varpi}\right]\xi^2 + \left[\frac{1}{\varpi^3}\frac{\partial C^2}{\partial z} + g_\varpi \frac{\partial \ln q}{\partial z} + g_z \frac{\partial \ln q}{\partial \varpi}\right]\xi + g_z \frac{\partial \ln q}{\partial z} \quad (3.3)$$

is positive definite everywhere. Here g_ϖ and g_z are the ϖ and z components of the apparent gravitational acceleration g' (which includes the centrifugal acceleration) C is the circulation $\varpi^2\Omega$ and q is the potential density [i.e. the density the fluid would have if brought to a standard pressure; thus the difference dq in potential density between two neighbouring points is $d\rho - \left(\frac{\partial \rho}{\partial p}\right)_s dp = \frac{\rho}{C_p}\left(\frac{\partial \ln \rho}{\partial \ln T}\right)_p ds$ if the fluid is chemically homogeneous]. The form $I(\xi)$ is positive definite if the conditions

$$\Lambda_1 \equiv \frac{1}{\varpi^3}\frac{\partial C^2}{\partial \varpi} + g_\varpi \frac{\partial \ln q}{\partial \varpi} \geq 0 \quad (3.4)$$

and

$$\Lambda_2 \equiv (\nabla q \wedge \nabla C^2) \cdot (\underset{\sim}{g}' \wedge \underset{\sim}{\varpi}) \geq 0 \quad (3.5)$$

are simultaneously satisfied. In deriving the second condition the curl of the momentum equation governing the steady state in the form

$$\underset{\sim}{g}' \wedge \nabla \ln q = \frac{1}{\varpi^3}\frac{\partial C^2}{\partial z}\underset{\sim}{e}_\phi \quad (3.6)$$

was used, where $\underset{\sim}{e}_\phi$ is a unit toroidal vector. These conditions were obtained earlier from an approximate analysis by Solberg [48] who considered the motion of a displaced parcel of fluid in pressure equilibrium with its surroundings.

The analysis of Høiland provides sufficient but not necessary conditions for stability. A more recent derivation, which amounts almost to the same thing, is presented by Fricke and Smith [49] using a variational principle derived by Lynden-Bell and Ostriker [50]. Using the variational principle is potentially more powerful, for if it can be shown that the eigenfunctions of the linear stability problem form a complete set it is a simple matter to show without solving the equations that conditions (3.4) and (3.5) are also necessary.

In certain special cases conditions (3.4) and (3.5) reduce to previously known criteria. When $\Omega = 0$, $\Lambda_2 = 0$ and equation (3.6) implies that ∇q and $\underset{\sim}{g}$ are parallel. Condition (3.4) then reduces to the well known requirement that for stability the potential density must decrease upwards; for a compressible atmosphere this is the condition for convective stability [51, 52]. For rotation independent of z in the absence of gravity, Λ_2 is again zero; if the flow is incompressible $q = \rho$ and (3.4) is just the condition (3.2).

In the more general baroclinic case Λ_2 is not zero. As pointed out by Høiland [47], since ∇q and $\underset{\sim}{g}'$ are not parallel there is a region of directions for a displacement $\underset{\sim}{\xi}$ within which $(\underset{\sim}{\xi}.\underset{\sim}{g}')(\underset{\sim}{\xi}.\nabla q) < 0$, so that such a displacement would liberate energy via the buoyancy. Similarly there is a region of directions for $\underset{\sim}{\xi}$ satisfying $(\underset{\sim}{\xi}.\underset{\sim}{\varpi})(\underset{\sim}{\xi}.\nabla C^2) < 0$ within which rotational energy could be liberated. The inequalities (3.4) and (3.5) are simply the conditions that these two regions do not intersect, and that differential rotation and the combined effect of gravity and the centrifugal force on the density stratification always act in opposition. They are satisfied if the circulation increases away from the rotation axis in surfaces of constant q [53], or equivalently if q increases in the direction of apparent gravity in surfaces of constant C.

In the discussion above perturbations $\delta\bar{\Phi}$ in the gravitational potential have been ignored. This is a good approximation for disturbances of short wavelength, but is not necessarily so otherwise. Taking $\delta\bar{\Phi}$ into consideration does not alter the criterion for convective stability in the absence of rotation because here the neutral modes of the marginal state generate no density perturbations and so $\delta\bar{\Phi} = 0$ [54,55]. But in a rotating configuration one would not expect that to be the case if q is not constant in the equilibrium configuration. Fricke and Smith [49] have shown that the perturbation $\delta\bar{\Phi}$ is never stabilizing, so criteria (3.4) and (3.5) are not even sufficient for stability to large scale axisymmetric disturbances, and Fricke [56] has constructed a cylindrically symmetric example in which perturbations in gravitational potential are destabilizing.

Very different stability criteria are obtained when the perturbations are no longer constrained to be adiabatic. Now thermal diffusion can weaken the buoyancy forces responsible for stabilizing adiabatic disturbances, and provided there is some driving force, sufficiently slow motion cannot be prevented. This was pointed out by Yih [57] who demonstrated that in the absence of gravity the steady flow of a low Prandtl number fluid between two rotating coaxial cylinders can be unstable if the Rayleigh criterion (3.1) is not satisfied, even though (3.2) is. He showed also that under some circumstances viscosity can destabilize an otherwise stable flow if $\frac{d\rho}{d\varpi} < 0$.

A consistent analysis for baroclinic flows has not been published, though one can guess at the stability criteria. If (3.4) and (3.5) are not simultaneously satisfied there are directions in which both buoyancy and rotation tend to drive a displaced fluid element. Thermal diffusion acts to reduce buoyancy, but does not change its sign, so instability is likely to occur. Again, perturbations in the gravitational potential are being ignored. If (3.4) and (3.5) are

satisfied, then the criterion for stability can be estimated by setting the buoyancy terms in (3.3) to zero [cf 53]: $I(\xi)$ is then positive definite if and only if

$$\frac{\partial C^2}{\partial \varpi} \geq 0 \quad \text{and} \quad \frac{\partial C^2}{\partial z} = 0. \tag{3.7}$$

These conditions were first obtained by Goldreich and Schubert [58] and Fricke [56], using a plane wave approximation to the eigenfunctions of the linear stability analysis. It was suggested that the conditions were necessary and sufficient for stability. In addition to Rayleigh's criterion (3.1) it is also required that Ω be independent of z if the star is to be stable. This condition is automatically satisfied if $\nabla q = 0$ in the equilibrium configuration, but not otherwise : ∇q was set to zero in (3.3) because it was argued that thermal diffusion destroys buoyancy in a sufficiently slowly moving flow, even though it is not zero in the equilibrium state.

The growth of the instabilities discussed by Yih, Goldreich and Schubert, and Fricke is controlled by thermal diffusion, though the energy source is the rotation. The dynamics is essentially the same as that of the Eddington-Sweet circulation. Nevertheless the growth time is much shorter than the Eddington-Sweet circulation time because these modes can occur with very short wavelength; the reduction of the growth rates by buoyancy cannot be eliminated entirely, however, because at extremely short wavelengths viscous forces come into play. It appears, therefore, that criteria (3.7) are likely to apply even to steady configurations with meridional circulation.

The instability of Goldreich and Schubert and Fricke which seems to occur when $\partial\Omega/\partial z \neq 0$ has a profound implication concerning rotating stars: since it appears that there are no steady solutions to the equations governing the structure of a nondegenerate star for which Ω is independent of z, any steady state that might exist must be unstable. Although no proof of the instability has yet been found, it seems likely that the result is correct. The arguments supporting it predict also the instability demonstrated by Yih, which is hardly different, and can also be used to predict similar diffusively controlled instabilities such as salt fingers [59], whose existence has been well established [60].

The discussion so far has been concerned solely with axisymmetric instabilities. Less progress has been made with nonaxisymmetric instabilities because they are more difficult to analyse. Rayleigh [61] showed that steady shear flow of a homogeneous incompressible inviscid fluid in which the motion is either rectilinear or pure rotation is stable to two dimensional infinitesimal perturbations in the plane of the shear unless the vorticity somewhere has a turning point. Fjørtoft [62] showed that this turning point must be a maximum in the magnitude of the vorticity. General necessary and sufficient conditions have not been obtained [63] and it appears that each flow must be analysed separately. However, the results suggest that a concentration of vorticity that isn't bounded too closely by rigid walls is unstable.

Vertical density stratification can stabilize a horizontal flow

with velocity $u(\zeta)$ where ζ is a vertical coordinate, provided there is no thermal diffusion and the locally defined Richardson number

$$Ri = -g' \frac{dq}{d\zeta} / \left(\frac{du}{d\zeta}\right)^2 \qquad (3.8)$$

is everywhere greater than $\frac{1}{4}$ [64,65]. Thermal diffusion reduces the influence of a gravitationally stable density distribution, just as in Yih's problem, and instabilities can develop on a diffusion timescale [66]. Guesses at how these results generalize to more complicated flows must be made with caution because the dynamics of shear instability is not thoroughly understood. One is warned, for example, by Huppert's [67] result that a gravitationally stable density gradient can destabilize an otherwise stable shear.

It is argued by Zahn [68] that shear instabilities provide an important angular momentum mixing mechanism in rotating stars. Zahn pointed out that all flows at very high Reynolds number appear to be unstable, and shear in isentropic surfaces in particular will not be stabilized by a gravitationally stable density gradient. The important distinction between flows characterized by a high but finite Reynolds number and inviscid flows is that the former can generate vorticity with viscous stresses, though in stars this must occur in thin boundary layers if a resulting instability is to be generated in a time short enough to be interesting. In terrestrial conditions it is usually against a rigid wall that vorticity is so created. This cannot be the case in stars, but internal boundary layers such as those discussed by Mestel [33] in the vicinity of a near discontinuity in chemical composition can arise, and coupling with other motions such as convection may be important. If shear instabilities do commonly occur, then, as Zahn stresses, angular momentum transport resulting from them will generally dominate any transport by the diffusivily controlled instabilities discussed above.

EVOLUTION OF THE ROTATION OF STARS

Since it appears that no stable steady state of a nondegenerate star exists, stars must evolve to states of time dependent motion so long as there is nuclear energy enough to keep them on the main sequence. The state to which a star evolves finally, however, after all of its available nuclear fuel has been exhausted must be a state of minimum energy, which is rigid body rotation. This assumes, of course, that an equilibrium state is available to it and that it has not collapsed into a black hole.

The angular momentum distribution in a main sequence star is therefore determined by the competing transports due to large scale meridional circulation and the smaller scale probably turbulent motions arising from the rotational instabilities discussed in the previous section. In addition, angular momentum is transported by convection and by large scale oscillations, if they are present.

To what distribution of angular momentum does a star evolve ? The only star for which we have direct evidence is the sun. Observations of the surface show that the equator rotates faster than the poles by about 20%, the precise amount varying somewhat with time, and that the rotation of features directly related to variations in the magnetic field is greater than the results from Doppler measurements. Magnetic field

variations are produced by fluid motions beneath the photosphere, where the kinetic energy density exceeds the magnetic energy density, so the latter observation suggests that the angular velocity of the sun at least near the surface increases with depth (though Yoshimura [69] has argued against this interpretation). This is not inconsistent with Dicke's [12] conclusion that his measured oblateness of the radiant intensity of the solar disk results from an oblateness in the gravitational potential caused by rapid rotation of the interior. The situation has been reviewed recently by Gilman [70].

Little is known about angular momentum transport by motions resulting from the instabilities to which a star is subject. It is usually assumed that turbulence in a convection zone, for example, acts on large scale motion in the manner of molecular viscosity, forcing the zone towards a state of rigid rotation. Durney [71,72], Gilman [73] and Gierasch [74], for example, have studied models of the solar convection zone in which meridional circulation is acted upon by such a turbulent viscosity with a view to explaining the observed differential rotation. The circulation is driven by the horizontal pressure gradients resulting from rotational distortion, just as in radiative zones. In Durney's models an assumed preferred rotational inhibition of the convective heat flux in polar regions contributed further to these gradients [cf 75]. The models can produce equatorial acceleration at the surface, though the dependence of angular velocity on depth is not in all cases that suggested by the observations, and in all cases but Durney's latest model the variations in surface energy flux from pole to equator are too great to be consistent with observation. The models are not consistently coupled to the radiative interior and, as Gierasch has emphasized, this may have led to serious errors in the results.

Another possible source of error is the assumption that the Reynolds stresses act like a scalar viscosity. This could be a reasonable approximation only if the turbulence were isotropic, but since buoyancy and rotation both impose preferred directions on the forces driving the flow, anisotropy in the Reynolds stresses is inevitable. Wasiutyński [76] and Biermann [77] pointed out that anisotropy arising from buoyancy would drive nonuniform rotation in stars, and Kippenhahn [78], Cocke [79] and Köhler [80] subsequently employed simple anisotropic stress tensors to compute differentially rotating solar envelopes. Models with equators rotating faster than the poles can be constructed, with an appropriate choice of turbulent stresses, but in the latest ones [80] the angular velocity decreases with depth. The anisotropy induced by the rotation itself has been discussed by Gough and Lynden-Bell [81] who argued that there is a weak tendency for turbulence to force motion on a larger scale towards a state of no vorticity. Experiments were performed to support their arguments, but later Strittmatter, Illingworth and Freeman [82] showed that they had been misinterpreted; the vorticity expulsion hypothesis remains unconfirmed. If it is true, however, and if all other transport mechanisms are ignored, the Reynolds stresses would act to distribute the angular velocity in the solar convection zone such that it decreases with latitude and increases with depth. The ideas that led to vorticity expulsion have not been developed enough for Reynolds stresses to be calculated.

Busse [83,84] has studied the dynamics of the convection itself by expanding the solutions of the equations of motion about the marginally stable state. The conditions are highly idealized and so the results

are not directly applicable to solar convection, though it is hoped that some aspects of the solar dynamics are revealed. In the models, the motion develops an anisotropy which leads to increasing surface angular velocity from pole to equator.

A completely consistent picture of the rotation of the solar convection zone is not yet at hand, but considerable progress has clearly been made in the last decade.

In computations of the structure of rotating stars, convective cores are invariably assumed to be constrained by large isotropic turbulent stresses. Tayler [43] has discussed the effect of the anisotropy that must be present and concluded that for practical purposes it is probably not necessary to take into account the anisotropy in energy flow due to convection, but that one must, of course, worry about the distribution of angular momentum.

Angular momentum transport resulting from the development of rotationally driven instabilities has been discussed less. Kippenhahn [85] pointed out that the transport of angular momentum by the diffusive modes discovered by Yih, Goldreich, Schubert and Fricke would lead to the formation of a shear which would become unstable to nonaxisymmetric instabilities. He argued that this would limit the development of the diffusive modes, and by a simple-minded argument estimated the time scale for gross readjustment of a star's angular momentum to be at least the thermal diffusion (Kelvin-Helmholtz) time τ_{KH}. James and Kahn [86,87] looked at the development of the instability more carefully and concluded that the shear would be concentrated in narrow corridors. Thus there would be separate regions of diffusively controlled motion and dynamically unstable shear. This is not dissimilar to the separate layers of fingers and convection in thermohaline convection [60,88,89]. James and Kahn estimated that the time for global readjustment of angular momentum is as great as the Eddington-Sweet circulation time τ_{ES}. It appears that the timescale obtained was as long as τ_{ES} because the possibility that motion in the diffusive region be on the small viscously controlled scale realized by salt fingers was overlooked. If fingering does occur, angular momentum should be transported globally in a time shorter than τ_{ES} and possibly τ_{KH}. However such argument by analogy may be too naive. The vectorial nature of angular momentum and the complicated geometry may act such that this comparatively simple layered structure cannot persist, and the growth time of the large scale diffusive instabilities, namely τ_{ES}, may then be the shortest time in which global angular momentum redistribution can occur.

Throughout this discussion I have had in mind that the angular momentum of a star is conserved. This is not always so. For example, Kraft [5] has shown that the rotation rates of solar-type main sequence stars decrease with age. This appears to be a result of angular momentum loss at the surface associated with mass loss in stellar winds [90].

Stars like the sun have surrounding their photospheres high temperature coronae which are thought to be maintained by the dissipation of energy from mechanical waves which originated in their convection zones below. The coronal pressure is too great merely to hold up the outer atmosphere hydrostatically [91], and gas streams outwards exerting a torque on the subphotospheric regions of the star via a magnetic field. This process has been studied by Ferraro and Bhatia [92], Modisette [93], Weber and Davis [94] and Mestel [95,96],and for the sun leads to significant deceleration in a time comparable with its age. The mass lost is a negligible fraction of the stellar mass.

The depth of the convection zones of main sequence stellar models decreases abruptly with mass at about $M = 1\frac{1}{4}\ M_\odot$; and it has been suggested [e.g. 90] that only deep convection zones can support strong coronae and stellar winds. Consequently it is plausible that only stars at the low mass end of the main sequence have been significantly decelerated on the main sequence, which would explain at least in part the strange dependence of angular velocity on mass mentioned in the introduction. However Kraft's [5] observations of solar-type stars in the Pleiades group, which have arrived on the main sequence only recently, also show an abrupt change in surface rotation rate. It is possible that this is a result of very different angular momentum distributions inside upper and lower main sequence stars. Alternatively it reflects different total angular momentum, which must either have been present at the time of formation of the stars or is a product of Kelvin-Helmholtz contraction to the main sequence. During part of the gravitational collapse phase all stars have extensive convective envelopes, and many are probably convective throughout, so conditions seem ripe for something like the stellar wind deceleration mechanism to operate very efficiently. There are no reliable estimates of the angular momentum that should be lost by this mechanism, but since the contraction time decreases with stellar mass it is plausible that the low mass stars have been slowed down the most. It is perhaps worth mentioning at this point that vorticity expulsion in a fully convective star implies angular momentum expulsion [81], and estimates of the expulsion rate during gravitational contraction based on analogy with magnetic field expulsion [97] leads to a sharp break in the main sequence rotation rate at just about the place where it is observed.

The continual extraction of angular momentum from the sun adds yet further complexity to the problem of determining its present state of rotation. The magnetic field in the solar atmosphere is too weak to be dynamically important much below the photosphere, and so can transmit a torque only to the outer regions of the sun. Dicke [12] claimed that therefore only the outer convection zone has been decelerated, because viscous diffusion would take about 10^{13} yr to affect the core, which is much longer than the age of the sun (about 5×10^9 yr). The argument is invalid, for aside from the existence of the angular momentum transport processes more efficient than viscosity, discussed above, the changing centrifugal force field near the surface induces pressure inbalance which drives currents like the Eddington-Sweet circulation, causing the entire sun to respond faster than it would by viscous diffusion

alone. This process is called spin-down, and has been reviewed recently by Benton and Clark [98].* It occurs in homogeneous incompressible fluids in rigid containers, angular momentum being exchanged between fluid and container in thin viscous boundary layers which were first discussed by Ekman [99]; Einstein [100], Prandt [101] and Bondi and Lyttleton [102] studied the problem further. The sun is not in a rigid container, so the details must be somewhat different, but estimates of the time to spin down the solar core based on this analysis and postulating a turbulent Ekman layer at the base of the convection zone [103], or on an analysis treating the convection zone as a rigid porous medium [104], suggest values considerably less than the solar age. However, aside from the details of the coupling of the convection zone to the radiative interior, these estimates must be treated cautiously because they were obtained without taking the stratification of the sun into account.

For a while there was some dispute over the effect of gravitationally stable thermal stratification [98] but now it appears, as one would naively expect, that thermal diffusion can in general remove any buoyancy tending to prevent the spin-down currents. The timescale of the resulting flow depends on the properties of the fluid, and linearized theory suggests that it is certainly bounded above by τ_{ES} [98,105,106]. Analogous results hold when stratification is by chemical composition, but in stars the spin-down timescales are then much greater because particle diffusion acts more slowly than thermal diffusion. Experiments are in general agreement with the theoretical findings [107]. Compressibility appears to make no qualitative difference to the conclusions [108].

The stability and spin-down arguments all lead one to the conclusion that global angular momentum readjustments occur in stars in a time which is at most the Eddington-Sweet time, but is probably much less. In any case, if the sun arrived on the main sequence rotating ten or twenty times faster than its surface is now, as Dicke [12,18] believes, angular momentum will already have been redistributed at least throughout its chemically homogeneous envelope. Approximate calculations by Sakurai [38] considering the evolution of the large scale circulation in an initially uniformly rotating solar model are consistent with this conclusion. If, on the other hand, the entire sun has always rotated on the main sequence at a rate comparable with its present surface value the issue is less clear. It can be argued that gravitationally stable gradients in chemical composition generated in the core by nuclear reactions might have prevented the core from spinning down. This is possible, though it has been suggested that the core is periodically mixed [109], which would render this conclusion less likely.

From a fluid dynamical point of view it is therefore quite uncertain what the angular momentum history of the sun has been, though in balance the evidence favours that a global readjustment has taken place on the main sequence. This does not necessarily imply that the solar core is not in a state of comparatively rapid rotation, however, for advection of angular momentum by meridional currents generally leads

*The problem usually studied is one where the external torque increases the rotation rate. This is called spin-up.

to higher angular velocity near the rotation axis [cf 38]. This is opposed by turbulent mixing which may tend to make the angular velocity more uniform.

Observational evidence that may have some bearing on the degree of mixing that has taken place concerns the abundances of lithium and beryllium. Beryllium is destroyed by nuclear reactions under conditions prevailing within the inner 50% by radius of the sun. The agreement of the solar surface abundance of beryllium with the relative abundance in the chondritic meteorites [e.g. 110] might lead one to believe that significant mixing of the sun's surface layers with the interior has not occurred. On the other hand lithium, which is destroyed inside a radius of about 0.6 $R_\odot$, is almost absent in the surface. By the same argument it appears that mixing down to this level has occurred, and since it is below the bottom of the convection zone (which is about 0.8 $R_\odot$) rotationally induced mixing of some kind has presumably taken place. There is no clear fluid dynamical reason why partial mixing to this degree should occur. Dicke [111] has concluded that this apparent lack of complete mixing implies that the solar core is not coupled to the surface, and is therefore still rotating at its initial rapid rate. Contrarily, Goldreich and Schubert [58] argued that incomplete mixing is indicative of slow rotation throughout the entire main sequence history of the sun, and that the core is therefore unlikely to be rotating rapidly. The problem is unresolved, and is complicated by the possibility that element separation within the fluid obscures the implications surface abundance measurements have on the degree of mixing that has occurred [112].

Finally, let us return to the solar oblateness measurements. Dicke and Goldenberg [16,17] have measured the oblateness of only the radiative intensity distribution in the solar image, and interpreted this as a direct consequence of a similar oblateness in the gravitational equipotentials. This interpretation has been questioned [113-116] and it was suggested in particular that effects of radiative transfer and intensity inhomogeneities in the diffuse solar atmosphere may have been responsible for the apparent oblateness. Recently Hill and Stebbins [117] have measured the shape of the sun, paying careful attention to surface nonuniformities [118]. They found time varying brightness fluctuations sufficient to account for Dicke and Goldenberg's measurement without recourse to assuming any deviation from the spherical shape, and during a period when the brightness was nearly uniform they inferred an oblateness no greater than what one would expect if the sun were rotating at approximately the surface angular velocity throughout. No doubt the controversy is not yet over, but at present it cannot be said that the sun provides convincing evidence against the theory of general relativity.

ACKNOWLEDGEMENTS

I am grateful to Dr R.C. Smith and Dr J.-P. Zahn for useful discussions. Much of this review was prepared during a visit to the National Center for Atmospheric Research, which is sponsored by the National Science Foundation; I am grateful to Dr P.A. Gilman for the hospitality of the Advanced Study Program.

REFERENCES

1. Strittmatter, P.A. 1969 Stellar Rotation Ann. Rev. Astr. Ap, 7, 665
2. Fricke, K.J. and R. Kippenhahn 1972 Evolution of rotating stars Ann. Rev. Astr. Ap, 10, 45
3. Slettebak, A. (ed) 1970 Stellar Rotation (Proc. IAU colloquium, Columbus, Ohio; Sep. 1969) (Reidel, Dordrecht)
4. Chandrasekhar, S. 1939 An introduction to the study of stellar structure (Univ. Chicago Press)
5. Kraft, R.P. 1967 Studies in stellar rotation. V. The dependence of rotation on age among solar-type stars Ap J., 150, 551
6. Howard, R. and Harvey, J. 1970 Spectroscopic determinations of solar rotation Solar Phys., 12, 23
7. Leverrier, U.J. 1859 Ann. Obs. Paris, 5, 104
8. Airy, G.B. 1862 On the circularity of the sun's disk Mon. Not. Roy. astr. Soc., 22, 80
9. Auwers, A. 1891 Astr. Nachr., 128, 360
10. Newcomb, S. 1895 Fundamental constants of Astronomy (U.S Gov. Printing Office, Washington)
11. Einstein, A. 1915 Erklärung der Perihelbewegung des Merkur aus der allgemeinen Relativitätstheorie Sitzungsber. Preuss. Akad. Wiss., 831
12. Dicke, R.H. 1964 The sun's rotation and relativity Nature, 202, 432
13. Roxburgh, I.W. 1964 Solar rotation and the perihelion advance of the planets Icarus, 3, 92
14. Brans, C. and R.H. Dicke 1961 Mach's principle and a relativistic theory of gravitation Phys. Rev., 124, 925
15. Jordan, P. 1948 Fünfdimensionale Kosmologie Astr. Nachr., 276, 193
16. Dicke, R.H. and H.M. Goldenberg 1967 Solar oblateness and General Relativity Phys. Rev. Lett., 18, 313
17. Dicke, R.H. and H.M. Goldenberg 1974 The oblateness of the sun Ap J. Suppl., 27, 131
18. Dicke, R.H. 1970 Internal rotation of the sun Ann. Rev. Astr. Ap, 8, 297
19. Ostriker, J.P. and J.W.-K. Mark 1968 Rapidly rotating stars. I. The self-consistent-field method Ap J., 151, 1075
20. Chandrasekhar, S. 1931 The maximum mass of ideal white dwarfs Ap J., 74, 81
21. Salpeter, E.E. and T. Hamada 1961 Models for zero-temperature stars Ap J., 134, 683
22. Mestel, L. 1965 The theory of white dwarfs Stars and Stellar Systems (ed. L.H. Aller and D.B. McLaughlin, Chicago Univ. Press) 8, 297

23. Ostriker, J.P., P. Bodenheimer and D. Lynden-Bell 1966 Equilibrium models of differentially rotating zero-temperature stars Phys. Rev. Lett., 17, 816

24. Eddington, A.S. 1925 Circulating currents in rotating stars Observatory, 48, 73

25. Vogt, H. 1925 Zum Strahlungsgleichgewicht der Sterne Astr. Nachr., 223, 229

26. Eddington, A.S. 1929 Internal circulation in stars Mon. Not. Roy. astr. Soc., 90, 54

27. von Zeipel, H. 1924 Festschrift für H. von Seelinger, p 144

28. Roxburgh, I.W. 1966 On stellar rotation III. (Appendix) Mon. Not. Roy. astr. Soc., 132, 201

29. Sweet, P.A. 1950 The importance of rotation in stellar evolution Mon. Not. Roy. astr. Soc., 110, 548

30. Mestel, L. 1965 Meridian circulation in stars Stars and Stellar Systems (ed. L.H. Aller and D.B. McLaughlin, Chicago Univ. Press) 8, 465

31. Baker, N. and R. Kippenhahn 1959 Untersuchungen über rotierende Sterne Zs f. Ap, 48, 140

32. Smith, R.C. 1966 A note on meridian circulation in rotating stars Zs f. Ap, 63, 166

33. Mestel, L. 1953 Rotation and stellar evolution Mon. Not. Roy. astr. Soc., 113, 716

34. Smith, R.C. 1970 Meridional circulation in rotating stellar atmospheres Mon. Not. Roy. astr. Soc., 148, 275

35. Brand, D. and R.C. Smith 1971 Meridional circulation in rotating stellar atmospheres - II Mon. Not. Roy. astr. Soc., 154, 293

36. Osaki, Y. 1966 On the atmosphere of a rotating star Publ. Astr. Soc. Japan, 18, 7

37. Osaki, Y. 1972 Meridional circulation in a rotating star Publ. Astr. Soc. Japan, 24, 509

38. Sakurai, T. 1972 The evolution of the solar inner rotation by the Eddington-Sweet type circulation under the influence of the solar wind torque Publ. Astr. Soc. Japan, 24, 153

39. Schwarzschild, M. 1947 On stellar rotation II Ap J., 106, 427

40. Roxburgh, I.W. 1964 On stellar rotation I. The rotation of upper main-sequence stars Mon. Not. Roy. astr. Soc., 128, 157

41. Roxburgh, I.W. 1964 On stellar rotation II. The rotation of lower main sequence stars Mon. Not. Roy. astr. Soc., 128, 237

42. Clement, M.J. 1969 Differential rotation in stars on the upper main sequence Ap J., 156, 1051

43. Tayler, R.J. 1973 Convection in rotating stars Mon. Not. Roy. astr. Soc., 165, 39

44. Lebovitz, N.R. 1974 The fission theory of binary stars Ap J., 190, 121 (see also the article in this volume)

45. Lord Rayleigh 1916 On the dynamics of revolving fluids Proc. Roy. Soc., A93, 148 (also Scientific Papers, 6, 447, CUP Cambridge 1920)

46. Synge, J.L. 1933 The stability of heterogeneous liquids Trans. Roy. Soc. Canada, Third Ser., 27 III, 1

47. Høiland, E. 1941 On the stability of the circular vortex Avhandl. utgitt Norske Vidensk.-Akad. Oslo I, Mat.-naturv. Kl. No 11

48. Solberg, H. 1936 Le mouvement d'inertie de l'atmosphère stable et son rôle dans la théorie des cyclones Procès-verbaux de l'Assn de météor., Edinbourg, Sept. 1936

49. Fricke, K.J. and R.C. Smith 1971 On global dynamical stability of rotating stars Astr. Ap, 15, 329

50. Lynden-Bell, D. and J.P. Ostriker 1967 On the stability of differentially rotating bodies Mon. Not. Roy. astr. Soc., 136, 293

51. Reye, T. 1872 Die Wirbelstürme, Tornados und Wettersäulen (Gegenius, Halle)

52. Schwarzschild, K. 1906 Ueber das Gleichgewicht der Sonnenatmosphäre Gottinger Nachr., Math-phys Kl., 41

53. Zahn, J.-P. 1974 Rotational instabilities and stellar evolution Hightlights in Astronomy, 3

54. Lebovitz, N.R. 1965 On Schwarzschild's criterion for the stability of gaseous masses Ap J., 142, 229

55. Lebovitz, N.R. 1965 On the onset of convective instability Ap.J., 142, 1257

56. Fricke, K.J. 1968 Instabilität stationärer Rotation in Sternen Zs f. Ap, 68, 317

57. Yih, C.-S. 1961 Dual role of viscosity in the instability of revolving fluids of variable density Phys. Fluids, 4, 806

58. Goldreich, P. and G. Schubert 1967 Differential rotation in stars Ap J., 150, 571

59. Stern, M.E. 1960 The "salt-fountain" and thermohaline convection Tellus, 12, 172

60. Turner, J.S. 1973 Buoyancy effects in fluids (CUP, Cambridge)

61. Lord Rayleigh 1880 On the stability or instability of certain fluid motions Proc. London Math. Soc., 11, 57 (also Scientific Papers, 1, 474, CUP Cambridge 1899)

62. Fjørtoft, R. 1950 Application of integral theorems in deriving criteria of stability for laminar flows and for the baroclinic circular vortex Geofys. Publ., 27, No 6

63. Drazin, P.G. and L.N. Howard 1966 Hydrodynamic stability of parallel flow of inviscid fluid Adv. Appl. Mech., 9, 1

64. Miles, J.W. 1961 On the stability of heterogeneous shear flows J. Fluid Mech., 10, 496

65. Howard, L.N. 1961 Note on a paper by John W. Miles J. Fluid Mech., 10, 509

66. Jones, C.A. 1975 The effect of diffusion on stratified shear flow (to be published)

67. Huppert, H.E. 1973 On Howard's technique for perturbing neutral solutions of the Taylor-Goldstein equation J. Fluid Mech., 57, 361

68. Zahn, J.-P. 1975 Differential rotation and turbulence in stars Problems in stellar hydrodynamics (19th Liège Intern. Ap Colloq., July 1974)

69. Yoshimura, H. 1971 Complexes of activity of the solar cycle and very large scale convection Solar Phys., 18, 417

70. Gilman, P.A. 1974 Solar rotation Ann. Rev. Astr. Ap, 12

71. Durney, B.R. 1971 Differential rotation, meridional velocities, and pole-equator difference in temperature of a rotating convective spherical shell Ap J., 163, 353

72. Durney, B.R. 1974 On the sun's differential rotation: it's maintenance by large-scale meridional motions in the convection zone Ap J., 190, 211

73. Gilman, P.A. 1972 Nonlinear Boussinesq convective model for large scale solar circulations Solar Physics, 27, 3

74. Gierasch, P.J. 1974 The differential rotation of the solar surface Ap J., 190, 199

75. Weiss, N.O. 1965 Convection and differential rotation of the sun Observatory, 85, 37

76. Wasiutyński, J. 1946 Studies in hydrodynamics and structure of stars and planets Ap Norv., 4

77. Biermann, L. 1951 Bemerkungen über das Rotationsgesetz in irdischen und stellaren Instabilitätszonen Zs f. Ap, 28, 304

78. Kippenhahn, R. 1963 Differential rotation in stars with convective envelopes Ap J., 137, 664

79. Cocke, W.J. 1967 On the solar differential rotation and meridional currents Ap J., 150, 1041

80. Kohler, H. 1970 Differential rotation caused by anisotropic turbulent viscosity Solar Physics, 13, 3

81. Gough, D.O. and D. Lynden-Bell 1968 Vorticity expulsion by turbulence : astrophysical implications of an Alka-Seltzer experiment J. Fluid Mech., 32, 437

82. Strittmatter, P.A., G. Illingworth and K.C. Freeman 1970 A note on the vorticity expulsion hypothesis J. Fluid Mech., 43, 539

83. Busse, F.H. 1970 Differential rotation in stellar convection zones Ap J., 159, 629

84. Busse, F.H. 1973 Differential rotation in stellar convection zones II Astr. Ap, 28, 27

85. Kippenhahn, R. 1969 Secularly unstable differential rotation in stars Astr. Ap, 2, 309

86. James, R.A. and F.D. Kahn 1970 Non-linear limiting of the Goldreich-Schubert instability Astr. Ap, 5, 232

87. James, R.A. and F.D. Kahn 1971 Angular momentum transport in stars, following the Goldreich-Schubert instability Astr. Ap, 12, 332

88. Stern, M.E. and J.S. Turner 1969 Salt fingers and convecting layers Deep-Sea Res., 16, 497

89. Shirtcliffe, T.G.L. and J.S. Turner 1970 Observations of the cell structure of salt fingers J. Fluid Mech., 41, 707

90. Schatzman, E. 1962 A theory of the role of magnetic activity during star formation Ann. d'Ap, 25, 18

91. Parker, E.N. 1963 Interplanetary dynamical processes (Interscience, New York)

92. Ferraro, V.C.A. and V.B. Bhatia 1967 Corotation and solar wind in the solar corona and interplanetary medium Ap J., 147, 220

93. Modisette, J.L. 1967 Solar wind induced torque on the sun J. Geophys. Res., 72, 1521

94. Weber, E.J. and L. Davis Jr 1967 The angular momentum of the solar wind Ap J., 148, 217

95. Mestel, L. 1968 Magnetic braking by a stellar wind -I Mon. Not. Roy. astr. Soc., 138, 359

96. Mestel, L. 1968 Magnetic braking by a stellar wind - II Mon. Not. Roy. astr. Soc., 140, 177

97. Weiss, N.O. 1966 The expulsion of magnetic flux by eddies Proc. Roy. Soc., A293, 310

98. Benton, E.R. and A. Clark Jr 1974 Spin-up Ann. Rev. Fluid Mech., 6, 257

99. Ekman, V.W. 1905 On the influence of the earth's rotation on ocean-currents Ark. Math. Astr. Fys., 2, No 11

100. Einstein, A. 1916 Elementare Theorie der Wasserwellen und des Fluges Naturwiss., 4, 509

101. Prandtl, L. 1931 Abriß der Stromungslehre (Friedr. Vieweg & Sohn, Braunschweig) p103

102. Bondi, H. and R.A. Lyttleton 1948 On the dynamical theory of the rotation of the earth Proc. Camb. Phil Soc., 44, 345

103. Howard, L.N, D.W. Moore and E.A. Spiegel 1967 Solar spin-down problem Nature, 214, 1297

104. Bretherton, F.P. and E.A. Spiegel 1968 The effect of the convection zone on solar spin-down Ap J., 153, L77

105. Sakurai, T., A. Clark Jr and P.A. Clark 1971 Spin-down of a Boussinesq fluid of small Prandtl number in a circular cylinder J. Fluid Mech., 49, 753

106. Clark, A., Jr 1973 The linear spin-up of a strongly stratified fluid of small Prandtl number J. Fluid Mech., 60, 561

107. Buzyna, G. and Veronis, G. 1971 Spin-up of a stratified fluid : theory and experiment J. Fluid Mech., 50, 579

108. Clark, A., Jr, P.A. Clark, J.H. Thomas and N.-H. Lee 1971 Spin-up of a strongly stratified fluid in a sphere J. Fluid Mech., 45, 131

109. Dilke, F.W.W. and D.O. Gough 1972 The solar spoon Nature, 240, 262

110. Wallerstein, G. and P.S. Conti 1969 Lithium and beryllium in stars Ann. Rev. Astr. Ap, 7, 99

111. Dicke, R.H. 1972 Rotation and lithium abundance in solar-type stars Ap J., 171, 331

112. Schatzman, E. and S. Vauclair 1974 Radiation pressure and the lithium-beryllium problem Comments Ap Sp. Sci., 6, 159

113. Ingersoll, A.P. and E.A. Spiegel 1971 Temperature variation and the solar oblateness Ap J., 163, 375

114. Chapman, G.A. and A.P. Ingersoll 1972 Photospheric faculae and the solar oblateness Ap J., 175, 819

115. Dicke, R.H. 1972 Faculae and the solar oblateness Ap J., 175, 831

116. Dicke, R.H. 1974 Faculae and the solar oblateness II Ap.J., 190, 187

117. Hill, H.A. 1974 The intrinsic visual oblateness of the sun (submitted to Ap J.)

118. Hill, H.A., P.D. Clayton, D.L. Patz, A.W. Healy, R.T. Stebbins, J.R. Oleson and C.A. Zanoni 1974 Solar oblateness, excess equatorial brightness, and relativity (submitted to Phys. Rev. Lett.)

THE ELECTRON BUBBLE IN LIQUID HELIUM

P. H. Roberts
University of Newcastle upon Tyne,
Newcastle upon Tyne, NE1 7RU, England

ABSTRACT

The bose condensate model of helium is used to examine the structure of the electron bubble in helium. The solution obtained makes use of the fact that the parameter $(am/\ell M)^{1/5}$ is small and m/M is negligible, where m is the electron mass, M is the boson mass, ℓ is the electron-boson scattering length, and a is the healing length. It is shown that, to leading order, the radius of the bubble is $b = (\pi M^2 a^2/m\rho_\infty)^{1/5}$, when ρ_∞ is the helium density. The effects of (quantum) surface tension and of polarization are discussed, and are shown to be small. Consideration is given to the effective mass and radius of the bubble, and the ellipticity induced in it by slow motion is given. The normal modes of pulsation of the bubble are found and the mobility of the ion is computed. The theory is compared with experiment.

1. INTRODUCTION

It has become increasingly apparent over the past decade that the deliberately introduced impurity can be a fruitful experimental probe of the structure and dynamics of helium II, the superfluid phase of helium. Of particular interest is the negative ion which consists of an electron that, through its zero point motion, carves out a soft bubble of about 16Å in radius in the surrounding helium (1Å = 10^{-8}cm.). The induced hydrodynamic mass of such a large structure is greatly in excess of its physical mass, and it therefore responds to applied forces as would a much more massive ion. The experimental situation has been reviewed by Donnelly[1], and more recently by Fetter[2].

The negative ion provides an interesting and, as we shall see, a sensitive testing ground for theories of helium II. We examine in this paper one particularly simple model of helium near absolute zero, the bose condensate. The approach is expounded by, for example, Gross[3] and by Fetter and Walecka[4]. The theory is so simple to apply that most of the properties of the electron bubble can be calculated in an elementary way. We will present our arguments in a hydrodynamic framework originally proposed by Madelung[5]. Since this may be unfamiliar to the reader, it is developed in §2 for the simple single-particle Schrödinger equation. It is generalized in §3 to the bose condensate. The two theories are brought together in §4, where the theory of the electron bubble is developed. The final section (§5) confronts the theory with experiment.

2. MADELUNG'S TRANSFORMATION

It appears to have been Madelung[5] who first realized that Schrödinger's equation could be cast into a fluid mechanical mold, by expressing the wavefunction, $\psi(\vec{x},t)$, in terms of its amplitude, $f(\vec{x},t)$, and phase, $\phi(\vec{x},t)$. Consider a particle of mass m in a field of fixed potential, $w(\vec{x})$, and therefore obeying

$$i\hbar\partial\psi/\partial t = -(\hbar^2/2m)\,\nabla^2\psi + w\psi. \qquad (1)$$

By writing

$$\psi = f \exp(im\phi/\hbar), \qquad (2)$$

where f and ϕ are real, we can divide (1) into

$$2\frac{\partial f}{\partial t} + f\nabla^2\phi + 2\vec{\nabla}f\cdot\vec{\nabla}\phi = 0, \tag{3}$$

$$\frac{\partial \phi}{\partial t} + \frac{1}{2}(\vec{\nabla}\phi)^2 + \frac{w}{m} - \frac{\hbar^2}{2m^2}\frac{\nabla^2 f}{f} = 0. \tag{4}$$

When we introduce the (probabilistic) mass density, ρ, and current $\vec{j}$, by writing

$$\rho = m|\psi|^2 = mf^2, \quad \vec{j} = (\hbar/2i)(\psi^*\vec{\nabla}\psi - \psi\vec{\nabla}\psi^*) = \rho\vec{\nabla}\phi, \tag{5}$$

and define a velocity, $\vec{u}$, by their ratio

$$\vec{u} = \vec{j}/\rho = \vec{\nabla}\phi, \tag{6}$$

we recognize that (3) and (4) are the continuity and momentum equations governing the potential flow (6):

$$\frac{\partial \rho}{\partial t} + \vec{\nabla}\cdot(\rho\vec{u}) = 0, \tag{7}$$

$$\frac{\partial \phi}{\partial t} + \frac{1}{2}\vec{u}^2 + \frac{w}{m} + \mu = 0, \tag{8}$$

where

$$\mu = -(\hbar^2/2m^2)\nabla^2\rho^{1/2}/\rho^{1/2}. \tag{9}$$

There are three main differences from classical potential flow. First, the total quantity of 'fluid' is not only conserved by (7): it is fixed by

$$\int|\psi|^2 d\vec{x} = 1, \quad \text{or} \quad \int\rho d\vec{x} = m. \tag{10}$$

Second, even if through the presence of walls ($w=\infty$) or otherwise the fluid is confined to a certain multiply-connected domain, $\mathcal{R}$, ψ must remain single-valued. It follows from (2) that, round any contour Γ in $\mathcal{R}$ not reducible to a point by a continuous deformation, ϕ can change by a multiple of h/m only. The circulation round Γ cannot freely take any value: it is quantized by the Bohr-Sommerfeld condition

$$\oint_\Gamma \vec{u}\cdot d\vec{x} = \frac{nh}{m}, \quad (n=0, \pm1, \pm2.....). \tag{11}$$

Third, a completely new term has appeared in the momentum equation (8), namely μ.

The term μ is often called 'the quantum pressure'. This is a misnomer for at least three reasons. First, its dimensionality is incorrect, and it would be better regarded as a chemical potential per unit mass. Second, since

$$\partial\mu/\partial x_i = -\rho^{-1}\partial\sigma_{ij}/\partial x_j, \tag{12}$$

where[6-8]

$$\sigma_{ij} = \frac{\hbar^2}{2m^2}\rho\,\frac{\partial^2}{\partial x_i \partial x_j}(\ln\rho^{1/2}), \tag{13}$$

a rival, and properly dimensioned, contender for the title of quantum pressure exists as part of the unusual and complicated stress tensor (13). Third, the word 'pressure' suggests a phenomenon that depends only on 'the local thermodynamic state' (here fixed by ρ), and the presence of derivatives in (9), or (13), shows that all neighboring points are involved in its definition. Despite these objections, we follow the common usage.

As may be seen by setting $\hbar = 0$ in (9), the quantum pressure is the essential ingredient that distinguishes our subject from the classical theory. The fluid dynamicist can gather experience of its effects

by translating some of the elementary situations of quantum theory into their corresponding fluid mechanical statements.

'Hydrostatics' arises from the quantum mechanical bound states by writing

$$\phi = -Et, \tag{14}$$

where E, the energy of the state, is a constant. By (8) the quantum pressure balances E-w everywhere. It is best to avoid the usual fluid mechanical practice of absorbing E into w, since some energy levels may be inaccessible. For example, when (8) is written as

$$-(\hbar^2/2m)\ \nabla^2 f = [E - w(\vec{x})]f, \tag{15}$$

and it is supposed that w increases indefinitely with distance, r, from some origin, 0, one family of solutions to (15) is found that increase with r, so that the normalization integrals (10) do not converge. The condition that only the normalizable solutions of the other family are used transforms (15) into an eigenvalue problem that confines E to discrete levels. Of course a continuum of eigenvalues exists when w is bounded above.

A well-known application of (15), that is particularly relevant to the bubble, is the potential well for which

$$w = \begin{cases} w_I, \text{ in } r<b \text{ ('Region I');} \\ w_{II}, \text{ in } r>b \text{ ('Region II');} \end{cases} \tag{16}$$

where w_I and w_{II} ($>w_I$) are constants. Writing

$$\lambda_I^2 = (2m/\hbar^2)\ (E - w_I), \qquad \lambda_{II}^2 = (2m/\hbar^2)(w_{II} - E), \tag{17}$$

we see that, for $w_I < E < w_{II}$, (15) is obeyed by

$$f = f_I \equiv A j_\ell(\lambda_I r)\ Y_\ell(\theta,\chi), \text{ in } r \le b; \tag{18}$$

$$f = f_{II} \equiv A k_\ell(\lambda_{II} r)[j_\ell(\lambda_I b)/k_\ell(\lambda_{II} b)]\ Y_\ell(\theta,\chi), \text{ in } r \ge b; \tag{19}$$

where $j_\ell(z)$ is the spherical Bessel function of the first kind, $k_\ell(z)$ is the modified spherical Bessel function of the second kind, and $Y_\ell(\theta,\chi)$ is a surface harmonic of integral degree, ℓ, in spherical coordinates (r, θ, χ). The exclusion of the other spherical Bessel functions ensures that (10) can be met for some choice of the constant A. Continuity of f has been realized, and $\vec{\nabla}f$ is continous provided

$$\lambda_I b j_\ell'(\lambda_I b)/j_\ell(\lambda_I b) = \lambda_{II} b k_\ell'(\lambda_{II} b)/k_\ell(\lambda_{II} b). \tag{20}$$

This dispersion relationship determines a discrete spectrum of admissible E. It may be seen that, when $\Delta w \equiv w_{II} - w_I$ is large compared with h^2/mb^2, eigensolutions exist for which $E - w_I \ll w_{II} - E$. For these, (19) takes the approximate form

$$f_{II} \doteq A \exp[-\lambda_{II}(r - b)]\ Y_\ell(\theta,\chi), \text{ in } r \ge b. \tag{21}$$

The fluid is confined in region II to a boundary layer of thickness $1/\lambda_{II}$, or

$$a_m = \hbar\ (2m\Delta w)^{-1/2}. \tag{22}$$

This phenomenon is often called 'healing', the layer itself a 'healing layer', and a_m the 'healing length'. To the fluid mechanicist, the abrupt increase Δw in w at r = b can only be hydrostatically balanced by an equally abrupt increase in quantum pressure. It is the non-local character of quantum pressure that causes the fluid to pass through the barrier at r = b and, when lower potentials are available externally, permits it to seep out of region I.

In view of later developments, it is worth elaborating the situation just described. First we allow the well to have any shape, defining n to be a coordinate that measures distance from the discontinuity normally outwards from I to II. Second, we allow w_I and w_{II} to vary, and suppose that the large transition from w_I up to w_{II} does not occur abruptly as in (16), but continuously over some distance, a, comparable with a_m. Within this distance, there is evidently no unique way of defining 'the' surface, S, of the well. We note, however, that in the case of discontinuous w just considered, $j_\ell(\lambda_I b)$ is small, by (20). This suggests we should locate S on the surface of zero f_I.

To elucidate the healing layer structure, we introduce a stretched coordinate, ξ, and cast (15) into dimensionless form by writing

$$\xi = n/a, \qquad f = ax(\xi), \tag{23}$$

$$q = a/a_m, \qquad w = w_I + g(\xi)\Delta w, \tag{24}$$

where we suppose g is exponentially small at the inner ($\xi = -\infty$) edge of the boundary layer, and is unity at the outer ($\xi = +\infty$) edge. It should be realized that x, w_I, Δw and g will generally depend on position on S. To the first two orders, however, this dependence only occurs parametrically in the solution, and will therefore be suppressed. Writing

$$x = x_o(\xi) + ax_1(\xi) + \ldots, \tag{25}$$

substituting into (15), and equating like powers of a, we obtain

$$d^2x_o/d\xi^2 - q^2 g(\xi)x_o = 0, \tag{26}$$

$$d^2x_1/d\xi^2 - q^2 g(\xi)x_1 = -(C_1^{-1} + C_2^{-1})dx_o/d\xi, \tag{27}$$

where C_1 and C_2 are the principal radii of curvature of S at the point concerned. Since f_{II} is identically zero, the solutions to (26) and (27) must obey

$$x_o \to 0, \quad x_1 \to 0, \quad \text{for } \xi \to +\infty. \tag{28}$$

Successful matching to the interior solution, f_I, requires

$$x_o \sim (\partial f_I/\partial n)_S \xi, \qquad x_1 \sim -\tfrac{1}{2}(C_1^{-1} + C_2^{-1})(\partial f_I/\partial n)_S \xi^2, \quad \text{for } \xi \to -\infty. \tag{29}$$

Explicit solutions can generally be obtained only by numerical means. They obey integral conditions which we will later find useful (§4):

$$\frac{1}{q^2}\left(\frac{\partial f_I}{\partial n}\right)_S^2 = \int_{-\infty}^{\infty} x_o^2 \frac{dg}{d\xi}\, d\xi, \tag{30}$$

$$-\frac{2}{q^2}\left(\frac{1}{C_1} + \frac{1}{C_2}\right) \bar{\int}_{-\infty}^{\infty} \left(\frac{dx_o}{d\xi}\right)^2 d\xi = \int_{-\infty}^{\infty} 2x_o x_1 \frac{dg}{d\xi}\, d\xi, \tag{31}$$

where the bar through the integral sign signifies that the convergent part of the integral is taken. Despite appearances, this integral is negative.

The integral relationships (30) and (31) may be interpreted in the light of the Grant tensor (13). The terms on the left give the main parts of the leap of σ_{nn} across the boundary layer; the terms on the right give the corresponding integrated effects of the external force $f^{2\vec{\nabla}}w$ balancing them. The dominant term, given on the left of (30), arises from the 'pressure' of the particle trying to escape the well. The next largest term, shown on the left of (31), clearly has the form of a quantum surface stress, with

$$T_m = \frac{2a\Delta w}{q^2} \int_{-\infty}^{\infty} (a \frac{dx_0}{d\xi})^2 d\xi \quad . \tag{32}$$

as coefficent of surface tension. It is easy to make an estimate of T_m. If we take g to be a unit step function, we find from (26) that

$$T_m \doteq -a_m^3 \Delta w \, (\partial f_I/\partial n)_S^2. \tag{33}$$

Passing from 'hydrostatics' to 'hydrodynamics' by abandoning (14), we see from (8) that another type of healing phenonmenon will occur when u is large. A particularly significant case occurs at a vortex line where, by (11), u is of order $nh/m\tilde{\omega}$, at small distances, $\tilde{\omega}$, from the vortex axis. It follows from (8) and (9) that ρ is of order $\tilde{\omega}^{2n}$ for $\tilde{\omega} \to 0$. The fact that ρ is zero on the axis itself means that a closed vortex ring, or a vortex line terminating on boundaries ($w = \infty$), will transform an otherwise simply-connected container into a multiply-connected domain, $\mathcal{R}$, so justifying a posteriori the application of (11). Unlike the healing at a wall considered earlier, the depression of ρ at the vortex axis occurs over distances comparable with the scale of the container. The corresponding vortices in the condensate discussed in §3 have cores confined to much smaller distances from their axes.

Before concluding this section we make one remark, obvious perhaps, but relevant to §4. When the particle is trapped in a potential well with moving walls [$w = w(\vec{x},t)$], ϕ is necessarily non-zero and ρ is time-dependent. Nevertheless, provided the time-scales over which w changes are large compared with the reciprocal of the quantum frequency h/mb^2, we can regard the fluid as being in a quasi-hydrostatic state, ignore the time derivative in (1), and treat t in w parametrically. In quantum language, the Born-Oppenheimer approximation is said to apply.

3. THE CONDENSATE MODEL

We now consider an assembly of N identical particles (bosons) of mass M in a potential field $W(\vec{x})$. If the particles did not interact, the wavefunction for the system could be written down as a symmetrized product of the N one-particle wavefunctions, $\Psi(\vec{x},t)$, obeying (11) with W and M replacing w and m. It would be probably more convenient, however, to replace the normalization condition (10) by

$$\int |\Psi|^2 d\vec{x} = N, \quad \text{or} \quad \int \rho d\vec{x} = \rho_\infty v, \tag{34}$$

where v is the volume of the system and $\rho_\infty = MN/v$. The resulting theory is well-understood, and contains features that fruitfully represent helium near absolute zero[8]. It may be seen from (18), however, that the ground state for, say, the potential well (16) would be one in which all the particles would be at the origin, with high probability. To eliminate this unphysical behavior, the imperfect bose condensate has been devised. A short-range repulsive potential $V(\vec{x} - \vec{x}')$ is introduced in an ad hoc way, and to W the potential

$$\int V(\vec{x} - \vec{x}') |\Psi(\vec{x}')|^2 d\vec{x}' \tag{35}$$

is added which increases as the density of nearby bosons increases. The simplest case arises when V is taken to be

$$V(\vec{x} - \vec{x}') = V_0\, \delta(\vec{x} - \vec{x}'). \tag{36}$$

Equation (1) is then replaced by

$$i\hbar\partial\Psi/\partial t = -(\hbar^2/2M)\nabla^2\Psi + (V_0|\Psi|^2+W)\Psi. \tag{37}$$

A fuller and more satisfactory derivation of (37) may be found elsewhere[3,4]. It is of some interest that non-linear Schrödinger equations of the form (37) have been the subject of close scrutiny in recent years in non-quantal contexts, particularly in theories of weak non-linear waves and stability[9]. The Madelung transformation

$$\Psi = F\exp(iM\Phi/\hbar), \tag{38}$$

follows the course of §2 with minor changes. Most significant is the addition of a 'gas pressure',

$$p = (V_0/2M^2)\rho^2, \tag{39}$$

which (multiplied by δ_{ij}) should be included in the stress tensor (13). Thus (8) is replaced by

$$\frac{\partial\Phi}{\partial t} + \frac{1}{2}\vec{u}^2 + \frac{W}{M} + \frac{2p}{\rho} + \mu = 0. \tag{40}$$

The presence of the repulsion, V_0, and its associated gas pressure restores a number of physical effects absent in §2. The tendency towards condensation is eliminated for all sufficiently large systems. To see this, return to the hydrostatic theory of §2 and the potential well (16). The spherically symmetric (ℓ=0) ground state now obeys

$$\frac{d^2F}{dr^2} + \frac{2}{r}\frac{dF}{dr} = \frac{2M}{\hbar^2}(E-W)F - \frac{2MV_0}{\hbar^2}F^3. \tag{41}$$

If NV_0 and ΔW are both large compared with h^2/Mb^2, (41) gives everywhere except near the surface, S, of the well

$$\rho = \rho_\infty = MF_I^2 = MN/v, \tag{42}$$

the corresponding one-particle energy being given by

$$E - W_I = \rho_\infty V_0/M. \tag{43}$$

The fluid is spread out uniformly in the well.

Near S the derivatives of F become large, and the constant solution (42) breaks down. We may follow the argument of §2. Introducing a new healing length

$$a = \hbar(2\rho_\infty V_0)^{-1/2}, \tag{44}$$

writing

$$\xi = n/a, \quad F = X(\xi), \quad W = W_I + (\rho_\infty V_0/M)G(\xi), \tag{45}$$

where $G(\xi)$ is exponentially small for $\xi \to -\infty$, expanding X as

$$X(\xi) = X_0(\xi) + aX_1(\xi) + \ldots, \tag{46}$$

substituting into (15), and equating like powers of a, we obtain

$$d^2X_0/d\xi^2 - [G(\xi) - 1 + (X_0/F_I)^2]\, X_0 = 0, \tag{47}$$

$$d^2X_1/d\xi^2 - [G(\xi) - 1 + 3(X_o/F_I)^2]\, X_1 = -(C_1^{-1} + C_2^{-1})dX_o/d\xi. \quad (48)$$

Matching at the edges of the boundary layer requires

$$X_o \to 0, \quad X_1 \to 0, \quad \xi \to +\infty; \quad (49)$$

$$X_o \to F_I, \quad X_1 \to 0, \quad \xi \to -\infty. \quad (50)$$

Again, explicit solutions generally require numerical integrations, though useful integral relations may be established, for instance

$$\frac{1}{2} F_I^2 = \int_{-\infty}^{\infty} X_o^2 \frac{dG}{d\xi}\, d\xi , \quad (51)$$

$$-2\left(\frac{1}{C_1} + \frac{1}{C_2}\right) \int_{-\infty}^{\infty} \left(\frac{dX_o}{d\xi}\right)^2 d\xi = \int_{-\infty}^{\infty} 2X_o X_1 \frac{dG}{d\xi}\, d\xi. \quad (52)$$

Once more, the dominant contribution to the leap in stress across the healing layer arises from the interior solution, although now it is the gas pressure and not the quantum pressure that is mainly responsible. Again, the next largest term can be interpreted as a quantum surface tension, with positive coefficient

$$T_M = 2a\left(\frac{\rho_\infty V_o}{M}\right) \int_{-\infty}^{\infty} \left(\frac{dX_o}{d\xi}\right)^2 d\xi . \quad (53)$$

As before, T_M may be estimated[3] from a simple model of X_o. If we suppose that G is a step function of infinite height ($\Delta W = \infty$), (46) may be solved as $X_o = F_I \tanh(-\xi/\sqrt{2})$, and (53) gives

$$T_M \doteq \sqrt{2}\,\pi^2 \rho_\infty / 3M^2 a. \quad (54)$$

Passing again from 'hydrostatics' to 'hydrodynamics', we note that the gas pressure can supply the restoring force necessary for compressional waves. Perturbing about the static solution (41), we readily find that long wavelength sound propagates at the velocity

$$c = \sqrt{(dp/d\rho)} = \sqrt{(2p/\rho)} = \pi/Ma\sqrt{2}. \quad (55)$$

At wavelengths of order a and smaller, the quantum pressure increases the phase speed, decreases the group velocity, and introduces weak dispersion.

Vortex lines may be studied as in §2. Unlike their classical counterparts, the cores of these vortices do not have sharply defined surfaces separating regions of zero and non-zero vorticity. All the vorticity they contain is concentrated as δ-functions on their axes. Such a vortex, if classical, would have infinite self-energy. Here, however, the density decreases over the characteristic distance a as the axis is approached, so ensuring a finite tension. The depletion of fluid in the core makes the vortex resemble the classical hollow core model. The permanence of vortex rings implied by the Kelvin-Helmholtz theorem makes them excellent candidates for quasi-particle models, so reviving in a novel context the ideas underlying the vortex atoms proposed by Kelvin in the nineteenth century.

4. STRUCTURE OF THE NEGATIVE ION

It is possible[3,10-12] to account with relative ease for many features of the negative ion by combining the methods of §§2 and 3 above. We use the theory of §1 to represent the electron, regarding w as the potential created by the surrounding condensate; we apply the formalism of §2 to the

exterior of the bubble, taking for W the potential of the electron. More explicitly, we introduce the energy,

$$\int\int U(\vec{x} - \vec{x}')|\psi(\vec{x})|^2|\Psi(\vec{x}')|^2 d\vec{x}d\vec{x}', \tag{56}$$

representing the repulsion of an electron at $\vec{x}$ and a boson at $\vec{x}'$. Taking again the simplest case of a δ-function interaction

$$U(\vec{x} - \vec{x}') = U_o \delta(\vec{x} - \vec{x}'), \tag{57}$$

we then have

$$w(\vec{x}) = \int U(\vec{x} - \vec{x}')|\Psi(\vec{x}')|^2 d\vec{x}' = U_o|\Psi(\vec{x})|^2, \tag{58}$$

$$W(\vec{x}') = \int U(\vec{x} - \vec{x}')|\psi(\vec{x})|^2 d\vec{x} = U_o|\psi(\vec{x}')|^2. \tag{59}$$

By (10) and (58), $\Delta w = U_o\rho_\infty/M$ so that by (22), (23) and (44), $q^2 = mU_o/MV_o$. Equations (1) and (37) become coupled:

$$i\hbar\partial\psi/\partial t = -(\hbar^2/2m)\nabla^2\psi + U_o|\Psi|^2\psi, \tag{60}$$

$$i\hbar\partial\Psi/\partial t = -(\hbar^2/2M)\nabla^2\Psi + (V_o|\Psi|^2 + U_o|\psi|^2)\Psi. \tag{61}$$

As in §2, we define the electronic surface, S, of the bubble by the zero of ψ.

The key to a simple 'hydrostatic' solution of (60) and (61) lies in the fact, which we can verify a posteriori, that the radius, b, of the bubble is large compared with a and a_m, so that the boundary layer methods of §§2 and 3 can be used with minor emendations. We must not forget however that, since the roles of interior and exterior of the bubble have been exchanged for the condensate, the sign of ξ in §3 must be reversed. The mainstream value of F, denoted in §3 by F_I is now written F_S.

To leading order, we set $g(\xi) = X_o^2/F_S^2$ and $G(\xi) = (a^2U_o/F_S^2V_o)x_o^2$ in (26) and (47), as (58) and (59) require. The integral relations (30) and (51) may then be combined to give

$$\frac{a^2}{q^2}\left(\frac{\partial f}{\partial n}\right)_S^2 - \frac{V_o}{2U_o}F_S^2 = \frac{a^2U_o}{F_S^2}[x_o^2X_o^2]_{-\infty}^{\infty} = 0, \tag{62}$$

where we have appealed to (28) and (50). To the next order, the forms of g and G require reconsideration[12]. In place of (27) and (48) we have

$$d^2x_1/d\xi^2 - (q/F_S)^2(X_o^2x_1 + 2x_oX_oX_1) = -(C_1^{-1} + C_2^{-1})dx_o/d\xi, \tag{63}$$

$$d^2X_1/d\xi^2 - (3X_o^2/F_S^2 - 1)X_1 - (a^2U_o/F_S^2V_o)(x_o^2X_1 + 2X_ox_ox_1) = -(C_1^{-1} + C_2^{-1})dX_o/d\xi. \tag{64}$$

The integral consequences (31) and (52) are modified accordingly, and the result (62) is altered to

$$\frac{a^2}{q^2}\left(\frac{\partial f}{\partial n}\right)_S^2 - \frac{V_o}{2U_o}F_S^2 = 2a\left(\frac{1}{C_1} + \frac{1}{C_2}\right)\int_{-\infty}^{\infty}\left[\frac{a^2}{q^2}\left(\frac{dx_o}{d\xi}\right)^2 + \frac{V_o}{U_o}\left(\frac{dX_o}{d\xi}\right)^2\right]d\xi, \tag{65}$$

which now includes the effects of interfacial tension.

The jump conditions (62) or (65) across the boundary layer suffice to match the mainstream electron solution to the mainstream condensate solution. Applied to the electron bubble, we have by (18)

$$f = A(\sin\lambda_I r)/\lambda_I r, \tag{66}$$

showing that $\lambda_I b = \pi$. By (10) the solution is normalized to the first two orders[12] in a/b, if $A^2 = \pi/2b^3$. By (10) and (11) we obtain

$$b = \left(\frac{\pi M^2 a^2}{m\rho_\infty}\right)^{1/5} - \frac{8M^2 a}{5\rho_\infty} \int_{-\infty}^{\infty} \left[\frac{1}{m}\left(a\frac{dx_a}{d\xi}\right)^2 + \frac{1}{M}\left(\frac{dX_a}{d\xi}\right)^2\right] d\xi. \qquad (67)$$

It is not at once clear whether b will be decreased by the positive surface tension (53) of the condensate or increased by the negative surface tension (32) of the electron. If we use estimates (33) and (54) however, we see that $|T_m|/T_M$ is of order q^{-1} and, since experiments indicate (§5) that $q < 1$, it appears that the bubble radius should be larger than $(\pi M^2 a^2/m\rho_\infty)^{1/5}$. Direct numerical integrations[12] of x_o and X_o, and evaluation of the integral seen in (67), suggest that the difference is of the order of a.

The effects of polarization induced by the electron in the surrounding helium can be included by adding[12] to (56) the term

$$-(\tilde{\alpha}e^2/8\pi) \iint |\psi(\vec{x})|^2 |\psi(\vec{x}')|^2 |\vec{x} - \vec{x}'|^{-4} d\vec{x} d\vec{x}', \qquad (68)$$

where $\tilde{\alpha}$ is the polarizability of the helium and e is the electronic charge. This has the effect of contracting the bubble by order $\tilde{\alpha}Me^2a^2/4\pi\hbar^2b^3$. A detailed theory[12] shows that the reduction is of order a/3 in the practically interesting cases.

Further complications arise when the dynamics of the bubble are considered, although the time-scales of interest are usually large enough compared with the electronic frequencies to justify the neglect of $\partial\psi/\partial t$ in (60); see §2. To evaluate the effective hydrodynamic mass, we consider the bubble in steady motion U, at small Mach numbers $\mathcal{M}=U/c$. The electronic radius, b, of the bubble is increased by about $5\mathcal{M}^2\%$ because of the pressure forces associated with the flow of condensate over its surface. It is also made slightly oblate, with an ellipticity close to $\mathcal{M}^2/2$. Ignoring this effect, it is found that the dipolar back-flow created by the ion coincides with that of a hard sphere whose radius, b_e, is less than the electronic radius, b, by one to two healing lengths:

$$b_e = b - (aM/\rho_\infty) \int_{-\infty}^{\infty} X_o^2(\xi) d\xi. \qquad (69)$$

It is this radius, rather than b, that determines the induced mass of the ion.

Further details of the calculations outlined above may be found in the paper by Roberts and Grant already cited[12]. We conclude this section by breaking new ground. We consider the oscillations of the bubble, their implications for phonon-ion collisions, and the mobility of negative ions at low temperatures. We again adopt the boundary layer methods described above but, of course, retain the term $\partial\Psi/\partial t$ in (61), so introducing a velocity potential, Φ, in the condensate. We retain only the dominant part of the boundary layer structure, excluding both surface tension and polarization effects. We write,

$$f = f_o + \alpha a f', \quad F = F_o + \alpha a F', \quad \Phi = \alpha\Phi', \qquad (70)$$

where the suffix o stands for the steady solution obtained earlier, and the terms in α represent time-dependent perturbations, where $0 < \alpha << 1$.

It is readily seen from (7) and (40) that Φ' and F' both obey the acoustic wave equation

$$\partial^2\Phi'/\partial t^2 = c^2\nabla^2\Phi'. \qquad (71)$$

We could, by following Celli, Cohen and Zuckerman[13], examine solutions in the form of outgoing waves. The eigenfrequencies would be complex, because of the reduction in oscillation amplitude at a point fixed in space as the energy of surface motion is radiated to infinity. The corresponding eigenfunction must tend to infinity with r since, the more distant a wave is, the earlier it must have left the surface, and the greater the amplitude of surface oscillation must then have been. We will not consider solutions of this type below. We will confine our attention to the scattering problem in which an incoming plane wave travelling in the z-direction

$$S'_{INC} = \exp[i(kz - \omega t)], \tag{72}$$

where k and $\omega = ck$ are real, is scattered by the bubble into a set of outgoing waves. We first aim to calculate the scattering amplitude, $h_\ell(k)$, of the ℓth partial wave[13]

$$h_\ell = \frac{1}{1 + iQ_\ell}, \quad Q_\ell = \frac{kby_\ell(kb) + K_\ell y_\ell'(kb)}{kbj_\ell(kb) + K_\ell j_\ell'(kb)}, \tag{73}$$

where $y_\ell(z)$ is the spherical Bessel function of the second kind and K_ℓ is the spring constant of the bubble for this mode. We then use h_ℓ to compute the differential cross-section[14] of the bubble

$$\sigma(k,\theta) = k^{-2}\left|\sum_{\ell=0}^{\infty}(2\ell + 1)h_\ell(k)P_n(\cos\theta)\right|^2, \tag{74}$$

and hence the momentum-transfer cross-section[14]

$$\sigma_T(k) = \int\int\sigma(k,\theta)(1 - \cos\theta)\sin\theta d\theta d\chi. \tag{75}$$

From this we finally evaluate the mobility, μ_e, of the ion from[14]

$$\frac{e}{\mu_e} = -\frac{\hbar}{6\pi^2}\int_{-\infty}^{\infty}\sigma_T(k)\frac{\partial n(k)}{\partial k}k^4 dk, \tag{76}$$

where

$$n(k) = [\exp(\hbar ck/KT) - 1\ ]^{-1}, \tag{77}$$

is the density of phonons (in $\vec{\hbar k}$-space) at temperature T. Here K is Boltzmann's constant.

To determine the spring constants, K_ℓ, we have to match solutions of (71) across the boundary layer on S', the deformed electronic surface, to the quasi-static solutions (18) of the electron mainstream. We first consider the case $\ell \geq 1$. The fact that

$$\psi = A_0 j_0(\lambda_I r) + \alpha a A' j_\ell(\lambda_I r)\ Y_\ell(\theta,\chi), \tag{78}$$

implies that S' has the equation

$$r = b(\theta,\chi,t) \equiv b_0 + \alpha a b'(t)Y_\ell(\theta,\chi), \tag{79}$$

where (using $\lambda_I b_0 = \pi$)

$$b'/b_0 = j_\ell(\pi)\ A'/A_0. \tag{80}$$

We will continue to refer the boundary layer structure to the unperturbed position, S_0, of the electronic surface, and not to S'. We introduce x', X' and η', the boundary layer forms of f', F' and Φ', and expand these in ascending powers of a

$$x' = a^{-1}x_0' + x_1' + \ldots, \quad X' = a^{-1}X_0' + X_1' + \ldots, \quad \eta' = \eta_0' + a\eta_1' + \ldots, \tag{81}$$

where the coefficients shown depend on t and $\xi = (r - b_o)/a$ and parametrically on Θ and χ. We substitute these into the boundary layer forms of (60) and (61) which, in the Madelung framework, give to the first two orders

$$\partial^2 x'/\partial\xi^2 - (q/F_S)^2(X_o^2 x' + 2x_o X_o X') = -(2a/b)\partial x'/\partial\xi, \tag{82}$$

$$\partial^2 X'/\partial\xi^2 - (3X_o^2/F_S^2 - 1)X' - (a^2 U_o/F_S^2 V_o)(x_o^2 X' + 2X_o x_o x') = -(2a/b)\partial X'/\partial\xi + (M/F_S^2 V_o)X_o \partial\eta'/\partial t, \tag{83}$$

$$X_o \partial^2\eta'/\partial\xi^2 + 2(dX_o/d\xi)\partial\eta'/\partial\xi = -(2a/b)X_o\partial\eta'/\partial\xi - 2a^2\partial X'/\partial t. \tag{84}$$

It seems clear from (84) that $X_o^2 \partial\eta_o'/\partial\xi$ is independent of ξ and, since there is no net condensate flow through the boundary layer at any point, that constant must be zero. Thus η_o' takes throughout the boundary layer the mainstream value Φ_S' of Φ, evaluated on S_o. The right-hand side of (83) does not contribute to leading order in a, and (82) and (83) may be solved to give

$$x_o' = \zeta dx_o/d\xi, \quad X_o' = \zeta dX_o/d\xi, \tag{85}$$

where ζ is independent of ξ. These forms represent a net displacement of the equilibrium boundary layer from S_o to S', without change of form; we conclude that $\zeta = -b'Y_\ell$.

In proceeding to the next order we note that, since the velocity of sound (55) is of order 1/a, the time derivatives in (83) and (84) now contribute. In fact, excluding again a net flux of condensate through the boundary layer, (84) shows that $\partial\eta_1'/\partial\xi$ takes the value $-a^2\partial\zeta/\partial t$ throughout, and in particular on the outer edge ($\xi = \infty$) of the boundary layer. It follows that

$$a\partial b'/\partial t = (\partial\Phi'/\partial r)_S, \tag{86}$$

an equation with an obvious interpretation. The equations (82) and (83) again admit an integral, namely

$$\frac{MX_o^2}{2U_o F_S^2}\frac{\partial\eta_o'}{\partial t} = \frac{a^2}{q^2}\left[\frac{dx_o}{d\xi}\frac{\partial x_1'}{\partial\xi} - x_1'\frac{d^2x_o}{d\xi^2}\right]_{-\infty}^{\xi} + \frac{V_o}{U_o}\left[\frac{dX_o}{d\xi}\frac{\partial^2 X_1'}{\partial\xi^2} - X_1'\frac{d^2X_o}{d\xi^2}\right]_{-\infty}^{\xi}. \tag{87}$$

On taking the limit $\xi \to +\infty$, and using (18) to evaluate the contributions from the lower limits, we find

$$\partial\Phi_S'/\partial t = c^2 K_\ell a b'/b_o, \tag{88}$$

where

$$K_\ell = \begin{cases} 5/2, & \text{if } \ell = 0; \\ 1 - \ell + \pi j_{\ell-1}(\pi)/j_\ell(\pi), & \text{if } \ell \geq 1. \end{cases} \tag{89}$$

The numerical values of K_ℓ for the first 20 values of ℓ are given in table I. That of K_o was obtained from an analysis too similar in spirit to the one just described to be repeated here. It may be noted that K_1 is zero, representing the fact that the bubble is neutrally stable to a uniform displacement. Equations (86) and (88) are applied on S_o, and provide the boundary conditions to which solutions of (71) must be subjected.

We developed a program for an Hewlett-Packard 9820 A desk computer to evaluate $\sigma_T(k)$ and μ_e from an arbitrary set of the spring constants. The

results were tested with the values ($K_0 = 0.23474$; $K_1 = 0$; $K_2 = 0.45045$; $K_n = 0$, $n>2$) used by Baym, Barrera and Pethick[14], and good agreement was obtained. The programme was then used to generate the results shown in Figures 1 and 2. The effect of truncating series (74) at $\ell = 2$ and $\ell = 19$ are shown in both cases. The prominent peak in $\sigma_T(k)$ seen in Figure 1 is due to a d-wave resonance ($\ell = 2$). A new minor peak is added every time ℓ is incremented by 1. The curve appears to approach its geometrical value[15] ($\sigma_T/4\pi b_0^2 \to 1/2$) with an oscillation of amplitude $(kb_0)^{-2/3}$ and period $2^{-1/3}$. In Figure 2, we see $\mu_e T^3$ plotted in units of L_0, as a function of T measured in units of T_0 where

$$T_0 = \hbar c/b_0 K, \qquad L_0 = 3\pi e\hbar^2 c^3/2b_0 K. \tag{90}$$

TABLE 1
Spring Constants

ℓ	K_ℓ	ℓ	K_ℓ
0	2.500000000	10	11.56327795
1	0.000000000	11	12.59928101
2	2.289868134	12	13.62973970
3	3.771253431	13	14.65585350
4	5.032253885	14	15.67849696
5	6.198547165	15	16.69832328
6	7.314641577	16	17.71583055
7	8.400646541	17	18.73140537
8	9.467085072	18	19.74535255
9	10.520037400	19	20.75791573

5. EXPERIMENTAL COMPARISONS

The condensate model of helium II is essentially a theory having only one disposable parameter, namely the pseudo-potential, V_0, or equivalently the healing length, a. It is natural to seek to choose this so that theory and observation are in optimum accord. Clearly a choice of a made to fit one physical phemomenon well is likely to conflict with others, and an overall consistency with the experimental facts is not to be anticipated. One notes particularly that, since the condensate is a gas obeying the equation of state (39), we should not expect the theory to perform well at the vapor pressure.

One can obtain an estimate of $V_0 = 4\pi d\hbar^2/M$ from measurements of the atomic diameter, d, by α-particle scattering experiments. Values of d of about 2.7 Å have been found. If ρ_∞ is 0.145 g/cm^3, the healing length would be 0.82 Å, leading to too small a velocity of sound. One popular procedure has been to extract a from accurate experimental determinations of the relation between the velocity and energy of circular vortex rings. This had led to estimates of $a \doteq 1.28$ Å, giving much too small a value of c. The reliability of the approach can, however, be questioned. One would have expected a to decrease with increasing pressure, but the reverse seems to be true[16]. It is now believed[17] that the core of a superfluid vortex is the seat of excitations (normal fluid), and that the surface of a vortex core marks the distance from the axis at which the Landau critical velocity is reached, rather than a quantum healing distance; such a belief is consistent with the increase of a with ρ_∞.

Perhaps the most satisfactory way of estimating a is through the velocity of sound (55). To give an example, if we take c = 238 m/s, we obtain a ≐ 0.47 Å and for ρ_∞ = 0.145 g/cm^3 we find that V_0 ≐ 1.7 10^{-37} g cm^5/s^2, a value admittedly three times larger than the scattering experiments suggest, and moreover one which will alter as c and ρ_∞ change through applied pressure. Nevertheless, by using c to determine a, we obtain a coefficient of surface tension, T_M, from estimate (54) of 0.37 g/s^2, which is in good agreement with the experimental value of 0.34 g/s^2 at low temperatures.

Turning to the bubble, we see that, in the first approximation, the theory does not require a knowledge of the pseudo-potential, U_0, either for its equilibrium structure or for its oscillation spectrum. The radius, $(\pi M^2 a^2/m\rho_\infty)^{1/5}$, predicted by the first approximation is somewhat small, 11.8 Å using the values quoted above. Since c and ρ_∞ increase with increasing pressure, p, this radius decreases with increasing pressure, although somewhat more slowly than experiments indicate. The bubble radius is increased when the effects of surface tension are added. Unfortunately, Grant and Roberts[12] did not examine values of a as small as 0.47 Å, so that the value of the integral appearing in (67) is not known. Using our earlier estimates, however, it appears that b will be increased to about 13.3 Å by surface tension effects. Table 2 gives $\mu_e T^3$ for a few values of T for both the ℓ = 2 and the ℓ = 19 truncations, and for values of b of 11.8 Å, 13.3 Å and 16.0 Å. At the ℓ = 2 level of truncation, there is a clear tendency for $\mu_e T^3$ to approach a limiting value, of about 36 cm^{2}K^{3}Vs in the case of the 16 Å bubble, as T increases. The explanation of this behavior was provided by Baym, Barrera and Pethick[14] in terms of the shape of the d-wave resonance of Fig. 1. Not surprisingly in view of the very different form of σ_T obtained at ℓ = 19 truncation, the constancy of $\mu_e T^3$ is not as marked at this level. Nevertheless, the values shown for ℓ = 19 in Table 1 are not ridiculously far from the experimental value[18] of about 32.5 cm^{2}K^{3}Vs in the range of T in which Baym, Barrera and Pethick measured the success of the work.

When we take the theory of the bubble to the second approximation, a new disposable parameter enters, namely the psuedo-potential, U_0, or equivalently $q = a/a_m$, a relation we can also write as $q^2 = mU_0/MV_0$. Roughly speaking q, as the ratio of the two healing lengths, measures the relative penetration of the condensate wavefunction into the cavity to the penetration of the electron wavefunction into the condensate. If q were zero, it would be legitimate to treat the condensate as an abrupt edge and only consider the electronic boundary layer of §2. At first sight it might appear that, since q^2 is proportional to m/M ≐ 1.37 10^{-4} it would be admissible to follow Celli, Cohen and Zuckerman[13] in taking this view. The indications are, however, that U_0/V_0 is large. Scattering experiments give an electron-helium scattering length, λ, of about 0.60 Å, implying that $U_0 = 2\pi\lambda\hbar^2/m$ is about 4.6 10^{-35} g cm^5/s^2. Taken with the experimental value of 5.7 10^{-38} g cm^5/s^2 for V_0, we obtain U_0/V_0 ≐ 810 and q ≐ 0.33. It would be interesting to see whether the effect of restoring q to the Celli-Cohen-Zuckerman theory would have serious repercussions. The indications are that it would not.

The neglect of q in the condensate theory described here would eliminate the condensate surface tension, T_M, and transform the interfacial boundary layer into the structure considered in §2. The associated negative surface tension, T_m, would tend to expand the bubble, an effect confirmed by the calculations of Grant and Roberts[12]. All influences of interfacial tension are, however, of second order in the condensate theory. In the approach of Celli, Cohen and Zuckerman[13], the interfacial tension, σ, is a first order effect.

These authors regarded σ as a disposable parameter that could be legitimately chosen to fit the observed bubble radius at the applied pressure of interest. It is easy to verify that the interfacial tension they require is positive and, particularly at higher pressures, several times larger than the condensate surface tension, T_M, considered earlier. It may be wondered why, with this sign difference, the bubble radii they obtain are, being in perfect agreement with experiment, larger than those obtained from the condensate. The answer is to be found in (39). The condensate is a gas and, to obtain agreement with the observed helium densities, it is necessary to choose a large V_o, leading to pressures (39) of the order of 40 atmospheres. In contrast, the Celli, Cohen and Zuckerman theory treats the helium as a classical compressible fluid, not containing the pressure (39), and to avoid large bubble radii at the vapor pressure, a positive interfacial tension is needed. As we have stated above, we regard (39) as an artificial construct of the theory, not to be identified with the applied pressure, and base our comparison with experiment on density and velocity of sound data.

As Schwarz[15] observes, if the spring constants were regarded as disposable parameters, there would be no difficulty in reproducing any ion mobility data precisely. It appears that even the added flexibility given to the theory by the ad hoc interfacial tension, σ, already permits an excellent account of the mobilities. Schwarz[15] has shown that, for their spring constants, the constancy of $\mu_e T^3$ in the range of T of interest is not lost when the truncation level is increased as it is in ours. In comparing our theory with theirs, one must be perplexed by the substantial difference in the spring constants and in the shape of the mobility curve (labelled 'ℓ = 19' in Fig. 2). He must wonder if, in the disappointing form of that curve on the present theory, and in the sensitivity of the mobility itself to the healing length [as evinced by the c-dependence of (90)], the condensate theory has not met its most severe test to date. He may also speculate on the physical basis of the ad hoc interfacial tension required by the other approach to survive its trial by experiment, and also whether the effects of roton-ion collisions at the higher temperatures have been underestimated.

TABLE 2

Ion Mobilities, μ_e

(T in degrees K, $\mu_e T^3$ in units of cm^2K^3Vs)

ℓ = 2 Truncation						ℓ = 19 Truncation					
b_o=11.8 Å		b_o=13.3 Å		b_o=16.0 Å		b_o=11.8 Å		b_o=13.3 Å		b_o=16.0 Å	
T	$\mu_e T^3$	T	$\mu_e T^3$	T	$\mu_e T^3$	T	$\mu_e T^3$	T	$\mu_e T^3$	T	$\mu_e T^3$
0.34	229.	0.37	117.	0.31	97.0	0.32	265.	0.33	158.	0.35	70.5
0.41	131.	0.45	77.2	0.43	51.8	0.37	178.	0.42	84.9	0.39	59.0
0.51	86.7	0.52	62.3	0.53	41.7	0.48	95.3	0.46	71.0	0.43	49.0
0.58	70.0	0.56	56.9	0.58	39.5	0.52	79.7	0.52	59.0	0.50	40.0
0.63	63.9	0.64	50.2	0.65	37.6	0.58	66.2	0.57	51.1	0.59	33.1
0.72	56.3	0.70	47.5	0.73	36.6	0.64	57.3	0.71	39.8	0.70	28.1
0.78	53.4	0.78	45.2	0.78	36.5	0.80	44.7	0.85	33.8	0.83	24.6
0.98	49.5	0.94	43.9	0.95	37.4	1.01	36.0	1.01	29.6	1.02	21.0
1.18	49.7	1.15	45.0	1.16	39.9	1.13	30.1	1.13	26.8	1.14	19.4

ACKNOWLEDGEMENT

I am extremely grateful to Professor Russell J. Donnelly for his criticism of this work, and particularly for his contributions to §5. The work described was supported by the Air Force Office of Scientific Research under grant AF-AFOSR-71-1999 and by the National Science Foundation under grant NSF GH 35898.

REFERENCES

1. R. J. Donnelly, "Experimental Superfluidity," Chicago University Press, Chicago (1967).
2. A. L. Fetter, "The Physics of Liquid and Solid Helium," ed. K. H. Bennemann and J. B. Ketterson, Wiley, New York (1975).
3. E. P. Gross, "Quantum Fluids," ed. D. F. Brewer, North Holland, Amsterdam (1966).
4. A. L. Fetter and J. D. Walecka, "Quantum Theory of Many Particle Systems," McGraw Hill, New York (1971).
5. E. Madelung, Z. fur Phys. 40, 322 (1927).
6. J. Grant, Ph.D. Thesis, University of Newcastle (1972).
7. J. Grant, J. Phys. A, 6, L151 (1973).
8. S. Putterman, "Superfluid Hydrodynamics," North Holland, Amsterdam (1974).
9. L. M. Hocking and K. Stewartson, Mathematika 18, 219 (1971).
10. R. C. Clark, Phys. Lett. 16, 42 (1965).
11. R. C. Clark, "Superfluid Helium," ed. J. F. Allen, North Holland, Amsterdam (1966).
12. J. Grant and P. H. Roberts, J. Phys. A., 7, 260 (1974).
13. V. Celli, M. H. Cohen and M. J. Zuckerman, Phys. Rev. 173, 253 (1968).
14. G. Baym, R. E. Barrera and C. J. Pethick, Phys. Rev. Lett. 22, 20 (1969).
15. N. F. Mott and H. S. W. Massey, "The Theory of Atomic Collisions," Third Edition, Clarendon Press, Oxford (1965).
16. M. Steingart and W. I. Glaberson, Phys. Rev. A., 5, 985 (1972).
17. W. I. Glaberson, J. Low Temp. Phys. 4, 289 (1969).
18. K.W. Schwarz and R. W. Stark, Phys. Rev. Lett. 21, 967 (1968).
19. K. W. Schwarz, Phys. Rev. A., 6, 1958 (1972).

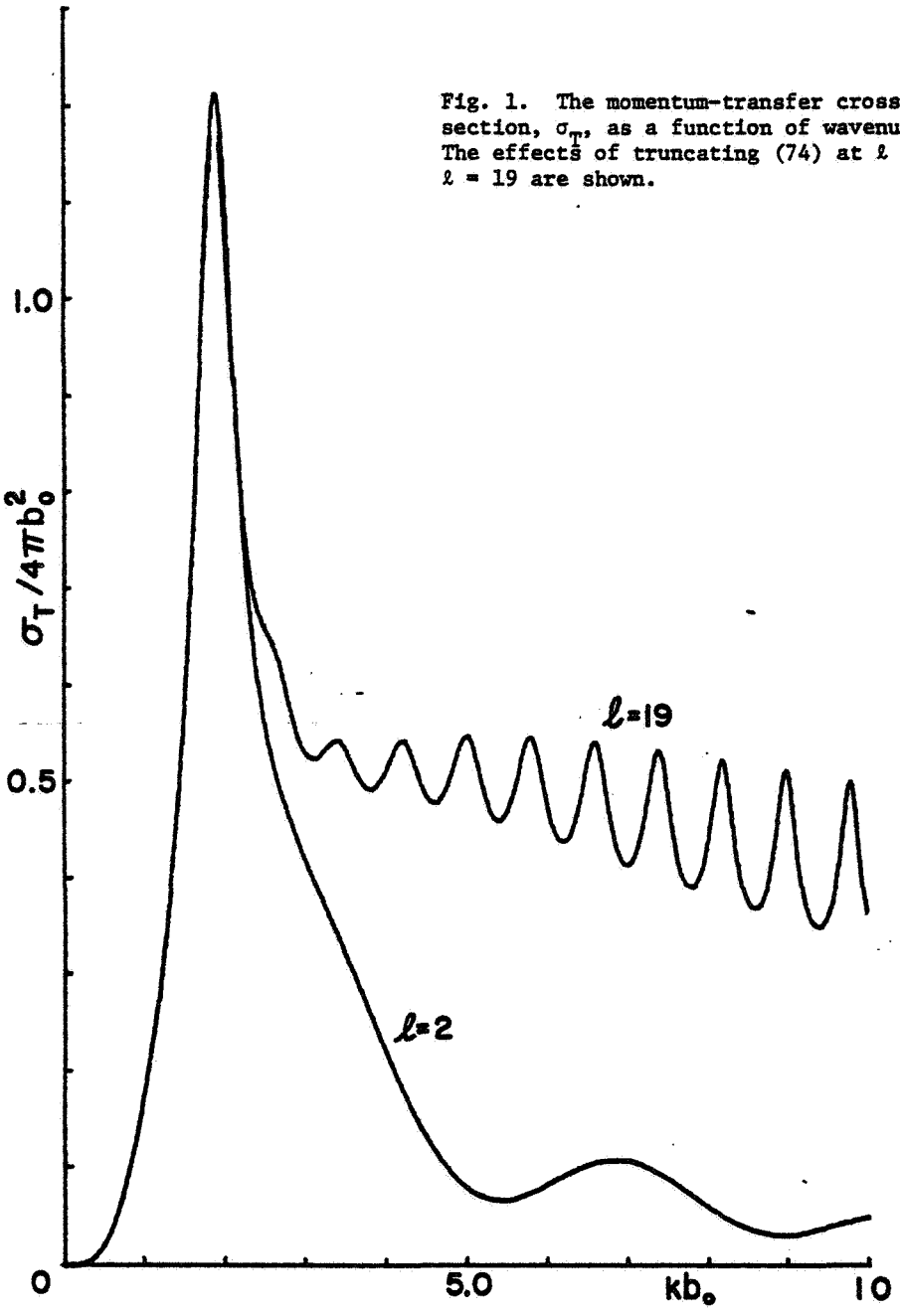

Fig. 1. The momentum-transfer cross-section, σ_T, as a function of wavenumber, k. The effects of truncating (74) at ℓ = 2 and ℓ = 19 are shown.

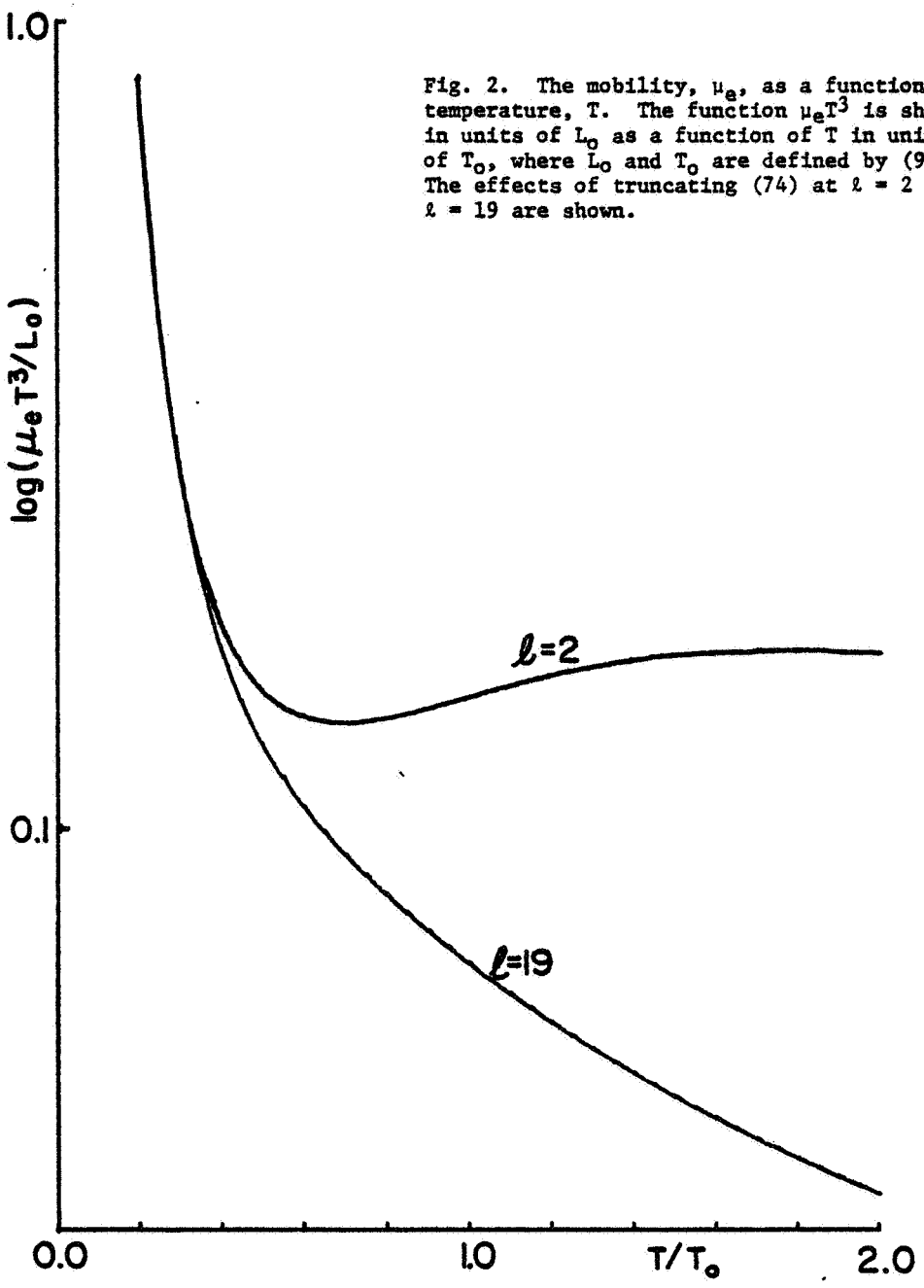

Fig. 2. The mobility, μ_e, as a function of temperature, T. The function $\mu_e T^3$ is shown in units of L_o as a function of T in units of T_o, where L_o and T_o are defined by (90). The effects of truncating (74) at $\ell = 2$ and $\ell = 19$ are shown.

D4

THE ROTATING, CHARGED OR GRAVITATING LIQUID DROP, AND PROBLEMS IN NUCLEAR PHYSICS AND ASTRONOMY

W. J. Swiatecki
Lawrence Berkeley Laboratory, University of California, Berkeley, CA 94720

ABSTRACT

A survey is presented of the equilibrium configurations of a rotating charged or gravitating liquid mass in a way that unifies the treatment of idealized rotating heavenly bodies, rotating drops in a weightless environment, and idealized rotating nuclei. A number of applications, especially to nuclear physics, is described.

I. INTRODUCTION

Figure 1 is a photograph of the planet Jupiter. The slightly flattened appearance is caused by rotation.

Figure 2 is a glass droplet from the lunar soil returned by the Apollo 11 mission (length about 1 mm). Presumably it was ejected from a meteorite impact on the moon as a molten, rotating blob, which solidified in flight.

Figure 3 is a picture of a series of sketches made by Niels Bohr on November 7, 1950 (his 65th birthday), during a conversation on the liquid drop theory of nuclear fission. On the right is a sequence of shapes of a fissioning nucleus of Np^{237}, calculated in 1968 by J. R. Nix using that theory. (Ref. 1)

These figures illustrate three fields in which the theory of rotating, charged or gravitating masses has found an application: astronomy, hydrodynamics in a weightless environment and nuclear physics.

Historically the theory of rotating homogeneous masses as idealized representations of planets, stars and nebulae goes back to Newton's investigations on the figure of the earth. In the past two and a half centuries the theory has been developed by many illustrious mathematicians, among them Maclaurin, Jacobi, Riemann, Poincaré, Liapunov, Jeans, Darwin, Cartan, Appell, and Lyttelton. In the last decade the subject was taken up anew by S. Chandrasekhar and N. Lebovitz and brought to a rare degree of perfection in Chandrasekhar's monumental work on "Ellipsoidal Figures of Equilibrium." (Ref. 2)

The theory of a rotating liquid mass endowed with a surface tension but no gravitational forces was stimulated by Plateau's experiments 100 years ago with globes of oil suspended in a liquid of the same density. The experiments were discussed in connection with Laplace's nebular hypothesis of the origin of the solar system. An account of the earlier investigations is given in Appell's "Mécanique Rationnelle". (Ref. 3, Vol. 4, Ch. IX)

The theory of rotating liquid masses with a surface tension and a uniform electric charge arose in nuclear physics in connection with the

study of nuclei endowed with large angular momenta. The major part of the binding energy of a nucleus is well represented by the model of a uniformly charged liquid drop with a surface tension, and the addition of a rotational energy to the conventional volume, surface, and electrostatic energies of the liquid drop model constitutes an interesting generalization. A number of authors, among them Pik-Pichak, Beringer and Knox, Hiskes, Sperber, Carlson and Pau Lu, Cohen, Plasil and Swiatecki, Chandrasekhar, Rosenkilde, Mollenauer and Wheeler have addressed themselves to this problem in the past 15 years. (See list of references in Ref. 4.)

It was soon realized that the astronomical problem, Plateau's problem and the nuclear problem are formally special cases of a single mathematical structure. They can in fact be discussed in a unified way by varying continuously a single parameter in the equations, the parameter being the relative intensity of the inverse-distance (gravitational or electrostatic) energy. In this way a problem or irresistible scope presents itself: to discuss in a unified manner the equilibrium shapes of rotating masses representing at one extreme idealized atomic nuclei, at the other idealized heavenly bodies, and covering in between engineering applications in weightless space laboratories. In this talk I would like to give you a survey of the problem from this unified point of view.

2. STATEMENT OF THE PROBLEM

Let me first state the idealized mathematical problem precisely. We consider a given volume of an incompressible fluid with a sharp boundary (which may or may not be simply connected--it may be in two or more pieces). The fluid may be gravitating and/or uniformly charged, it is endowed with a surface tension, and is rotating with a given angular momentum about its center of mass. The question is: what are the shapes of gyrostatic equilibrium of the fluid, i.e., shapes in which the only motion of all fluid elements is a uniform rotation with a common angular velocity?

The way one answers such a problem in gyrostatics is by writing down an effective potential energy and making it stationary with respect to all infinitesimal variations of the fluid boundary. This effective potential energy E is the ordinary potential energy augmented by a rotational energy. Thus in our case

$$E = E_S + E_I + E_R \ . \tag{1}$$

Here E_S is the surface energy, equal to the surface area of the configuration in question times the surface energy coefficient γ:

$$E_S = \gamma \oint d\sigma \ .$$

The quantity E_I is the inverse-distance energy, the sum of interactions between pairs of volume elements $d\tau_1$ and $d\tau_2$ interacting according to an inverse-distance potential:

$$E_I = (\rho_e^2 - G\rho^2)\frac{1}{2}\iiiint\frac{d\tau_1\, d\tau_2}{r_{12}} \quad .$$

Here ρ_e is the uniform density of electric charge, ρ is the mass density and G is the constant of gravitation. (In most cases of practical interest one of the two quantities ρ_e^2, $G\rho^2$ is negligible compared to the other.)

The rotational energy is the square of the angular momentum L divided by twice the moment of inertia of the configuration in question:

$$E_R = L^2 \Big/ 2\rho \iiint r_\perp^2 \, d\tau \, . \qquad (1a)$$

Here $r_\perp$ is the perpendicular distance of the volume element $d\tau$ from the axis of rotation (passing through the center of mass of the whole system).

For a spherical configuration with radius R these energies reduce to

$$E_S^{(0)} = 4\pi R^2 \gamma$$

$$E_I^{(0)} = \frac{3}{5}(Q^2 - GM^2)\frac{1}{R} \, ,$$

$$E_R^{(0)} = \frac{1}{2} \cdot \frac{L^2}{\frac{2}{5}MR^2} \, ,$$

where Q is the total charge and M the total mass of the system. The above energies provide convenient units in which to express the three quantities E_S, E_I, E_R, and we may then rewrite the effective potential energy in a dimensionless way that is especially suited for a unified discussion of the problem. Picking $E_S^{(0)}$ as the unit for the effective potential energy we may write

$$\varepsilon \equiv \frac{E}{E_S^{(0)}} = \Phi_S + \frac{E_I^{(0)}}{E_S^{(0)}}\Phi_I + \frac{E_R^{(0)}}{E_S^{(0)}}\Phi_R \, . \qquad (2)$$

Here Φ_S, a function of the shape of the configuration in question, is the surface energy in units of the surface energy of the spherical shape. (Thus $\Phi_S(\text{sphere}) = 1$.) Similarly Φ_I is the inverse-distance energy in units of its value for the sphere, and Φ_R is the rotational energy, given by Eq. (1a), in units of what it would be for a sphere.

This way of writing the energy brings out the fact that since there are three energies in the problem (surface, inverse distance, rotational) there are two dimensionless ratios, which may be taken as the parameters of the unified theory. These ratios are often denoted by x and y, and defined as follows:

$$x \equiv \frac{1}{2}\frac{E_I^{(0)}}{E_S^{(0)}} = \frac{(\text{Charge})^2 - G(\text{Mass})^2}{10(\text{Volume})(\text{Surface Tension Coeff.})} \qquad (3a)$$

$$y \equiv \frac{E_R^{(0)}}{E_S^{(0)}} = \frac{5}{12}\frac{(\text{Angular Momentum})^2}{(\text{Volume})(\text{Mass})(\text{Radius})(\text{Surface Tension Coeff.})} \; . \qquad (3b)$$

The parameter y is a measure of the square of the angular momentum, and thus of the size of the disruptive centrifugal forces compared to the cohesive surface tension forces. When GM^2 is negligible the parameter x reduces to the conventional 'fissility parameter' of nuclear physics, a measure of the disruptive electrostatic forces compared to the surface tension forces.

The dimensionless effective potential energy now reads

$$\varepsilon = \Phi_S(\text{Shape}) + + 2x\,\Phi_I(\text{Shape}) + y\,\Phi_R(\text{Shape}) \; . \qquad (4)$$

The Φ's are dimensionless functions of the shape only. For example, for spheroidal shapes specified by semi-axes a,c (where c is along the axis of symmetry) one finds the following formulae in terms of the eccentricity e (equal to $\sqrt{1 - a^2/c^2}$):

$$\Phi_S = \frac{1}{2}(1 - e^2)^{1/3}\left[1 + \frac{\sin^{-1} e}{e(1 - e^2)^{1/2}}\right] \qquad (5a)$$

$$\Phi_I = \frac{1}{2}(1 - e^2)^{1/3}\frac{1}{e}\ln\frac{1 + e}{1 - e} \qquad (5b)$$

$$\Phi_R = \frac{1}{2}(1 - e^2)^{-2/3}(2 - e^2) \; . \qquad (5c)$$

For configurations specified by several shape parameters the Φ's are functions of several variables. In any case the important thing is that the Φ's can be calculated and tabulated once and for all, independently of the

particular physical system that is being investigated. Imagine that such a tabulation of the Φ's has been carried out. Then to find the configurations of gyrostatic equilibrium for a given system we first calculate the values of x and y that specify that system (using Eqs. 3a, 3b), insert these in Eq. (4), and vary the shape until ε is stationary. For a different system we will have another pair of x,y values. To cover all possible systems we would vary both x and y in the full range from $-\infty$ to $+\infty$ and file away the results in a two-parameter filing cabinet illustrated in Fig. 4. This figure brings out the relations to one another of various physical systems. To orient ourselves: $y = 0$ means no rotation, so along the positive x-axis we have the domain of nonrotating idealized nuclei, from light to heavy with increasing x. For negative x we have gravitating globes. The classic case of astronomical masses for which surface tension is negligible corresponds to $x \to -\infty$, indicated on the left. Plateaus rotating globes, with no charge and negligible gravitation, correspond to the positive y-axis. Rotating nuclei and rotating gravitating masses with surface tension fill the upper half-plane.

What about negative values of y? At first this sounds silly (a negative centrifugal force--an imaginary angular momentum?). In fact, however, systems with negative y-values are quite possible. Thus the negative y-axis corresponds to a bubble in a rotating container filled with a liquid. The bubble is an object with negative intertial mass relative to the surrounding liquid, and experiences a negative centrifugal force which, instead of flattening the bubble tends to elongate it along the axis of rotation. (Similarly a bubble in a container filled with gravitating matter belongs in the lower right-hand quadrant and a bubble in rotating, uniformly charged nuclear matter belongs in the lower left-hand quadrant.)

So now we have a filing system in which results on idealized stars and planets, weightless globes, idealized nuclei and bubbles may be displayed in a unified way. Let us remind ourselves what it is that we will be displaying in the filing cabinet. Take a rotating system with a given value of x,y. You might think at first that there will be just one entry, the equilibrium shape of that system. In fact there will be several entries because a given system with a given angular momentum has, in general, many configurations of equilibrium. Thus the effective potential energy for a given system, plotted as a function of, say, two shape degrees of freedom, might look something like Fig. 5. This shows a metastable minimum A, as well as an absolute minimum C, separated by a saddle-point B. Off to the side there is a mountain top D. All such points A, B, C, D are equilibrium shapes, although only some are stable whilst others are unstable, with different degrees of instability. Some of the unstable shapes are of great interest--for example a saddle-point shape of the type B is of crucial importance in the theory of nuclear fission and must be calculated in order to estimate fission barrier heights and spontaneous fission lifetimes of nuclei in situations of practical relevance.

Here let me make an important qualification of the words stable and unstable. In Fig. 5 one would be tempted to call A and B stable and C and D unstable configurations of equilibrium. For truly static, nonrotating systems ($y = 0$) that is indeed the case and that's all there is to it. But for gyrostatic systems it is not so, and it is possible--sometimes--

to have a system oscillating around a mountain top with bounded oscillations--rather than sliding down. This is an effect of coriolis (gyroscopic) forces, which are not contained in the effective potential energy E: the effective potential energy does not have in it the information about the full dynamical problem. This makes it obviously extremely dangerous to jump to conclusions about the stability or instability of the dynamical motion on the basis of the appearance of the effective potential energy landscape. There is, however, a mitigating circumstance which partly restores to the effective potential energy its role as a guide to the stability or instability of equilibrium points. Thus if there are dissipative effects present in the system (friction, viscosity), then, if one waits long enough so that these effects can assert themselves, saddles and mountain tops will, after all, behave in an unstable way, as one would have expected to begin with. This kind of instability, which requires that you wait long enough for dissipation to assert itself, is called secular instability.

In what follows when I say 'unstable' I shall always mean 'secularly unstable'.

Coming back to our x-y filing cabinet we see that the full problem of discussing the shapes of gyrostatic equilibrium of rotating masses consists of calculating all the important shapes, stable and unstable, for a given pair of x,y values, and then tracing out the behavior of these shapes as functions of x and y in the full x-y plane.

How much of this complete picture is known today? I will try to give you an impression of that in my talk, but let me say at once that the problem has been only partly explored, and there remains a beautiful project for mathematicians, physicists and astronomers to work on.

Let me first give you a bare-bones summary of what happens in various regions of the x-y plane, and then let me fill in some of the details.

3. SUMMARY OF STABILITY REGIONS

By piecing together old results in the three familiar regions in the x-y plane (astronomical masses, Plateau globes, nonrotating nuclei) and adding calculations and estimates in the other portions, one arrives at the following picture, summarized in Fig. 6.

For small amounts of rotation the originally spherical drop is flattened by the centrifugal force into an oblate spheroid, independently of the value of x, i.e., independently of whether we discuss a gravitating liquid mass with or without surface tension, or a charged nuclear droplet. For finite values of y the equilibrium configurations are no longer exact spheroids and we shall refer to these shapes as pseudospheroids or Hiskes shapes. In the astronomical limit of zero surface tension the oblate shapes of equilibrium do happen to be exact spheroids: they are the Maclaurin spheroids. The spheroids or pseudospheroids continue to flatten with increasing rotation and they remain stable until a certain critical value of y, denoted by y_I, which is a function of x. (Fig. 6) At this point the pseudospheroids become secularly unstable and a qualitative change takes place. The nature of the change depends on whether x is below or above a certain critical value x_c,

which is today not yet determined exactly, but appears to be in the neighborhood of $x_c = 0.81$. This corresponds to heavy nuclei towards the end of the periodic table.

If $x > x_c$ the flat pseudospheroids become secularly unstable towards disintegration, by way of a triaxial deformation.

If $x < x_c$, and this includes the rest of the periodic table as well as uncharged droplets, molten asteroids and astronomical gravitating masses, the flat pseudospheroid becomes secularly unstable towards conversion into a nonaxially symmetric configuration of equilibrium, which branches off the pseudospheroids at the critical value y_I. This new configuration has the symmetry of an ellipsoid with three unequal axes and rotates about its shortest axis. The other two axes are at first almost equal (when y exceeds the critical value by an infinitesimal amount and the equilibrium configuration is almost axially symmetric). Later these two axes become rapidly unequal, one of them becoming longer and longer as y increases, and the other tending to approximate equality with the shortest axis about which the rotation is taking place. The general appearance of these configurations is that of flattened cylinders with rounded ends and a somewhat elliptic cross section. In the astronomical limit of large negative x these configurations are exact ellipsoids (the Jacobi ellipsoids): otherwise the tips of the figure are more rounded. For certain values of x (in the neighborhood of 0) there is even a suggestion of a dumb-bell or hourglass shape. We shall refer to these configurations as pseudo-ellipsoids, or as Beringer-Knox shapes.

As the angular momentum is increased beyond the first critical value y_I the pseudo-ellipsoids which exist for $x < x_c$ become more and more elongated under the influence of the centrifugal force until a second critical value of y is reached, denoted by y_{II}. At this value of y the family of triaxial pseudo-ellipsoids comes to an end by way of loss of equilibrium towards a reflection symmetric disintegration mode. If x is greater than a second critical value of x, denoted by x_{cc} (and equal to about -0.4), the pseudo-ellipsoids are stable shapes up to the critical value y_{II}, when they cease to exist. If, however, $x < x_{cc}$, the pseudo-ellipsoids lose stability against a reflection asymmetric disintegration mode along the critical curve denoted by y_{III} in Fig. 6. This occurs before the disappearance of the pseudo-ellipsoids at y_{II}, so that in the case of $x < x_{cc}$ the pseudo-ellipsoids exist but are unstable against asymmetry in the region between y_{III} and y_{II}.

We may summarize the situation as follows: A sufficient amount of rotation will always disintegrate a fluid mass, be it gravitating or charged. The critical amount of rotation is, naturally, a decreasing function of x, being given by the curve $y_I(x)$ for $0.81 \lesssim x < 1$, by $y_{II}(x)$ for $-0.4 \lesssim x \lesssim 0.81$ and by $y_{III}(x)$ for $-\infty < x \lesssim -0.4$.

The disintegration occurs by way of a loss of stability against a triaxial mode in the first case, by way of a loss of equilibrium against a reflection symmetric mode in the second case, and by way of loss of stability against a reflection asymmetric mode in the third case. Note the distinction

between loss of stability and loss of equilibrium. Loss of stability in a family of equilibrium shapes means that for a parameter (e.g., y) in excess of a critical value an equilibrium shape exists but has changed from stable to unstable, i.e., the second derivative of the energy has changed sign. Loss of equilibrium means that the family of equilibrium shapes has ceased to exist: with the parameter in excess of the critical value the condition for equilibrium, $\delta E = 0$, cannot be satisfied, i.e., the condition of the vanishing of the first derivative of the energy has no (real) solutions. As noted before, when we say "unstable" we mean "secularly unstable".

Finally a note about the astronomical limit $x = -\infty$, or $x^{-1} = 0$. The situation is similar to the case of $-\infty < x < x_{cc}$ in that increasing angular momentum leads to a loss of stability against a reflection asymmetric mode. Nevertheless the case of zero surface tension ($x^{-1} = 0$) is a special case, different from the case of a finite surface tension, however small, in that for $x^{-1} = 0$ the Jacobi ellipsoids are shapes of equilibrium for any value of y, even exceeding y_{II}. In this (astronomical) case y_{II} does not mark the end of the ellipsoids (a loss of equilibrium) but merely a loss of stability against a reflection symmetric disintegration mode. More about this later.

Now let me amplify this summary by discussing more fully various regions in the x-y diagram.

4. NONROTATING NUCLEI, $y = 0$, $x > 0$

Let me start with the simplest example, the case of a nonrotating idealized nucleus. If one is asked what are the configurations of equilibrium of a nonrotating, uniformly charged drop, the obvious answer is: a sphere. A sphere is a shape of equilibrium for any amount of charge on the drop, i.e., for any value of x. This isn't the complete answer, however, since n equal spherical fragments dispersed to infinity are also equilibrium configurations. It follows that in the many-dimensional configuration space of the system there will be many potential energy hollows, one for each n. (You may verify trivially from the definitions of Φ_S and Φ_I that for n equal fragments at infinity $\Phi_S = n^{1/3}$, $\Phi_I = n^{-2/3}$, so the energy of the nth potential energy hollow is given by

$$\epsilon = n^{1/3} + 2x\, n^{-2/3} \quad .$$

This simple equation tells interesting things about the relative depths of the hollows. For example one learns the important fact that the absolute minimum (the lowest hollow) for any given x is the one corresponding to approximately $n \approx 4x$.

The realization that the potential-energy landscape has many hollows leads to an important discovery. Thus it is a simple topological requirement that if you have several hollows in a landscape then there must be saddle-point passes between them. The simplest case is a one-dimensional landscape: if a continuous curve has two minima there must be a maximum--a barrier--between them. (Essentially Rolle's theorem.) For example let us focus attention on a sequence of deformations leading from a single charged spherical drop to two equal fragments at infininte separation. Figure 7

indicates how the two minima must be separated by a maximum, corresponding to the so-called Bohr-Wheeler saddle-point shape for nuclear fission. To be specific, the configuration of a Lead nucleus at the Bohr-Wheeler saddle point is a somewhat necked-in cylinder with rounded ends--a little like an hour-glass figure with two equal bulbs. The energy of this shape is a maximum with respect to the division coordinate, but a minimum with respect to other shape coordinates (e.g., an asymmetry coordinate, which changes the relative sizes of the two bulbs of the hour-glass figure). Figure 7 illustrates further that even though the saddle shape is stable with respect to small changes in the relative sizes of the bulbs, a sufficiently large asymmetry makes the energy decrease again, after passage over a mountain top. The mountain-top configuration of a nucleus--an asymmetric hour-glass figure with unequal bulbs--is called the Businaro-Gallone shape and is of importance for the question of "fission asymmetry"--i.e., whether an idealized nucleus would divide into equal or unequal pieces. Thus a central problem in the early years of the theory of nuclear fission was, first, the tracing out of the Bohr-Wheeler saddle-point shape (and the associated barrier height) as a function of the fissility parameter x and, second, the tracing out of the Businaro-Gallone mountain tops. Many authors have contributed to the solution of this problem. Figure 8 shows some calculations of saddle-point shapes from Ref. 5. The shapes range from tangent spheres for $x = 0$, through hour-glass figures, to spheroids and finally a sphere at $x = 1$. As x tends to 1 and the saddle shape approaches the sphere the height of the potential energy barrier against fission decreases and finally vanishes at $x = 1$. This is illustrated in Fig. 9, taken from Ref. 1. You may veryify by using Eqs. (5a) and (5b), expanded to the leading power of the eccentricity, that the loss of stability of a charged sphere does indeed occur at $x = 1$. With a little more trouble, by expanding to the next power in e^2, you may also calculate from these expressions that the barrier height for fission, in units of $E_S^{(0)}$, is given by

$$\frac{\text{Barrier}}{E_S^{(0)}} = \frac{98}{135}(1 - x)^3 + \text{higher powers of } (1 - x) \ . \qquad (6)$$

When $1 - x$ is not small this formula is not applicable and numerical methods have to be resorted to in order to calculate the barrier heights in their dependence on x. Numerical methods, using digital computers, were also necessary to trace out the behavior of the Businaro-Gallone mountain tops, and to establish the important result that they exist only if x is greater than 0.396. (A consequence of this is that the Bohr-Wheeler saddle shapes are stable against reflection asymmetric deformations for $x > 0.396$ and unstable for $x < 0.396$.)

It would be too cumbersome for me to display all these symmetric and asymmetric shapes in detail, so let me show you a condensed summary of the behavior of the Bohr-Wheeler and Businaro-Gallone equilibrium shapes as functions of x.

Figure 10 shows just the major and minor semi-axes, essentially the tip-to-center-of-mass distance and the neck radius of these elongated figures. In the upper part of the figure you see the major semiaxis of the Bohr-Wheeler shape as it increases at first with increasing x and then, rather suddenly, begins to decrease around $x \approx 2/3$, finally tending

to 1 (the sphere) at $x = 1$. The Businaro-Gallone shapes, being reflection asymmetric, have two unequal tip distances, indicated by the dashed curve which branches off (bifurcates from) the solid curve at $x = 0.396$. The lower part of the figure shows the behavior of the neck radius.

Through such numerical studies the properties of the Bohr-Wheeler shapes are now known adequately. But the story of the Businaro-Gallone dumbbells is not completely cleared up even today. It is only relatively recently that one realized that they probably disappear again for x greater than about 0.8, so we have the peculiar result that a charged drop possesses a Businaro-Gallone asymmetric shape of (unstable) equilibrium only if its fissility parameter is between about 0.4 and 0.8 (in round numbers).

Let me now give you a few examples of the relevance of this theory of the equilibrium shapes of an idealized charged liquid drop to nuclear physics. To begin with, Fig. 11 illustrates how the sum of a volume energy, a surface energy and an electrostatic energy of the stable spherical equilibrium configuration of an idealized liquid drop reproduces the principal features of the nuclear binding energies. (The quantity plotted in Fig. 11 is the "mass decrement", closely related to the nuclear binding energy.) The curve is a liquid drop model fit to the experimental data. The deviations, up to ~ 12 MeV, are caused by nuclear "shell effects", which set a limit to the applicability of the liquid drop model. The total binding energy of a heavy nucleus is almost 2000 MeV, so on a gross scale the fit is satisfactory. On a finer scale one has to worry about the shell-effect deviations. This is illustrated in the lower part of Fig. 12, where the deviations from the liquid-drop model fit to nuclear masses are shown for some heavy nuclei. The largest deviation is at the "doubly magic" nucleus Pb^{208}, where the shells at $N = 126$ and $Z = 82$ give an additional binding of some 12 MeV.

The upper part of Fig. 12 compares the experimental and calculated masses for the same set of nuclei, but when their shapes are the deformed Bohr-Wheeler configurations instead of the near-spherical ground states. As expected (from the theory of shell effects) the deformation seems to have destroyed the extra shell-effect binding, and the liquid drop theory now reproduces the masses to within a couple of MeV. The increase of the saddle-point masses with decreasing x is essentially that predicted by the barrier formula, Eq. (6).

It is from such fits to nuclear ground state and saddle-point masses that one estimates that the surface energy coefficient of nuclei is about 1 MeV/fm^2 or, equivalently, that the surface energy of a nucleus with mass number A is about (18 MeV)$A^{2/3}$. Knowing this fact we may calculate the fissility parameter of a nucleus with mass number A and charge Ze as follows:

$$E_I^{(0)} = \frac{3}{5}\frac{(Ze)^2}{R}$$ (the electrostatic energy of a uniformly charged sphere of radius R)

$$E_S^{(0)} = 18\, A^{2/3} \text{ MeV}.$$

Remembering that $R \approx 1.2\, A^{1/3}$ fm and $e^2 = 1.44$ MeV fm ($1 \text{ fm} = 10^{-13}$ cm) we find

$$x = \frac{E_I^{(0)}}{2E_S^{(0)}} \approx \frac{1}{50}\frac{Z^2}{A} \quad \text{in round numbers.}$$

As we saw, the barrier against nuclear fission vanishes at $x = 1$, which we can now translate into the statement that $(Z^2/A) \lesssim 50$ for stability against fission. This is a most fundamental prediction of the liquid drop theory of nuclei, for it provides an interpretation of the termination of the periodic system of chemical elements somewhere in the vicinity of atomic number 100. The basic reason why there are only some 100 elements found in nature is that (even after stability against alpha and beta decay has been assured) the intensity of electrification for heavier nuclei begins to violate the liquid drop stability criterion $x < 1$.

I have given you only a few specific examples of the application of the liquid drop theory to nuclei. To get a broader perspective let me say that in the last 10 years we have learned how to calculate the potential energies of nuclei, in their dependence on N, Z and the nuclear shape, with an accuracy of about 1 in 1000. This has been possible in virtue of a two-part approach, where shell corrections of about 10 MeV are added to a smooth background of hundreds of MeV. This smooth background, an indispensable part of the nuclear energy, is provided by the model of a charged liquid drop.

5. ROTATING NUCLEI AND THE PLATEAU CASE, $x \geq 0$, $y > 0$

If an uncharged globe with surface tension is rotated, it flattens at first into an oblate pseudospheroid which, with increasing angular momentum (increasing y), eventually goes over into a torus. (See Fig. 13.) Well before this happens, at the critical value y_I equal to 0.2829, the oblate shape becomes secularly unstable towards conversion into a triaxial pseudo-ellipsoid rotating about its shortest axis, analogous to the Jacobi ellipsoid. In contrast to the Jacobi ellipsoids, the family of pseudo-ellipsoids comes to an end at the critical value y_{II}, equal approximately to 0.785 for $x = 0$. (See Fig. 6.) For uniformly charged (nuclear) drops the critical values y_I and y_{II} decrease with x. Figure 14 gives some details of the case $x = 0.3$, corresponding to nuclei in the general vicinity of atomic numbers $Z \approx 35$. The major semiaxis R_{max}/R for the pseudo-spheroidal (Hiskes) shapes increases gradually with y. At $y = 0.18$ the pseudo-ellipsoidal (Beringer-Knox) shapes bifurcate. The curve for the semimajor axis of this family continues to increase with y up to the critical turning point y_{II}, where it goes around a bend. After the bend the curve describes the semimajor axis of the triaxial saddle-point shape (the Pik-Pichak saddle) for fission. This shape is the generalization to the case with angular momentum of the hour-glass Bohr-Wheeler saddle. The $y = 0$ member of this family of Pik-Pichak saddles is in fact a Bohr-Wheeler shape.

Figure 15 gives an indication of the actual appearance of these shapes For example, in the upper right-hand part the sphere labeled H (for Hiskes)

is the equilibrium shape and the hour-glass figure PP (for Pik-Pichak) is the saddle-point shape for $y = 0$. At $y = 0.16$ the Hiskes shape has flattened into a pseudo-spheroid and the neck of the Pik-Pichak shape has thickened. At $y = 0.24$ the stable ground state is now a Beringer-Knox psuedo-ellipsoid. For $y = 0.4$ the Beringer-Knox shape shows some necking and is about to coalesce with the Pik-Pichak saddle shape. All the Beringer-Knox shapes and all the Pik-Pichak shapes (except the one for $y = 0$) are slightly triaxial. In the figure only tne mean section of these triaxial shapes is indicated.

A practical application of these calculations is the prediction of the existence of "super-deformed" nuclei, elongated into cylinder-like shapes with a ratio of axes of about 2:1 by the centrifugal forces arising from the collision of two nuclei. As an example the bombardment of a Si target with Ar ions of about 170 MeV energy might lead in a fraction of the collisions to super-deformed compound nuclei.

The discovery of such nuclei, stretched out by the centrifugal force into triaxial shapes, so closely analogous to the classic Jacobi ellipsoids, would be an exciting event. So far insufficient effort has been devoted to the identification of such nuclei and they have not been seen experimentally.

6. ASTRONOMICAL LIMIT $x \to -\infty$, $y > 0$

Let me now review the left-hand edge of our filing cabinet: the classic problem of a rotating gravitating mass (without surface tension).

First a small change in notation. Since there is now no surface energy the ratio of $E_R^{(0)}$ to the gravitational energy of a sphere is a natural parameter. Thus we introduce

$$t \equiv \frac{E_R^{(0)}}{-E_I^{(0)}} = \frac{E_R^{(0)}}{E_S^{(0)}} \frac{E_S^{(0)}}{-E_I^{(0)}} = -\frac{1}{2}\frac{y}{x} \ .$$

This parameter is a measure of the disruptive centrifugal force compared to the gravitational cohesion. (It is half the tangent of the angle to a point x,y in the $x - y$ plane, measured clockwise from the negative x-axis.)

As you know a gravitating mass with small angular momentum (small t) assumes the shape of an oblate spheroid (the Maclaurin spheroid). Such a spheroid remains a shape of equilibrium for all values of t, flattening more and more towards a thin disc as t tends to infinity. In 1834 Jacobi made the startling discovery that if the angular momentum exceeds a certain critical value ($t > 0.192$) a triaxial ellipsoid is also a configuration of equilibrium, and in fact secular stability passes from the Maclaurin to the Jacobi shapes. Towards the end of the last century Poincaré showed that as one moves along the Jacobi sequence of ellipsoids, other distinct families of equilibrium shapes bifurcate at definite values of the angular momentum. The first such crossing occurs at $t = 0.316$. For values of t

less than 0.316 there exist, in addition to the Maclaurin and Jacobi ellipsoids, also reflection-asymmetric ("pear-shaped") figures of equilibrium. At $t = 0.486$ another crossing occurs, this time by a reflection symmetric family. For $t > 0.486$ these shapes have the appearance of a Jacobi ellipsoid modified by a necking or waist in the middle, and for $t < 0.486$ they look like a Jacobi ellipsoid with a bulge in the middle and two neckings on either side. (One might give Paul Appell's name to this family.) Further such crossings at $t = 0.903$, 1.161, etc. correspond to higher ellipsoidal harmonic ripples on the basic Jacobi figure. (I have called them Humbert and Orlov families, respectively, after two mathematicians who contributed to locating their bifurcation points).

Figure 16 summarizes the behavior of these families in the usual way by plotting the semi-major axis as a function of t. Also shown in Fig. 16 is a further family of equilibrium shapes, the system of two equal fragments rotating about their common center of mass (Darwin's binary "star" system). In this configuration of equilibrium each half has to a good approximation the shape of a triaxial ellipsoid. The length of the whole figure goes to infinity with increasing angular momentum. With decreasing angular momentum the two "stars" approach each other and, finally, as the centrifugal force becomes too weak to support the increasing gravitational attraction, the family of Darwin's binaries comes to an end around $t = 0.484$. Combining some of Jeans' early speculations with our own more recent studies, I have sketched in (as a dashed curve) the probable fate of this family. After bending out at $t = 0.484$ it probably bends back again at $t \approx 0.65$ (this value is not known accurately), to join the dumb-bell-like Appell family of shapes! We anticipate a similar connection between the Orlov family and a three-star family (a system of three colinear fragments with reflection symmetry rotating about the common center of mass).

The most important feature of Fig. 16 is the critical value $t = 0.316$, where the Poincaré pears bifurcate. Its physical significance is that beyond this value the Jacobi ellipsoids are unstable and any additional angular momentum would make them disintegrate. A lot has been written in the past 100 years about the question what a Jacobi shape would disintegrate into, and the question remains unanswered. There are two aspects of the problem that have not been stressed, as far as I know, but which seem obvious when you exploit the analogy of this problem to the phenomenon of nuclear fission. The first is that the Poincaré pears are saddle-point shapes in the same sense that the Bohr-Wheeler dumb-bells are saddle-point shapes, i.e., they both determine the barrier against disintegration for a system that has not yet reached the limit of stability (which limit is given by $x = 1$ in the nuclear case and $t = 0.316$ in the gravitating case). From this point of view it is strange that the Poincaré pears have received so little attention once it was found they were unstable. In the nuclear case, you will remember, the tracing out of the unstable Bohr-Wheeler saddles was the outstanding problem of fission theory. By contrast, in the gravitational case, we still don't know what happens to the Poincaré pears as t is decreased below 0.316! This is a fascinating riddle. It seems rather certain that for $t = 0$ the Poincaré pears no longer exist, so where and how did they disappear?

The second neglected aspect of the question how the Jacobi ellipsoids might disintegrate is what lies beyond the Poincaré saddle-point pass? In particular, what is the absolute minimum in the effective potential energy towards which the disintegrating Jacobi ellipsoid is presumably drawn after overcoming the saddle pass in the barrier against disintegration? In the nuclear case the absolute minimum in the energy is n equal fragments at infinity, the optimum value of n depending on the value of x (approximately $n_{opt} \approx 4x$). In the gravitational case it does not seem ever to have been stated clearly what the absolute minimum in the effective potential corresponds to. The answer is pathological but instructive. Thus in order to reduce E in Eq. (1) to its lowest possible value (in the case of negative x) one should divide the total mass into one large spherical part and one very small part (a "satellite"), and place the small part so far away that, despite its smallness, the moment of inertia of the whole figure is very large. By making the size of the satellite tend to zero but its distance tend to infinity sufficiently rapidly one can make the moment of inertia tend to infinity, and thus make the rotational energy vanish. One thus arrives at a configuration whose gravitational and surface energies are no greater than those of a single sphere, but whose rotational energy has been reduced to zero by the artifice of making the satellite carry all the angular momentum at a vanishingly small rate of rotation.

This simple observation, that the absolute minimum in the effective potential corresponds to a very asymmetric configuration of a small satellite at infinity, may be the basic reason why the Jacobi ellipsoid becomes unstable with respect to an asymmetric (pear-shaped) deformation. This asymmetry, which makes one tip of the ellipsoid more pointed (and the other less) may be an expression of the underlying urge of the rotating figure to emit a small satellite and send it off to infinity. This speculation also suggests a solution to the riddle of what happens to the Poincaré pear as t is decreased below 0.316. My guess is that as the tip of the Pear becomes more elongated with decreasing t it eventually reaches out to the "neutral point" in the potential surrounding the pear (the neutral point in the sum of the gravitational and centrifugal potentials). Such neutral points are always outside the surface of a Maclaurin or Jacobi ellipsoid, but for the Pear there is no reason why the elongating tip should not touch the neutral point. Physically this means that at the tip the centrifugal force has overcome the gravitational attraction and matter begins to stream out from it. (An analogous streaming occurs when a dielectric drop is put between the plates of a condenser, and the electric field increased. The drop stretches at first into an elongated pseudospheroid, but at a critical field the tips sharpen up and begin to emit a stream of droplets. See also Ref. 6.)

A further thought which is suggested by these considerations is that, in general, the configuration of an infinitesimal satellite placed at the neutral point (or the lowest neutral point, if there are several) i.e., a satellite in synchronous orbit around the central body, is a configuration of equilibrium whose formal significance is that of a saddle-point pass that must be overcome when converting a given rotating configuration of equilibrium into the absolute minimum configuration of a sphere and a satellite at infinity. Thus, in addition to all the families of equilibrium mentioned so far, there is a matching set of "Ghost Families", identical to the basic set but with an infinitesimal satellite (or satellites) in a synchronous orbit.

Figure 17 is an attempt to summarize these speculations. The maximum radius vector (tip-distance) of the Ghost Families is the radius of the synchronous orbit and thus the Maclaurin and Jacobi Ghosts are shown as dashed curves above the conventional families. In the case of the Poincaré pear the elongating tip meets its Ghost in a typical limiting point (when the tip touches the synchronous satellite), with the result that no Poincaré pears exist below some critical value of t, yet to be determined. Similar turning points probably mark the limits, on the left, of the Appell, Humbert and Orlov families as their tips touch the relevant neutral points.

7. THE LIMIT $x^{-1} \to 0$. THE BROKEN SYMMETRY HYPOTHESIS

A puzzle arose in trying to fit together the case of large negative x and the astronomical case of $x^{-1} = 0$. Thus for large but finite negative x values our calculations indicated that the rotating triaxial Beringer-Knox pseudo-ellipsoids come to an end at a finite value of the angular momentum, given by y_{II}, which corresponds to a limiting t of about 0.6-0.7. But in the astronomical case the Jacobi ellipsoids are known to continue on to infinite values of t. What then happens between x^{-1} small, and x^{-1} zero, i.e., what is the difference between the case of a finite surface energy, however small, and no surface energy? I think the answer is as sketched in Fig. 18. In the case of no surface energy the Jacobi and Appell families cross (at $t = 0.486$), as discussed in Sec. 5. When the surface energy is switched on the crossing is, I believe, broken, and the Jacobi-like shapes continue on to become the Appell symmetric dumb-bells, whereas the double-waisted Appell figures merge into what used to be the Jacobi shapes beyond the crossing. Formally such a breaking of the crossing between families of solutions is well-known, for example in atomic or nuclear spectroscopy. Crossings (of eigenvalues) are in fact the exception rather than the rule and are only possible if special symmetries are satisfied. I believe the analogy carries through to the present situation. (In both cases the formal problem is the diagonalization of a secular determinant.) It is only because of the special symmetry (in a generalied sense) of the pure inverse-distance problem (which also results in pure ellipsoids being exact solutions) that a crossing between two families like the Appell and Jacobi shapes is possible. The addition of the slightest amount of surface energy breaks this symmetry and the families no longer cross. From this point of view the astronomical case, which had been studied for centuries, is an <u>atypical</u> situation, and a study of the case with surface tension is important, among other things, in restoring the proper perspective on the general problem.

With the above hypothesis it is possible to connect the case with surface tension with the astronomical case in a way indicated in Fig. 19. The continuation to minus infinity of the critical curve $y_{II}(x)$ in Fig. 6, where the Beringer-Knox shapes bend back into the Pik-Pichak shapes (see Fig. 14) corresponds to the critical value $t \approx 0.65$, where the Appell shapes bend down to become the Darwin-Jeans shapes. (Fig. 16) The second bend in Fig. 16 at $t = 0.484$, where the Darwin-Jeans shapes become the Darwin binaries, may be traced to finite values of x and is indicated as the critical curve y_{IV} in Fig. 6.

The continuation to minus infinity of the dashed part of the curve $y_{III}(x)$ in Fig. 6, where the Beringer-Knox shapes lose stability against asymmetry, corresponds to the critical value $t = 0.316$, where the Jacobi shapes lose stability against a pear-shaped deformation. According to our broken symmetry hypothesis there is no critical curve for finite values of x corresponding to the crossing at $t = 0.486$ of the Jacobi and Appell families. On the other hand, one is led to the prediction (quite unexpected unless one is aware of the astronomical limit) that in the case of finite (negative) x there must exist further families of equilibrium shapes beyond the limiting angular momentum y_{II}. These families would correspond to the astronomical Jacobi family and its bifurcations, but with the crossings at even harmonic bifurcations (Appell, Orlov etc.) broken according to the scheme of Fig. 18. The fate of these families as the surface tension increases is completely unknown.

8. LOOSE ENDS

I have already mentioned several questions and puzzles that have not been answered satisfactorily. I should also say that many of the results I quoted are only approximate and in some cases quite uncertain. In addition there is a whole list of families of equilibrium shapes that I have not even mentioned, some of which have been studied to a limited extent. Let me make a partial list:

1. Equilibrium shapes for $y < 0$.
2. Equilibrium shapes in the form of spherical harmonic distoritions of a sphere, which cross the spherical family as x increased beyond 1. (These crossings are like the infinitely many Poincaré crossings of the Jacobi ellipsoids.)
3. Families of multiply-necked cylinders which for $y = 0$, $x \to 0$ tend to strings of equal spheres in contact. Branchings from these families that occur as x increases.
4. Families which for $y = 0$, $x \to 0$ tend to other arrangements of equal spheres (triangular, tetrahedral, etc.).
5. Thick-walled spherical shells (nuclear bubbles); a pair of such configurations appears when x exceeds 2.0216.
6. Unequal spherical fragments at infinity.

The list could be extended indefinitely.

CONCLUSION

I hope that I have succeeded in giving you an impression of the richness of the problem defined so innocently as the search for equilibrium shapes of a rotating mass. Even in the nuclear case with no rotation one is drawn by stages from thinking of a single sphere as the solution, to the inclusion of many equal fragments at infinity as formal solutions, and then through topological arguments to the realization that there must also be dumb-bells with equal or unequal bulbs and many other families as well. With rotation included the mathematical structure acquires baroque ramifications. One of the joys of disentangling this structure has been the unification of the astronomical, hydrostatic and nuclear problems, and the insights gained by confronting the different fields.

Let me end by stressing that the problem of the equilibrium configurations of a rotating drop or bubble with inverse-distance interactions defines a beautiful mathematical structure which has been only partially explored. Even gross qualitative questions remain unanswered, and there is a serious lack of quantitative results.

REFERENCES

1. J. R. Nix, Nucl. Phys. A130, 241 (1969) and Los Alamos report LA-DC-72-769, Aug. 15, 1972.

2. S. Chandrasekhar, "Ellipsoidal Figures of Equilibrium", Yale University Press, 1969.

3. P. Appell, "Traité de Mécanique Rationnelle", Gauthier-Villars, Vol. 4, Paris, 1932.

4. S. Cohen, F. Plasil, and W. J. Swiatecki, Annals of Physics 82, 557 (1974).

5. J. R. Nix and W. J. Swiatecki, Nucl. Phys. 71, 1 (1965).

6. G. I. Taylor, Proc. Roy. Soc. A280, 383 (1964).

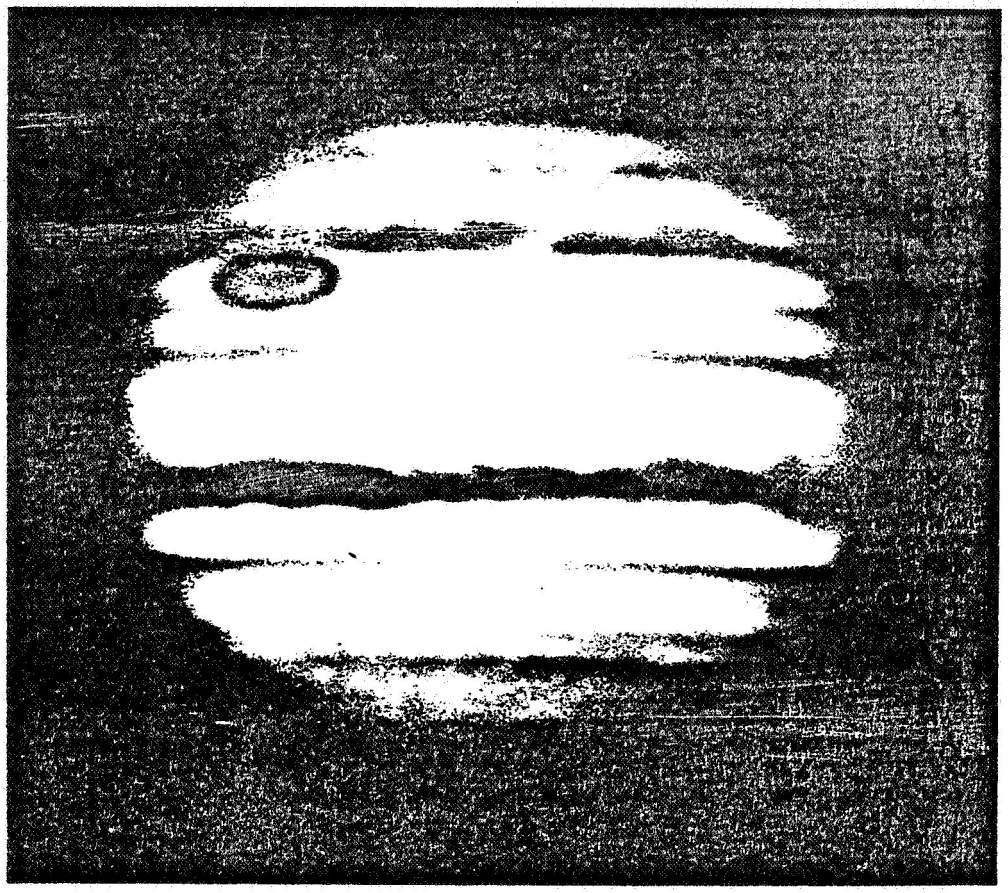

Figure 1. The planet Jupiter

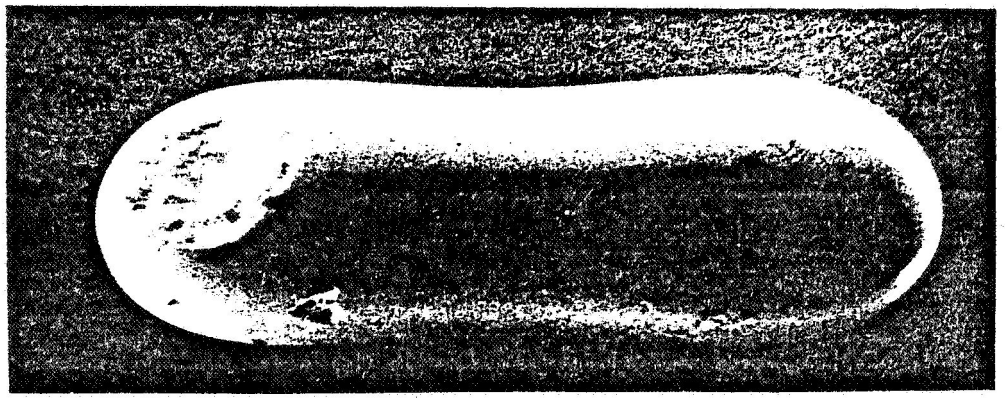

Figure 2. A solidified glass droplet, about 1 mm in length, from the lunar soil.

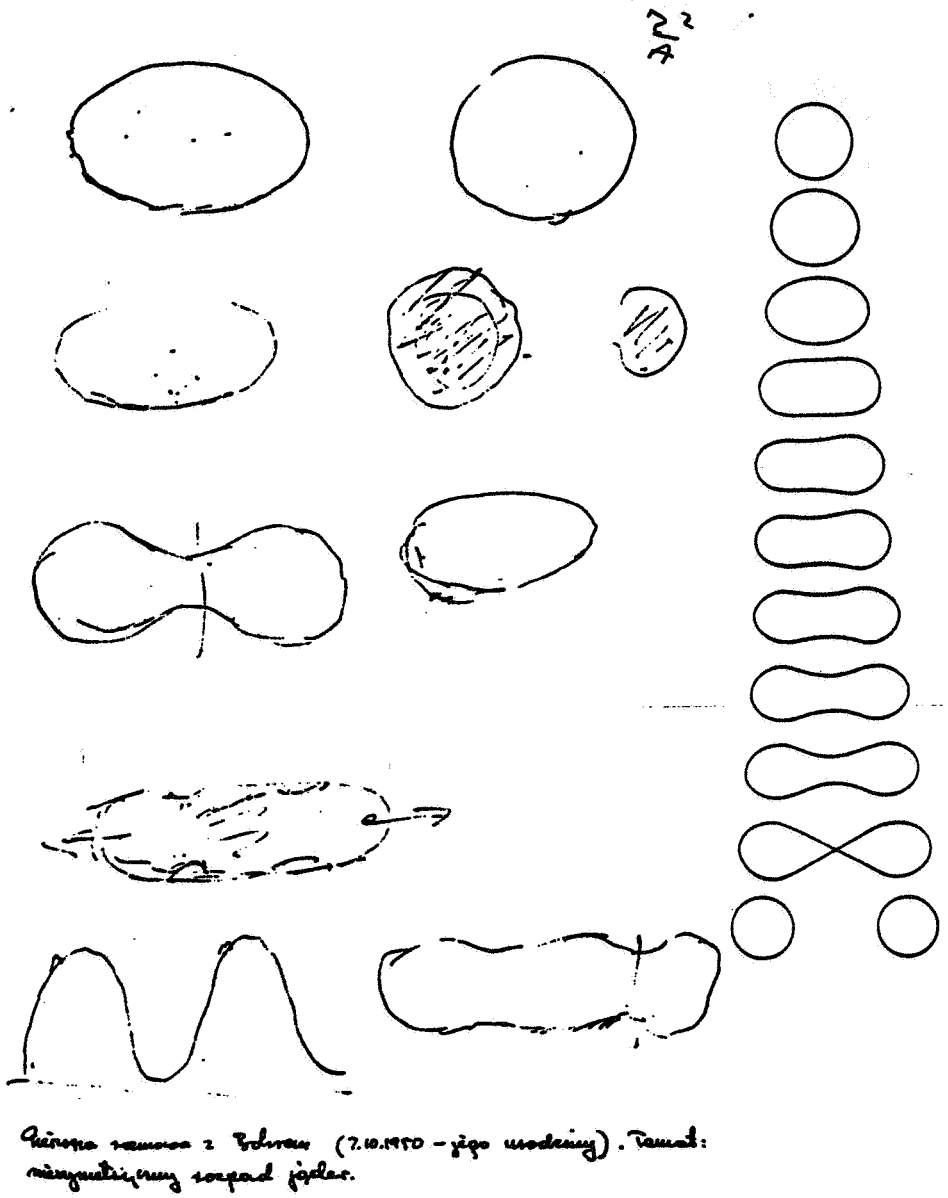

Figure 3. Sketches made by Niels Bohr during a conversation on the liquid drop theory of nuclear fission and (on the right) shapes of a fissioning Np^{237} nucleus calculated by J. R. Nix according to that model.

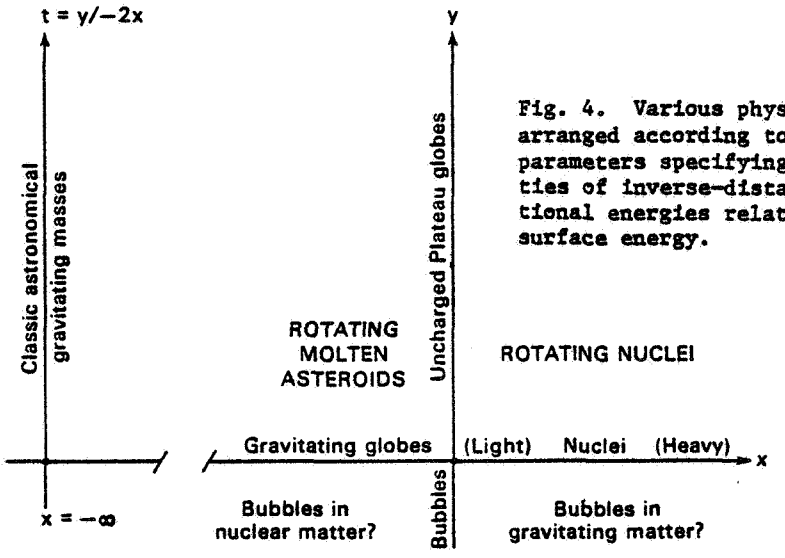

Fig. 4. Various physical systems arranged according to the x and y parameters specifying the intensities of inverse-distance and rotational energies relative to the surface energy.

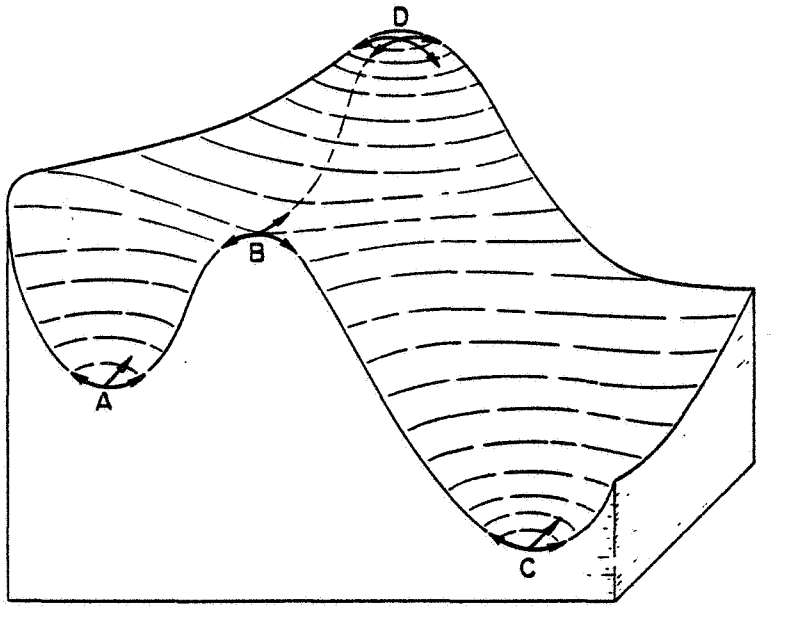

Figure 5.

A schematic potential energy surface illustrating a metastable hollow A, the absolute minimum C, a saddle-point B and a mountain top D.

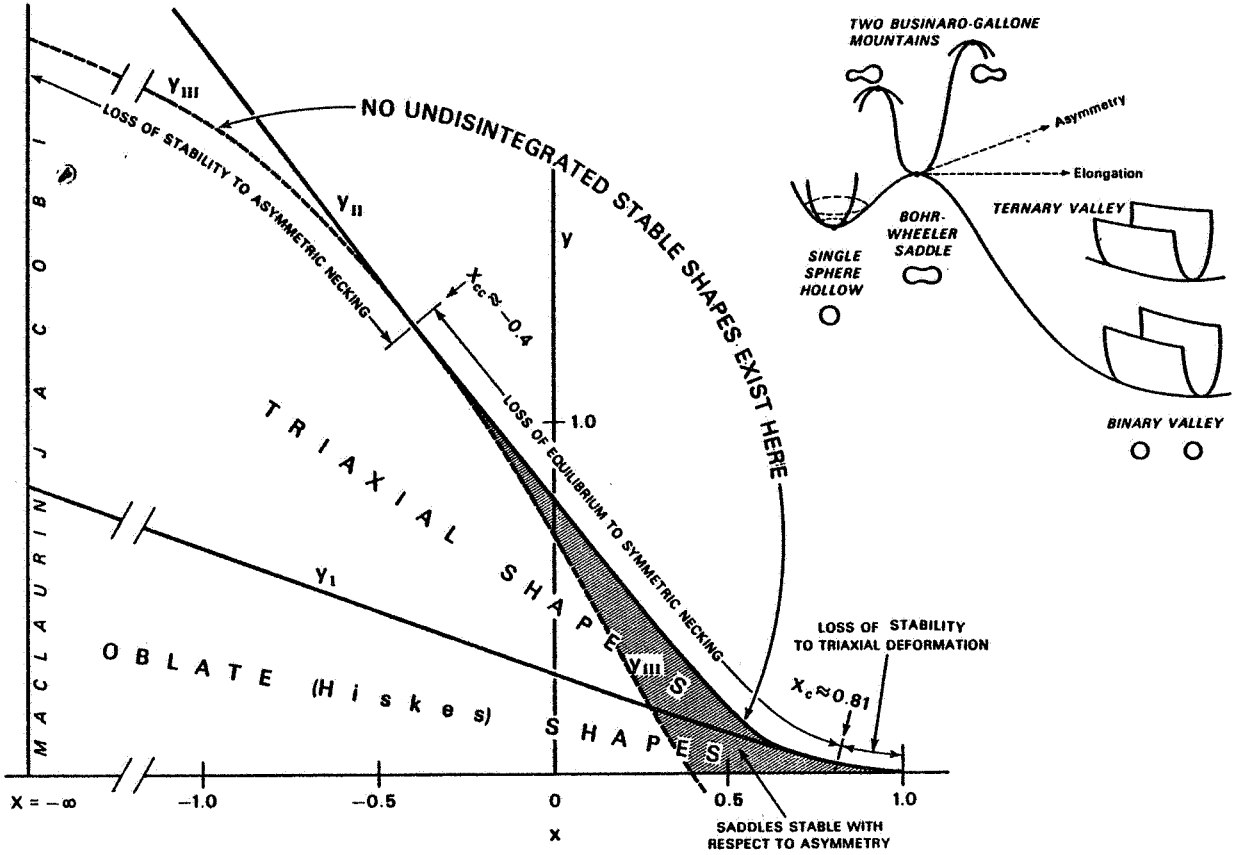

Figure 6. Stability properties of various systems in the x-y parameter plane.

Fig. 7. Schematic potential energy map for a nucleus, showing the spherical equilibrium hollow, the two- and three-fragment valleys, the Bohr-Wheeler saddle pass and the Businaro-Gallone mountain tops

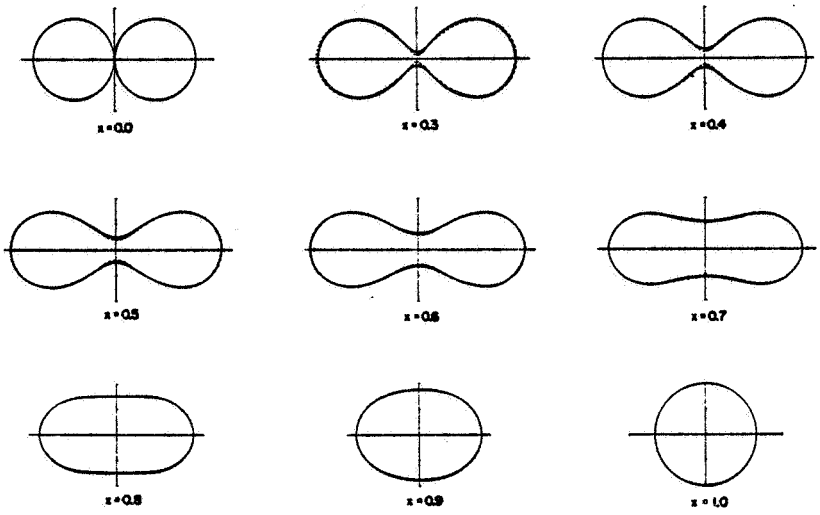

Figure 8. Nuclear saddle-point shapes in their dependence on the fissility parameter x.

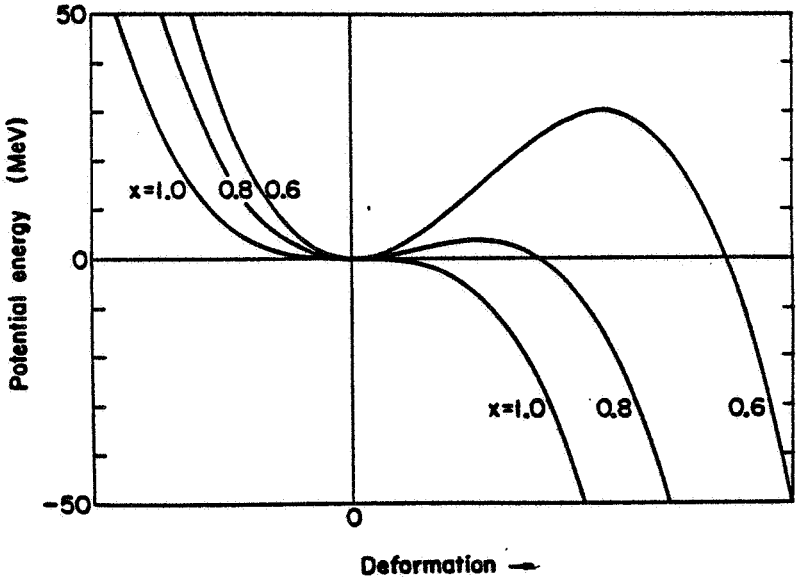

Figure 9. The deformation energy of three heavy nuclei with fissility parameters, 0.6, 0.8, and 1.0. At x = 1.0 the fission barrier vanishes.

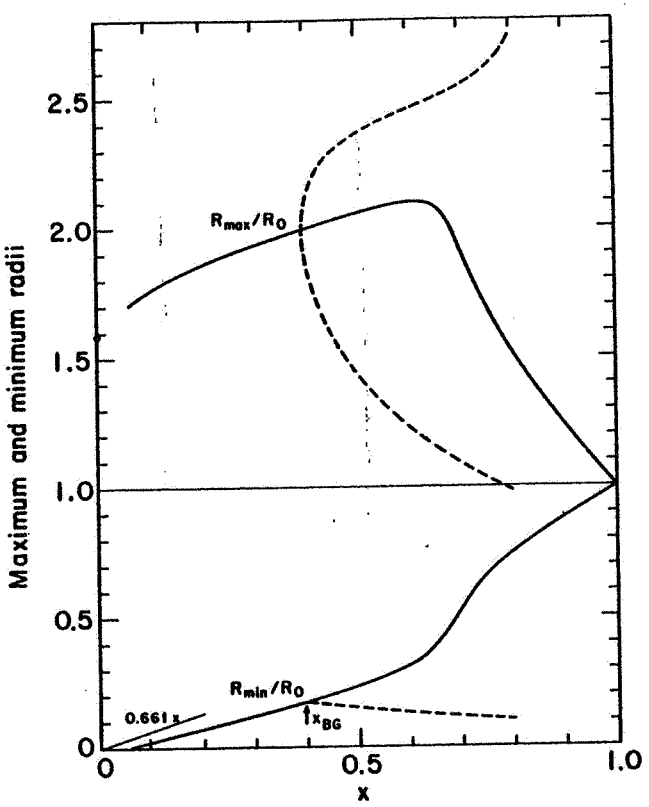

Fig. 10. The major and minor semi-axes of the Bohr-Wheeler saddle shapes in their dependence on the fissility parameter x. The dashed curves give the semi-axes of the Businaro-Gallone shapes.

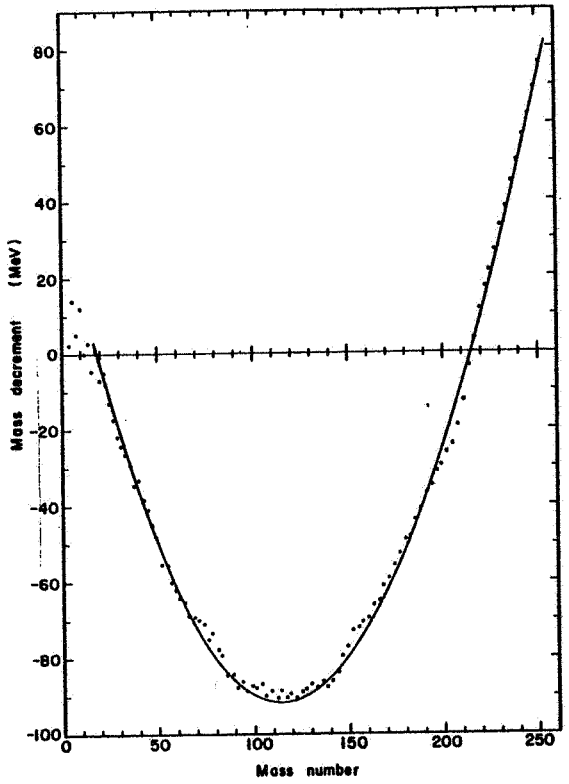

Fig. 11. The mass decrements (related to binding energies) of nuclei and the fit obtained by means of the liquid drop model.

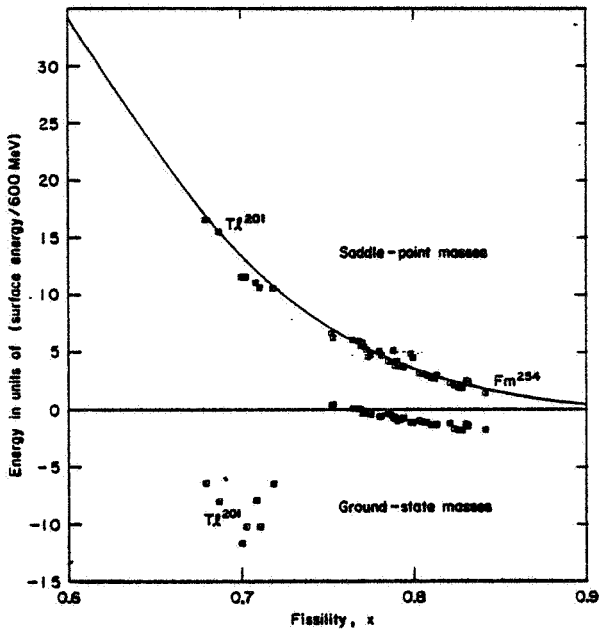

Fig. 12. The lower part shows the deviations of the ground state masses of heavy nuclei from a liquid drop model fit. The upper part compares the experimental and calculated masses for the same nuclei deformed into their saddle-point configurations.

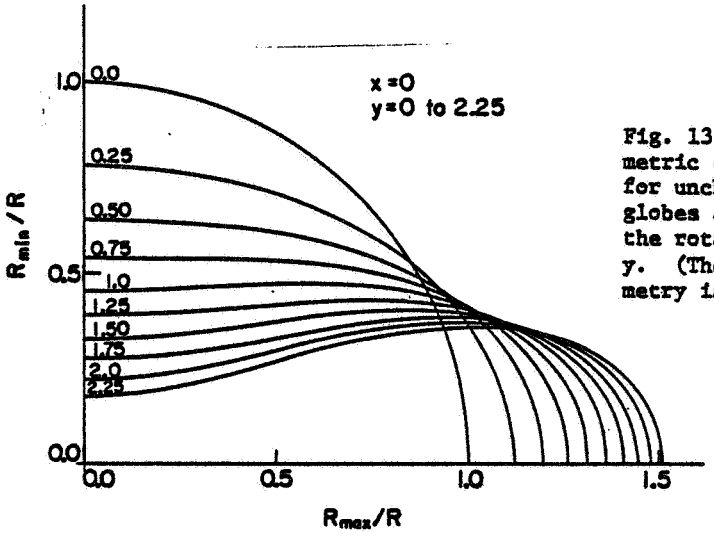

Fig. 13. Axially symmetric equilibrium shapes for uncharged (Plateau) globes as function of the rotational parameter y. (The axis of symmetry is vertical.)

Fig. 14. Major semi-axis for Hiskes oblate shapes, Beringer-Knox triaxial shapes, and Pik-Pichak saddles as functions of y, for x = 0.3.

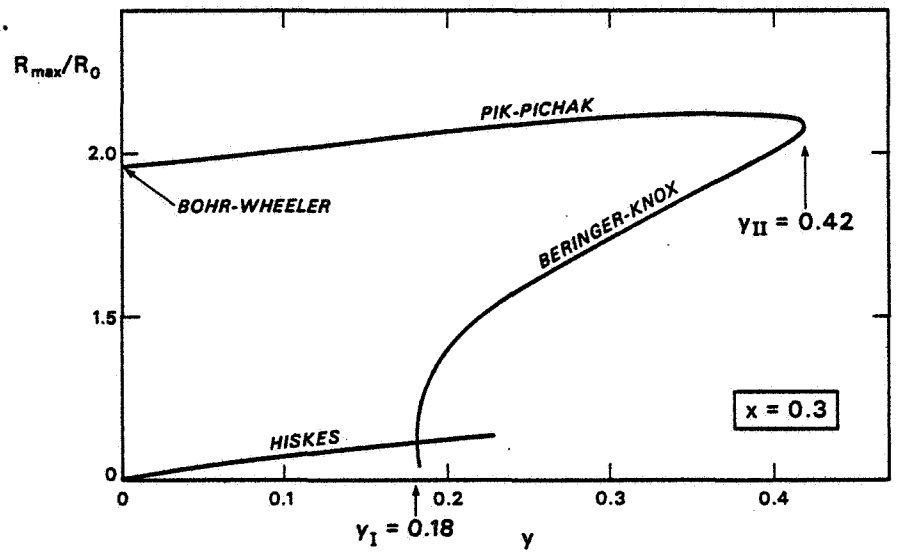

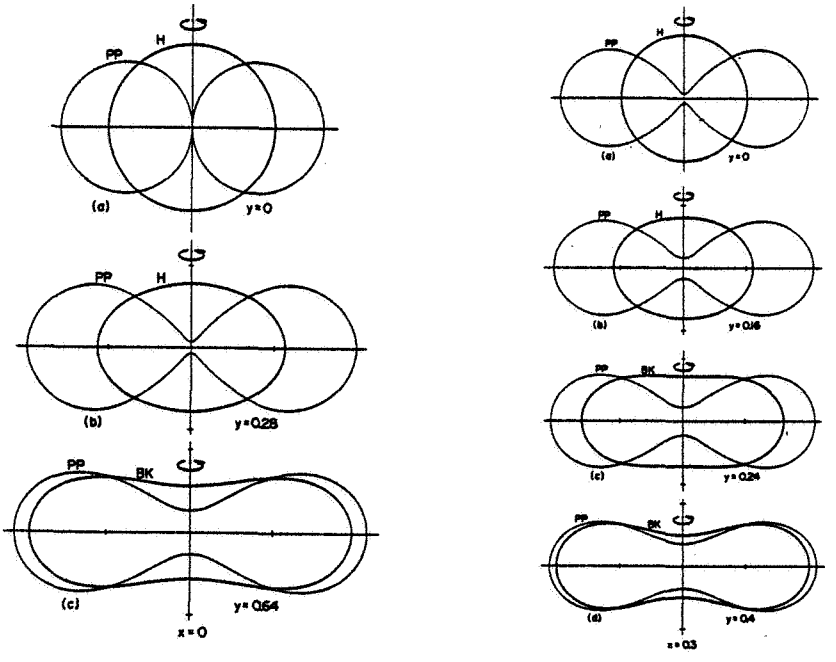

Fig. 15. Ground states (heavier lines) and saddle shapes (lighter lines) for x = 0 and x = 0.3 and various values of y. In all figures H refers to "Hiskes", Bk to "Beringer-Knox" and PP to "Pik-Pichak". Hiskes shapes have axial symmetry about the axis of rotation (vertical axis). The Beringer-Knox and Pik-Pichak shapes shown have approximate symmetry about the horizontal axis and only a mean transverse section is displayed for these shapes. (For x = 0, y = 0 the saddle shape is two spheres in contact.)

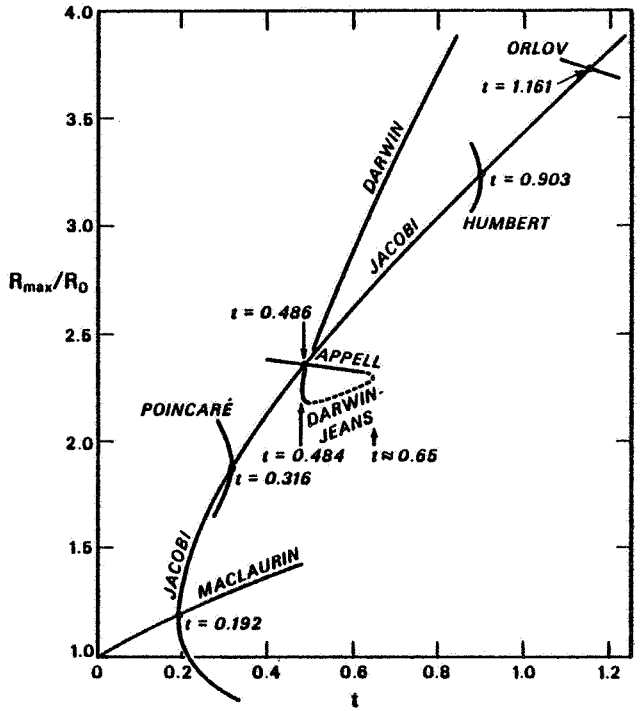

Fig. 16. Major semi-axis for astronomical families of shapes.

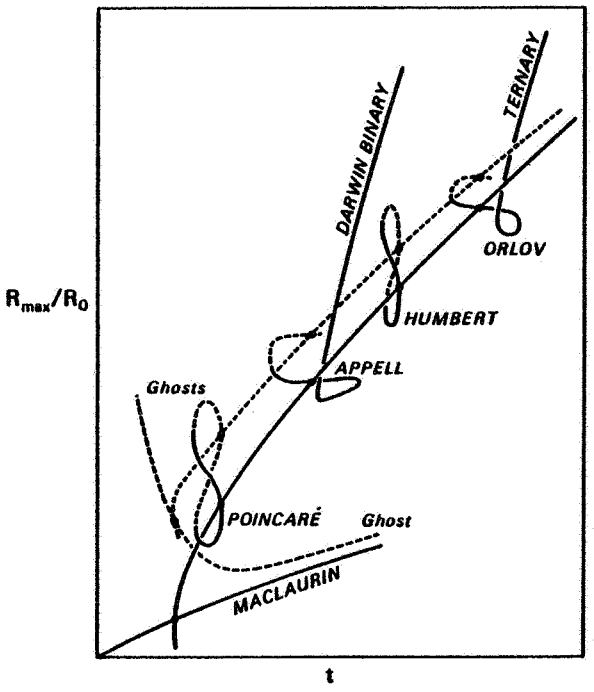

Fig. 17. Speculative (and schematic) extension of Fig. 16 to indicate the probable relation of the known equilibrium families to their "ghosts" (configurations with an infinitesimal satellite in synchronous orbit).

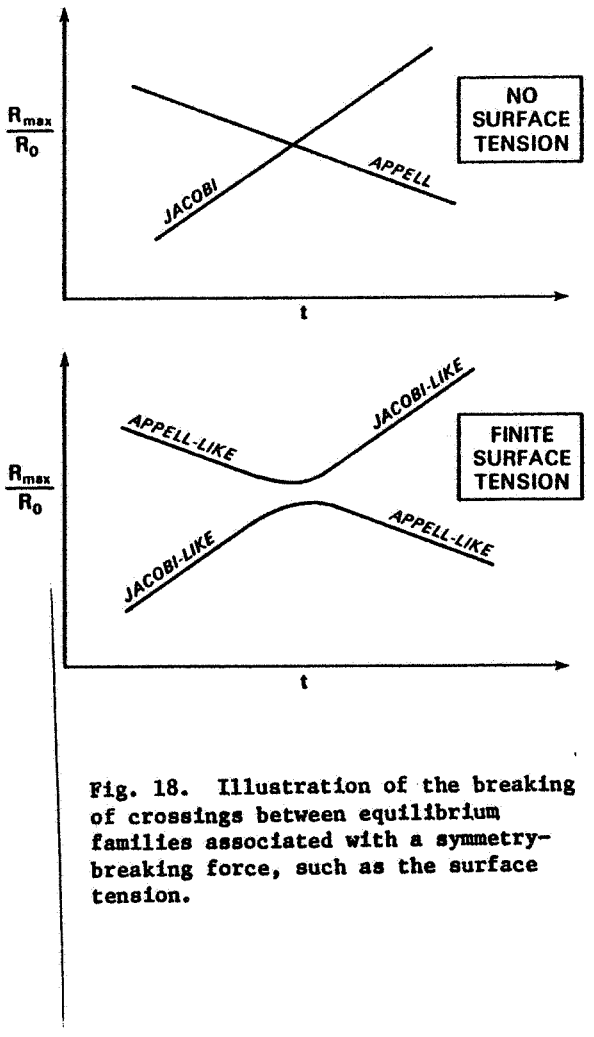

Fig. 18. Illustration of the breaking of crossings between equilibrium families associated with a symmetry-breaking force, such as the surface tension.

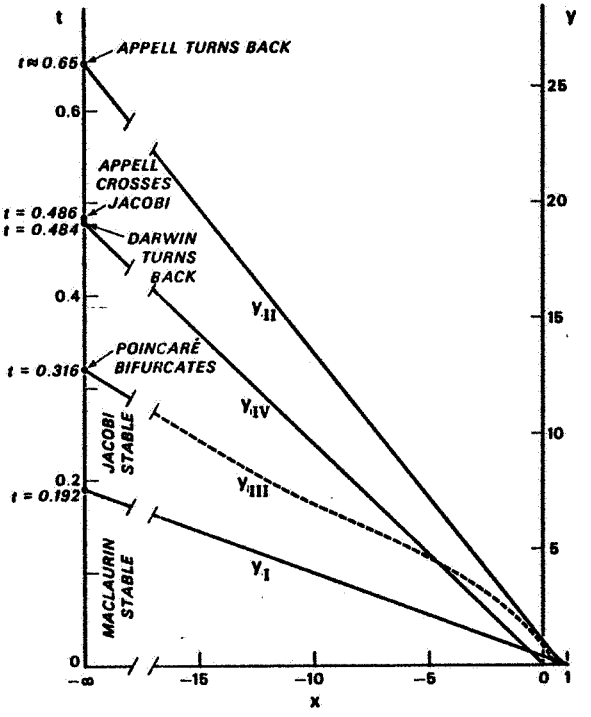

Fig. 19. The fitting together of the nuclear and astronomical domains in the x-y plane.

D5

VIBRATIONAL FREQUENCY OF A NON-CONDUCTING CHARGED LIQUID DROP*

C. Y. Wong
Oak Ridge National Laboratory
Oak Ridge, Tennessee 37830

and

H. H. K. Tang†
Kalamazoo College
Kalamazoo, Michigan 49001

ABSTRACT

We consider the vibration of a non-conducting liquid drop endowed with a surface charge, in supplement to the well-known case of a conducting liquid drop studied by Lord Rayleigh in the last century. It is assumed that there is no charge conduction except by hydrodynamical transport due to the flow motion. It is found that the surface flow is of such a form that the charge again maintains an electrostatic equipotential at the surface of the drop at all instants of the vibrational motion, and the same Rayleigh result is obtained. Thus, the Rayleigh result is applicable to more general classes of liquid drops, irrespective of the conductivity of the liquid in these two limits.

INTRODUCTION

The vibrational frequency of a charged liquid drop under the restoring force of its own surface tension was first derived by Lord Rayleigh (1) about a hundred years ago. The case considered was, in Lord Rayleigh's own words, for "liquid conducting masses charged with electricity". Implicit in the assumption of a conducting mass was that the dielectric relaxation time was much shorter than the mechanical vibrational period so that the charge could always redistribute itself to maintain an equipotential surface at the surface of the drop (see, for example, the re-derivation of Lord Rayleigh's result by Hendricks and Schneider (2)). Recent tests of Rayleigh's relation for a charged water drop indicated good agreement with experimental measurements (3,4).

It is of interest to study the influence of the conductivity of the liquid on the vibrational frequency. In the case of water, conductivity increases with the degree of salinity; one wishes to know whether the vibrational frequency may depend on the degree of purity of water under consideration. As

*Research sponsored by the U. S. Atomic Energy Commission under contract with Union Carbide Corporation.

†Present address: Yale University, New Haven, Connecticut.

the vibrational frequencies have been used to estimate the drop size and degree of electrification of water drops in the atmosphere by means of the backscattering effect on radar (5), such a question is of practical interest. On the other hand, there are also insulating liquids which can be readily charged (6). For these liquids, the dielectric relaxation time can be large compared to the mechanical vibrational period. One would be interested to see if the Rayleigh relation needs modification which may have some bearing on the electrohydrodynamical spraying process studied by many authors (6,7,8).

We consider a non-viscous liquid drop endowed with a surface charge. The charge is assumed to be uniformly distributed when the drop assumes its equilibrium spherical shape. We study the case in which the charge element is not free to move except to follow the motion of the surface element in which it resides. We shall see that this motion of the charge in the liquid drop results again in an equipotential surface at the surface of the drop at any instant of the vibrational motion, even though the charge is not free and moves by hydrodynamical transport only. Thus, surprisingly enough, the vibrational frequency of a charged liquid drop turns out to be independent of the conductivity of the liquid in these two limits!

HYDRODYNAMICAL FLOW AND VIBRATIONAL FREQUENCY

The starting point of the present discussion is the Euler equation for a fluid element in the interior

$$\frac{d\vec{u}}{dt} = -\nabla\left(\frac{\delta p}{\rho_M}\right) \tag{1}$$

where $\vec{u}$ is the velocity characterizing the motion of the fluid element, ρ_M the mass density, δp the deviation of pressure from the equilibrium value. We linearize the Euler equation by assuming the amplitude ϵ_o to be small. A normal mode is specified by describing the sharp surface as

$$r = R_o + \epsilon_o e^{i\omega t} Y_{\ell m}(\theta,\phi) \tag{2}$$

where R_o is the radius of the liquid drop in equilibrium and $Y_{\ell m}(\theta,\phi)$ is a spherical harmonic and ω gives the frequency of the vibrational motion. We further assume that the mass is incompressible and the density is uniform. Thus, from the equation of continuity, we have

$$\nabla\cdot\vec{u} = 0. \tag{3}$$

This condition, together with the solenoidal nature of the restoring force vector leads to the important implication that $\vec{u}$ is purely poloidal (Chandrasekhar (9)) (which means that $\vec{u}$ can be written in the form $\vec{u} = \nabla \times [\nabla \times (\phi/r)\vec{r}]$, where ϕ is a scalar function). From this, the mathematical analysis can be considerably simplified. In spherical coordinates, the various components of $\vec{u}$ (for the poloidal solution) are:

$$u_r = e^{i\omega t} \frac{\ell(\ell+1)}{r^2} U(r)\, Y_{\ell m}(\theta,\phi) \tag{4a}$$

$$u_\theta = e^{i\omega t} \frac{1}{r} \frac{dU(r)}{dr} \frac{\partial Y_{\ell m}(\theta,\phi)}{\partial \theta} \tag{4b}$$

$$u_\phi = e^{i\omega t} \frac{1}{r\sin\theta} \frac{dU(r)}{dr} \frac{\partial Y_{\ell m}}{\partial \phi} \tag{4c}$$

where U(r) is some function to be determined by the boundary conditions.

Taking the divergence of Eq. (1), we have, from Eq. (3),

$$\nabla^2 \left(\frac{\delta p}{\rho_M}\right) = 0. \tag{5}$$

A solution to this Laplace equation satisfying the boundary condition at the origin is

$$\delta p/\rho_M = \varepsilon_o e^{i\omega t}(\ell+1)\, \Pi_o r^\ell Y_{\ell m}(\theta,\phi) \tag{6}$$

where Π_o is a constant to be determined.

Replacing each side of Eq. (1) by its defining function as in Eqs. (4) and (6), we have

$$i\omega\, U(r) = -\varepsilon_o\, \Pi_o\, r^{\ell+1}. \tag{7}$$

Thus, the radial component of the velocity is

$$u_r = -\frac{\varepsilon_o e^{i\omega t}}{i\omega}\, \Pi_o\, \ell(\ell+1) r^{\ell-1}\, Y_{\ell m}(\theta,\phi). \tag{8}$$

There are two boundary conditions to be satisfied. First, from the requirement of consistency between the radial component of the velocity (Eq. (8)) and the form of the boundary (Eq. (2)), we have

$$\omega^2 = \ell(\ell+1)\, \Pi_o R_o^{\ell-1}. \tag{9}$$

The second boundary condition requires the balance of pressure at the boundary as arising from surface tension and the electrostatic stress. For the latter quantity, it is necessary to know how the charge redistributes itself. In a conducting liquid, the charge is free to move to maintain an equipotential at the surface of the drop. This was the case considered by Lord Rayleigh. On the opposite extreme, suppose the conductivity of the liquid is such that the charge cannot move freely, then, a surface charge element must follow the motion of the surface element in which it resides. What will be the instantaneous charge distribution?

It is easy to follow the hydrodynamics of any fluid element. From Eqs. (4), (7) and (9), we know that a fluid element at (r_o,θ_o,ϕ_o) is mapped into (r,θ,ϕ) by

$$\begin{cases} r = r_o + \varepsilon_o e^{i\omega t} \dfrac{r^{\ell-1}}{R_o^{\ell-1}} Y_{\ell m}(\theta,\phi) & (10a) \\ \theta = \theta_o + \varepsilon_o e^{i\omega t} \dfrac{r^{\ell-2}}{R_o^{\ell-1}} \dfrac{\partial Y_{\ell m}(\theta,\phi)}{\partial\theta} & (10b) \\ \phi = \phi_o + \varepsilon_o e^{i\omega t} \dfrac{r^{\ell-2}}{R_o^{\ell-1}} \dfrac{\partial Y_{\ell m}(\theta,\phi)}{\sin\theta\,\partial\phi}. & (10c) \end{cases}$$

A surface element at point (R_o,θ_o,ϕ_o) goes into another surface element at point (R,θ,ϕ) as follows

$$\begin{cases} R = R_o + \varepsilon_o e^{i\omega t} Y_{\ell m}(\theta,\phi) & (11a) \\ \theta = \theta_o + \varepsilon_o e^{i\omega t} (\partial Y_{\ell m}/\partial\theta)/\ell R_o & (11b) \\ \phi = \phi_o + \varepsilon_o e^{i\omega t} (\partial Y_{\ell m}/\partial\phi)/\ell R_o \sin\theta. & (11c) \end{cases}$$

On assumption of no conduction except by mechanical transport via the hydrodynamical flow, the surface charge density ρ_Q is related to the uniform equilibrium density $\rho_Q^{(o)}$ by

$$\rho_Q = \rho_Q^{(o)} \frac{R_o^2}{R^2} \frac{\sin\theta_o}{\sin\theta} \frac{D(\theta_o,\phi_o)}{D(\theta,\phi)} \qquad (12)$$

where $D(\theta_o,\phi_o)/D(\theta,\phi)$ is the Jacobian of the transformation. From Eqs. (11a), (11b) and (11c), we obtain the surface charge distribution at any instant of the vibrational motion

$$\rho_Q = \rho_Q^{(o)} [1 + \varepsilon_o e^{i\omega t} (\ell-1) Y_{\ell m}(\theta,\phi)/R_o]. \qquad (13)$$

This charge distribution is exactly the same if the liquid is a conducting liquid (see Hendricks, et al. (2)). One therefore obtains the important result that whether the liquid is conducting or not, the hydrodynamical transport carries the charge so that the surface of the liquid drop is also a surface of electrostatic equipotential as a result of the transport. In fact, a surface charge in the form of Eq. (13) gives rise to a potential

$$V_c(r) = \frac{kQ}{R_o} \text{ for } r \leq R_o + \varepsilon_o e^{i\omega t} Y_{\ell m} \qquad (14)$$

and $$V_c(r) = \frac{kQ}{r} + kQ\,\varepsilon_o e^{i\omega t}\frac{R_o^{\ell-1}}{r^{\ell+1}}Y_{\ell m} \text{ for } r \geq R_o + \varepsilon_o e^{i\omega t}Y_{\ell m} \tag{15}$$

where k is the Coulomb coupling constant (it equals $(4\pi\varepsilon_o)^{-1}$ in the usual convention) and Q is the total charge. The electric field as approached from the outside is

$$E_r = \frac{kQ}{R_o^2}\left[1 + (\ell-1)\frac{\varepsilon_o e^{i\omega t}}{R_o}Y_{\ell m}\right]. \tag{16}$$

The increment in pressure at the surface due to electrostatic interaction is

$$\frac{1}{2}\rho_Q E_r - \frac{kQ^2}{8\pi R_o^4} = (\ell-1)\frac{kQ^2}{4\pi R^5}\varepsilon_o e^{i\omega t}Y_{\ell m}. \tag{17}$$

Combining the contribution from electrostatic interaction and surface tension (10), we have

$$\left(\frac{\delta p}{\rho_M}\right)_{R_o+\varepsilon_o e^{i\omega t}Y_{\ell m}} = \left[(\ell-1)(\ell+2)\frac{T}{\rho_M R^2} - (\ell-1)\frac{kQ^2}{4\pi\rho_M R^5}\right]\varepsilon_o e^{i\omega t}Y_{\ell m}. \tag{18}$$

From Eqs. (18), (5) and (9), we get the vibrational frequency

$$\omega^2 = \frac{\ell(\ell-1)(\ell+2)T}{\rho_M R^3}\left(1 - \frac{kQ^2}{(\ell+2)4\pi TR^3}\right) \tag{19}.$$

which is just the Rayleigh result.

DISCUSSIONS

We have shown that in the vibration of a charged non-viscous liquid drop, the hydrodynamical transport of the surface charge results again in an equipotential surface at the surface of the drop at any instant. Thus, if the liquid is non-conducting in the sense of having a large dielectric relaxation time, the behavior of the surface charge is the same as in a conducting liquid. One concludes that Rayleigh's result is more general than it was formulated.

Our discussion has been limited to the inviscid case for which a potential flow is possible. The fact that an electrostatic potential is again maintained is probably intimately related to the potential flow of the fluid. Some differences in the vibrational behavior due to differences in conductivity may be expected in the vibration of a <u>viscous</u> charged liquid drop for which the flow becomes rotational and the vorticities reside mostly at the surface. In a

conducting liquid, a charge element is free to move to the surface even though the surface fluid element may flow inside the surface. For a non-conducting liquid, the motion of the charge toward the surface may not be fast enough, and the electrostatic stress is modified as a consequence. As a viscous conducting charged liquid drop follows the Chandrasekhar equation (9,11) based on an instantaneous surface charge redistribution, the behavior of a viscous non-conducting charged liquid drop will deviate from the Chandrasekhar equation. This may be checked experimentally.

REFERENCES

1. Lord Rayleigh, Phil. Mag. 14, No. 5, 184 (1882).
2. C. D. Hendricks and J. M. Schneider, Am. J. Phys. 31, 450 (1962).
3. P. R. Brazier-Smith, M. Brook, J. Latham, C. P. R. Saunders, and M. H. Smith, Proc. Roy. Soc. Lond. A322, 523 (1971).
4. C. P. R. Saunders and B. S. Wong, J. Atm. Ter. Phys. 36, 707 (1974).
5. M. Brook and J. Latham, J. Geo. Res. 73, 7137 (1968).
6. R. J. Pfeifer and C. D. Hendricks, Phys. Fluids 10, 2149 (1967).
7. S. A. Ryce, Phys. Fluids 16, 452 (1973).
8. R. J. Pfeifer, Phys. Fluids 16, 454 (1973).
9. S. Chandrasekhar, "Hydrodynamic and Hydromagnetic Stability", Clarendon Press, Oxford (1968).
10. L. D. Landau and E. M. Lifshitz, "Fluid Mechanics", Chap. VII, Pergamon Press, Oxford (1958).
11. H. H. K. Tang and C. Y. Wong, Jour. Phys. A, in press. In that paper, the vibrational frequency of a non-conducting charged liquid drop is erroneous and is superseded by the results presented here in this paper.

D6

SIMILARITIES AND DIFFERENCES BETWEEN VOLUME-CHARGED (NUCLEAR) DROPS AND CHARGED CONDUCTING (RAIN) DROPS*

C. F. Tsang

Lawrence Berkeley Laboratory
University of California
Berkeley, California 94720

August 1974

INTRODUCTION

The liquid drop model of nuclear fission was suggested (1) thirty five years ago. The model has been very useful for the understanding of nuclear fission data and has recently been found to be an important element in what has come to be known in nuclear physics as the Strutinsky method by which the predictions on the masses and stability of the yet-undiscovered superheavy nuclei are made (2).

There are two aspects of the model. The more difficult and less certain is the dynamical study of the liquid drop model. This involves assumptions regarding the fluid flow patterns, the viscosity and other properties to be assumed for the nucleus. Furthermore, the liquid drop may undertake a great variety of shapes, making the calculation very involved. In the last ten years, various attempts (3) have been made to tackle this problem and I believe that these have only been partially successful and there is still the basic question whether a nucleus is (dynamically) like a liquid drop at all. On the other hand, the other aspect of the model, the statics, has been fairly well established (4) and has demonstrated its value in nuclear fission in many ways. One studies basically the balancing of two forces present in the deformable liquid drop, the Coulomb and surface tension forces. Some works (5) include also the centrifugal "force." No other properties of the liquid drop such as short range correlations and flow patterns need to be assumed in such a study. Indeed, it can be demonstrated (6) that the theory represents a more general system in which a liquid drop is a special example. This is what we call the leptodermous system, that is, a system with a thin surface region and a volume region of uniform density. In all these studies, the objective is to find the shapes of equilibrium of the system and their energies. These can be either a stable equilibrium point (a minimum) or an unstable equilibrium point (a saddle or a mountain top) in a multi-dimensional space with co-ordinates representing various deformation parameters. By looking at these equilibrium points a lot can be said about the system: whether the system tends to remain a sphere or undergo fission, whether the system

*Work performed under the auspices of the U. S. Atomic Energy Commission.

prefers to divide into two, three, or four droplets, and, with some generalization of the model, whether two droplets can coalesce into one.

With all that has been developed in the nuclear fission problem, it would be interesting to apply it to actual macroscopic rain drops which are electrically conducting and consider their shapes of equilibrium. This has the great advantage over the nuclear case that direct measurements in the laboratory on a drop can be made. Besides studying the rain drops on its own merit, a parallel theoretical and experimental study of the conducting drop may also throw light on the nuclear drop. Of course properties of the charged conducting drop is not a new area of study. In 1882, Lord Rayleigh (7) published a paper on the stability of a charged conducting drop under small oscillations. Other studies are made more recently (8). However, in the present work† we shall make a close comparative study of the nuclear drop and the rain drop using methods developed in the liquid drop theory of nuclear fission.

In the next section, some basic concepts of nuclear fission theory (9) will be described, before discussing, in the following section, simple similarities and differences between volume-charged and charged conducting drops. After that a method will be described to calculate the symmetric equilibrium shapes of the conducting drop and the results will be compared to those of a volume charged drop.

SOME BASIC CONCEPTS IN FISSION THEORY

For an incompressible volume charged drop, two forces are acting: a Coulomb force which tends to break up the drop and a surface tension which tends to keep it together. A quantity of importance is then the ratio of the Coulomb energy and the surface energy. One may define what is called the fissility parameter, x, as

$$x = \frac{E_c^{(o)}}{2E_s^{(o)}} \propto \frac{Q^2/R}{R^2} \propto \frac{Q^2}{V} ,$$

where $E_c^{(o)}$ and $E_s^{(o)}$ are Coulomb and surface energies of a sphere with charge Q, radius R, and volume V. For $x < 1$, the spherical drop is stable with respect to deformations and for $x > 1$, it turns out that the forces are such that the drop is in unstable equilibrium. The energy excess of a deformed drop over the original spherical drop may be written as

†This work was done in collaboration with W. J. Swiatecki.

$$E_s - E_s^{(o)} + E_c - E_c^{(o)} = E_s^{(o)}(B_s - 1) + E_c^{(o)}(B_c - 1)$$

$$= E_s^{(o)}\{(B_s - 1) + 2x\,(B_c - 1)\} \quad ,$$

where E_s and E_c are the surface and Coulomb energies of the drop and the superscript (o) implies that the quantity is evaluated for a sphere; also $B_s = E_s/E_s^{(o)}$ and $B_c = E_c/E_c^{(o)}$. If ξ is the energy excess in units of $E_s^{(o)}$, then

$$\xi = B_s - 1 + 2x(B_c - 1). \qquad (1)$$

In Fig. 1, we sketch the behavior of ξ as a function of deformation for a particular value of $x < 1$. The configuration at zero deformation, i.e., a sphere, is a potential energy minimum. The energy is increased as one deforms the drop until a point is reached where the disruptive Coulomb force is just balanced by the stabilizing surface tension. This point is called a saddle point. It is unstable with respect to the deformation leading to fission (but is stable with respect to other deformations). Obviously the curve will be different for different values of charge on the drop, i.e., different values of x (see Fig. 2). Thus for $x > 1$, the sphere is at a potential maximum.

Let ξ_R denote the difference in energy between the initial sphere and the final fragments at infinity in units of $E_s^{(o)}$. For division into two equal spheres which is illustrated in Figure 2, $\xi_R = 0$ at $x = 0.351$. For $x > 0.351$, $\xi_R < 0$, and for $x < 0.351$, $\xi_R > 0$. In the general case of division into n equal spheres, a general formula (4) may be written for ξ_R. The charge on each sphere is Q/n and its radius is $(R^3/n)^{1/3} = R\,n^{-1/3}$, so that the Coulomb energy of the n spheres is n multiplied by the Coulomb energy of each sphere:

$$E_c = n\,\frac{3}{5}\,\frac{(Q/n)^2}{R\,n^{-1/3}}$$

$$= \frac{3}{5}\,\frac{Q^2}{R}\,n^{-2/3}$$

thus

$$B_c = n^{-2/3}$$

Total surface energy of the n sphere is

$$E_s = \gamma\, n.\ 4\pi (R\, n^{-1/3})^2 = 4\pi R^2 \gamma n^{1/3}$$

thus

$$B_s = n^{1/3} \quad .$$

Hence the energy excess over the sphere in units of $E_s^{(o)}$ is

$$\xi_R = (n^{1/3} - 1) + 2x(n^{-2/3} - 1) \quad . \qquad (2)$$

For each value of n, this equation gives a straight line relation between ξ_R and x. By studying the system of straight lines for various values of n, the following can be deduced. For $x < 0.35$, the sphere has the lowest energy. For $0.35 < x < 0.61$, the division into two spheres gives the lowest energy. For $0.61 < x < 0.87$, the division into three equal spheres gives the lowest energy. Finally, for $0.87 < x < 1.12$, the division into four equal spheres gives the lowest energy.

In Fig. 3, we present the shapes of equilibrium of a volume charged drop as a function of the x values (10), so that we can compare them with the results we are going to obtain for a surface charged drop. The abscissa gives the fissility parameter x from 0 to 1. The ordinate gives R_{MIN}/R and R_{MAX}/R as a measure of the shape, where for an asymmetric shape radius R_{MIN} is the minimum radius of the neck of the drop and the two maximum radii R_{MAX} are the distances from the center of the neck (at its minimum radius) to the two ends of the drop. For a symmetric shape the two maxium radii are equal.

Along $R_{MAX}/R = 1$ is the sphere which is at a potential energy minimum for all $x < 1$. The rest of the curves represent a family of reflection symmetric equilibrium shapes and a family of reflection asymmetric equilibrium shapes. The two families cross each other at $x = 0\ 396$. Their shapes are schematically indicated in the figure. A point to notice is that along the symmetric family there is a fairly rapid change in the trend of R_{MAX}/R_o at x values around 0.7. It is found below that for a conducting drop a similar change occurs at a larger value of x. The notation (1) and (2) in the figure indicates whether the equilibrium shape is at (respectively) a saddle (unstable in only one direction) or a mountain top (unstable in two different directions).

COMPARISON OF A VOLUME CHARGED DROP AND A CHARGED CONDUCTING DROP

It is straightforward to apply the methods described in the last section to a charged conducting drop. Thus the fissility parameter x can be defined

similarly as the ratio of the Coulomb energy to twice the surface energy. The equation (1) for the energy excess ξ over a spherical drop will be the same as for the volume charged drop case. Of course, the Coulomb energies will now be evaluated on the assumption that the drop is conducting.

Three simple similarities may be pointed out.

(a) For $x = 0$, there is no charge on the drop so that the equilibrium shapes are the same whether the drop is conducting or not. Also, it turns out nontrivially that as in the case of a volume charged drop (11), $x = 1$ represents the transition point where the spherical drop is stable for $x < 1$ and is unstable for $x > 1$.

(b) A second similarity is apparent if we look at the energy difference ξ_R from the initial to the final state when the drop is divided into equal spheres. We have described this in detail for a volume charged drop in reference to Eq. (2). When we make a similar study for a conducting drop, we get a completely identical equation and the corresponding discussions are applicable. The reason is that only spherical shapes are involved in both the initial and final states, and the Coulomb energy of a volume charged sphere (which is $\frac{3}{5} Q^2/R$) and that of a conducting sphere (which is $\frac{1}{2} Q^2/R$) differ by only a numerical factor, 6/5, that is the same for both states. Hence B_s and B_c are the same for both cases and the same energy Eq. (2) holds good.

(c) It also turns out that the Coulomb energy of a volume charged ellipsoid and that of a conducting ellipsoid differ also by the same numerical factor. Thus, the Coulomb energy of a conducting ellipsoid is given by (12)

$$E_c = \frac{1}{4} Q^2 \int_0^\infty \left[(a^2 + \lambda)\ (b^2 + \lambda)\ (c^2 + \lambda)\right]^{-\frac{1}{2}} d\lambda$$

so that

$$B_c = \frac{1}{2} R \int_0^\infty \left[(a^2 + \lambda)\ (b^2 + \lambda)\ (c^2 + \lambda)\right]^{-\frac{1}{2}} d\lambda$$

where a, b, and c are the lengths of the axes of an ellipsoid. This integral may be carried out analytically in the case of a spheriod where two of the axes are equal. B_c for a volume charged case is given (13) by exactly the same formula. Hence, if we make the drop to take on only ellipsoidal shapes, then any conclusions about the statics of the volume charged drop will be true for the conducting drop.

The first difference between the volume charged drop and a conducting drop can be found if we consider the division of the drop into two unequal spheres at an infinite distance apart, one with volume βV and the other with volume $(1 - \beta)V$. In Fig. 4 is plotted the energy change ξ_R between the initial and final states (14) as a function of β for various values of the fissility parameter x. For $\beta = 0$ and $\beta = 1$ we get a sphere with volume V which is just the initial state. For $\beta = 0.5$, we get two equal spheres. The energy change is zero at $x = 0.35$ for $\beta = 0.5$, as was pointed out above in connection with Fig. 2. For a conducting drop Fig. 5 is found (14). We note that here again the energy is zero at $x = 0.35$ for $\beta = 0.5$. However, except for the points at $\beta = 0$, 0.5, and 1.0 the curves in the two figures are very different. A potential minimum for a volume charged drop occurs at $\beta = 0.5$ for $x > 0.2$, but a potential maximum for a conducting drop occurs at $\beta = 0.5$ for all x values less than one. In the latter case minima occur at points where the fragments are unequal.

The major reason for the above differences is that the charge to mass ratio for a volume charged drop is a constant, but for a conducting drop it is not required to be a constant. This is also the underlying cause for the second difference that appears when we try to find the configuration with the absolute lowest energy for a drop with a given fissility parameter x. For a volume charged drop, this configuration is n equal droplets at infinity (4) and the number n depends on the x values of the drop [Eq. (2)]. One would at first expect that the same conclusion might hold for a conducting drop. But, as we shall show, for a conducting drop, the configuration at the lowest energy is one with all the charges Q on the drop taken off and distributed among many infinitesimal droplets at infinity. The total energy of the droplets may be made to vanish and only the surface energy of the original drop is left. The possibility of such a configuration is shown as follows. Let $\frac{1}{n}$ of the original drop of radius R be taken off carrying all the charge Q. This is then divided into m equal spheres, each with a charge Q/m. Thus for each sphere the sum of the Coulomb and surface energy is

$$4\pi R^2\gamma \left(\frac{1}{nm}\right)^{2/3} + \frac{1}{2}\frac{Q}{R}^2 (nm)^{1/3} \left(\frac{1}{m}\right)^2$$

Hence the total energy of the small spheres is m times this quantity:

$$4\pi R^2\gamma\, m(nm)^{-2/3} + \frac{1}{2}\frac{Q^2}{R}\,(nm)^{1/3}\, m^{-2} \cdot m$$

$$= 4\pi R^2\gamma\, m^{1/3}\, n^{-2/3} + \frac{1}{2}\frac{Q^2}{R} n^{1/3}\, m^{-2/3} \quad .$$

Now let us choose $m \propto n^s$. The energy of the droplets is now equal to

$$4\pi R^2 \gamma\, n^{\frac{2}{3}+\frac{s}{3}} + \frac{1}{2}\frac{Q^2}{R}\, n^{\frac{1}{3}-\frac{2s}{3}} ,$$

which is zero when n goes to infinity provided

$$+2 > s > +\frac{1}{2}$$

and the proposed configuration is obtained. In other words, we have made the Coulomb energy of the given drop zero by dispersing the charge onto an infinite number of infinitesimal droplets without increasing the surface energy by a finite amount.

PARAMETERIZATION OF A CHARGED CONDUCTING DROP

In this part of the work we shall try to determine the equilibrium shapes of a charged conducting drop to be compared with those for a volume-charged drop (Fig. 3).

The calculation of the Coulomb energy of a conducting drop with an arbitrary shape is in general a difficult problem. However, it can be sidestepped by requiring the drop to assume a prescribed family of shapes,†† in fact, making the calculation of its Coulomb energy is a trivial matter. It is well-known from the theory of electrostatics that the electric potential due to a system of charges (total charge Q) at any point outside a given equipotential, is the same as that due to a charged conductor with the shape of this equipotential having a charge Q. Hence, if we require the drop to assume the shape of an equipotential of potential α, its Coulomb energy is just $\frac{1}{2}\alpha Q$. If R is the radius of a sphere that has the same volume as the drop and possesses the same amount of charge, its Coulomb energy is $\frac{1}{2} Q^2/R$. Hence we get

$$B_c = \alpha R/Q .$$

The surface energy relative to that of the sphere, B_s, can simply be found by calculating its area numerically. Hence for a given fissility x the

††This is a common practiced procedure in the liquid drop model of fission. The true equilibrium points can be determined by looking at the convergence as one enlarges the family of shapes. An independent condition on equilibrium may also be used as illustrated below.

energy of the drop is calculated [Eq. 1], and equilibrium shapes, whose energies are stationary, are then determined.

For illustration, the shapes of equipotentials that enclose two equal points charges are shown in Fig. 6, where the volumes of the shapes have been normalized to the same value. We shall refer to these shapes as the symmetric N = 2 family, since they are generated with two point charges and are reflection symmetric. This figure displays a very restricted series of shapes. However, it is easy to increase the possible shapes by generating equipotentials of a larger number of point charges, which may be placed on a straight line so that the shapes are axially symmetric. The reflection symmetric N = 3 family is generated with two equal charges situated at equal distances on opposite sides of a third point charge. The shapes are shown in Fig. 7. They include the symmetric N = 2 family. Similarily, we can go on to N = 4, 5, ... family of shapes.

In general, the N-family of axially symmetric shapes may be specified by giving the magnitudes of the N point charges and their positions as well as the value of the potential on the equipotential we are looking at. These are 2N + 1 numbers. However, not all these numbers are required to specify a shape. Three numbers may be arbitrary: (1) The center of mass of all the point charges may be at any point in space; (2) The total charge may be fixed beforehand; (3) We can also present a scale by which the distances between the point charges are measured. Thus, we are left with 2N - 2 parameters. (For reflection symmetric shapes, the distribution of point charges and their magnitudes are reflection symmetric with respect to the origin and we have only N - 1 parameters).

However, the shapes generated even by a large number of point charges are not general enough to represent an arbitrary shape. Thus, an oblate shape cannot be found in our scheme. This raises the question whether the equilibrium shapes we have determined are indeed true equilibrium configurations when the drop is free to take on any arbritrary shape. To answer this question a criterion can be developed to test a given shape for equilirbium. (A similar criterion exists for a volume charged drop (11).)

If the surface element dS is displaced normally by a small smount, δn, without affecting its local charge, σ, the Coulomb energy change is (12)

$$\delta E_c = -\int \frac{1}{2}\sigma\, \mathcal{E}\, \delta n\, dS \quad .$$

where $\mathcal{E}$ is the electric field at dS. The change in surface energy is

$$\delta E_s = \gamma \int \kappa\, \delta n\, dS$$

where γ is the surface tension coefficient, and κ is the curvature at dS. The total energy change is

$$\delta E = \delta E_c + \delta E_s \quad .$$

Subtracting $\delta n dS$ times a Lagrange multiplier k to ensure conservation of volume and equating the integrand to zero (for equilibrium shapes $\delta E = 0$ for any δn) gives

$$k = \gamma \kappa - \frac{1}{2} \sigma \mathcal{E}$$

By Gauss' Theorem,

$$\sigma = \frac{1}{4\pi} \mathcal{E}$$

$$k = \gamma \kappa - \frac{\mathcal{E}^2}{8\pi}$$

$$= \gamma \kappa_o \left(\frac{\kappa}{\kappa_o} - \frac{\mathcal{E}_o^2}{8\pi\gamma\kappa_o} \frac{\mathcal{E}^2}{\mathcal{E}_o^2} \right)$$

where κ_o is the curvature on a sphere with the same volume as the drop and $\mathcal{E}_o$ is the electric field on the sphere.

Since

$$x = \frac{E_c^{(o)}}{2E_s^{(o)}} = \frac{1}{\gamma\kappa_o} \frac{\mathcal{E}_o^2}{8\pi}$$

Thus

$$k = \gamma\kappa_o \left(\frac{\kappa}{\kappa_o} - x \frac{\mathcal{E}^2}{\mathcal{E}_o^2} \right)$$

Thus for an equilibrium shape, any point on its surface should satisfy $\Delta = 0$, where Δ is given by

$$\Delta = \frac{\frac{\kappa}{\kappa_o} - x\frac{\mathcal{E}^2}{\mathcal{E}_o^2}}{B_s - xB_c} - 1$$

As a measure of the deviation from equilibrium we can define a root-mean-square value of Δ over the surface of the drop:

$$\text{RMS} = \left(\int |\Delta|^2 \, dS \right)^{\frac{1}{2}} .$$

If RMS $\ll$ 1, the drop is close to equilibrium. If RMS $>$ 1, the shape is far from equilibrium. This quantity can be used as a measure of how close the shapes we obtain are to the true equilibrium.

SYMMETRIC EQUILIBRIUM SHAPES OF A CHARGED CONDUCTING DROP

Instead of going into mathematical details (6) we shall present here the results based on a family of shapes generated by two, three up to six point charges shown in Fig. 8. The figure should be compared to Fig. 3 for a volume charged drop. The series of curves with different N values are just successive orders of approximation of true equilibrium shapes. One hopes that for a high enough order of approximation, the results would be very close to the true ones, so that an even higher order will change the results very little. Typically, for successive orders the RMS values improve by a factor of two. For N = 6 parameterization, RMS $\sim$ 0.01 for x close to 1 and $x < 0.8$, but RMS $\sim$ 0.1 for $x \sim 0.9$. This indicates that for $x < 0.8$ and $x \sim 1.0$, the shapes we obtain are close to true equilibrium shapes, but for $x \sim 0.9$, there are more uncertainties. By studying the change of RMS values at $x \sim 0.9$ for successive approximations, the RMS values are found to decrease very slowly, much less than factors of two. This indicates that our model of a conducting drop using the equipotential surfaces of point charges is probably not good enough in this region. A more general or more appropriate family of shapes appears to be in demand here. Hence, one should regard the calculated results in this region with great reservations.

Let us take the N = 6 curve at its face value and examine its main features. As the value of x goes ~~from 1 toward small x values, the~~ equilibrium shape elongates from a sphere, i.e., R_{MAX}/R increases with

decreasing x in the region near x = 1. This is in constrast to cases of small x values ($x \lesssim 0.7$) where R_{MAX}/R is slowly decreasing with decreasing values of x. The shapes in the latter case are long and look like a dumb-bell. Similar to the volume charged drop case there exists a region where there is a rapid change of shape, but it occurs at $x \approx 0.9$ in the present case. Actually the curve for R_{MAX}/R even turns back at s = 0.887 and again at x = 0.906. However, it is in exactly this region that our results become unreliable and the double turn might be spurious (see Refs. 15 and 4 for a similar uncertainty which once existed in the volume charged case).

The nature of these equilibrium shapes may be found by looking at the signs of the second derivatives of their energy with respect to all the parameters. The following results are found when the shapes are restricted to only the degrees of freedom that allow reflection symmetric shapes. For $1 > x > 0.887$ the energy of the drop is a maximum in one degree of freedom, but a minimum in the other symmetric degrees of freedom. Between the bends, for $0.887 < x < 0.906$, the energy is a minimum. For values of x smaller than 0.906, it is again a maximum in one degree of freedom. With respect to the degrees of freedom that describe reflection asymmetric deformation, the energy of the drop is a minimum from x = 1 to x = 0.892. From x = 0.892 to x = 0.68, it is a maximum in one degree of freedom. Below x = 0.68 it appears to be a maximum in two degrees of freedom. Hence, the equilibrium point is a saddle from x = 1 to x = 0.892. From x = 0.892 to x = 0.887 it is a mountain top (unstable in more than one direction). Between the bends at x = 0.887 and x = 0.906 it is again a saddle. For x smaller than 0.906, it turns out to be a mountain top also. As discussed before the shapes close to x = 1 is fairly well determined, but at the bends the results are not reliable.

SUMMARY AND CONCLUSIONS

The static properties of a charged conducting drop are compared with those of a volume charged drop. Similarities as well as some of the differences are discussed. The symmetric equilibrium shapes of a conducting drop are determined with reasonable confidence for values of the fissility parameter x not in the neighborhood of 0.9. For x close to 0.9 a more general or more appropriate shape parameterisation than employed in this work has to be found so that equilibrium shapes at these values of x can be determined with greater reliability. This is important because it is in this region that we find possibilities of interesting stability features, such as the occurrence of a bend in the family of equilibrium shapes and of points at which there is a change in the number of degrees of freedom with respect to which the shape has a maximum energy.

It is interesting to note that even some ninety years after Lord Rayleigh's study of a charged conducting drop, the whole problem is still a very open subject. The present calculations have been able to determine the saddle points of a charged conducting drop for values of x from 0.892 to 1 where they are reflection symmetric. But for the region up to 0.892, one is still very ignorant of the saddle point shapes and energies of a charged conducting drop.

REFERENCES

1. N. Bohr and J. A. Wheeler, Phys. Rev. 56,426 (1939).

2. S. G. Nilsson, C. F. Tsang, A. Sobiczewski, Z. Szymanski, S. Wycech, C. Gustafson, I-L. Lamm, P. Möller, and B. Nilsson, Nucl. Phys. A131, 1 (1969).
M. Brack, J. Damgaard, A. S. Jensen, H. C. Pauli, V. M. Strutinsky, and C. Y. Wong, Rev. Mod. Phys. 44,320 (1972).

3. J. R. Nix and W. J. Swiatecki, Nucl. Phys. 71, 1 (1965); also Ref. 10.
R. W. Hasse, Nucl. Phys. A128, 609 (1969); Phys. Rev. C 4, 572 (1970).
C. T. Alonso, Lawrence Berkeley Laboratory report LBL-2993 (1974).

4. W. J. Swiatecki, Deformation Energy of a Charged Drop, III, Paper No. P/651, Proceedings of the Second United National International Conference on the Peaceful Uses of Atomic Energy, Geneva, 1958, United Nations, Geneva, 1958).
S. Cohen and W. J. Swiatecki, Ann. of Phys. 22, 406 (1973).
See also references 11 and 15.

5. S. Cohen, F. Plasil, and W. J. Swiatecki, Ann. Phys. 82, 557 (1974).

6. C. F. Tsang, Thesis, University of California, Lawrence Radiation Laboratory report UCRL-18899 (1969).

7. Lord Rayleigh, Phil. Mag. XIV, 184 (1882).

8. B. Vonnegut and R. L. Neubaeur, J. Collid. Sci. 7, 616 (1952).
S. A. Ryce and R. R. Wyman, Can. J. Phys. 42, 2185 (1964).
S. A. Ryce and D. A. Partiarche, Can. J. Phys. 43, 2192 (1965).
S. A. Ryce, Nature 1343 (1966).
Proceedings of the International Symposium on Electrodynamics at Massachusetts Institute of Technology, March 31-April 2, 1969). (International Unions of Theoretical and Applied Mechanics, Pure and Applied Physics).
P. R. Brazier-Smith, M. Brook, J. Latham, C. P. R. Saunders, and M. H. Smith, Proc. Roy. Soc. A322, 523 (1971).
P. R. Brazier-Smith, Phys. Fluids 14, 1 (1971).
P. R. Brazier-Smith, Quart. J. R. Met. Soc. 98, 434 (1972).
C. P. R. Saunders and B. S. Wong, J. Atoms. Terr. Phys. 36, 707 (1974).

9. E. K. Hyde, The Nuclear Properties of Heavy Elements, Vol. III, Fission Phenomena, Prentice-Hall, Inc., Englewood Cliffs, N. J. (1964).

10. J. R. Nix, Nucl. Phys. A130, 241 (1969).

11. W. J. Swiatecki, Phys. Rev. 104, 993 (1956).

12. J. Jeans: The Mathematical Theory of Electricity and Magnetism (Cambridge University Press, Fifth Edition 1958).

13. See Horace Lamb, Hydrodynamics (Dover Publications, New York, Sixth Edition, 1945) p. 700, where one is looking at the case of gravitational potential; however, the case of electrostatic potential can be easily written down from the results.

14. S. A. Ryce and R. R. Wyman, Can. J. Phys. 42, 2185 (1964).

15. S. Cohen and W. J. Swiatecki, Ann. of Phys. 19, 67 (1962).

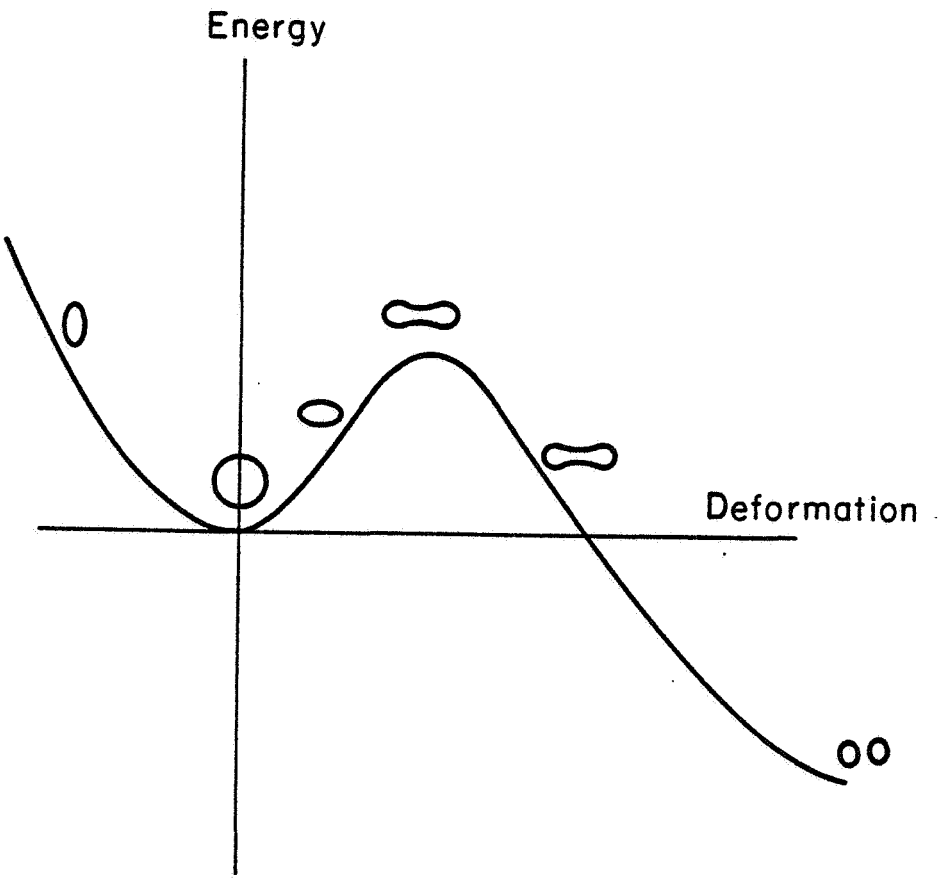

Fig. 1. Energy excess of a volume-charged liquid drop as a function of deformation.

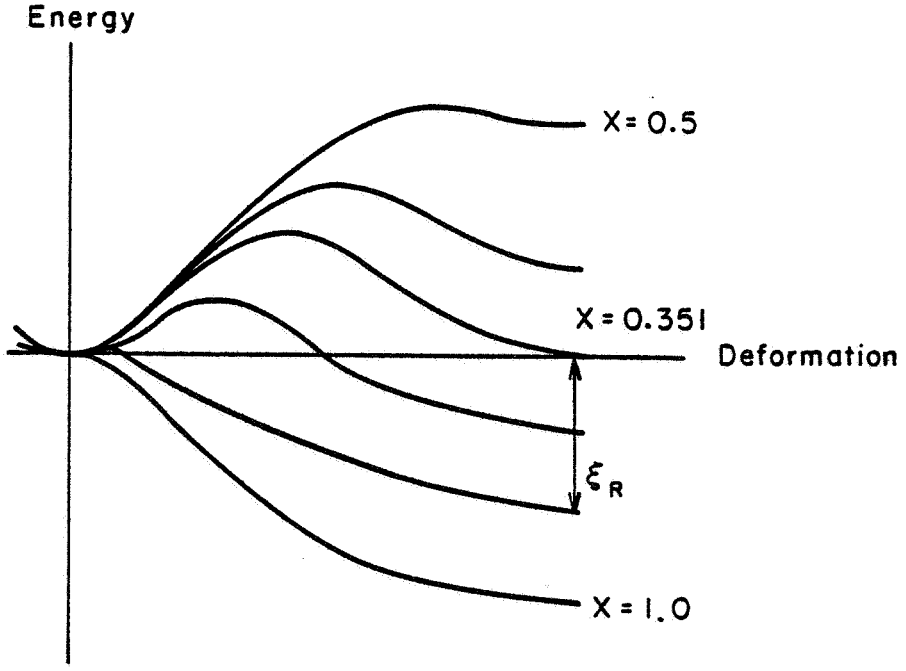

Fig. 2. Energy excess of a volume-charged liquid drop deformation for different values of the fissility parameter x.

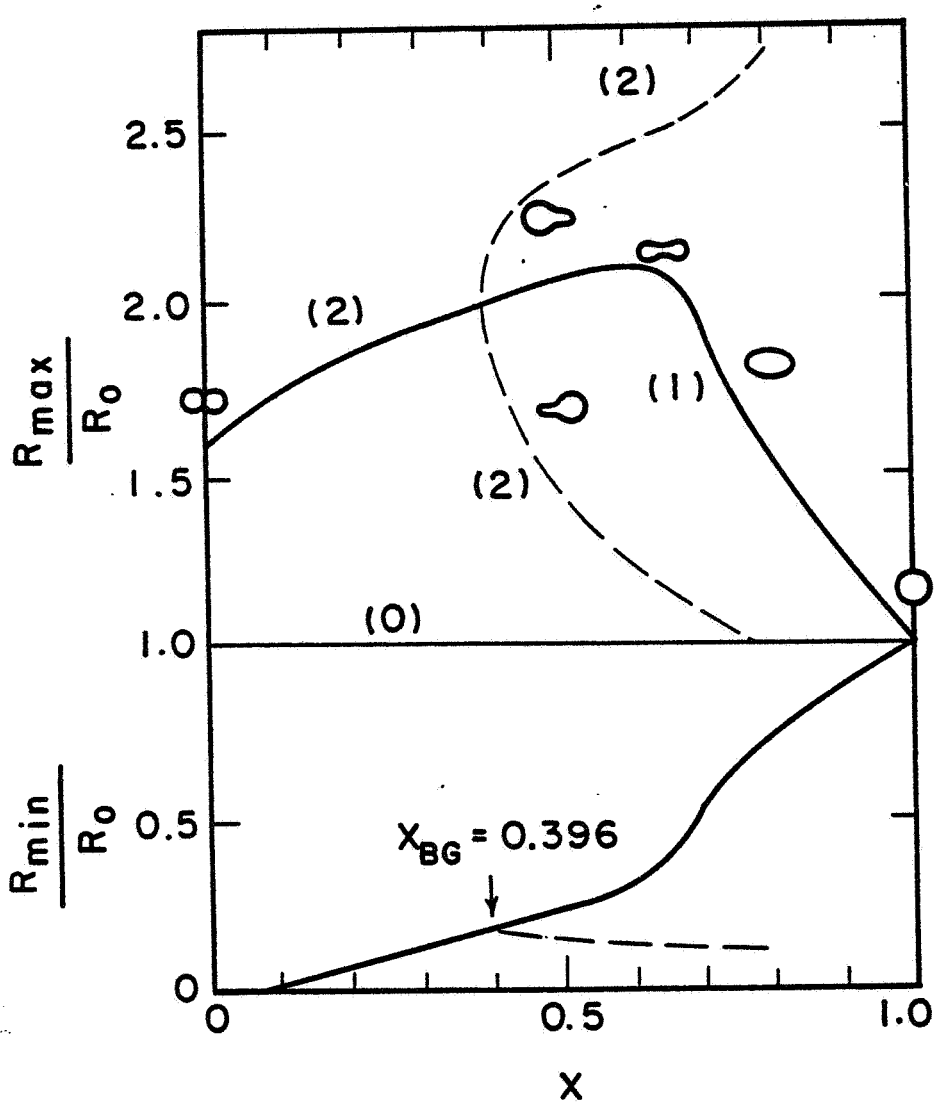

Fig. 3. The maximum and minimum radii of saddle point shapes of a volume-charged drop as a function of the fissility parameter x. The results for the symmetrical saddle point shapes are given by the solid curves, and the results for the asymmetric saddle point shapes by the dashed curves. (Data taken from Ref. 10).

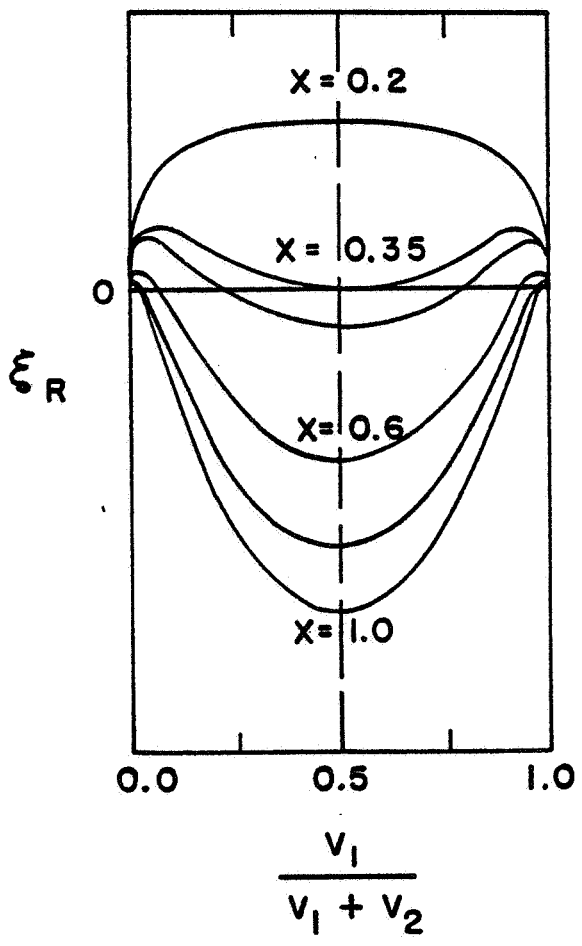

Fig. 4. The energy change in the division of a volume-charged drop into two spheres for various values of x.

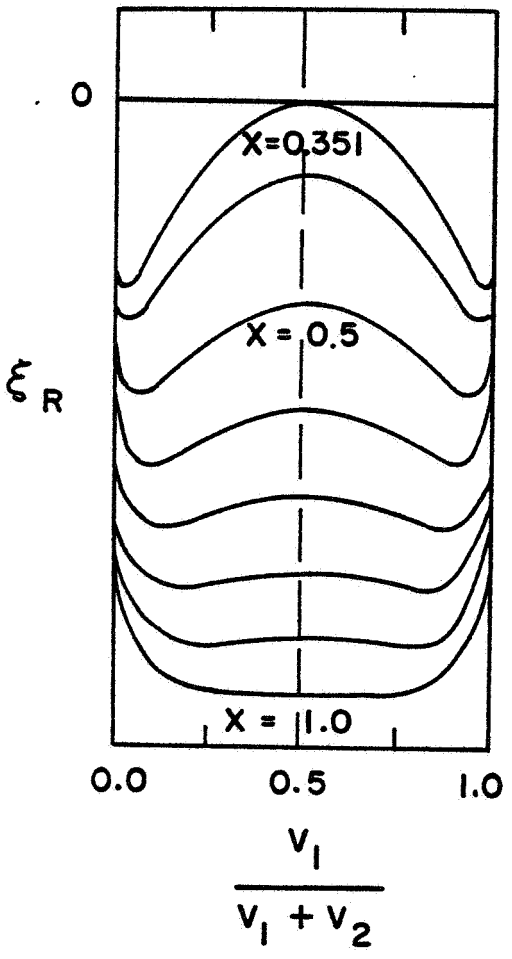

Fig. 5. Same as Fig. 4 for the case of a charged conducting drop.

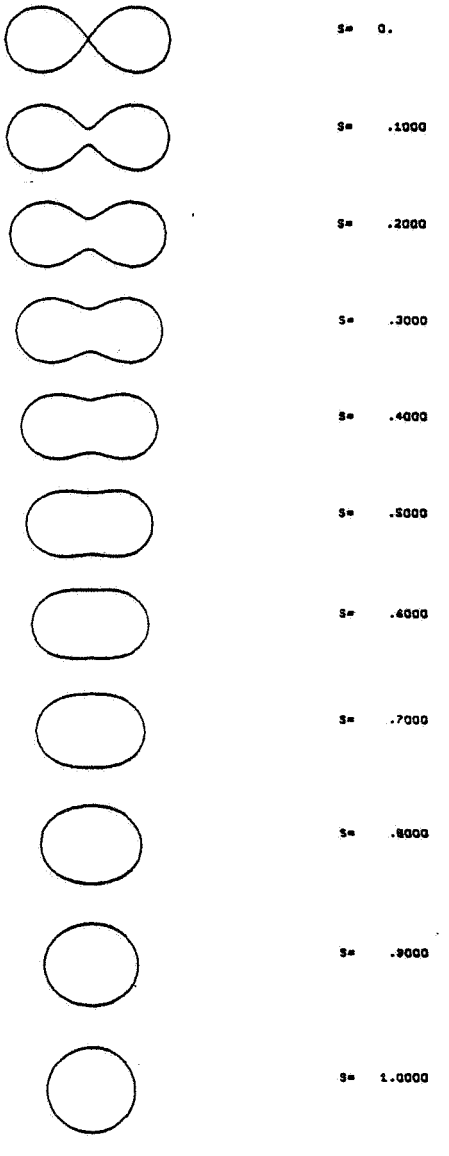

Fig. 6. Shapes in the symmetry N = 2 family of equipotential surfaces.

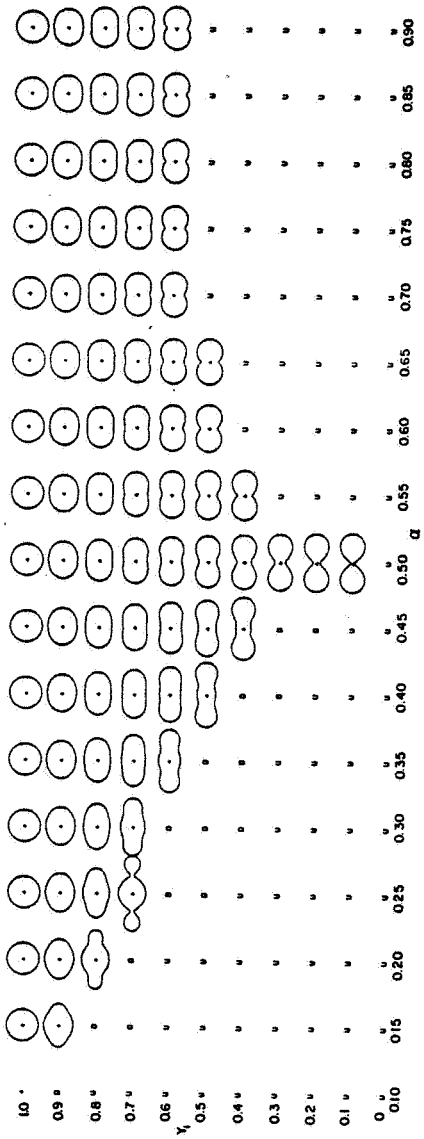

Fig. 7. Shapes in the symmetry N = 3 family of equipotential surfaces.

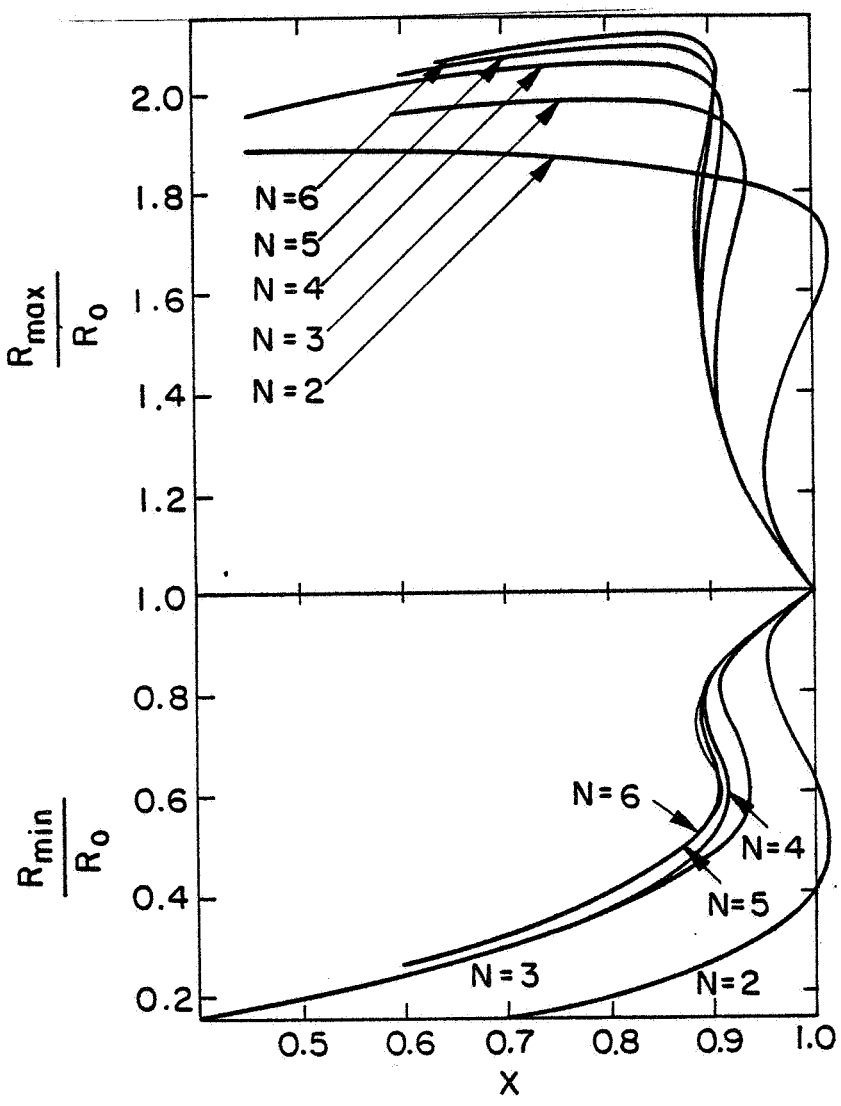

Fig. 8. The maximum and minimum radii of the symmetric saddle point shapes of a charged conducting drop as a function of the fissility parameter x. Different curves correspond to the restriction to different families of shapes indicated by the values of N.

D1

THE ROLES OF ELECTROHYDRODYNAMIC PHENOMENA IN THE MOTION OF DROPS AND BUBBLES

R.B. Spertell and D.A. Saville
Princeton University, Princeton, New Jersey 08540

ABSTRACT

The dynamics of small drops and bubbles are investigated with regard to the effects of an external electric field and an electrically charged layer situated on their interfaces. Specifically, stresses engendered due to the convection of surface charge alter both the motion and shape of single droplets and the bulk properties of suspensions.

INTRODUCTION

Motions produced inside and outside a neutrally buoyant drop immersed in a viscous fluid when an electric field is present are due to the interaction of induced charge with the field, an interaction which produces tangential shear stresses at the interface. A theory developed by G.I. Taylor[1] describes how the sense of the motion and the deformation depend on the various parameters when both fluids are poor conductors. He showed that, to leading order, the deformation and speed of circulation are proportional to $a\varepsilon E_o^2/\gamma$. Here a denotes the radius, ε the dielectric constant of the outer fluid, E_o the field strength and γ the interfacial tension. This dimensionless group is, in essence, a comparision between the electrical stress tending to deform the drop and the restoring force of interfacial tension. Electrical and physical properties alone determine whether the deformed spheroid is oblate or prolate.

In Taylor's theory the distribution of induced charge, which depends on the electrical relaxation times for the two fluids, plays a central role. The distribution is antisymmetric with respect to the equitorial plane normal to the field. If the charge relaxation time, ε/σ, (σ denotes conductivity) of the inner fluid exceeds that of the outer fluid then flow is from the poles towards the equator. When the ratio of relaxation times is less than unity the charge distribution and flow are reversed. That theory, moreover, is in substantial agreement with experiments by Allan and Mason[2] and Torza, Cox and Mason,[3] who studied the deformation and burst of neutrally buoyant drops of various fluids.

Taylor's theory and its extensions to oscillatory electric fields by Torza, Cox and Mason[3] and Sozu[4] ignore, quite properly, the charge convection process which takes place at the interface. Bulk free charge is taken to be identically zero and the induced surface charge is convected by a motion which is $O(a\varepsilon E_o^2/\gamma)$. Thus, the alteration of stress due to convection of charge is $O(a\varepsilon E_o^2/\gamma)^2$ and therefore small.

If the drop undergoes translation, however, as is frequently

the case if the densities are unmatched or the drop carries a charge, then charge convection induces electrical stresses which are $O(\eta U/\gamma \cdot a\varepsilon E_o^2/\gamma)$. These alter the translational speed and the shape. The purpose of this paper is to describe the influences of charge convection both because of its intrinsic interest and its relevance to drop breakup and coalescence.

It is readily seen that the shape alteration will differ from that found by Taylor since stresses resulting from charge convection due to streaming will be asymmetric. Thus, instead of a symmetrical deformation proportional to $P_2(\cos\theta)$ * the deformation will be represented in terms of $P_2(\cos\theta)$ and $P_3(\cos\theta)$. Experimental evidence for this sort of shape arising in the fashion proposed is sparse since all of the published work relates to neutrally buoyant drops. However, one prescient sequence of photographs by Torza, Cox and Mason does show the expected asymmetry [Figure 10, plate 7 of their paper]. It shows a drop flattened into an oblate spheroid, as would be expected from Taylor's theory. Then, perhaps due to the accumulation of charge, it begins to migrate and loses its symmetrical form. Although the amount of deformation is greater than that which could be rigorously modelled by a linearized theory the shape is clearly of the form expected from the consequences of charge convection.

Asymmetric deformation could also result from movement of the surface of a charged drop. Such a charge might be in the form of a monolayer or double-layer. Extant theories of the motion of drops with double-layers[5,6] allow for the convection of charge to some extent but the deformation is identically zero due to the extremely simple forms of the velocity and potential when charge relaxation is rapid. A more comprehensive theory is presented here which is applicable as well to cases where charge relaxation is slow enough for convection to be important.

The development proceeds along familiar lines with electrical effects described by the electrohydrodynamic simplifications of Maxwell's equations and motion inside and outside the globule described by solutions of the linearized Navier-Stokes equations. A key feature is the proper accounting for convection of surface charge. The system under study is depicted in Figure 1. A fluid sphere of radius a is immersed in another immiscible fluid. Both are Newtonian and incompressible with interfacial tension γ. Density and viscosity are denoted by ρ and ν, the shear viscosity by η. Carets are used to distinguish the variables pertaining to the globule. Three situations will be discussed:

(a) An uncharged globule in the presence of a uniform electric field, both fluids being ohmic conductors.

(b) A charged globule in a viscous non-conductor (the monolayer problem).

(c) A charged globule in a viscous conductor with a perfectly polarized interface (the double layer problem).

---

* $P_n(\cos\theta)$ is a Legendre polynomial of order n, θ is measured from the rear stagnation point.

It will be assumed in the formal analysis that electrical stresses are small compared to interfacial tension, viz., $a\varepsilon E_o^2/\gamma<1$.

The remainder of the presentation is divided into sections dealing with the formal aspects of electric fields, forces and boundary conditions; fluid motion; then results for the uncharged drop, or drop with a mono-layer, and a drop with a double-layer. Before concluding, the effect of charge convection on the electrical conductivity of a suspension of fluid drops is discussed briefly.

ELECTRIC FIELDS, FORCES AND BOUNDARY CONDITIONS

Maxwell's equations in the form appropriate to electrohydrodynamic phenomena read

$$\nabla\times\underset{\sim}{E} = 0, \quad \nabla\cdot\underset{\sim}{D} = 4\pi q, \quad \text{and} \quad \frac{\partial}{\partial t} q + \nabla\cdot\underset{\sim}{J} = 0. \tag{1}$$

$\underset{\sim}{E}$, $\underset{\sim}{D}$, q, and $\underset{\sim}{J}$ stand for the electric field strength, dielectric displacement, bulk free charge density, and current, respectively. The constitutive relations are

$$\underset{\sim}{D} = \varepsilon\underset{\sim}{E}, \quad \underset{\sim}{J} = \sigma\underset{\sim}{E} + q\underset{\sim}{v} . \tag{2}$$

In the situation under investigation free charge is initially concentrated at the interface either as a mono- or a double-layer and remains there. It follows then that electrical phenomena can be described by means of potential functions which are

$$\hat{\phi}(r,\mu) = \sum_1^\infty c_n r^n P_n(\mu) \tag{3}$$

inside and

$$\phi(r,\mu) = \phi_d(r) - rP_1(\mu) + \sum_0^\infty D_n r^{-(n+1)} P_n(\mu) \tag{4}$$

outside. Here $\phi_d(r)$ denotes the double-layer potential in the absence of convection. Its precise form is unimportant here since we are dealing with thin layers and all that is required is the gradient at the interface. $\phi_d(r)$ is suppressed in the absence of a double-layer; when the external field is absent the term $-rP_1(\mu)$ is omitted.

The physical phenomena are determined by boundary conditions and they are set forth next.

A. Uncharged globule in the presence of an external field. Here both fluids are presumed to be ohmic conductors and at the interface the tangential components of the field are to be continuous,

$$E_t = \hat{E}_t \tag{5}$$

The other condition arises from the conservation of induced charge, Q, at the interface. Q is defined by the jump in εE_n, viz., $\langle \varepsilon E_n \rangle = Q$, where $\langle \varepsilon E_n \rangle$ stands for $\varepsilon E_n - \hat{\varepsilon} \hat{E}_n$. Balancing conduction to and from the interface against convection leads to the expression

$$\langle \sigma E_n \rangle + \nabla_s \cdot (Q \underset{\sim}{v}) = 0 \ . \tag{6}$$

$\nabla_s \cdot$ denotes the surface divergence, $\underset{\sim}{v}$ the velocity.

B. Charged globule in a viscous non-conductor (charge monolayer). Here the boundary conditions are the same as before although the absence of conductivity in the outer fluid, which serves to keep the globule charged, does simplify Equation 6 somewhat.

C. Charged globule in a viscous conductor with the interface perfectly polarized (charge double-layer). In this situation a thin double-layer approximation is employed wherein that part of the double-layer residing in the outer fluid is collected into a spherical sheath of charge. Charge is transported to and from this sheath by conduction and in it by convection; no charge crosses the interface. The balance expression reads

$$\sigma E_n + \nabla_s \cdot (Q \underset{\sim}{v}) = 0 \tag{7}$$

Processes which are ignored are tangential currents due to conduction, which are vanishingly small since the layer is thin, and radial charge convection, which vanishes since the radial velocity is zero at the interface. The net charge on the outer sheath is related to the gradient of the potential in the usual manner,[7] viz.,

$$\left[\frac{d\phi_d}{dr}\right]_{r=1} + D_o = \frac{4\pi Q_o}{\varepsilon E_o} \tag{8}$$

Here and elsewhere the potentials have been made dimensionless with the scale aE_o. The scale for length is a, Q_o is the average charge per unit area, and E_o is the (uniform) field strength far from the drop. Coefficients in Equation 3 are evaluated by requiring the tangential components of the field to be continuous.

FLUID MOTIONS

Since the fluids being considered are isothermal, incompressible and Newtonian and inertial effects neglected the well-known simplifications[8] of the equations of motion can be made. Solutions to the linearized equations can then be expressed in terms of stream functions for the motion inside the drop,

$$\hat{\psi}(r,\mu) = \frac{1}{2}\frac{\eta U}{\gamma}\frac{r^2-r^4}{1+\kappa}Q_1(\mu) + \sum_1^{\infty}[\hat{A}_n r^{n+3} + \hat{B}_n r^{n+1}]Q_n(\mu),$$

and outside,

$$\psi(r,\mu) = -\frac{1}{2}\frac{\eta U}{\gamma}\left(2r^2 - \frac{2+3\kappa}{1+\kappa}r + \frac{\kappa}{1+\kappa}r^{-1}\right)Q_1(\mu) + \sum_1^{\infty}[A_n r^{-(n-2)} + B_n r^{-n}]Q_n(\mu) . \qquad (9)$$

These expressions are in dimensionless form with U denoting the streaming speed far from the object, $\kappa = \eta/\eta$ and

$$Q_n(\mu) = \int_{-1}^{\mu} P_n(\alpha)\,d\alpha . \qquad (10)$$

The set of coefficients denoted as $\hat{A}_n$, $\hat{B}_n$, A_n, and B_n are evaluated from boundary conditions applied at the interface. These are: (i) continuity of the various components of velocity and (ii) continuity of the tangential components of the stress. The former reveals that

$$\hat{A}_n = -\hat{B}_n = A_n = -B_n \quad ; \quad n \geq 1 . \qquad (11)$$

Continuity of the stress is expressed as

$$\left\{r\frac{\partial}{\partial r}\frac{v_\theta}{r} + \frac{1}{r}\frac{\partial}{\partial\theta}v_r\right\} + T_t^{(e)} = \kappa\left\{r\frac{\partial}{\partial r}\frac{\hat{v}_\theta}{r} + \frac{1}{r}\frac{\partial}{\partial\theta}\hat{v}_r\right\} + \hat{T}_t^{(e)} \qquad (12)$$

with the electrical stresses, $T_t^{(e)}$, evaluated from Maxwells stress tensor,[9]

$$T_t^{(e)} = \frac{a\varepsilon E_o^{\,2}}{4\pi\gamma}E_r E_\theta\Big|_{r=1} \qquad (13)$$

in dimensionless form. The balance of normal stresses fixes the shape.

BEHAVIOR OF AN UNCHARGED GLOBULE

Explicit analytical solutions are obtained from simultaneous solution of the equations resulting from enforcing the boundary

conditions. The calculations are straightforward and so tedious details are omitted. Complete expressions can be derived from those given in Reference 10.

Continuity of electrical stress and velocity enable one to reduce the problem to the evaluation of two sets of coefficients, B_n and C_n, say. Then an expansion scheme with $a\varepsilon E_o^2/\gamma \equiv \delta$ treated as a small parameter is employed. From expressions of the form

$$\left.\begin{aligned} B_n &= B_n^{(0)} + B_n^{(1)} + \ldots \quad n = 1, 2, \ldots \\ C_n &= C_n^{(0)} + C_n^{(1)} + \ldots \quad n = 1, 2, \ldots \end{aligned}\right\} \tag{14}$$

we find

$$B_1^{(0)} = B_3^{(0)} = B_4^{(0)} = C_2^{(0)} = C_3^{(0)} = 0 \tag{15}$$

The orders of the coefficients that survive are:

$C_1^{(0)}: 0(1)$; $C_2^{(1)}: 0(\eta U/\gamma)$; $B_2^{(0)}, C_1^{(1)}, C_2^{(2)}, C_3^{(1)}: 0(\delta)$; and

$B_1^{(1)}, B_3^{(1)}: 0(\delta\eta U/\gamma)$. The other coefficients are of an even smaller order and therefore neglected. The formulas for $C_1^{(0)}$ and $B_2^{(0)}$ correspond to those given by Taylor.[1] $C_1^{(1)}$, $C_2^{(2)}$ and $C_3^{(1)}$ are associated with convection of induced charge by the electrically induced field and $C_2^{(1)}$ from the streaming. The velocity field consists of terms representing flow due to uniforming streaming and electrical stress arising from the induced charged whose distribution is altered, in turn, by the streaming.

For the settling velocity we find

$$\frac{U}{U_{st}} = \frac{3}{\frac{2+3\kappa}{1+\kappa} + f(R,S,\kappa)\frac{(\varepsilon E_o)^2}{\eta\sigma}} \tag{16}$$

when the direction of the uniform electric field is opposite to the gravitational field. Here $U_{st} = 2a^2 g(1-\hat{\rho}/\rho)/9\nu$ and

$$f(R,S,\kappa) = \frac{6}{5}\,\frac{1}{(1+\kappa)^2}\,\frac{R^2}{(3+2R)(2+R)^2}\,[3(1+R^{-1}) - \frac{\hat{\tau}_r}{\tau_r}][1 - \frac{\hat{\tau}_r}{\tau_r}] .$$

R stands for $\hat{\sigma}/\sigma$ and τ_r for the ratio of an electrical relaxation time, ε/σ, to the time scale for fluid motion, $a\eta/\gamma$, based on the outer fluid. Note that $\hat{\tau}_r/\tau_r = 1/RS$.

It is easy to show that the electric field can either increase or decrease the rate of translation of the globule, depending upon

the electrical properties of the fluids under discussion. The particular condition under which the speed will increase is $1 < \hat{\tau}_r/\tau_r < 3(1+R^{-1})$. If this restriction is not met the motion of the droplet will be retarded. Figure 2 illustrates the magnitude of the effect for typical values of the parameters.

For an explanation of these results we examined the manner in which the streaming motion alters the induced charge and the tangential stresses (see Figure 3). In the case of a neutrally buoyant drop both the polarization and direction of fluid circulation are determined by the ratio of electrical relaxation times in the droplet and medium in the manner depicted. When the ratio of electrical relaxation times is unity the drop remains unpolarized and the electrical shearing stresses vanish.

When the electrical relaxation time of the droplet exceeds that of the surrounding fluid, the streaming motion alters the distribution as shown in Figure 3. In a manner analogous to that for the neutrally buoyant case, interaction of the altered charge distribution with the tangential component of the electric field results in the shear stress distribution indicated. These shearing stresses induce motions which enhance the streaming motion of the droplet. Compression of the negative charge toward the rear of the droplet results in electrical shearing stresses which retard motion. The settling speed of the droplet will be altered, then, depending upon the relative magnitudes of these two opposing phenomena.

A similar analysis for case (b) shows that the interaction of the altered charge distribution with the tangential component of the electric field always tends to retard the motion of the droplet when $\hat{\tau}_r/\tau_r < 1$. Motion is further retarded due to compression of positive charge toward the rear of the globule.

Deformation of the globule is due to electrical effects since uniform streaming per se causes no deformation if inertial effects are absent.[11] The deformation from the spherical form is represented as

$$\zeta(\mu) = \sum_{2}^{\infty} \beta_n P_n(\mu) \tag{17}$$

so that the center of mass is fixed and the globule is incompressible. The surviving coefficients, to $O(\delta)$, are β_2 and β_3. Normal stresses which give rise to β_2 are due to electrical phenomena present in the absence of streaming as found by Taylor while deformation due to charge convection is described by β_3.

Figure 4 depicts the manner in which a falling fluid sphere deforms when subject to a uniform electric field. The lack of fore to aft symmetry of the droplet can be understood in terms of the normal stresses engendered by the lack of symmetry of the charge distribution with respect to the equitorial plane of the droplet. This may be contrasted with the oblate spheroid which develops when charge convection is not taken into account (Figure 5).

The shape shown in Figure 4 is quite similar to the form depicted by Torza, Cox and Mason to which earlier reference was made. Calculations made using the parameters given in their paper are qualitatively the same although a direct comparison is not possible due to the lack of information on the rate of translation.

BEHAVIOR OF A CHARGED GLOBULE IN A VISCOUS NON-CONDUCTOR

Results for this situation, obtained in a fashion similar to that employed earlier, show that deformation tends to be prolate since the conductivity ratio is effectively infinite. Charge convection alters the symmetry, however. The translational velocity is altered by convection of both the induced charge and the net surface charge, viz.,

$$U = -\frac{\frac{2aQ_oE_o}{\eta}}{\frac{2+3\kappa}{1+\kappa} + \frac{9}{5}\frac{(\epsilon E_o)^2}{(1+\kappa)^2 4\pi\,\eta\hat{\sigma}} + \frac{2}{3}\frac{1}{(1+\kappa)^2}\frac{4\pi Q_o^2}{\eta\hat{\sigma}}} \tag{18}$$

for a charged, neutrally buoyant drop in a viscous dielectric. It is worth noting here that convection of charge always produces shearing stresses which retard motion. This is consistent with the behavior identified with the uncharged globule where it was shown that if the ratio of electrical relaxation times is less than unity then motion is impeded.

BEHAVIOR OF A CHARGED GLOBULE WITH A PERFECTLY POLARIZED INTERFACE

A typical shape is shown as Figure 6. The asymmetry due to charge convection is evident and, in contrast to the situation shown in Figure 4, the front part of the drop is elongated due to the choice of physical properties. Nevertheless it should be noted that the deformation is $0(\tau_r)$ and when the relaxation is rapid as it would be with, say, a mercury drop in an ionic solution, the deformation will be quite small.

The translational velocity is

$$U = \frac{aQ_oE_o/\eta}{2+3\kappa+g} \tag{19}$$

where

$$g = \tau_r \frac{a\epsilon E_o^2}{4\pi\gamma}\left\{\left(\frac{4\pi Q_o}{\epsilon E_o}\right)^2 + \frac{3}{10(1+\kappa)S^2}\left[\frac{1}{4}(8+10\kappa) - \frac{3S}{5}(7+8\kappa)\right]\right\} .$$

This shows, again, how charge convection impedes the rate of translation. If internal electric stresses are ignored by taking $\hat{\epsilon} = 0$ $(S = \infty)$ then Equation (19) reduces the classical result due to Levich.[5,6]

CHARGE CONVECTION AND THE CONDUCTIVITY OF SUSPENSIONS

Processes of the sort just studied in connection with the behavior of single drops ought to manifest themselves in their effects on the properties of suspensions and drops. Two of the more obvious properties are electrical conductivity and viscosity. Indeed, just as it is possible to alter the properties of suspensions of solid, orientatible particles using external fields,[12] it will likewise be possible to alter matters in suspensions of fluid particles by, for example, controlling charge convection. Here we focus attention on the electrical conductivity of an otherwise motionless suspension of fluid particles.

The potentials inside and outside a single drop exposed to a uniform field are

$$\left.\begin{aligned} \hat{\phi}(r,\mu) &= -\frac{3}{2+R}\, rP_1(\mu) + C_1^{(1)} rP_1(\mu) + C_3^{(1)} r^3 P_3(\mu) \\ \text{and} \\ \phi(r,\mu) &+ \left[-r + \frac{R-1}{R+2}\, r^{-2}\right] P_1(\mu) + C_1^{(1)} r^{-2} P_1(\mu) \\ &\qquad + C_3^{(1)} r^{-4} P_3(\mu) \ . \end{aligned}\right\} \qquad (20)$$

Here

$$C_1^{(1)} = \frac{54}{25}\,\frac{1}{1+\kappa}\,\frac{R^2}{(2+R)^4}\left[1 - \frac{\hat{\tau}_r}{\tau_r}\right]^2 \frac{(\varepsilon E_o)^2}{4\pi\eta\sigma}$$

and

$$C_3^{(1)} = \frac{216}{25}\,\frac{1}{1+\kappa}\,\frac{R^2}{(4+3R)(2+R)}\left[1 - \frac{\hat{\tau}_r}{\tau_r}\right]^2 \frac{(\varepsilon E_o)^2}{4\pi\eta\sigma} \ .$$

From Equation 20 we find that charge convection always acts so as to decrease the potential drop across a single particle, leading us to expect that the effective conductivity of a dilute suspension will be below that given in Maxwell's theory (see Reference 12). This turns out to be the case and, using an adaption of Batchelor's formalism[12] so as to account for charge convection, the effective electrical conductivity σ^* is found to be

$$\frac{\sigma^*}{\sigma} = 1 + \left[3\,\frac{R-1}{R+2} - (2R+1)C_1^{(1)}\right]c \ . \qquad (21)$$

Here c denotes the volume fraction of fluid particles. Since $C_1^{(1)}$, which is always positive, depends on the field strength the conductivity is field dependent. Several other situations have been investigated[10] and results will be reported shortly.

CONCLUDING REMARKS

Attention was focused on two of the ways whereby the electrohydrodynamic effects of charge convection alter the behavior of single fluid drops, specifically their shape and rate of translation. In addition it was shown how the bulk conductivity of a suspension of drops can be altered by the same process. The principal limitations on the results arise from the restriction to small deformations, on the one hand, and the simplified models of interfacial behavior on the other.

REFERENCES

1. G.I. Taylor, "Studies in Electrohydrodynamics: I. The Circulation Produced in a Drop by an Electric Field", Proc. Roy. Soc. A291, 159 (1966).

2. R.S. Allan and S.G. Mason, "Particle Behavior in Shear and Electric Fields", Proc. Roy. Soc. A267, 45 (1962).

3. S. Torza, R.G. Cox and S.G. Mason, "Electrohydrodynamic Deformation and Burst of Liquid Drops", Phil. Trans. Roy. Soc. 269, 295 (1971).

4. C. Sozou, "Electrohydrodynamics of a Liquid Drop: The Time-Dependent Problem", Proc. Roy. Soc. A331, 263 (1972).

5. A. Frumkin and B. Levich, Zh. Fiz. Khim. 21, 1335 (1947) as cited in B.G. Levich, "Physicochemical Hydrodynamics", Prentice-Hall, Englewood Cliffs, New Jersey, 1962.

6. S. Levine and R.N. O'Brien, "A Theory of Electrophoresis of Charged Mercury Drops in Aqueous Electrolyte Solution", J. Colloid and Interface Science 43, 616 (1973).

7. A.W. Adamson, "Physical Chemistry of Surfaces", Wiley (Interscience), New York, 1967.

8. C.P. Illingworth, "Flow at Small Reynolds Number" in "Laminar Boundary Layers", L. Rosenhead, Editor, Clarendon Press, Oxford, 1963.

9. L.D. Landau and E.M. Lifshitz, "Electrodynamics of Continuous Media", Addison-Wesley, Reading, Massachusetts, 1960.

10. R.B. Spertell, "On the Roles of Convective and Diffusive Processes in the Electrohydrodynamics of Small Particles and Suspensions", Ph.D. Thesis, Princeton University, 1974.

11. T.D. Taylor and A. Acrivos, "On the Deformation and Drag of a Falling Viscous Drop at Low Reynolds Number", J. Fluid Mech. 18, 466 (1964).

12. G.K. Batchelor, "Transport Properties of Two-Phase Materials with Random Structure", Ann. Rev. Fluid Mech. 6, 227 (1974).

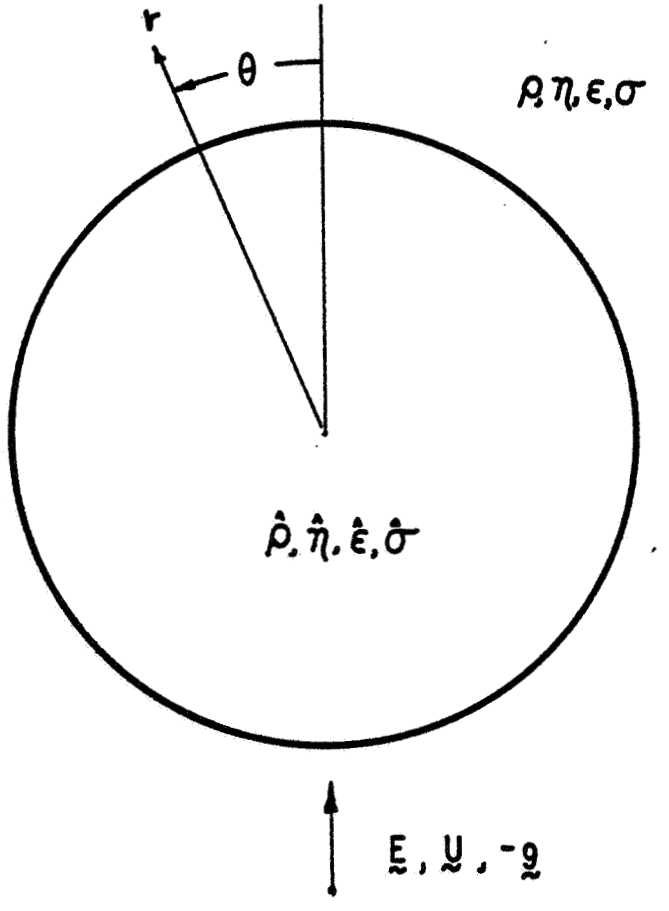

Definition Sketch

FIG. 1

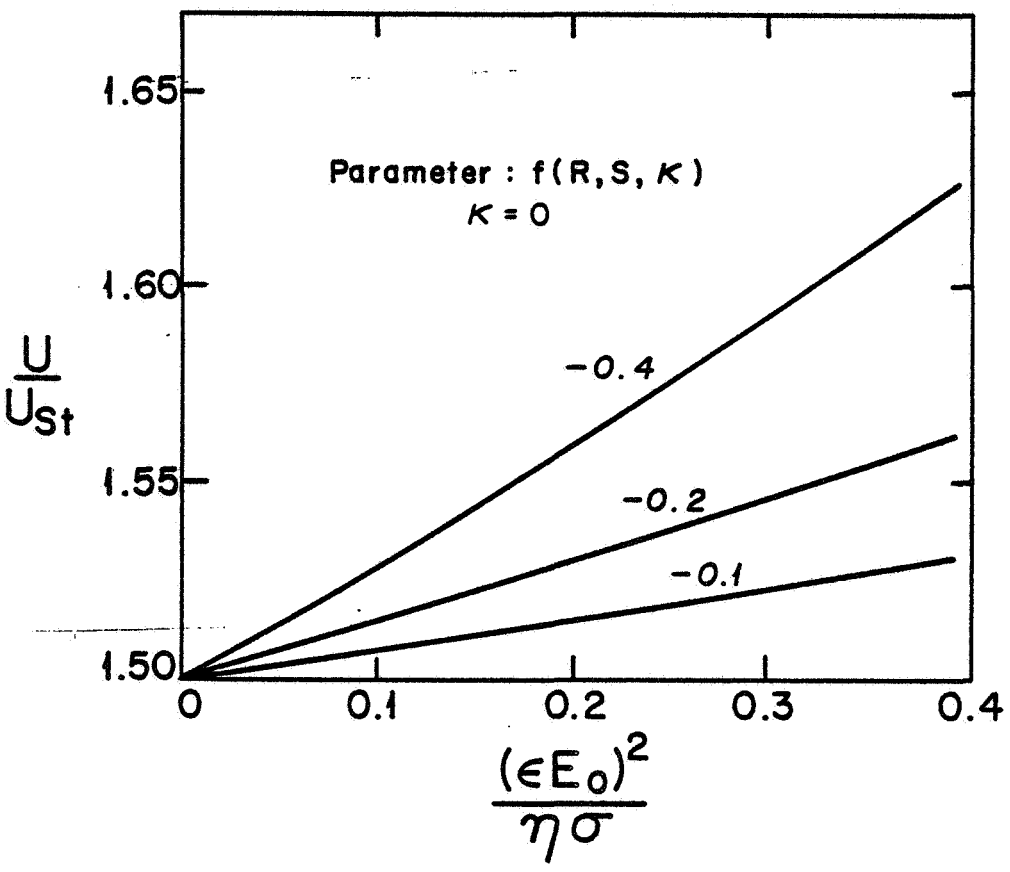

Translation of a Droplet in an External Field

FIG.2

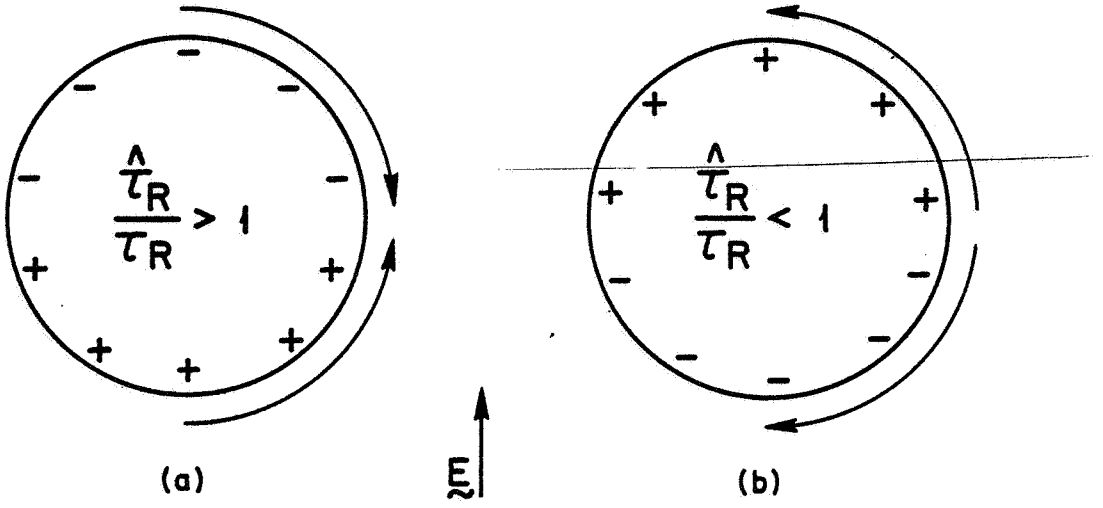

NEUTRALLY BUOYANT CASE

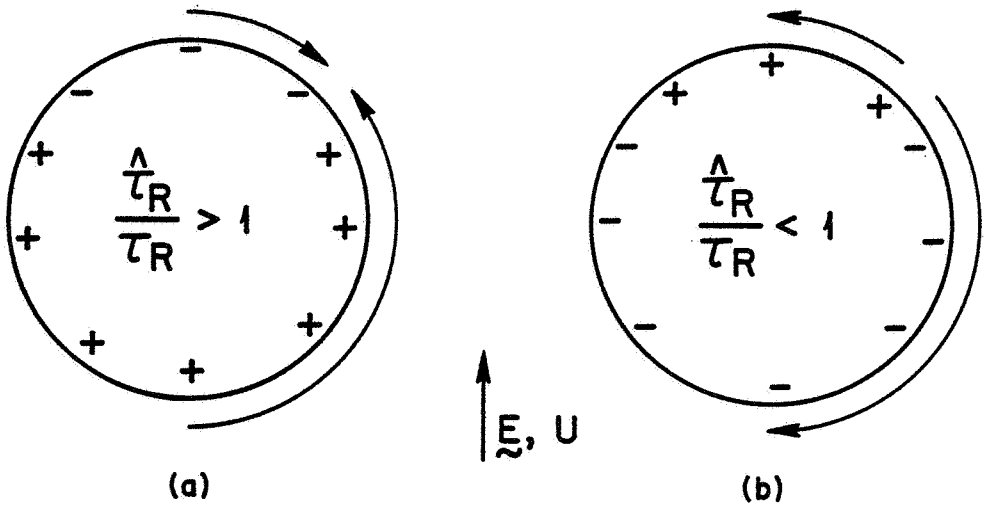

DROPLET SETTLING DUE TO GRAVITY

FIG 3

Qualitative Picture of Effect of External Electric Field on Settling Velocity

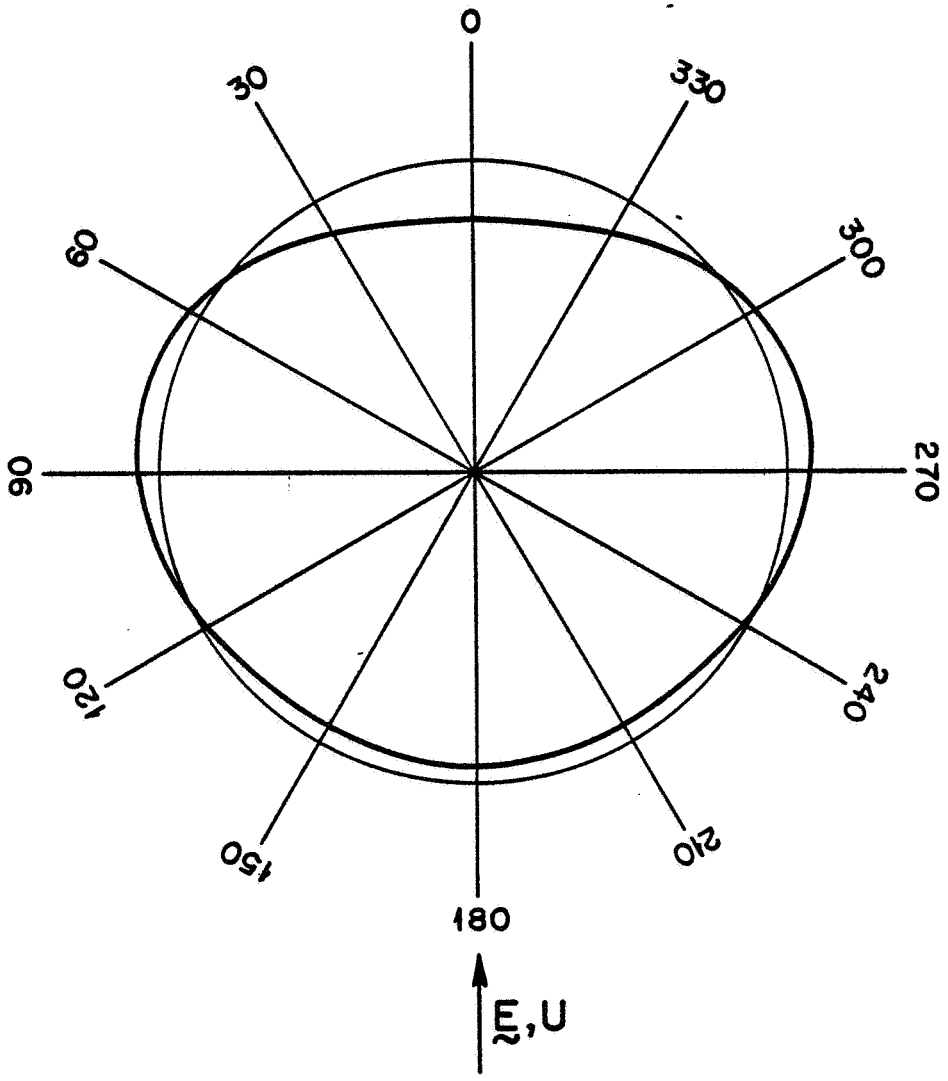

Shape of Droplet (with charge convection)

$K=0.1$ $S=0.25$ $R=1.0$ $\tau_R=1.0$ $\delta=0.2$

$\frac{\rho_\nu U}{\gamma}=0.4$ $\frac{Q_0}{\epsilon E_0}=0.0$

FIG. 4

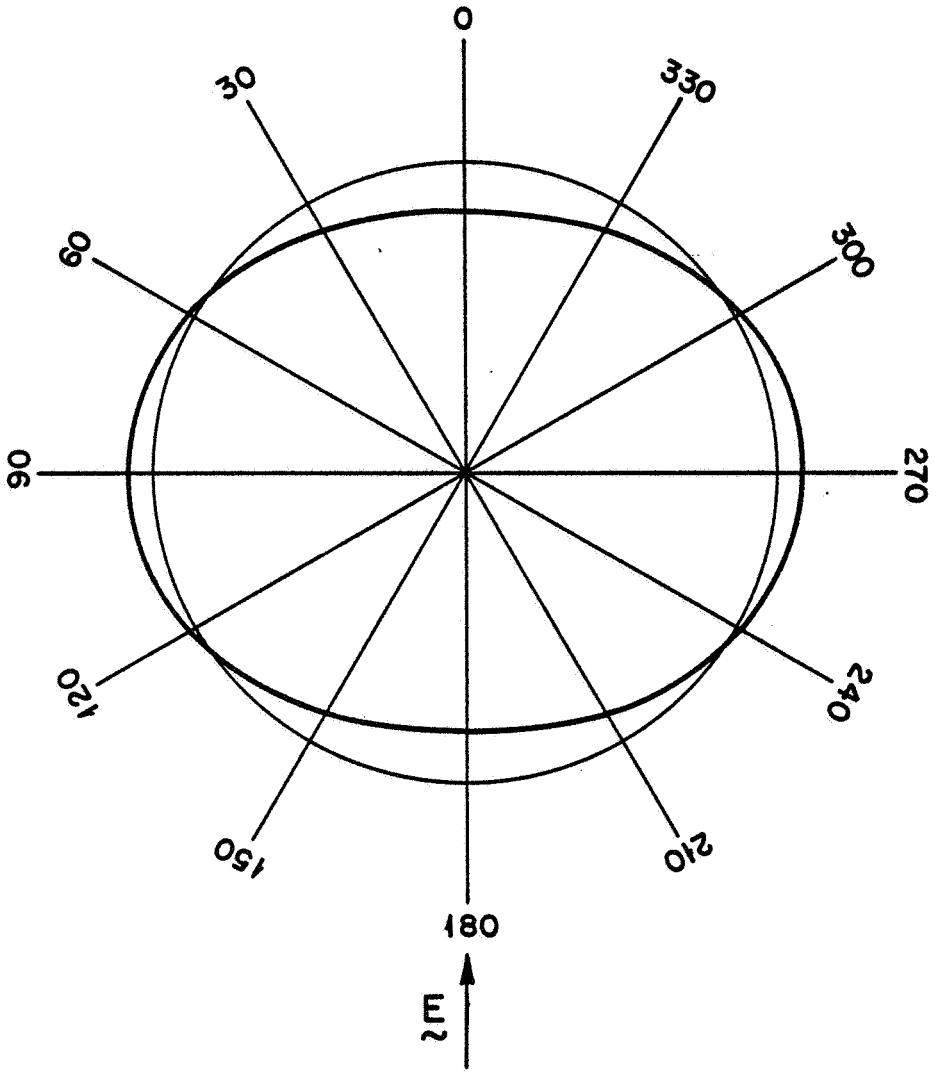

Shape of Droplet (no charge convection)

~~$K=0.1$~~ $S=0.25$ $R=1.0$ $\tau_R=1.0$ $\delta=0.2$

$\frac{\rho V U}{\gamma}=0.4$ $\frac{Q_0}{\epsilon E_0}=0.0$

FIG. 5

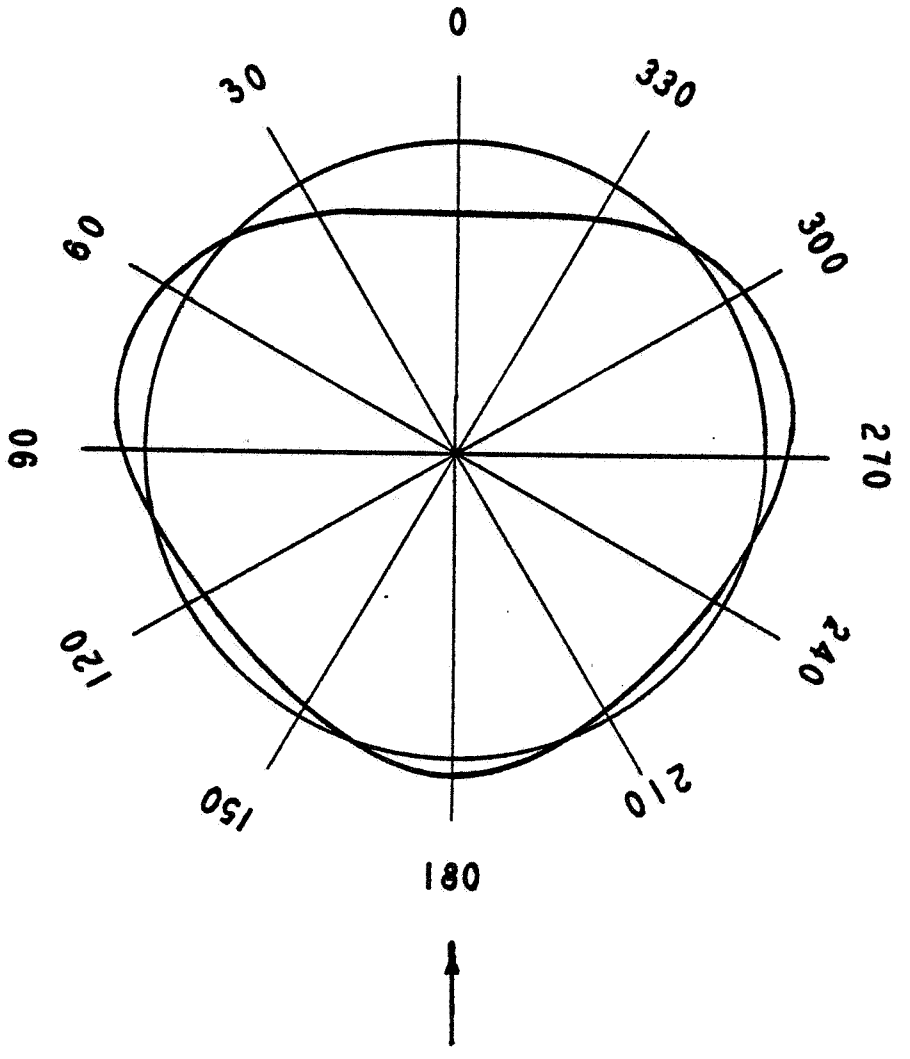

Shape of Droplet (with charge convection)

$K = 0.1$ $S = 0.5$ $R = 0.0$ $\tau_R = 1.0$ $\delta = 0.2$

$\frac{\rho V U}{\gamma} = 0.5$ $\frac{Q_\infty}{\epsilon E_\infty} = 1.0$

FIG. 6

D8

DUALITY BETWEEN SURFACE COUPLED INTERFACIAL WAVES FOR ELECTRICALLY CHARGED AND SELF-GRAVITATING DROPS

Markus Zahn
Department of Electrical Engineering
University of Florida
Gainesville, Florida 32611

I. Introduction

Many investigations of electro-fluid mechanical interactions consider only surface electrical forces, such as is the case of an interface supporting a surface charge distribution or of an interface between different dielectrics [1], [2]. For these cases, complications resulting from nonuniform equilibrium electric field intensities and interfacial curvature occur only for non-planar systems. In contrast, recent work has investigated electrohydrodynamic coupling of perfectly insulating fluids supporting volume space charge distributions [3], [4]. Such analysis is appropriate if the fluid is highly insulating and the dynamics of interest occur over time scales which are short compared with those required for initially injected charges to accumulate appreciably at a fluid surface. For this case, the volume space charge imposes a nonuniform electric field distribution even in planar geometry, which must be taken into account when the interfaces move as the interfacial equilibrium electric fields which act on the interfaces also change.

This work examined the propagation and instability characteristics of small signal electro-fluid mechanical space charge and polarization waves for electrohydrodynamic configurations similar to those of the classic fluid problems of the Rayleigh-Taylor instability for superposed charged planar layers, and of interfacial capillary oscillations of charged liquid cylinders (or jets) and charged spherical drops [5]. A systematic approach was developed to handle multi-interfacial systems of incompressible, inviscid, and perfectly insulating fluids in planar, cylindrical, and spherical geometry through the use of a general set of relations for perturbation field and flow variables on the perturbed surfaces of fluid layers having constant properties [3]. Although the methods developed are valid for any geometry, we limit ourselves here to systems initially in spherical equilibrium.

The analysis showed that the electrohydrodynamic coupling for uniformly charged layers could be represented as a purely surface coupled interaction, even though volume Coulomb forces are present. The pertinent electrical equation necessary in this development is Poisson's equation relating the electrical potential ϕ to the charge density q and permittivity ε (assumed constant)

$$\nabla^2\phi = \frac{-q}{\varepsilon} \tag{1}$$

The electrohydrodynamic coupling occurs through the Coulomb force density

$$\overline{f} = -q\nabla\phi \tag{2}$$

The methodical approach developed can be used for any system whose force density is curl free within a homogeneous layer (q = constant) with the resulting coupling occurring through the interfaces as the force density can then be lumped with the hydrodynamic pressure.

This work will also use this duality with the directly analogous equations to (1) and (2) for self-gravitating systems

$$\nabla^2 V = 4\pi G\rho \tag{3}$$

$$\overline{f} = -\rho\nabla V \tag{4}$$

where V is the gravitational potential, ρ is the mass density and G is the universal gravitational constant ($G \approx 6.67 \times 10^{-11}$ nt-m^2/kg^2), to deduce the dynamics and instability characteristics of spherical self-gravitating geometries [6]. It is a simple matter to obtain results for self-gravitating systems for those electrohydrodynamic problems already solved by making the simple substitutions

$$\phi \to V \; ; \; q \to \rho \; ; \; \varepsilon \to -\frac{1}{4\pi G} \tag{5}$$

However, an important distinction between self-gravitating and electrohydrodynamic systems remains. Whereas the charge density can be either positive or negative, the mass density is always positive. Thus there is always a force of attraction between masses, while because of the minus sign difference in Eqs. (1) and (3), like charges repel and opposite charges attract. Because of the absence of "negative mass" there are no gravitational analogs to polarization effects due to differences in permittivity or electrical shielding due to the presence of electrical conductors. The gravitational constant G is independent of material properties. Thus with the differences between electrical and gravitational systems in mind, we can immediately write down the solutions to those gravitational problems analogous to already solved electrohydrodynamic problems using the conversions of Eq. (5).

In this work, we will derive the general electrohydrodynamic "prototype" relations for a spherical shell and then derive and contrast the dispersion characteristics of perfectly conducting and perfectly insulating charged drops. Using duality we will then immediately write down the analogous solutions for self-gravitating drops.

II. Equations of Motion

1. General Development

No matter the geometry, the general equations of motion for an incompressible, inviscid, and perfectly insulating charged fluid with mass density ρ, velocity $\overline{v}$, pressure p, charge density q, permittivity ϵ, and electric field $\overline{E}$ are

Conservation of momentum -

$$\rho \frac{D\overline{v}}{Dt} + \nabla p = q\overline{E} - \frac{1}{2}\overline{E} \cdot \overline{E}\nabla\epsilon \tag{6}$$

Conservation of mass -

$$\frac{D\rho}{Dt} = 0 \; ; \; \nabla \cdot \overline{v} = 0 \tag{7}$$

Maxwell's equations -

$$\nabla \times \overline{E} = 0 \; ; \; \overline{E} = -\nabla\phi \tag{8}$$

Gauss's Law: $$\nabla \cdot (\epsilon\overline{E}) = q \; ; \; \frac{D\epsilon}{Dt} = 0 \tag{9}$$

Conservation of Charge: $$\frac{Dq}{Dt} = 0 \tag{10}$$

In the prototype layer, examples of which are shown in Fig. (1), the liquid is homogeneous such that the equilibrium properties of mass density ρ_Δ, charge density q_Δ, and dielectric constant ϵ_Δ, are constant. Then all quantities are assumed to have small perturbations from the equilibrium. Subject to the constraint of a homogeneous medium the equilibrium variables must obey the time independent form of (6)-(10) and must satisfy the boundary conditions between regions.

Because the fluid layer is homogeneous the charge density, mass density, and permittivity remain constant in spite of the fluid motion. This is to be expected, because any transport of material into a given region leads to a transport of material which has the same properties as that previously occupying the given region. This statement only applies to those portions of the fluid not swept out by interfacial motions. If a point of interest is adjacent to an interface, an excursion of the interface could result in an abrupt change of properties. However, if surface deflections are considered at a given instant, all properties everywhere between interfaces are uniform.

Denoting perturbation variables with primes, we take the divergence of the linearized form of (6), to yield the set of perturbation equations

$$\nabla^2\phi' = 0$$
$$\nabla^2\pi' = 0 \; ; \; \pi' = p' + q_\Delta\phi' \tag{11}$$

Thus regardless of the geometry, the problem reduces to solutions of

Laplace's equation, both for the perturbation potential and for the modified pressure π'.

2. Generalized Relations For a Spherical Prototype Layer

We consider the lower prototype layer shown in Fig. (1) with the understanding that the picture is a cross section of a spherical shell. In equilibrium the uniformly charged fluid extends over the range $\beta \leq r \leq \alpha$. We denote all variables at the inner interface with a superscript β and all variables at the outer interface with a superscript α. The radial perturbation displacement's are ξ^β and ξ^α. When these displacements are zero the equilibrium distributions are

$$p_o + q_\Delta \Phi_0 = \text{constant}$$

$$\phi_0 = \frac{-q_\Delta r^2}{6\epsilon_\Delta} + \frac{\text{constant}_1}{r} + \text{constant}_2 \tag{12}$$

$$\bar{E} = \left[\frac{q_\Delta r}{3\epsilon_\Delta} + \frac{\text{constant}_1}{r^2}\right]\bar{i}_r$$

All perturbation variables are assumed of the form

$$\pi' = \text{Re}\hat{\pi}(r)P_n^m(\cos\psi)\exp j[\omega t - m\theta] \; ; \; m > 0 \; , \; n > 0 \; , \; m \leq n \tag{13}$$

where $P_n^m(\cos\psi)$ are Legendre functions depending on the azimuthal angle ψ.

Substituting into Eq. (11) yields

$$\hat{\pi}(r) = A_1 r^n + A_2 r^{-(n+1)} \tag{14}$$

where A_1 and A_2 are constants to be determined from the boundary conditions

$$\hat{v}_r(\beta) = j\omega\hat{\xi}^\beta$$

$$\hat{v}_r(\alpha) = j\omega\hat{\xi}^\alpha \tag{15}$$

From Eq. (6) we know, that the perturbation velocity is relating to $\hat{\pi}(r)$ as

$$\hat{v}_r(r) = -\frac{1}{j\omega\rho_\Delta}\frac{d\hat{\pi}}{dr} \tag{16}$$

so that the interfacial displacements are related to the parameters A_1 and A_2 as

$$\begin{bmatrix} \hat{\xi}^{\alpha} \\ \hat{\xi}^{\beta} \end{bmatrix} = \frac{1}{\rho_{\Delta}\omega^2} \begin{bmatrix} n\alpha^{n-1} & -(n+1)\alpha^{-(n+2)} \\ n\beta^{n-1} & -(n+1)\beta^{-(n+2)} \end{bmatrix} \begin{bmatrix} A_1 \\ A_2 \end{bmatrix} \tag{17}$$

For the purposes of our analysis, the inverse relations are needed. Once A_1 and A_2 are determined in terms of $\hat{\xi}^{\alpha}$ and $\hat{\xi}^{\beta}$, substitution into Eq. (14) yields the relationship between the interfacial modified pressures and the interfacial displacements as

$$\begin{bmatrix} \hat{\pi}(\alpha) \\ \hat{\pi}(\beta) \end{bmatrix} = \begin{bmatrix} F(\alpha,\beta) & G(\alpha,\beta) \\ G(\beta,\alpha) & F(\beta,\alpha) \end{bmatrix} \begin{bmatrix} \hat{\xi}^{\alpha} \\ \hat{\xi}^{\beta} \end{bmatrix} \tag{18}$$

where

$$F(x,y) = \frac{\left(\frac{x}{y}\right)^n \frac{x^2}{n} + \left(\frac{y}{x}\right)^n \frac{xy}{n+1}}{\left[\left(\frac{x}{y}\right)^n x - \left(\frac{y}{x}\right)^n y\right]} (\omega^2\rho_{\Delta})$$

$$G(x,y) = \frac{-(2n+1)y^2}{n(n+1)\left[\left(\frac{x}{y}\right)^n x - \left(\frac{y}{x}\right)^n y\right]} (\omega^2\rho_{\Delta}) \tag{19}$$

Note that the analysis implicitly assumes the interfacial displacements to be small as Eqs. (15) and (16) were evaluated at the equilibrium positions (α,β) rather than at the interfaces themselves $(\alpha + \xi^{\alpha}, \beta + \xi^{\beta})$. Fortunately, because the velocity itself is a perturbation, the difference between evaluating it at the interface or at the equilibrium position is second order in the perturbation amplitudes. This illustrates the general approach used in linearized surface deformation problems. The boundary condition at the moving interface is replaced by one at the equilibrium position of the boundary, thus greatly simplifying the analysis.

The analysis is still not complete for as the interfaces deform, in addition to perturbing all variables, the equilibrium quantities acting on the interfaces also change. Thus to compute the total first order change in all variables evaluated at the interface, linear changes of equilibrium quantities must be included. For example, the total linear changes in the pressures are:

$$\hat{p}^{\alpha} = \hat{p}(\alpha) + \left.\frac{dp_0}{dr}\right|_{(r=\alpha)} \hat{\xi}^{\alpha}$$

$$\hat{p}^{\beta} = \hat{p}(\beta) + \left.\frac{dp_0}{dr}\right|_{(r=\beta)} \hat{\xi}_{\beta} \tag{20}$$

Similarly for the potentials

$$\hat{\phi}^{\alpha} = \hat{\phi}(\alpha) + \left.\frac{d\phi_0}{dr}\right|_{(r=\alpha)} \hat{\xi}^{\alpha} = \hat{\phi}(\alpha) - E^{\alpha}\hat{\xi}^{\alpha}$$

$$\hat{\phi}^{\beta} = \hat{\phi}(\beta) + \left.\frac{d\hat{\phi}_0}{dr}\right|_{(r=\beta)} \hat{\xi}^{\beta} = \hat{\phi}(\beta) - E^{\beta}\hat{\xi}^{\beta} \tag{21}$$

Using these definitions we have

$$\hat{p}^{\alpha} \equiv \hat{\pi}(\alpha) - q_{\Delta}\hat{\phi}(\alpha) + E^{\alpha}q_{\Delta}\hat{\xi}^{\alpha}$$

$$\hat{p}^{\beta} \equiv \hat{\pi}(\beta) - q_{\Delta}\hat{\phi}(\beta) + E^{\beta}q_{\Delta}\hat{\xi}^{\beta} \tag{22}$$

$$\varepsilon_{\Delta}\hat{e}_r^{\alpha} = \varepsilon_{\Delta}\,\hat{e}_r(\alpha) + \varepsilon_{\Delta}\left.\frac{dE_0}{dr}\right|_{r=\alpha}\hat{\xi}^{\alpha}$$

$$\varepsilon_{\Delta}\hat{e}_r^{\beta} = \varepsilon_{\Delta}\,\hat{e}_r(\beta) + \varepsilon_{\Delta}\left.\frac{dE_0}{dr}\right|_{r=\beta}\hat{\xi}^{\beta} \tag{23}$$

Then using Eqs. (20) - (22) we obtain the generalized mechanical relations evaluated at the interfaces

$$\begin{bmatrix}\hat{p}^{\alpha}\\ \hat{p}^{\beta}\end{bmatrix} = \begin{bmatrix}F(\alpha,\beta) & G(\alpha,\beta)\\ G(\beta,\alpha) & F(\beta,\alpha)\end{bmatrix}\begin{bmatrix}\hat{\xi}^{\alpha}\\ \hat{\xi}^{\beta}\end{bmatrix} - q_{\Delta}\begin{bmatrix}\hat{\phi}^{\alpha}\\ \hat{\phi}^{\beta}\end{bmatrix} \tag{24}$$

where F and G are given in Eq. (19)

Similar operations are performed in the solutions of Laplace's equation for the perturbation potential $\hat{\phi}(r)$ to yield the electrical relations at the interfaces

$$\begin{bmatrix}\varepsilon_{\Delta}\hat{e}_r^{\alpha}\\ \varepsilon_{\Delta}\hat{e}_r^{\beta}\end{bmatrix} = \varepsilon_{\Delta}\begin{bmatrix}B(\alpha,\beta) & C(\alpha,\beta)\\ C(\beta,\alpha) & B(\beta,\alpha)\end{bmatrix}\begin{bmatrix}\hat{\phi}^{\alpha} + E^{\alpha}\hat{\xi}^{\alpha}\\ \hat{\phi}^{\beta} + E^{\beta}\hat{\xi}^{\beta}\end{bmatrix} + \varepsilon_{\Delta}\begin{bmatrix}\left.\frac{dE_0}{dr}\right|_{r=\alpha}\hat{\xi}^{\alpha}\\ \left.\frac{dE_0}{dr}\right|_{r=\beta}\hat{\xi}^{\beta}\end{bmatrix} \tag{25}$$

where

$$B(x,y) = \frac{\left[n\left(\frac{x}{y}\right)^{n} + (n+1)\left(\frac{y}{x}\right)^{n+1}\right]}{\left[\left(\frac{y}{x}\right)^{n} y - \left(\frac{x}{y}\right)^{n} x\right]}$$

$$C(x,y) = -\frac{(2n+1)\left(\frac{y}{x}\right)}{\left[\left(\frac{y}{x}\right)^{n} y - \left(\frac{x}{y}\right)^{n} x\right]} \tag{26}$$

The general relations of (24) and (25) greatly simplify in various limits. As the inner radius goes to zero ($\beta \to 0$), so that the shell becomes a drop, the terminal relations reduce to

$$\lim_{\beta \to 0} \hat{p}^{\alpha} = \frac{\omega^2 \rho_{\Delta\alpha}}{n}\hat{\xi}^{\alpha} - q_{\Delta}\hat{\phi}^{\alpha}$$

$$\lim_{\beta \to 0} \varepsilon_{\Delta}\hat{e}_r^{\alpha} = -\frac{\varepsilon_{\Delta} n}{\alpha}\left(\hat{\phi}^{\alpha} + E^{\alpha}\hat{\xi}^{\alpha}\right) + \varepsilon_{\Delta}\left.\frac{dE_0}{dr}\right|_{r=\alpha}\hat{\xi}^{\alpha} \tag{27}$$

As the outer radius becomes very large, ($\alpha \to \infty$), the terminal relations become

$$\lim_{\alpha \to \infty} \hat{p}^{\beta} = \frac{-\omega^2 \rho_{\Delta\beta}}{(n+1)}\hat{\xi}^{\beta} - q_{\Delta}\hat{\phi}^{\beta}$$

$$\lim_{\alpha \to \infty} \varepsilon_{\Delta}\hat{e}_r^{\beta} = \frac{\varepsilon_{\Delta}(n+1)}{\beta}\left(\hat{\phi}^{\beta} + E^{\beta}\hat{\xi}^{\beta}\right) + \varepsilon_{\Delta}\left.\frac{dE_0}{dr}\right|_{r=\beta}\hat{\xi}^{\beta} \tag{28}$$

Equations (24) and (25) are useful because they relate the interfacial variables of pressure, displacement, electrical potential and electrical displacement, which appear in interfacial boundary conditions. The boundary conditions for all cases include mass and electric potential continuity, the second condition being equivalent to the continuity of the tangential component of electric field, as well as an interfacial force balance. For perfectly conducting interfaces, the perturbation potential must be zero but the surface charge imposes a surface force density. Because there are no electric fields inside the perfectly conducting fluids, there are no polarization effects. In contrast, perfectly insulating fluids with volume charge have nonzero interfacial potential and although free charge can make no contribution to an interfacial surface force density, there is a surface polarization force if the permittivity of the fluid and its surroundings differ. For non-perfect conductors (including perfect insulators) no surface charge can be allowed on

any interface for an inviscid analysis to be meaningful, as electrical shear stresses would accompany such a surface charge density, and our model would then necessarily have to include viscosity (or some other mechanism) to balance this shear stress [7], [8]. This requires the normal component of electric displacement to be continuous across an interface for non-perfect conductors. An inviscid formulation is allowed only if the interface has no surface charge or if the interface is perfectly conducting, as then the electric field terminates perpendicular to the interface, resulting in no electrical shear force. However, the same systematic techniques have been applied to a viscous prototype layer in planar geometry so that these limitations may be removed [9]. In general, considering viscous fluids greatly increases the mathematical complexity of the analysis but yet has no effect on the conditions for instability [10].

III. Stability and Dynamics of Charged Spherical Drops

The modes of oscillation and instability of charged, initially spherical drops are obtained for small perturbations by using the generalized relations of (24) and (25). Rayleigh's limit determines the maximum amount of charge distributed around the surface of an isolated perfectly conducting drop for it to be stable [11]. The isolated uniformly charged, perfectly insulating drop has historical significance through the liquid drop model for fission of the nucleus proposed by Bohr and Wheeler [12]. In this section we wish to generalize both these classic problems by immersing the charged spherical drops within a uniformly charged region. Figure 2 describes the geometry with the understanding that the picture is the cross section of a spherical system.

In spherical geometry, all perturbations due to small signal interfacial motions are assumed of the form

$$\xi = \mathrm{Re}\ \hat{\xi}\ \exp[j(\omega t - m\theta)]P_n^m(\cos\psi)\ ;\ m > 0\ ,\ n > 0\ ,\ m \leq n \tag{29}$$

For spherical drops we only need to know these relations in the two limits where the inner radius tends to zero, $\beta \to 0$, and when the outer radius gets very large, $\alpha \to \infty$, which are described by Eqs. (27) and (28).

1. Perfectly Conducting Drop With Surface Charge Within a Uniformly Charged Region

We first consider a configuration similar to that in Fig. (2) with a perfectly conducting spherical drop of radius R, mass density ρ_1 and surface tension γ with uniformly distributed surface charge density σ_f immersed within a perfectly insulating charged fluid of infinite extent with charge density q_2 and mass density ρ_2. The equilibrium electric field distribution is

$$E_r = \frac{\sigma_f R^2}{\varepsilon_2 r^2} + \frac{q_2(r - R^3/r^2)}{3\varepsilon_2} \qquad r > R \tag{30}$$

so that

$$E_1 = 0\ ,\ E_2 = \frac{\sigma_f}{\varepsilon_2}\ ,\ \left.\frac{dE_2}{dr}\right|_{r=R} = \frac{-2\sigma_f}{\varepsilon_2 R} + \frac{q_2}{\varepsilon_2} \tag{31}$$

Because the drop is perfectly conducting there are no electric fields inside ($E_1 = 0$). The perturbation interfacial boundary conditions are

$$\begin{aligned} &\hat{\xi}_1 = \hat{\xi}_2 \equiv \hat{\xi}\ ,\ \hat{\phi}_1 = \hat{\phi}_2 \equiv 0 \\ &\hat{p}_1 - \hat{p}_2 + \varepsilon_2 E_2 \hat{e}_{r2} - \left(\frac{\gamma}{R^2}\right)(n-1)(n+2)\hat{\xi} = 0 \end{aligned} \tag{32}$$

From Eqs. (27) and (28) we obtain

$$\hat{p}_1 = \rho_1 \omega^2 R\hat{\xi}/n$$

$$\hat{p}_2 = -\rho_2 \omega^2 R\hat{\xi}/(n+1) \tag{33}$$

$$\varepsilon_2 \hat{e}_{r2} = \varepsilon_2 E_2 (n+1)\hat{\xi}/R + \varepsilon_2 \left.\frac{dE_2}{dr}\right|_{r=R} \hat{\xi}$$

Substitution of Eq. (33) into Eq. (32) yields the dispersion equation as

$$\left(\frac{\omega^2 R^3}{\gamma}\right)\left(\frac{\rho_1}{n} + \frac{\rho_2}{(n+1)}\right) = (n-1)(n+2) - \left(\frac{\sigma_f^2 R}{\varepsilon_2 \gamma}\right)\left(n - 1 + \frac{q_2 R}{\sigma_f}\right) \tag{34}$$

We see that the self-field term proportional to σ_f^2 due to the interaction of the surface charge with its own field is always destabilizing, while the imposed field term proportional to $q_2\sigma_f$ due to the interaction of the space charge q_2 with the field due to σ_f can be stabilizing if q_2 and σ_f are of opposite sign. If $\sigma_f = 0$, there is no electromechanical coupling.

We examine (34) in Rayleigh's limit where there is no space charge in the outer region ($q_2 = 0$), so that Eq. (34) can be written as

$$\left(\frac{\omega^2 R^3}{\gamma}\right)\left(\frac{\rho_1}{n} + \frac{\rho_2}{(n+1)}\right) = (n-1)\left(n + 2 - \frac{\sigma_f^2 R}{\varepsilon_2 \gamma}\right) \tag{35}$$

We see that the $n = 0$ mode is not allowed if $\rho_1 \neq 0$ due to the incompressibility of the drop, and that the $n = 1$ mode is neutrally stable. As σ_f is increased, the first mode to become unstable is $n = 2$ with critical total charge $Q_T (Q_T = 4\pi R^2 \sigma_f)$

$$Q_T = 8\pi R(\varepsilon_2 \gamma R)^{1/2} \tag{36}$$

However if the drop has negligible density so that $\rho_1 = 0$, which is the case of a bubble within an infinite fluid with surface charge on the bubble fluid interface then the $n = o$ solution is allowed. In the absence of electrical forces, surface tension makes this case unstable by acting to collapse the bubble. However, with surface charge present, Coulombic repulsion could stabilize the system if

$$\sigma_f^2 R/\varepsilon_2 \gamma > 2 \tag{37}$$

For finite q_2, the $n = 1$ mode will be stable only if $q_2\sigma_f < 0$.

2. Perfectly Insulating Drop with Volume Charge Within a Uniformly Charged Region

We now consider a perfectly insulating spherical drop supporting a constant volume charge distribution within a uniformly charged region, as in Fig. (2). We include the possibility of having a point charge of value Q at r = o, and give the drop a dielectric constant different from the surrounding region to include polarization forces.

The equilibrium electric field distribution is

$$E_r = \begin{cases} \dfrac{Q}{4\pi\varepsilon_1 r^2} + \dfrac{q_1 r}{3\varepsilon_1} & r < R \\ \dfrac{Q}{4\pi\varepsilon_2 r^2} + \dfrac{(q_1 - q_2)R^3}{3\varepsilon_2 r^2} + \dfrac{q_2 r}{3\varepsilon_2} & r > R \end{cases} \tag{38}$$

which yields for the interfacial fields and field gradients

$$E_1 = \frac{Q}{4\pi\varepsilon_1 R^2} + \frac{q_1 R}{3\varepsilon_1} \; ; \; \left.\frac{dE_1}{dr}\right|_{r=R} = \frac{-Q}{2\pi\varepsilon_1 R^3} + \frac{q_1}{3\varepsilon_1}$$

$$E_2 = \frac{Q}{4\pi\varepsilon_2 R^2} + \frac{q_1 R}{3\varepsilon_2} \; ; \; \left.\frac{dE_2}{dr}\right|_{r=R} = \frac{-Q}{2\pi\varepsilon_2 R^3} + \frac{2q_1}{3\varepsilon_2} + \frac{q_2}{\varepsilon_2} \tag{39}$$

The interfacial boundary conditions result in the relations

$$\hat{\xi}_1 = \hat{\xi}_2 \equiv \hat{\xi} \; , \; \hat{\phi}_1 = \hat{\phi}_2 \equiv \hat{\phi}$$

$$\varepsilon_1 \hat{e}_{r1} = \varepsilon_2 \hat{e}_{r2} \tag{40}$$

$$\hat{p}_1 - \hat{p}_2 + \varepsilon_2 E_2 \hat{e}_{r2} - \varepsilon_1 E_1 \hat{e}_{r1} - \left(\frac{\gamma}{R^2}\right)(n-1)(n+2)\hat{\xi} = 0$$

From the general relations of Eqs. (27) and (28) we obtain

$$\hat{p}_1 = \rho_1 \omega^2 R \hat{\xi}/n - q_1 \hat{\phi}$$

$$\hat{p}_2 = -\rho_2 \omega^2 R \hat{\xi}/(n+1) - q_2 \hat{\phi} \tag{41}$$

$$\varepsilon_1 \hat{e}_{r1} = -(\varepsilon_1 n/R)(\hat{\phi} + E_1\hat{\xi}) + \varepsilon_1 \left.\frac{dE_1}{dr}\right|_{r=R} \hat{\xi}$$

$$\varepsilon_2 \hat{e}_{r2} = \frac{\varepsilon_2(n+1)}{R}(\hat{\phi} + E_2\hat{\xi}) + \varepsilon_2 \left.\frac{dE_2}{dr}\right|_{r=R} \hat{\xi} \qquad (42)$$

Substitution of Eqs. (41) and (42) into Eq. (40) yields the formidable dispersion relation

$$\left(\frac{\omega^2 R^3}{\gamma}\right)\left(\frac{\rho_1}{n} + \frac{\rho_2}{(n+1)}\right) = (n-1)(n+2)$$

$$+ \frac{(q_1 - q_2)R^3}{\gamma[\varepsilon_2 + (\varepsilon_1 + \varepsilon_2)n]}\,[q_1 - q_2 - (2n+1)\varepsilon_2 E_2/R] \qquad (43)$$

$$+ \frac{(\varepsilon_2 - \varepsilon_1)R^2 E_2}{\gamma[\varepsilon_2 + (\varepsilon_1 + \varepsilon_2)n]}\left[\frac{q_1\varepsilon_2(n+1)}{\varepsilon_1} + q_2 n - \frac{E_1}{R}\left[2[\varepsilon_2 + (\varepsilon_1 + \varepsilon_2)n] + n(n+1)(\varepsilon_2 - \varepsilon_1)\right]\right]$$

In Eq. (43), the last term on the right represents the polarization surface force due to the difference in permittivities and the fields from the space and point charges. The other electric term represents Coulomb forces acting even in the absence of a polarization. For simplicity, we examine Eq. (43) in various limits.

BOHR LIMIT ($\varepsilon_1 = \varepsilon_2 \equiv \varepsilon$, $q_2 = 0$, $Q = 0$).

In the liquid drop model of fission of the nucleus, Bohr and Wheeler considered an isolated uniformly charged spherical drop under surface tension [12]. Sufficient charging of the drop results in instability, which in the context of the nucleus amounts to nuclear fission. Under these conditions Eq. (43) can be reduced to

$$\left(\frac{\omega^2 R^3}{\gamma}\right)\left(\frac{\rho_1}{n} + \frac{\rho_2}{(n+1)}\right) = \frac{(n-1)}{(2n+1)}\left[(2n+1)(n+2) - \frac{2q_1^2 R^3}{3\varepsilon\gamma}\right] \qquad (44)$$

The $n = o$ mode is not allowed for finite ρ_1 due to the drop incompressibility. The $n = 1$ mode is neutrally stable, while the first mode to become unstable as q_1 is increased occurs for $n = 2$ with total charge Q_T($Q_T = 4\pi R^3 q_1/3$)

$$Q_T = 8\pi R(5\varepsilon\gamma R/6)^{1/2} \qquad (45)$$

We see from Eq. (45) compared to Eq. (36) that a perfectly conducting drop could support slightly more total charge before becoming unstable than the

perfectly insulating drop.

NO POLARIZATION EFFECTS ($\varepsilon_1 = \varepsilon_2 \equiv \varepsilon$)

There are no polarization forces if the dielectric constants of the two regions are the same. Generalizing the Bohr limit by allowing finite q_2 and Q simplifies Eq. (43) to

$$\omega^2\left(\frac{\rho_1}{n} + \frac{\rho_2}{(n+1)}\right) = \left(\frac{\gamma}{R^3}\right)(n-1)(n+2) + \frac{(q_1 - q_2)^2}{\varepsilon(2n+1)} - \frac{(q_1 - q_2)}{\varepsilon}\left(\frac{q_1}{3} + \frac{Q}{4\pi R^3}\right) \tag{46}$$

The second term on the right of Eq. (46) is a self-field term and is always stabilizing while the last term is an imposed field term and can be either stabilizing or destabilizing depending on the relative charge polarities. A sufficient condition for stability is for the last term in (46) to be negative.

NEUTRAL DROP ($q_1 4\pi R^3/3 + Q = 0$)

If the total charge within the spherical drop is zero, the equilibrium interfacial electric field is also zero. Under this condition even if the permittivities of the two regions are different, there would be no polarization effects as the interfacial electric field is zero. However, due to the electric field gradient, there is still an electromechanical coupling so that Eq. (46) is still appropriate with the last term being zero. This system is stabilized by the space charge. In fact, for the case of a bubble where $\rho_1 = 0$ the destabilizing nature of surface tension for the n = o mode can be opposed so that the system becomes stable if the difference of charge densities are of sufficient magnitude such that

$$(q_1 - q_2)^2 \geq 2\varepsilon\gamma/R^3 \tag{47}$$

UNIFORM SPACE CHARGE DENSITY THROUGHOUT ($q_1 = q_2$)

The interplay of the polarizability and the space charge is demonstrated by considering a case in which the respective space charges are equal ($q_1 = q_2$). Then the second term on the right of Eq. (43) drops out. If the relative permittivities were also equal, there would be no electromechanical effect.

IV. Gravitational Stability of Spherical Drops

For the space charge analysis, the mass density only contributed through inertial terms. For the self-gravitating counterpart, the mass density will also contribute via the force law of Eq. (4). We now consider the gravitational analog to Fig. 2 where a fluid sphere with mass density ρ_1 is immersed within an infinite medium of mass density ρ_2. A point mass M is at the origin r = 0. The equilibrium gravitational field in the negative radial direction at the interface is

$$g = \frac{MG}{R^2} + \frac{4\pi G\rho_1 R}{3} \tag{48}$$

We can use the results obtained for a perfectly insulating drop with volume charge within a uniformly charged region by using the dual relations of Eq. (5), substituted into Eq. (43) with $\varepsilon_1 = \varepsilon_2$ to obtain the self-gravitating dispersion relation

$$\omega^2\left(\frac{\rho_1}{n} + \frac{\rho_2}{(n+1)}\right) = \left(\frac{\gamma}{R^3}\right)(n-1)(n+2) - \frac{4\pi G(\rho_1 - \rho_2)^2}{(2n+1)} + 4\pi G(\rho_1 - \rho_2)\left(\frac{\rho_1}{3} + \frac{M}{4\pi R^3}\right) \tag{49}$$

KELVIN'S MODES

Kelvin first considered this problem in the limit, M = 0, $\rho_2 = 0$, and $\gamma = 0$ [13]. Then Eq. (49) describes the oscillation frequencies of an inviscid liquid globe under its own gravitational field.

$$\omega^2 = \frac{8\pi G\rho_1 n(n-1)}{3(2n+1)} \tag{50}$$

HOLLOW DROP

In the other extreme, a spherical void (M = 0, $\rho_1 = 0$) within a large medium is always unstable for n = 0 and n = 1 as the right hand side of Eq. (49) is always negative and thus unstable. Unlike the space charge dual, self-gravitating forces can never stabilize a spherical bubble.

V. Concluding Remarks

Because the perturbation electrical and gravitational force was curl free within a homogeneous layer, the broad class of interactions involving liquids with discrete stratifications in mass density, charge density, and permittivity are representable as surface coupled interactions. The transfer relations derived are useful since they relate interfacial variables that appear in the boundary conditions. The techniques developed here may also be used for other perturbation volume forces which are curl free within a homogeneous layer, or for surface forces which only act at an interface. Any system which is described by Poisson's equation and a Coulomb force law can be immediately solved using similar dual relations as in Eq. (5).

Since the fluids are modeled as inviscid, force equilibrium at the interface required only a normal stress balance. No electrical shear stresses are allowed because of the absence of viscous shear forces to oppose the electrical forces. A more general analysis which would allow electrical shear forces must include viscosity. Then the mechanical terminal relations must include relations between the shear and normal forces and the shear and normal interfacial displacements. Force equilibrium at the interface requires both a normal and shear stress balance. This results in the mechanical transfer relations becoming 4 x 4 matrices, rather than the simpler 2 x 2 matrices considered here, greatly increasing the algebraic complexity.

ACKNOWLEDGMENT

This work was supported by the National Science Foundation under Grant No. GK-37594.

REFERENCES

1. J. R. Melcher, "Field Coupled Surface Waves," M.I.T. Press, Cambridge, Mass. (1963).
2. E. B. Devitt and J. R. Melcher, "Surface Electrohydrodynamics with High Frequency Fields," Phys. Fluids 8, No. 6 (June 1965).
3. M. Zahn and J. R. Melcher, "Space Charge Dynamics of Liquids," Phys. Fluids 15, No. 7 (July 1972).
4. M. Zahn, "Dynamics of Stratified Liquids in the Presence of Space Charge," Phys. Fluids 15, No. 8 (August 1972).
5. M. Zahn, "Space Charge Coupled Interfacial Waves," Phys. Fluids 17, No. 2 (February 1974).
6. M. Zahn, "Surface Coupled Interfacial Waves for Self-Gravitating Systems," Phys. Fluids, (to be published).
7. J. R. Melcher and W. J. Schwarz, "Interfacial Relaxation Overstability In a Tangential Electric Field," Phys. Fluids 11, No. 12 (December 1968).
8. J. R. Melcher and C. V. Smith, Jr., "Electrohydrodynamic Charge Relaxation and Interfacial Perpendicular-Field Instability," Phys. Fluids 12, No. 4 (April 1969).
9. M. Zahn and R. J. Sojka, "Space Charge Dynamics of Viscous Liquids," Phys. Fluids, (to be published).
10. R. J. Turnbull and J. R. Melcher, "Electrohydrodynamic Rayleigh-Taylor Bulk Instability," Phys. Fluids 12, No. 6 (June 1969).
11. Lord Rayleigh, "On the Equilibrium of Liquid Conducting Masses Charged with Electricity," Phil. Mag. 14, p. 184 (1882).
12. N. Bohr and J. A. Wheeler, "The Mechanism of Nuclear Fission," Phys. Rev. 56, p. 426 (Sept. 1939).
13. S. Chandrasekhar, "Hydrodynamic and Hydromagnetic Stability," Clarendon Press, Oxford (1961).

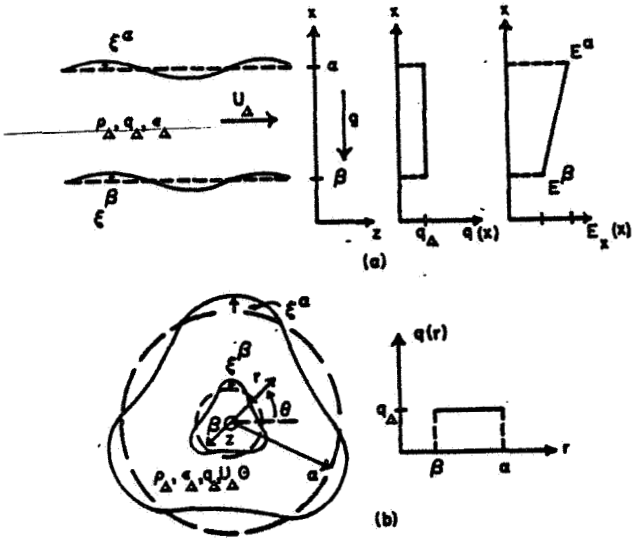

Fig. 1 Prototype layers of incompressible, inviscid, perfectly insulating fluids, supporting uniformly distributed charge densities, (a) planar geometry, (b) cylindrical or spherical geometry.

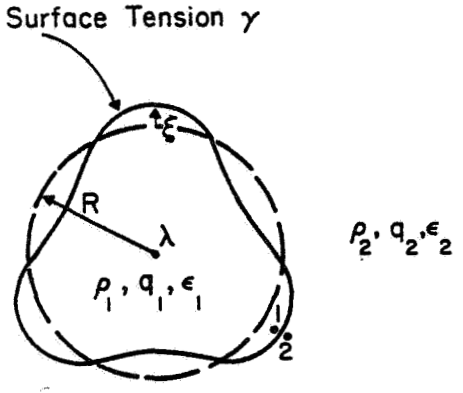

Fig. 2. Cross section of an initially spherical drop of radius R with charge density q_1, mass density ρ_1 and permittivity ϵ_1 placed within an infinite medium with charge density q_2, mass density ρ_2 and permittivity ϵ_2. A point charge ($Q = \lambda$) is at r = 0.

D9

THE DYNAMICS OF COLLIDING AND OSCILLATING DROPS*

Carol Travis Alonso
Lawrence Berkeley Laboratory, Berkeley, California

INTRODUCTION

In order to study the oscillations, fusions, and fissions of liquid drops, we are developing a hydrodynamic computer code which simulates these processes for viscous, incompressible drops endowed with a body charge and surface tension. Although our interest lies in the field of nuclear hydrodynamics, the application of this code to classical liquid drops is general. Our code traces the dynamic evolution of an axially symmetric system as a function of time. It utilizes a free surface that requires no parameterization and its velocity field can be rotational or irrotational as required. When completed, the present version will yield the following information about the classical dynamics of liquid drops: (a) free surface shape and energy, (b) free-flow velocity field, (c) kinetic energy distribution, (d) Coulomb energy, (e) free-flow moment of inertia, and (f) free-flow electric quadrupole moment. These quantities can be studied as a function of viscosity, initial shape, and energy.

We present here some studies of the oscillations of charged and neutral drops as a function of initial shape, charge, and viscosity. These studies are not restricted to small amplitudes. We also present some preliminary simulations of fissions and fusions of viscous charged drops, with some comments about the possible role of nuclear viscosity in the creation of "superheavy" elements in heavy ion accelerator reactions.

NUCLEAR HYDRODYNAMICS

The general problem of liquid drop dynamics, important as it is to many scientific investigations, has never been fully solved due to the complexity of the hydrodynamic equations involved. Even the linear problem of viscous small amplitude oscillations is described by complex Bessel functions (1). Large amplitude oscillations and distortions, including the fission and fusion of liquid drops, cannot be described analytically in complete detail.

In the particular field of nuclear hydrodynamics, it has become of critical importance to be able to follow in some way the dynamic path of those large amplitude motions leading to nuclear fusion and fission. Some studies of this problem using parameterized surfaces and irrotational flow have been carried out by Sierk and Nix (2). Other efforts have concentrated on solutions of Hamilton's equations using parameterized shapes (3). Disruptive processes such as fusion have not been studied dynamically because they do not lend themselves easily to shape parameterization.

While the atomic nucleus usually displays a quantum mechanical nature, the nuclei of the heavier elements, which contain hundreds of nucleons,

*Work performed under the auspices of the United States Atomic Energy Commission.

begin to show properties that are characteristic of classical fluid flow. The best example of this is the success of the celebrated liquid drop model of nuclear fission proposed by Bohr and Wheeler (4). Another example is that the moment of inertia of rotating nuclei lies somewhere between that of a rigid body and of a drop with irrotational flow. At low temperatures the nuclear liquid can become a superfluid and a classical description is probably not meaningful. However most accelerator reactions between nuclei take place at elevated temperatures where classical behavior, if not well established, becomes a reasonable assumption, at least for the heavier nuclei. In Figure 1 we have attempted to show where the physics of heavy nuclei fits in the transition from the classical to the quantum mechanical regimes. The transition point is taken to be at the temperature where the de Broglie wavelength equals the inter-nucleon spacing.

In the spirit of this classical assumption we have undertaken to simulate by computer methods the dynamics of colliding and oscillating viscous liquid drops in a very general way. The only previous attempt at such simulations was performed by Hill and Wheeler (5) for inviscid, irrotational fissions at a time when computers were not fast enough to handle the general problem. The overriding interest today is in the problem of fusing two charged liquid drops to make a large composite drop. This is the basic way in which the new transuranic elements are being produced: two nuclei are made to collide in an accelerator and the fused compound system becomes the new element.

Recent theoretical predictions by Nilsson and others (6) of the possibility of using fusion reactions such as this to produce the so-called "superheavy" elements with atomic number around 114 have not been substantiated by experiments (7). We now suspect that this disparity may be due to a finite nuclear viscosity at elevated temperatures. The effect of this viscosity would be to convert the energy of the forward motion of the fusion process into frictional heating, making fusion impossible due to the repulsive Coulomb forces that are always ready to pull distorted shapes apart.

Therefore we are developing a computer code, called SQUISH, that we hope will have sufficient accuracy to predict the correct bulk motion of charged viscous liquid drops with axial symmetry. This program is quite general. It can be used for any liquid drops, nuclear or otherwise, that are subject to a calculable external force. The code is still in development and although we are presently studying fusions the results are still preliminary, so we present in this paper mostly some simulations of the dynamics of large-amplitude motions of single drops.

THE COMPUTER CODE

Without going into details, we describe in Figure 2 how the code works. SQUISH is an example of the two-dimensional hydrodynamic finite-difference codes that are becoming very popular because of the increased capability of modern computers to handle them. SQUISH uses a basic hydrodynamic technique developed at Los Alamos by Harlow and Amsden (8) for low Reynolds number flow, the SMAC or Simplified Marker And Cell method. In this scheme, the drop is contained in a fixed Eulerian mesh and movable Lagrangian particles are injected

into the cells of the mesh. A special set of surface markers keeps track of the free surface. Typical full and surface cells are shown in the insets. The forces and pressures are calculated at the centers of the cells, and velocities are deposited on the cell boundaries. The computer is then instructed to move the particles according to Newton's laws, which in this case become the Navier-Stokes equation for a viscous and incompressible fluid. In our case the forces include surface tension and Coulomb forces. The method of Foote (9) has been used for the application of surface tension. The particles are moved by applying these equations in finite-difference form, and the whole system is adjusted to conserve volume according to $\nabla \cdot U = 0$. The program, after moving the particles, increments the time, recalculates the new forces and pressures, and proceeds in this cyclical manner to follow the dynamical paths of all the particles that make up the drop.

The advantages of this method are that it contains (a) a free surface that requires no parameterization, (b) a free-flow velocity calculation that can be rotational or irrotational, and (c) provisions for including any calculable external force, or any bulk property such as viscosity or elasticity. The limitations are that (a) the code must be axially symmetric if it is not to become extremely costly to run, (b) some accuracy must be surrendered by the choice of a reasonably large mesh size, and (c) the physics is purely classical, although it may be possible to simulate some quantum mechanical behavior in a pseudo-classical manner.

At present SQUISH is capable of calculating at any time step the following properties of a system of viscous charged liquid drops: (a) free surface shape and energy, (b) free-flow velocity field (rotational or irrotational), (c) kinetic energy distribution, (d) center of mass kinetic energy, position, and moments, (e) Coulomb energy, (f) free-flow moment of inertia, and (g) free-flow electric quadrupole moment. These quantities can be studied as a function of viscosity, initial shape, and initial energy. It should be pointed out that not all of these quantities will have analytical accuracy. The size of finite difference mesh employed sets a limit on the accuracy of the free surface shape, upon which most of these quantities depend. Computer simulations of this sort should be regarded as quasi-analytical experiments with definite errors associated with the variables. However the bulk motion should be correct, and the accuracy can be made as good as necessary, should the need merit the expense.

SIMULATIONS OF DROP DYNAMICS

As an illustration of the versatility of such a code, let us examine the motion of a particular drop as we change its size, viscosity, and charge. In the following figures the units are scaled to nuclear dimensions, but the dynamic evolution shown applies to any classical viscous drop by virtue of dynamic similarity. In Table 1 we present a unit conversion table for the benefit of non-nuclear scientists. The figures in this paper represent smoothed composites of motion picture sequences generated by the computer.

We begin with a study of the uncharged drop. Wong and Tang (1) have discussed the analytical solutions to small-amplitude oscillations of such drops. We shall now study large-amplitude oscillations, for which there is no analytical theory. The sequence shown in Figure 3 simulates the oscillations of a drop with an initial shape given by the second-order Legendre polynomial, with the coefficient $a_2 = 0.4$. The viscosity is of a medium value that results in a damped oscillatory motion. The drop is started at rest; the initial excess surface energy is then exchanged for kinetic energy as the drop oscillates from a prolate spheroid to a sphere (with minimum surface energy and maximum kinetic energy) and then back to an oblate spheroid (with minimum kinetic energy and maximum surface energy). The drop simulations at the top are from the film strip; the large dots are the surface markers and the small interior dots are the cell particles. There are about a thousand particles in this drop. The total energy is seen to decrease exponentially as the damping proceeds. The period of oscillation, 15.35×10^{-22} seconds, is slightly longer than the theoretical period for small-amplitude oscillations, which is 13.38×10^{-22} seconds. However the general motion exhibits the behavior described by Lord Rayleigh (10) for linear oscillations many years ago, even though the ratio of amplitude to drop radius is not very small. This result has been observed experimentally many times.

The simulation in Figure 4 shows this same drop except that the viscosity has been increased by a factor of ten. Now the motion is overdamped and the drop slowly damps out to a sphere without any oscillatory motion.

In Figure 5 the size of the drop is changed so that it now has an initial Legendre coefficient given by $a_2 = 1.0$. This is a very large-amplitude motion which no longer preserves the P_2 shape. In the least square fit of the free surface shown on the left, a substantial a_4 component is seen to grow with the motion, and this is also very evident in the simulated drop sequences at the top of the figure. The energy changes are shown on the right; at the end of this simulation we have been left with a sphere with a great deal of kinetic energy which will probably proceed into some complex oblate spheroidal type of shape, still following the general Rayleigh behavior. The extrapolated period for this oscillation is about twice the corresponding Rayleigh period. The Weber number for this simulation, defined by $We = \sigma d u^2/\gamma = 12\, E_{kin}/E_{sur}$ (where σ is the density, d the drop diameter, u an average velocity, and γ the surface tension coefficient), is $We = 1.37$, and there is no sign of extreme disruption in the simulation.

The addition of a full body charge to the drop involves a substantial increase in computer running time, and this tends to result in a loss of accuracy due to the necessity of using a larger mesh size. In Figure 6 we show the smoothed energy curves for the same drop that we discussed in Figure 3 except that now it has a body charge of 62 proton charges. The charge density, like the mass density, is assumed to be constant throughout the drop. This particular charge represents a ^{152}Sm nucleus, which is known to be stable against fission even for fairly large distortions. In this simulation the surface forces still predominate the motion, but now the surface

energy is exchanged for Coulomb energy as well as kinetic energy, resulting in a longer period for the oscillation. The Coulomb energy and kinetic energy are at a maximum for the spherical shape, while the surface energy is at a minimum. Toward the end of the simulation the motion has damped out to small amplitude oscillations about a sphere. The accuracy of these calculations is about one percent.

The motion of this same drop was studied as more charge was added to the drop. In Figure 7 we plot the kinetic energy of the drop after a fixed time interval as a function of the atomic charge Z of the drop. For small charges the motion is oscillatory. As the charge is increased, the Coulomb forces oppose the surface tension more and more, slowing down the motion until the two forces just balance at the minimum in the curve. This minimum represents a saddle point between oscillation and fission; for charge densities beyond this point the Coulomb forces predominate and the drop begins to fission with no oscillatory behavior. The saddle point charge predicted by SQUISH is in agreement with the theoretical saddle point charge of 76 predicted for this shape by Cohen and Swiatecki (11). In Figure 8 is shown the same drop of Figure 7 with charge Z = 110. Here the Coulomb energy plunges down as the fission proceeds, and the surface energy and kinetic energy move up almost equally in the initial stages of the motion.

The dimensionless parameter that is used to represent the relative strengths of the Coulomb force and the surface tension is the fissility, defined by $x = E_{coul}/(2 \cdot E_{surf})$. In Figure 9 is shown a comparison of two simulations of a drop that was initialized with a shape corresponding to an $x = 0.9$ saddle shape, but with enough charge to make $x = 1.56$. This highly charged drop was then expected to fission very rapidly. The drop at the right was given a high viscosity that overdamps oscillations at lower fissilities, and the drop at the left was given a lower viscosity that would lead to damped oscillations at lower fissilities. Instead of rapidly breaking apart into two drops, we find that the highly charged drop becomes very elongated and eventually develops a long, thin neck that will not pinch off until the neck has extended to virtually no width. This is an unsettling result, especially for nuclear physics, for such a thin neck would contain less than one nucleon and we could not expect to apply a classical treatment under such conditions. This is not entirely surprising because nuclear fission is usually a low-temperature phenomenon, unlike accelerator-induced fusion. However it means that classical treatments of the fission dynamics, and possibly the statics, may be misleading. One might hypothesize that in real charged drops, whether classical or quantum mechanical, the pinch-off is actually initiated by a surface fluctuation in the thin neck. This is substantiated to some degree by our knowledge that nuclear fission is not necessarily symmetric; one fission fragment often is larger than the other, which would be possible if the long neck predicted by SQUISH were to be broken off at a random place along its length at some time by a random surface fluctuation.

Experimental studies of charged drops would be very helpful in this respect, but it would be extremely difficult to charge them sufficiently to represent

nuclear liquid drops, which are held together by the strong nuclear forces despite their high charge density. In Figure 10, nonetheless, we show an approximation to a real charged drop. These profiles are from a film made by two nuclear physicists at LBL. They suspended a drop of water containing trichlorethylene in a bath of transformer oil of about the same density as the drop. Then they placed the drop between two capacitor plates and filmed its subsequent motion as a function of the applied voltage. The sequence shown here was at one of their higher voltages. These drops, of course, are not body-charged like a nucleus, but rather polarized. However we see in their development a pronounced elongation followed by asymmetric fission, which lends some credence to the computer simulations that we have presented. Further support is found in the experimental films of pendant drops presented at this conference by A. A. Kovitz.

Besides these simulations of the fission process, which require further study, we are examining the problem of fusion. This has required special programming to handle the cusp-like neck at the initial stages of the fusion. Our fusion results are still preliminary and will not be presented in detail at this time. In Figure 11 is shown, by way of example, a simulation of the fusion of two liquid spheres. The Weber number for this simulation was around 5.5, so surface tension effects are negligible compared to inertial effects, and large distortions are expected. The general features of this viscous fusion are that the necking process involves a large amount of viscous friction which hinders the formation of the neck and hence the fusion. The implication of this for the fusion of heavy nuclei is quite serious, if nuclear viscosity does indeed exist (and we do not yet know that it does), for it implies that at high accelerator velocities the viscosity may hinder the formation of compound nuclei, while at low velocities the Coulomb repulsion also hinders the fusion. Therefore there may be only a narrow range of energies for which fusion experiments can be performed in the heavy nuclei. We plan to explore many of these speculations in the near future.

ACKNOWLEDGEMENT

The author would like to thank Dr. Jose R. Alonso for his general assistance and his help in assembling the film package associated with this paper.

REFERENCES

1. H. H. K. Tang and C. Y. Wong, "Vibrations of a Viscous Liquid Sphere", Submitted to J. Fluid Mech.
2. A. J. Sierk and J. R. Nix, "Dynamics of Fission and Fusion with Applications to the Formation of Superheavy Nuclei", Los Alamos Scientific Laboratory Report LA-UR-73-981, (August, 1973).
3. R. W. Hasse, "Dynamic Model of Asymmetric Fission", Nuc. Phys. A128, 609, (1969).
4. N. Bohr and J. A. Wheeler, "The Mechanism of Fission", Phys. Rev. 56, 426, (1939).

5. D. L. Hill and J. A. Wheeler, "Nuclear Constitution and the Interpretation of Fission Phenomena", Phys. Rev. 89, 1102, (1953).
6. S. G. Nilsson, C. F. Tsang, A. Sobiczewski, Z. Szymanski, S. Wycech, C. Gustafson, I. L. Lamm, P. Moller, and B. Nilsson, "On the Nuclear Structure and Stability of Heavy and Superheavy Elements, Nuc. Phys. A131, 1, (1969) also V. M. Strutinsky, "Shells in Deformed Nuclei", Nuc. Phys. A122, 1, (1968).
7. G. N. Flerov and U. T. Oganesyan, "Nuclear Reactions Induced by Xenon Ions and Experiments on Synthesizing Superheavy Elements", Dubna P7-6523, (June, 1972).
8. A. A. Amsden and F. H. Harlow, "The SMAC Method: A Numerical Technique for Calculating Incompressible Fluid Flows", Los Alamos Scientific Laboratory Report LA-4370, (May, 1970).
9. G. B. Foote, "A Numerical Method for Studying Simple Drop Behavior: Simple Oscillation", J. Comp. Phys. 11, 507, (1973).
10. Lord Rayleigh, "On the Capillary Phenomena of Jets", Proc. Roy. Soc. (London) 29, 71, (1879).
11. S. Cohen and W. J. Swiatecki, "The Deformation Energy of a Charged Drop; Part V", Annals of Physics 22, 406, (1963).

Table I - Unit Conversion Table

Quantity	Nuclear Unit		SI Unit
Time	1 dsec	=	10^{-22} sec
Length	1 fm	=	10^{-15} m
Energy	1 Mev	=	1.602×10^{-13} j
Velocity	1 fm/dsec	=	10^{7} m/sec
Kinematic viscosity*	1 fm^2/dsec	=	10^{-8} m^2/sec
Surface tension**	1 Mev/fm^2	=	1.602×10^{17} nt/m

* The nuclear density is 0.13 amu/fm^3 = 1.66×10^{18} Kg/m^3. Thus a nuclear kinematic viscosity of 1 fm^2/dsec means a viscosity of 1.66×10^{8} poise.

** The nuclear surface tension is approximately 1 Mev/fm^2.

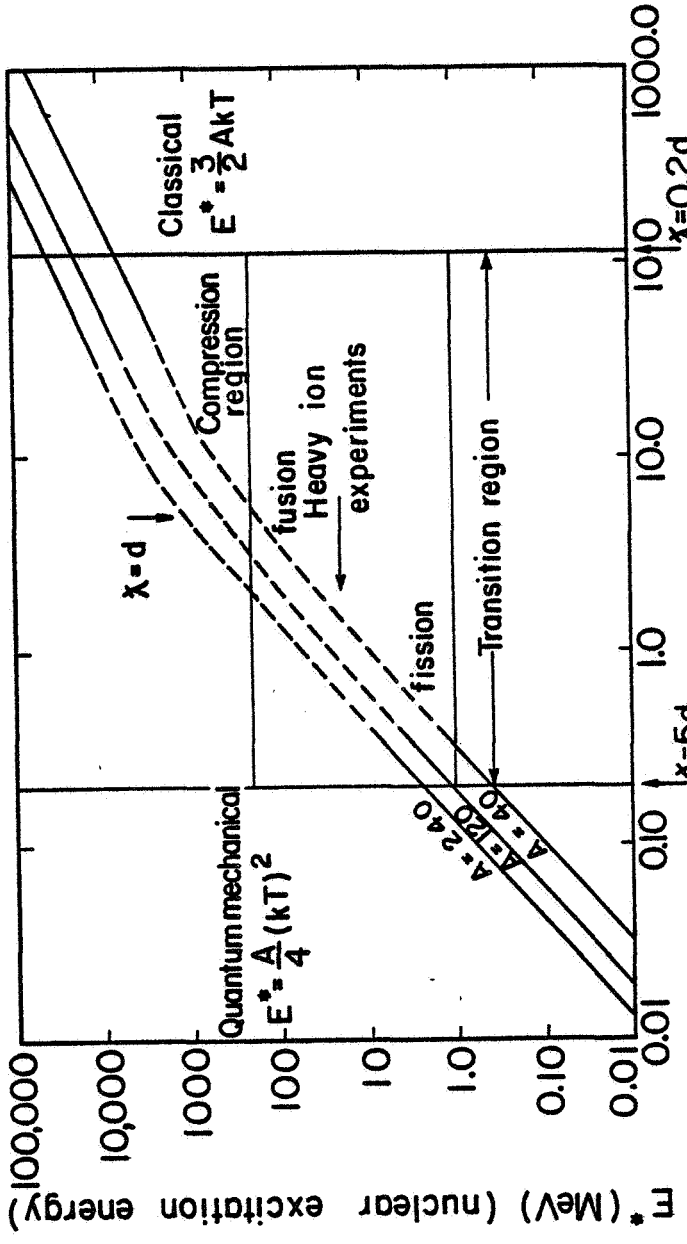

Figure 1. Transition from quantum mechanical to classical regime. Heavy ion accelerator experiments lie in the transition region where the de Broglie wavelength λ is close to the inter-nucleon spacing d.

SQUISH-HOW IT WORKS

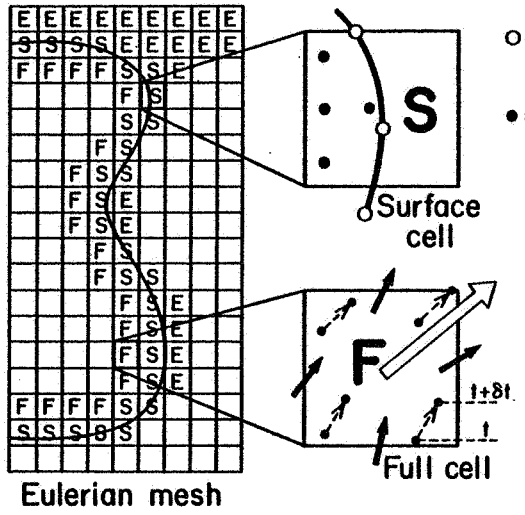

o=Free surface marker

•=Lagrangion particle

Velocities stored on cell boundaries

Resultant force applied at cell center

1. Forces calculated from free-flow shape (surface tension and coulomb forces)
2. Velocities calculated from Navier-Stokes equation $\left(\frac{\delta}{\delta t}+\bar{u}\cdot\bar{\nabla}\right)\bar{u}=-\frac{1}{\rho}\bar{\nabla}P+\frac{\bar{F}}{m}+\frac{n}{\rho}\nabla^2\bar{u}$
3. Volume conserved from incompressibility $\bar{\nabla}\cdot\bar{u}=0$
4. Move cell particles and surface markers and advance time to $t+\delta t$

The SMAC method (Harlow and Amsden, Los Alamos)

Figure 2.

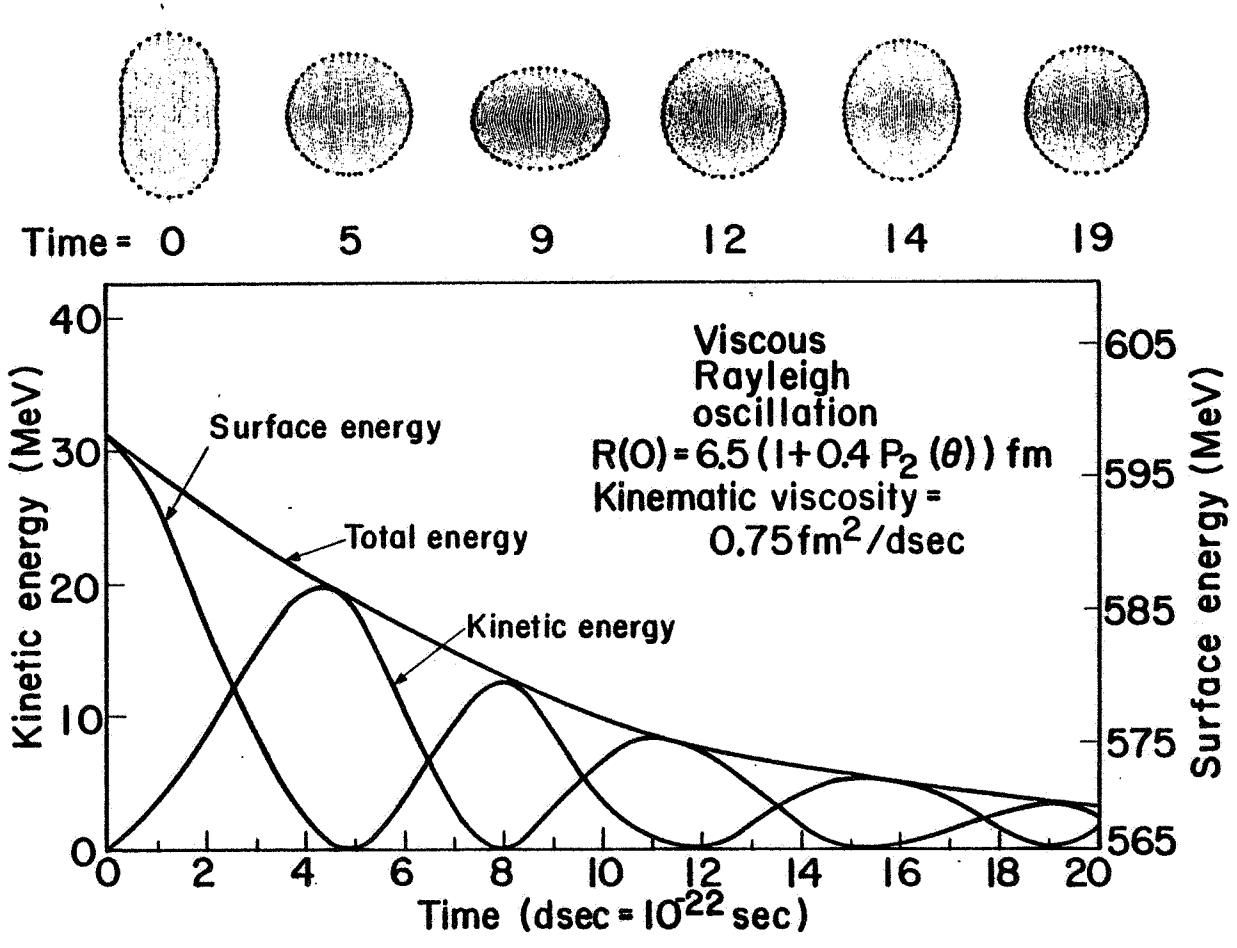
Time = 0
5
9
12
14
19
Viscous
Rayleigh
oscillation
R(0) = 6.5 (1+0.4 P2 (θ)) fm
Kinematic viscosity =
0.75 fm2/dsec
Surface energy
Total energy
Kinetic energy
Kinetic energy (MeV)
Surface energy (MeV)
Time (dsec = 10-22 sec)
0
10
20
30
40
565
575
585
595
605
0
2
4
6
8
10
12
14
16
18
20

Figure 3.

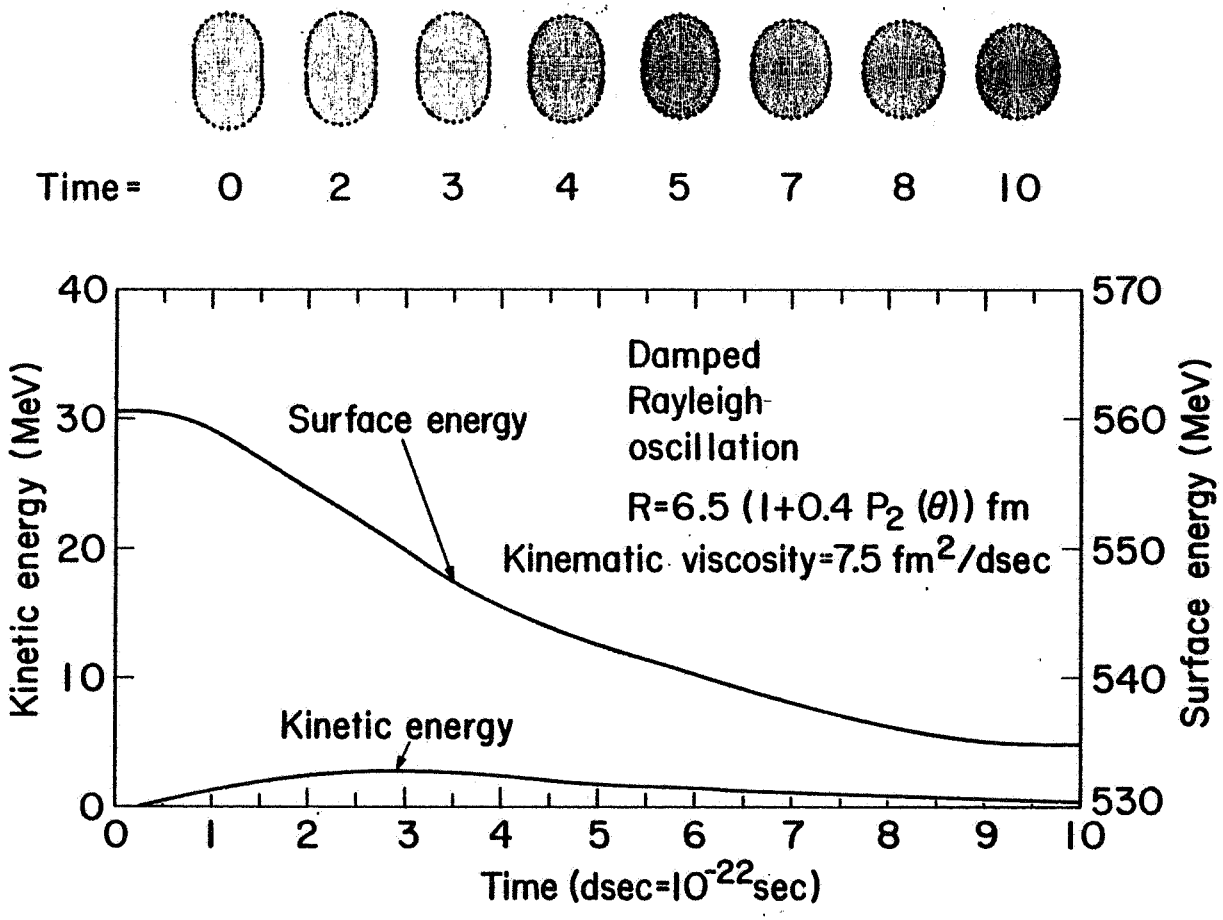
Time = 0 2 3 4 5 7 8 10
Damped
Rayleigh-
oscillation
R=6.5 (1+0.4 P2 (θ)) fm
Kinematic viscosity=7.5 fm2/dsec
Surface energy
Kinetic energy
Kinetic energy (MeV)
Surface energy (MeV)
Time (dsec=10-22sec)
0 1 2 3 4 5 6 7 8 9 10
0 10 20 30 40
530 540 550 560 570

Figure 4.

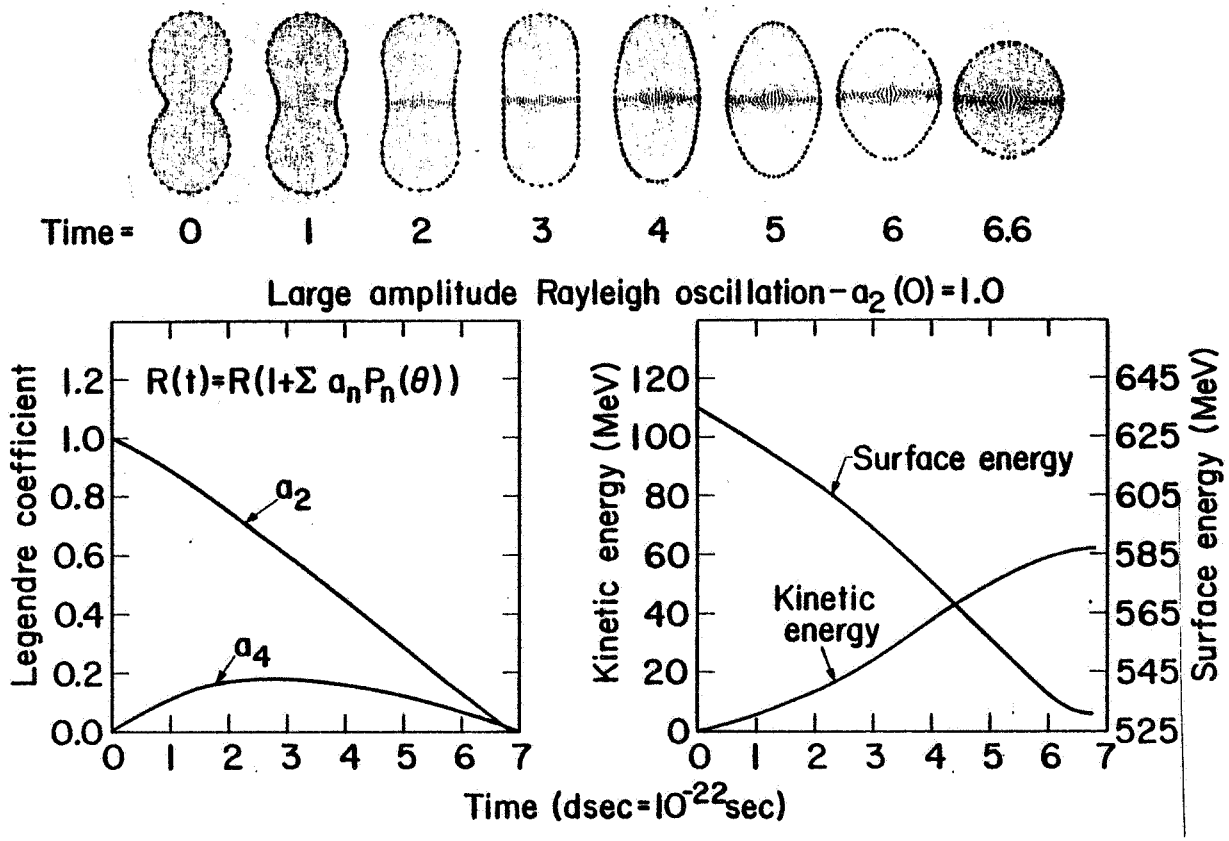
Time = 0 1 2 3 4 5 6 6.6
Large amplitude Rayleigh oscillation – $a_2(0) = 1.0$
$R(t) = R(1 + \Sigma\, a_n P_n(\theta))$
Legendre coefficient
1.2
1.0
0.8
0.6
0.4
0.2
0.0
a_2
a_4
0 1 2 3 4 5 6 7
Time (dsec = 10^{-22} sec)
Kinetic energy (MeV)
120
100
80
60
40
20
0
Surface energy
Kinetic energy
645
625
605
585
565
545
525
Surface energy (MeV)

Figure 5

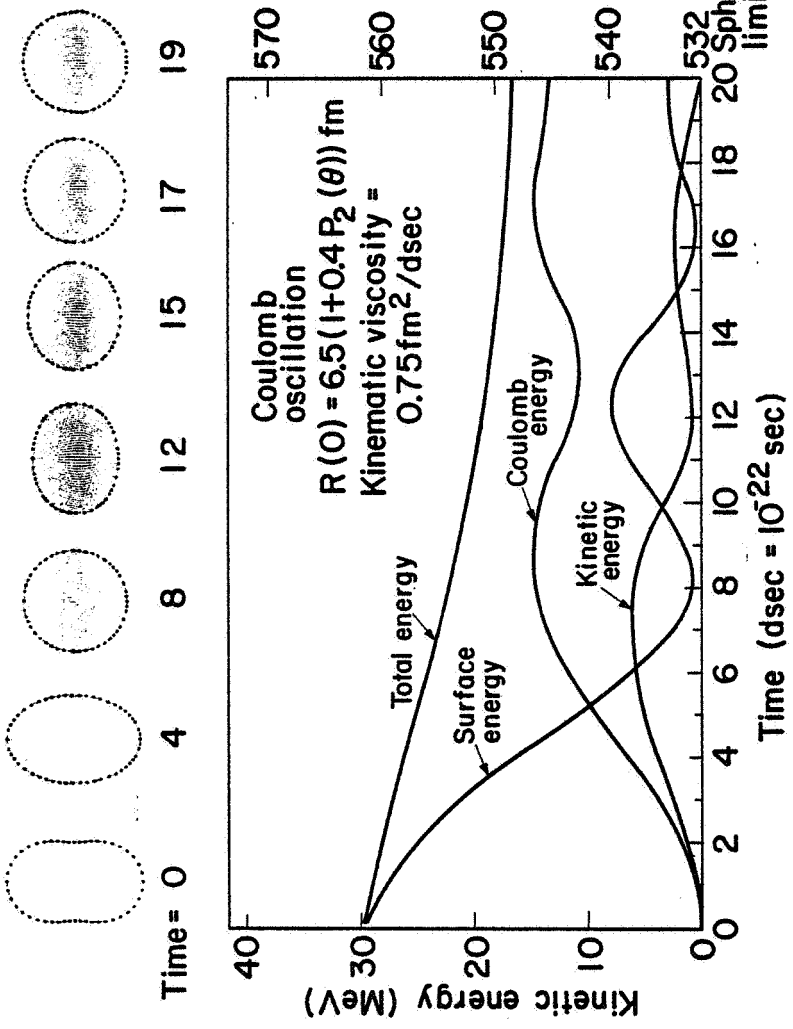
Time= 0
4
8
12
15
17
19
Coulomb oscillation
R(0) = 6.5(1+0.4 P2 (θ)) fm
Kinematic viscosity = 0.75fm2/dsec
Total energy
Surface energy
Coulomb energy
Kinetic energy
Kinetic energy (MeV)
Surface energy (MeV)
Coulomb energy (MeV)
Time (dsec = 10-22 sec)
Sphere limit
Sphere limit

Figure 6

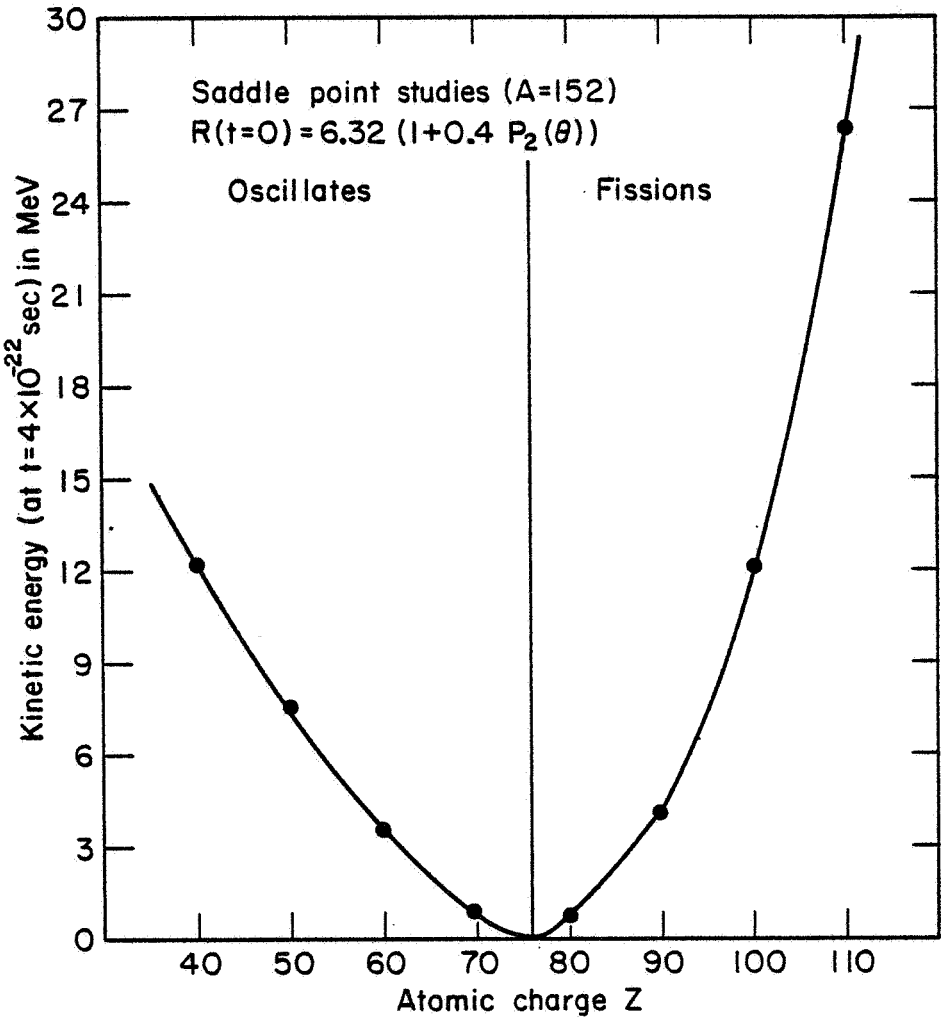
Saddle point studies (A=152)
R(t=0) = 6.32 (1+0.4 P2(θ))
Oscillates
Fissions
Kinetic energy (at t=4×10^-22 sec) in MeV
Atomic charge Z
0
3
6
9
12
15
18
21
24
27
30
40
50
60
70
80
90
100
110

Figure 7

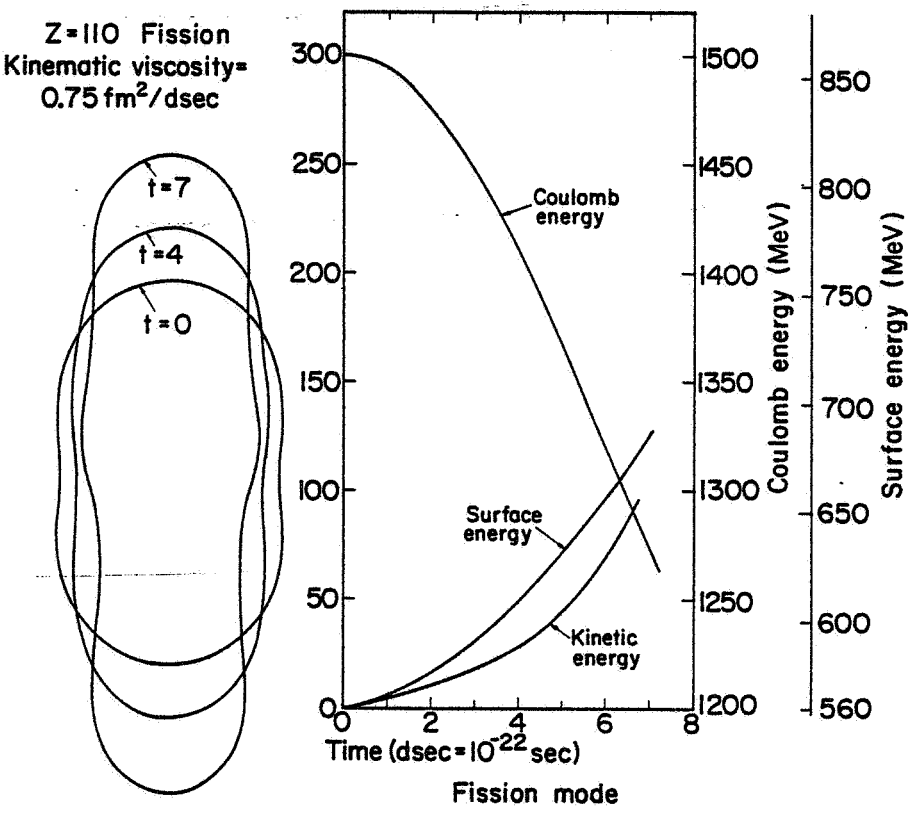
Z=110 Fission
Kinematic viscosity=
0.75 fm²/dsec
t=7
t=4
t=0
300
250
200
150
100
50
0
0
2
4
6
8
Time (dsec=10⁻²² sec)
Fission mode
Coulomb energy
Surface energy
Kinetic energy
1500
1450
1400
1350
1300
1250
1200
Coulomb energy (MeV)
850
800
750
700
650
600
560
Surface energy (MeV)

Figure 8

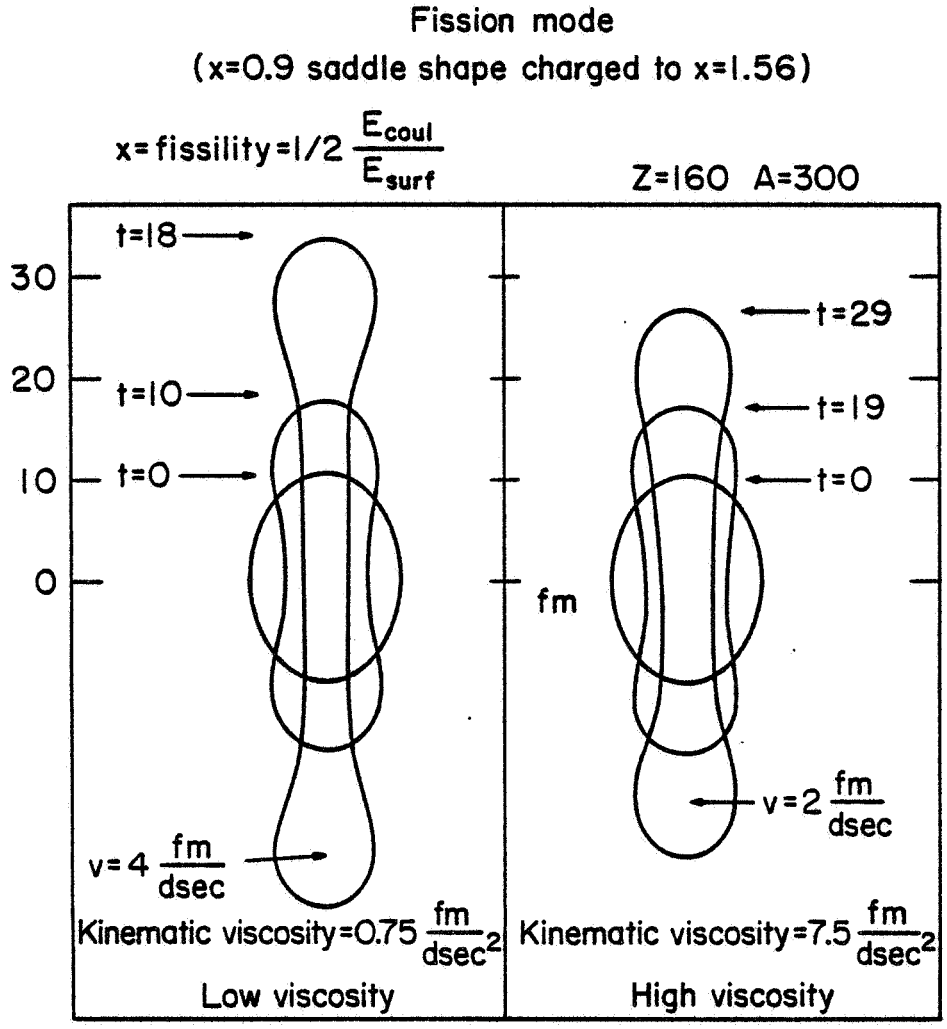
Fission mode
(x=0.9 saddle shape charged to x=1.56)
x= fissility = 1/2 Ecoul / Esurf
Z=160 A=300
t=18
t=10
t=0
30
20
10
0
fm
v = 4 fm/dsec
Kinematic viscosity = 0.75 fm/dsec²
Low viscosity
t=29
t=19
t=0
v = 2 fm/dsec
Kinematic viscosity = 7.5 fm/dsec²
High viscosity

Figure 9

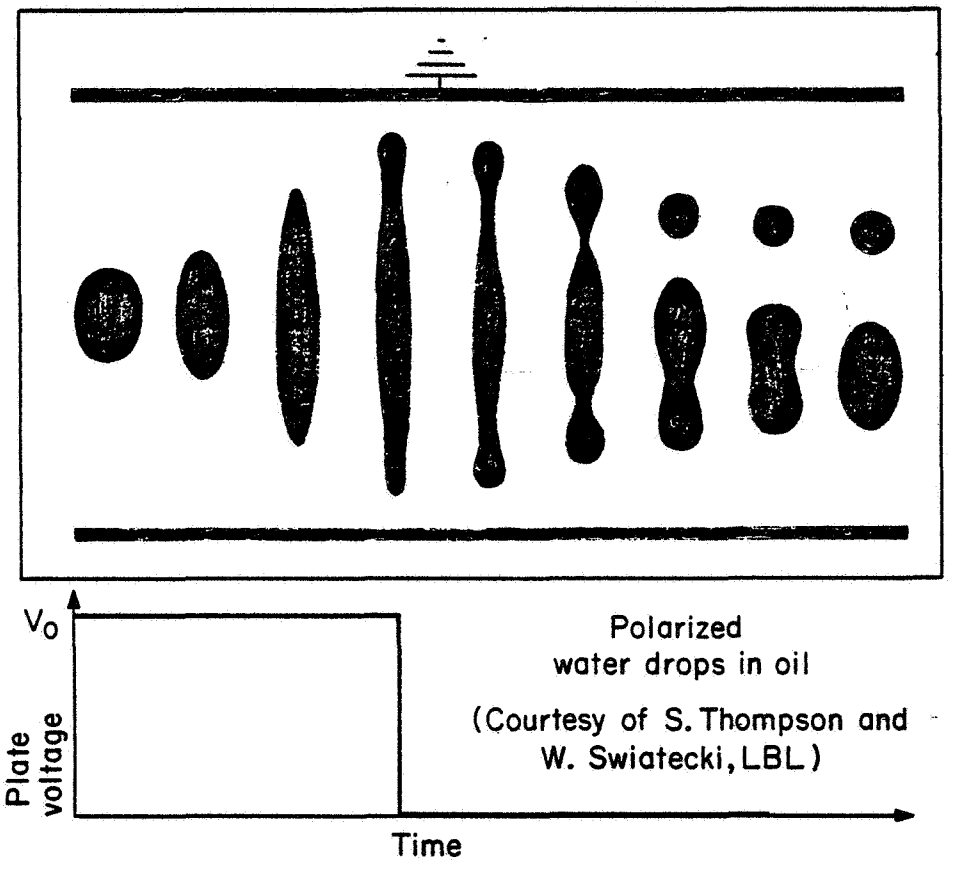
Vo
Plate voltage
Time
Polarized
water drops in oil
(Courtesy of S. Thompson and
W. Swiatecki, LBL)

Figure 10

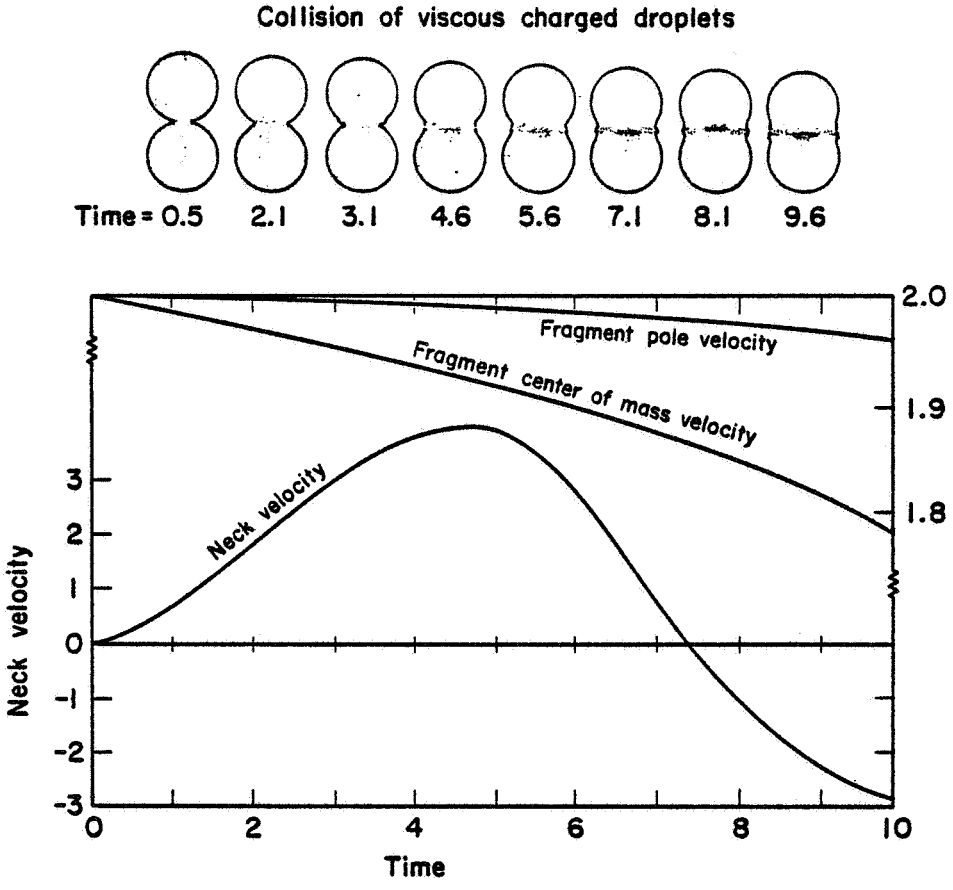
Collision of viscous charged droplets
Time = 0.5
2.1
3.1
4.6
5.6
7.1
8.1
9.6
Fragment pole velocity
Fragment center of mass velocity
Neck velocity
Neck velocity
Time
2.0
1.9
1.8
3
2
1
0
-1
-2
-3
0
2
4
6
8
10

Figure 11

D10

SKYLAB FLUID MECHANICS DEMONSTRATIONS

by

Edward G. Gibson
Science Pilot, Skylab III

The substance of this presentation is a motion picture film which illustrates some of the fluid mechanics demonstrations accomplished on the Skylab missions. It is representative of the many hours of data taken in flight, most of which is from the third and last manned mission. These demonstrations were conducted on an unscheduled basis whenever a member of the crew, usually the science pilot, could make some time available. Because these demonstrations were not proposed and approved for flight until very late relative to the other Skylab experiments, the amount of crew familiarization and training, additional hardware and inflight time which could be made available were minimal.

The improvement in the techniques of handling fluids in zero gravity during the course of the three missions is first shown. A very light thread was sometimes used to stabilize fluid drops. Syringes with large openings were found to be useful for dispensing the fluids. Ink or small amounts of drink juices were often added to water to provide better visualization. Most of the data was taken with the onboard television system. On the last flight the use of a close-up lens provided excellent viewing of the investigations. The list of phenomena to be explored also increased significantly with each mission.

The modes of oscillation of a fluid droplet on a flat plate were then presented. The drop was perturbed by either oscillation of the

plate or by impingement of a jet of air from above the drop and directed perpendicular to the plate. The motions of the drop were followed through many cycles to permit study of the damping and development of modes of oscillation different than the one excited.

A large portion of the film illustrates the characteristics of fluid spheres in zero gravity. Sphere sizes approximately 5 to 20 cc were used. Each sphere was perturbed symmetrically about a plane through the center of the sphere and the modes of oscillation and damping were followed. Spheres of a water-soap mixture or of a low density soap froth were observed to demonstrate the effects of changes in density, viscosity and surface tension on the modes of oscillation and damping. Water spheres were rotated and fission of the sphere was observed. With rotation of a sphere, a "dog bone" geometry developed before fission. A toroidial form was never observed. Collisions between water drops were also studied. Different relative drop sizes, velocities and impact parameters were used. Lastly, air was injected into water spheres so that a "sphere within a sphere" was observed. Bubble collapse and the very pronounced increase in damping of sphere oscillations was observed.

The largest fraction of effort was directed at the study of liquid floating zones, a demonstration suggested and developed by Dr. J. R. Carruthers of Bell Laboratories. Cylinders of 6, 14, and 20 cc of fluid were stabilized between two circular plates of 7/8 inch diameter. The fluid was allowed to wet the flat surface of each plate but was prevented from wetting the edges by use of Krytox lubricant. The plates were then

rotated at various speeds in either the same direction or opposite directions and the resultant fluid motions observed. The most commonly observed instability was a bowing of the cylinder or "C shaped" instability. Mixtures of soap and water and a soap froth were again used in addition to colored water. Bubbles were also injected into the cylindrical water column. The coalescence of the bubbles, their movement to the center of the axis of rotation and their effect of increasing the damping of the column were observed. Longitudinal vibration, that is, vibration of the end plates along the axis of the column, was studied with each column before rotation. When the vibration was of the correct frequency, standing waves were observed. An increase in the frequency produced an increase in the number of modes observed. In order to aid in flow visualization, soap fragments were added to clear water columns in several runs. Lastly, the maximum theoretical stable column length of π times the diameter (2.75 inches) was observed to be slightly exceeded (2.90 inches) but the shape was that of an unduloid which slightly increased the stability and made it possible.

The fluid mechanics demonstrations conducted on Skylab only scratched the surface of the useful fluid mechanics experiments that can and should be done on future shuttle missions in the 1980's.

D11

THE APPLICATION OF DROPS AND BUBBLES TO THE SCIENCE OF SPACE PROCESSING OF MATERIALS

by

J. R. Carruthers
Bell Laboratories
Murray Hill, New Jersey 07974

I. INTRODUCTION

One of the primary tasks of materials scientists is the preparation of solids with controlled shapes, compositions and structures. These characteristics in turn determine the properties of the solid material. The degree of our ability to exercise control over them ultimately limits the performance of the material for its intended application, whether it be structural, electronic, magnetic, optical, chemical or biological. Consequently studies of materials processing are highly important areas of research which involve interdisciplinary combinations of such diverse fields as solid state physics, surface physics and chemistry, fluid dynamics, heat and mass transfer, and high temperature thermodynamics and physical chemistry. Although there are many important processes such as metals casting and annealing, ceramic sintering, glass melting and homogenization, chemical vapor deposition, crystal growth, oxidation, and diffusion, this paper will consider only crystal growth from melts and solidification processes since these are uniquely affected by a reduced gravity. The basic configurations and problems associated with crystal

growth from melts will be outlined on earth as well as in space. The role of free liquid surfaces in crystal growth processes will be discussed for various liquid shapes and the relevance of the current state of the science of liquid drops and bubbles in liquids to these processes will be demonstrated.

II. CRYSTAL GROWTH AND SOLIDIFICATION PROCESSES ON EARTH

Melt crystal growth techniques can be classified in terms of the degree of confinement of the liquid by an external container as shown in Fig. 1. In the full confinement methods, the growth interface contacts the container over some region as shown for the horizontal and vertical Bridgman techniques.[1] The main problems associated with this contact are direct container contamination of the melt close to the interface itself and the thermal stresses occurring between the container and the grown crystal. In the partial confinement methods, the growth interface does not touch the melt container as shown for the Czochralski, flux and hydrothermal growth techniques.[1] Although contamination from the container does frequently occur in these methods, it can often be reduced through the use of special liners inside the structural support of a rigid container. The Czochralski technique is the most widely used method for growth of congruently melting materials by direct solidification. The growth interface is constrained by appropriate temperature gradients and the meniscus of the

free melt surface. Included here are the shape defining techniques such as the Stepanov method and edge-defined, film-fed method, both of which will be described later. The various flux techniques are basically isothermal and are used for materials that are incongruently melting or decompose at higher temperatures. The interface position and growth rate are constrained by the compositional gradients in the melt and the degree of supersaturation of the melt respectively. For some fluxes, the free surface results in undesirable vaporization of some constituents. Hydrothermal growth produces crystals from a supersaturated fluid near or above its critical temperature. The growth rate is controlled by a concentration gradient induced by a temperature difference between the nutrient and growth regions.

Crystal growth methods from unconfined or containerless melts involve both drops and zones as shown in Fig. 1. Constant volume sessile drops which are fed externally with "raw material" are used for both flux growth by the vapor-liquid-solid (VLS) technique and congruent solidification by the Verneuil technique. Similarly, liquid zones, where the melt surface is constrained by surface tension assisted in some cases by electromagnetic levitation, have been used for both congruent melting (floating zone, silver boat methods) and fluxed melt systems (temperature gradient zone melting or travelling solvent methods). None of these

techniques has been widely used on earth because they are complicated to control and because they require rather high temperature gradients due to the limits imposed on the liquid volume size by hydrostatic pressure considerations. The high temperature gradients cause extensive dislocation generation in the grown crystals and also give rise to highly nonuniform and unstable thermal convection in the melt which in turn leads to undesirable compositional variations in the crystal through its influence on mass transport at the growth interface. The removal of gravitational constraints however leads us to reconsider the detailed behavior of unconfined liquids and the influence of this behavior on crystal growth processes in a later section.

The use of bubbles in materials processing on earth has been mainly as a means of providing large surface areas for gas-liquid reactions in extractive metallurgical processes and for stirring purposes in glassmaking. In reduced gravity environments these techniques cannot be used because it would be difficult to remove the bubbles. On the other hand several novel uses of bubbles in materials processing are possible in reduced gravity which will be discussed in the next section.

III. CRYSTAL GROWTH AND SOLIDIFICATION PROCESSES IN SPACE

Some possible configurations for containerless crystal growth in space are shown in Fig. 2. A division

can be made into single, double and multiple solid access into the liquid drop.

In the single access techniques, the drop is solidified onto a crystal seed so that as the seed is withdrawn, the drop position must be maintained. There are two main techniques for holding the drop position; by external fields such as electromagnetic[2] and stationary acoustic[3,4] fields, and by the use of dies such as used in the Stepanov[5] and edge-defined, film-fed[6,7] techniques. The latter techniques may be used to grow noncircular cross-sectional shapes but reintroduce contamination problems. The use of external positioning fields possesses several complications of which the most important are uncontrolled convection, drop oscillations and what heating method is to be used. In the case of acoustic field positioning, drop oscillations (and associated fluid flow) may be present, optical image heating methods must be used to avoid distortion of the sound fields and the energy impedance mismatch which gives rise to the positioning force becomes weaker in high temperature gases. In the case of electromagnetic field positioning, only liquids with a reasonable electrical conductivity (to 1 mho cm^{-1}) may be used and uncontrolled electromagnetic stirring may be present at higher power levels if the field is used to simultaneously heat as well as position the drop. Both positioning field arrangements will soon be tested in the space environment achievable in sounding rockets.[8]

In all single access drop techniques, control of the meniscus shape at the freezing growth interface will be required for ease of growth-rate and crystal shape control. The role of the meniscus shape will be discussed in the next section but it is desirable that the liquid and solid surfaces meet at an angle of 180°.

The need for positioning fields may be eliminated by the use of double access liquid drop techniques where a melting rod of the same material as the solidifying crystal is introduced into the drop. The simplest concept is the cylindrical floating zone technique[9-11] where the end rods are of equal diameter. In this case, the maximum stable liquid zone length is equal to the circumference regardless of the surface tension.[12] Although this zone length is longer than that possible in earth gravity, a problem arises because the temperature distribution in the absence of thermal convection is not favorable. As shown in Fig. 3(b), the interface shapes will not be perpendicular to the crystal axis as shown in Fig. 2 but will rather follow the freezing point isotherm resulting from thermal conduction. The simplest remedy to this problem will be to use unequal and diameters as typified by the pedestal technique in Fig. 2. This geometry will allow heaters to be used which possess axial as well as radial temperature gradients. If zone lengths longer than the crystal circumference are desired, then floating drop shapes may be used

as shown in Fig. 2. However independent meniscus shape control is not possible for such drop shapes.

Multiple solid access in the liquid drop allows for compositional control of the molten zone during growth. In such a system, complex solid-solution systems could be grown at constant solid composition by continuously changing the liquid composition. However such a technique represents a degree of difficulty not presently attempted on earth with the exception of the feed-in, pull-out and floating crucible techniques.[1]

The role of bubbles in liquid drops has been shown in recent Skylab experiments[13] to effectively "stiffen" the outer liquid surface so that vibrational oscillation amplitudes are considerably diminished. Consequently any of the techniques shown in Fig. 2 may benefit by using liquid shells instead of liquid drops if drop oscillations are a problem.

Another area where bubbles may serve a useful function is in the production of foam solids - a new class of materials with potentially useful strength to weight ratios.

IV. LIQUID DROP STATICS AND DYNAMICS

In this section, we consider four major phenomena relevant to the space processing of molten materials; the degree to which a contained liquid adopts its equilibrium shape in zero gravity, the stable shapes of axisymmetric menisci at crystal-melt boundaries, the rotational stability

of liquid drop and zone surfaces, and the vibration-oscillation characteristics of liquid drops and zones. These phenomena are all basic to our understanding of containerless handling of melts for crystal growth purposes.

(a) Behavior of Confined Liquids at Zero Gravity

There are two important factors which determine the equilibrium shape of a liquid in a container under weightless conditions; the filling factor and the liquid-container contact angle. This problem has been solved analytically for a spherical container by Zenkevich[14] and his results are shown in Fig. 4. The transitions to the various morphological forms are given by the two curves A and B which denote the contact angle, θ, at which the liquid transforms from its earthbound position at an initial height, h, in a container of radius R. Below curve A, the liquid uniformly wets the container while above curve B, the liquid drop does not contact the container at all. A similar set of conditions applies to liquids contained in cylindrical tubes although no analytical solutions are available as yet. These results show that completely confined liquids may adopt a variety of shapes which may not be desirable from the standpoint of crystal growth and solidification, particularly in the vicinity of the transition points of Fig. 4.

(b) Static Meniscus Behavior at Zero Gravity

The behavior of the meniscus shape during Czochralski growth on earth has been discussed thoroughly

by Geist and Grosse.[15] The stabilities of such menisci have been dealt with by Huh and Scriven[16] as well as Padday and Pitts.[17] Basically the situation in Czochralski growth is shown in Fig. 5 where a solid cylinder is immersed in the free liquid-surface at a contact angle of zero. The preferred meniscus height, h_2, is shown in Fig. 5(b) since the freezing interface will tend to remain at constant diameter for small non-uniform displacements of the crystal pulling rate, V_o, or freezing point isotherm. The stabilities of menisci at zero gravity for the free surface, single access drop methods of Fig. 2 have not been investigated as yet but are going to depend quite sensitively on the configurations of the force fields used to constrain the liquid drop position. Some anticipated meniscus shapes at zero gravity are shown in Fig. 6. The maximum height, h, of the crystal interface above the original drop surface is determined primarily by the radial departure, R, allowed at the bottom of the meniscus. If R is constrained to be close to the crystal radius, R_c, then the height h cannot exceed $2\pi R$ without the meniscus becoming unstable. Otherwise longer liquid meniscus columns are allowed according to the approximate relation:

$$h_{max} \approx 2\pi[R^2-(R-R_c)^2]^{1/2} \qquad (1)$$

These considerations apply only if the liquid column base radius, R, is substantially smaller than the liquid drop radius. Otherwise the constant volume condition of the drop or zone will enter into the stability picture as pressure changes in addition to those caused by the liquid surface curvature. A treatment of the mathematical stability of liquid surfaces of revolution under such conditions has been given by Gillette and Dyson[18] for equal end radii. A summary of their calculated stability limits is shown in Fig. 7 for liquid zones of volume V, length L, radius R and diameter D. The limits for unequal end diameters and differential volumes have not been calculated or observed as yet.

(c) Dynamic Behavior of Liquid Surfaces at Zero Gravity

The behavior of free liquid surfaces under rotational and vibrational conditions is now examined.

(i) Rotational Stability

In crystal growth and solidification processes, rotation is usually required in order to provide radially symmetrical temperature distributions since such symmetry may not be present in the heating source and perfect alignment of the crystal axis with the thermal center of symmetry is difficult to achieve. For purposes of compositional homogeneity however, no convection is desired in the melt. Consequently only uniform "solid-body" rotation of the liquid (equal isorotation in the case of double access drop growth

techniques) may be considered and the absolute rotation velocity, ω, must be small enough so that the centrifugal acceleration, $\omega^2 r$, does not cause density gradient driven flows (rotation of a 10 cm radius drop at 5 rpm results in centrifugal accelerations of 2.5×10^{-3} g). Nevertheless such rotations will influence the surface stability criteria discussed in the previous section.

The rotational stability criteria for liquid spheres was first considered by Rayleigh[19] and more completely by Chandrasekhar.[20] The deformed shape considered was that of depression at the poles and expansion at the equator as shown in Fig. 8 for various values of the dimensionless rotation rate, $\rho\Omega^2 R^3/\sigma$ (where ρ is the density and σ the surface tension of the liquid drop of initial radius, R, being rotated at Ω rad/sec). A water drop of radius 10 cm would become toroidal at a rotation rate of 12 rpm. However recent crude experiments performed on Skylab with rotating liquid drops indicated that rather than the expected toroidal deformation shown in Fig. 9(a), a dumb-bell deformation (Fig. 9(b)) was produced when even small nonaxial perturbations are introduced into the rotating drop. The growth rate of such nonaxial perturbations is considerably reduced as the viscosity of the liquid drop increases. Such instabilities have not yet been analyzed theoretically.

The rotational stability criteria for cylindrical liquid columns has been analyzed theoretically by Hocking and Michael[21], Hocking[22], Gillis[23], and Ross[24]. For axisymmetric disturbances, the maximum zone length is reduced below that for a static zone:

$$L_{max} = \frac{2\pi R}{[1+\frac{\rho R^3 \Omega^2}{\sigma}]} \qquad (2)$$

This criterion has been tested experimentally in a Plateau simulation system by Carruthers and Grasso[12] and in real zero gravity on Skylab.[25] These data are summarized in Fig. 10 for equal isorotations and compared to Eq. (2). Discrepancies in the Plateau results occur because the actual zone rotation velocity is somewhat smaller than the end-member rotation velocity because of the viscous drug effects exerted by the viscous outer fluid containing the zone.[2] The Skylab data also shows a deviation from the theoretical curve - becoming unstable at lower rotation rates than expected. The reason for this behavior is that the failure mode in the Skylab experiments was nonaxisymmetric as shown in Fig. 11(b). It was possible to obtain axisymmetric failure modes of the type shown in Fig. 11(a) by replacing the water zone in the Skylab experiments with a soap solution/air foam which greatly increased the effective viscosity. The nonaxisymmetric failures clearly arise from disturbances created by misalignment of the rotation axes and nonparallelism of the discs at the ends of the zone. However viscosity

plays a very important and unsuspected role in determining which types of disturbances are amplified. A great deal of theoretical work is required here to analyze the nonaxisymmetric failure modes for both rotating liquid spheres and cylinder.

(ii) Vibrational Behavior of Free Liquid Surfaces

In crystal growth processes, the time dependent deformation of free liquid surfaces is undesirable because the meniscus shape at the freezing interface will change so as to cause crystal diameter perturbations and also because internal fluid flows will develop which influence the growth segregation behavior. There are two separate liquid shapes which can be considered here as was done for rotational behavior; spherical drops and cylindrical zones. We are interested in the natural resonant oscillation frequencies, which depend primarily on surface tension, and the decay rates, which depend mostly on viscosity. Knowledge of this behavior will permit apparatus designers to avoid vibrations which cause resonant, large amplitude oscillations in the liquid volumes used in space processing.

Lamb first calculated the oscillation frequencies of spherical liquid drops by assuming the viscosity was zero as:[26]

$$\beta^* = \left[\frac{\sigma \ell (\ell+1)(\ell-1)(\ell+2)}{R^3(\rho_o \ell + \rho_i(\ell+1))}\right]^{1/2} \qquad (3)$$

where ℓ is an integer greater than unity and ρ_o and ρ_i are the densities of the fluids outside and inside the drop respectively. The role of viscosity was determined analytically by Miller and Scriven[27] who found that the time dependent frequency, β, varied according to:

$$\beta = \beta_R + i\,\beta_I \tag{4}$$

where β_I is the oscillation frequency and β_R the decay rate and both are viscosity dependent:

$$\beta_R = \frac{(2\ \ell+1)^2(\beta^*\mu_i\mu_o\rho_i\rho_o)^{1/2}}{2\sqrt{2}\ R\Gamma[(\mu_i\rho_i)^{1/2}+(\mu_o\rho_o)^{1/2}]}$$

$$+ \frac{(2\ \ell+1)[2(\ell^2-1)\mu_i^2\rho_i+2\ \ell(\ell+2)\mu_o^2\rho_o+\mu_o\mu_i(\rho_i(\ell+2)-\rho_o(\ell-1))]}{2\ R^2\Gamma[(\mu_i\rho_i)^{1/2}+(\mu_o\rho_o)^{1/2}]^2} \tag{5}$$

$$\beta_I = \beta^* - \frac{(2\ \ell+1)^2(\beta^*\mu_o\mu_o\rho_i\rho_o)^{1/2}}{2\sqrt{2}\ R\Gamma[(\mu_i\rho_i)^{1/2}+(\mu_o\rho_o)^{1/2}]} \tag{6}$$

Here μ_i and μ_o are the dynamic viscosities of the inner and outer fluids respectively and

$$\Gamma = \rho_o\ell + \rho_i(\ell+1) \tag{7}$$

Experimental verification of these relationships can be found in the Plateau simulation work of Valentine et. al.[28] where drops of a carbon tetrachloride and benzene solution with a density of 1 gm cm^{-3} were suspended in water

and oscillated by coalescense with small cyclohexanol drops. More recent experiments[29] using sessile drops of the same organic solution suspended in water are shown in Fig. 12. The drops were deployed by simply filling a glass laboratory funnel so as to obtain the desired size (Fig. 12(a) and (c)) and then mechanically vibrated (Fig. 12(b) and (d)). The data are plotted in Fig. 13 and show that although the decay rates agree well with Eq. (5), the oscillation frequencies appear to lie between β^* and β_I. The contact of the carbon tetrachloride/benzene drop to the glass tube may be responsible for this discrepancy although the contact angle is 130° so that the drop does not wet tube itself.

More recent experimental data has been obtained with liquid drop experiments performed for the author on Skylab mission IV by scientist-astronaut E. Gibson. In these experiments sessile water drops were deployed on a circular disc which was then oscillated along an axis perpendicular to its face. The data are shown on Fig. 14 together with the theoretical predictions of Eqs. (3) and (5). One free drop experiment performed by astronaut W. Pogue on the same mission is included for comparison. In all cases, agreement with theory is excellent for both free and sessile drops.

The vibration behavior of cylindrical liquid zones was also studied extensively on Skylab IV. Preliminary data for the oscillation frequency of longitudinal modes

(vibration along the zone axis) are shown in Fig. 15 together with the theoretical prediction (solid curves) by Lamb[26] for an inviscid fluid:

$$\beta_\ell = \left[\frac{2\ \pi \ell^3 \sigma}{L^3 \rho}\right]^{1/2} \tag{8}$$

where L is the zone length. The frequency increase at longer zone lengths is not presently understood but may be a result of the viscous flow effects in the zone. The theoretical vibration analysis for zones should be redone including these effects as was done for spherical liquid drops (Figs. 13 and 14).

V. SUMMARY

The unique environment of space allows the containerless handling of melts to be used for controlled crystal growth and solidification processes. Some of the techniques currently used on earth together with their problems have been reviewed. Possible configurations for containerless methods in a space environment have been discussed. Such techniques require a detailed understanding of the behavior of free liquid surfaces under both static and dynamic conditions. The current state of knowledge in the science of liquid drops and bubbles relevant to containerless processing has been discussed together with the results of recent Plateau simulation and Skylab experiments. Many areas which require further theoretical and experimental work have been identified as a result of this preliminary work.

REFERENCES

1. See for example - J. C. Brice, The Growth of Crystals from Liquids, Elsevier, New York 1973.
2. R. T. Frost, Proc. Third Space Processing Symposium: Skylab Results, NASA, 1974.
3. T. Wang, ibid.
4. R. Whymark, ibid.
5. A. V. Stepanov, Bull. Acad. Sci. U.S.S.R. 33, 1775 (1969).
6. H. E. LaBelle and A. I. Mlavsky, Mat. Res. Bull. 6, 571-580 (1971).
7. H. E. LaBelle, Mat. Res. Bull. 6, 581 (1971).
8. NASA Sounding Rocket Program, Marshall Space Flight Center, Huntsville, Alabama.
9. P. H. Keck and M. J. E. Golay, Phys. Rev. 89, 1297 (1953).
10. R. Emeis, Z. Naturforsch. 9a, 67 (1954).
11. H. C. Theuerer, Trans. AIME 206, 1316 (1956).
12. J. R. Carruthers and M. Grasso, J. Appl. Phys. 43, 436 (1972).
13. T. C. Bannister, to be published.
14. V. B. Zenkevich, High Temp. 2, 203 (1964).
15. D. Giest and P. Grosse, Z. Angew. Phys. 14, 105 (1962).
16. C. Huh and L. Scriven, J. Coll. Interface Sci. 30, 323 (1969).
17. J. F. Padday and A. R. Pitt, Phil. Trans. Roy. Soc. (London) 275, 489 (1973).
18. R. D. Gillette and D. C. Dyson, Chem. Eng. J. 2, 44 (1971).
19. Lord Rayleigh, Phil. Mag. 28, 161 (1914).

20. S. Chandrasekhar, Proc. Roy. Soc. London A286, 1 (1965).

21. L. M. Hocking and D. H. Michael, Mathematika, 6, 25 (1959).

22. L. M. Hocking, Mathematika, 7, 1 (1960).

23. J. Gillis, Proc. Camb. Phil. Soc. 57, 152 (1961).

24. D. K. Ross, Z. Angew. Math and Phys. 21, 137 (1970).

25. J. R. Carruthers, Proc. Third Space Processing Symposium: Skylab Results, NASA, 1974.

26. H. Lamb, Hydrodynamics, sixth edition, Cambridge University Press, reprinted by Dover, New York 1945.

27. C. A. Miller and L. E. Scriven, J. Fluid Mech. 32, 417 (1968).

28. R. S. Valentine, N. F. Sather and W. J. Heideger, Chem. Eng. Sci. 20, 719 (1965).

29. J. R. Carruthers, unpublished work.

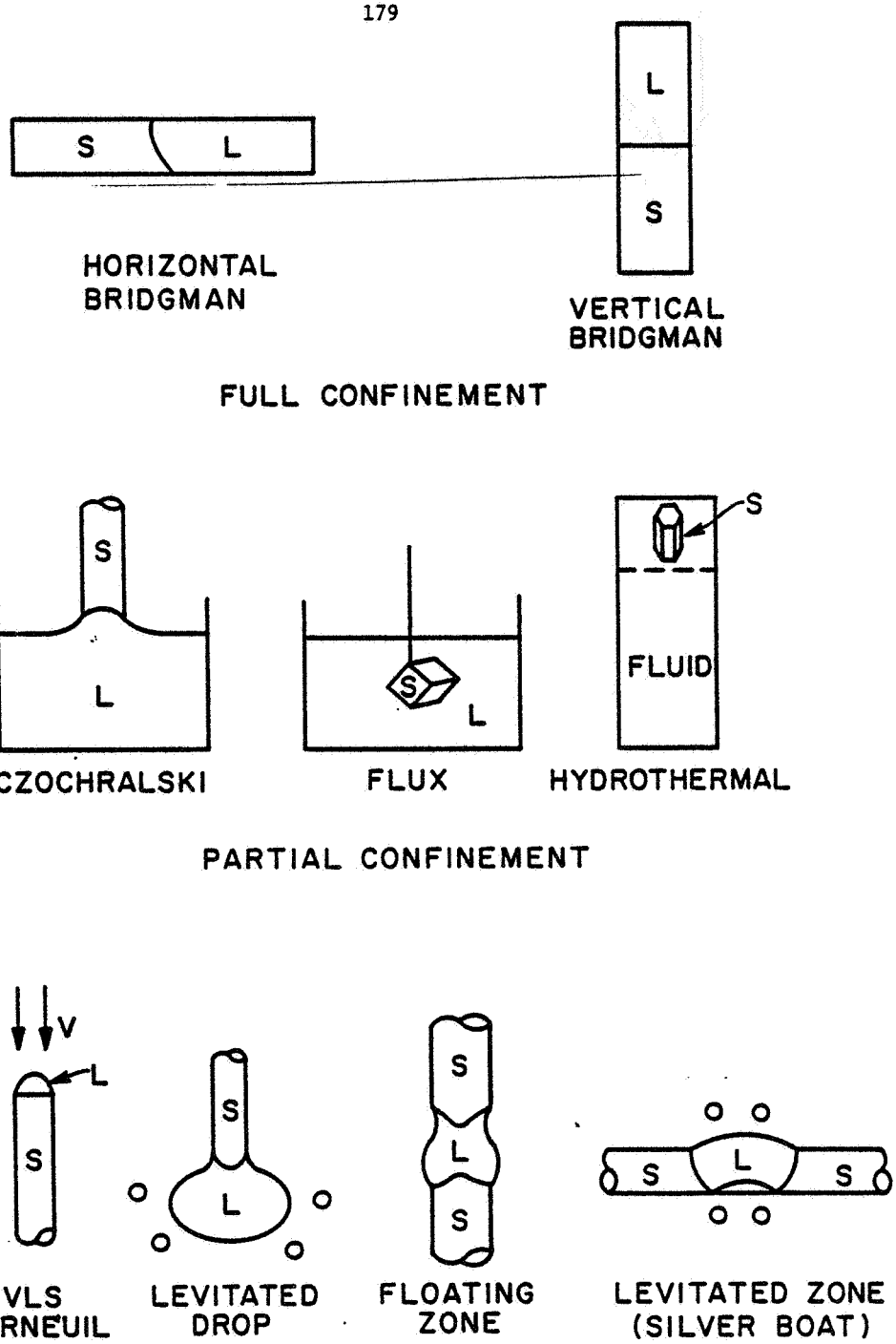

Fig. 1. Schematic classification of melt crystal growth processes on earth in terms of the degree of liquid confinement by a container.

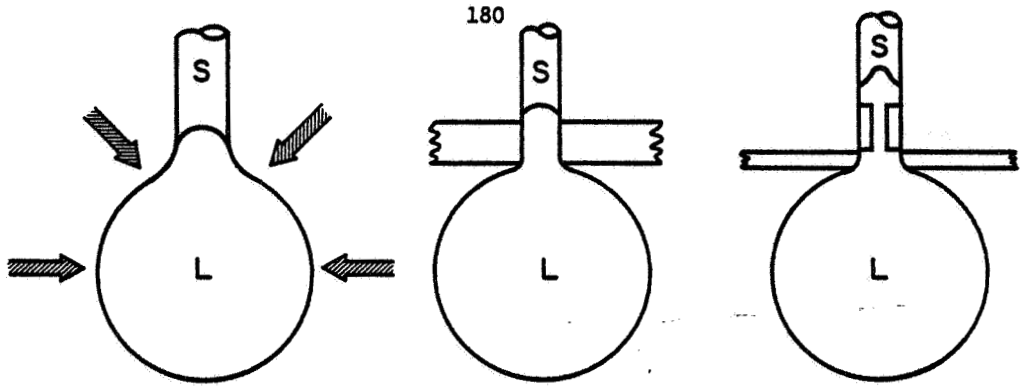

CZOCHRALSKI STEPANOV EDGE-DEFINED FILM-FED

SINGLE ACCESS DROP TECHNIQUES

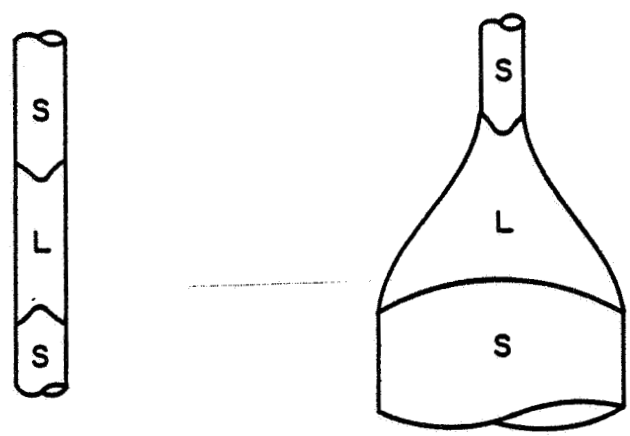

FLOATING ZONE PEDESTAL

DOUBLE ACCESS DROP TECHNIQUES

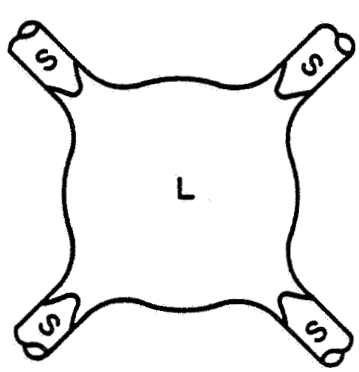

MULTIPLE ACCESS DROP TECHNIQUES

Fig. 2.
Schematic classification of melt crystal growth techniques in space in terms of solid access to the liquid drop.

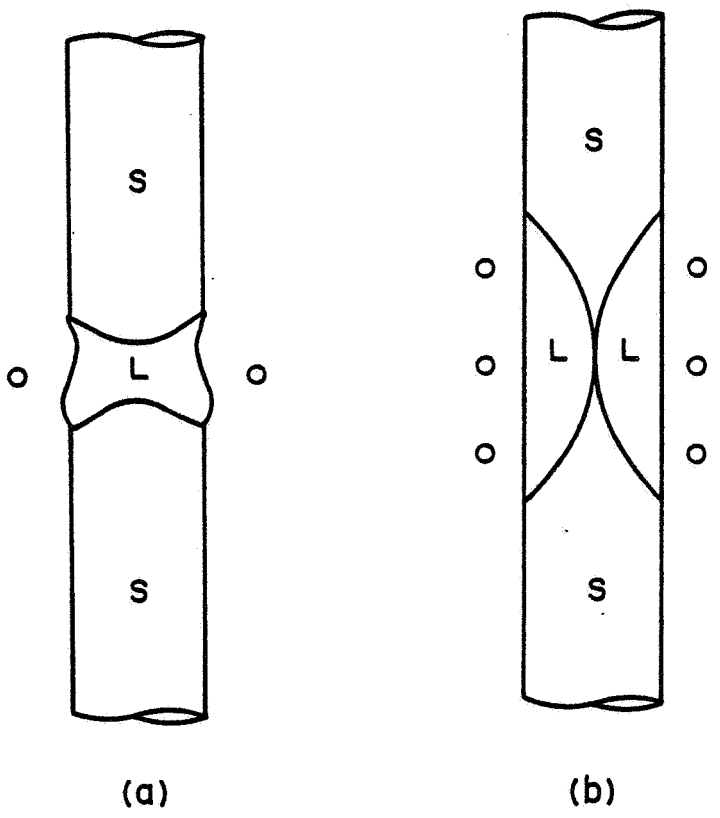

Fig. 3. Crystal-melt interface profiles in zones for (a) earth gravity with thermal convection in the melt and (b) zero gravity with only thermal conduction occurring in the melt.

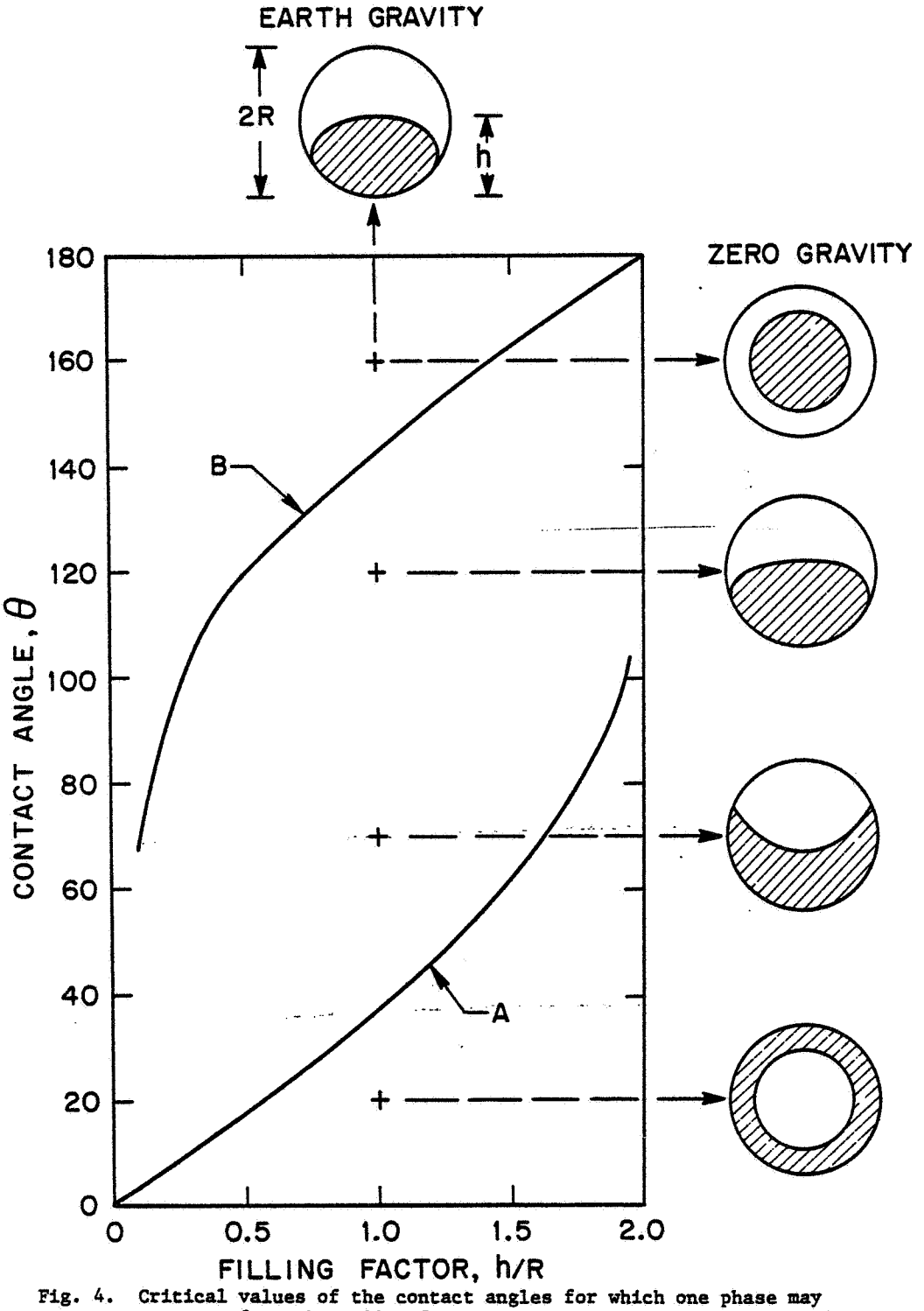

Fig. 4. Critical values of the contact angles for which one phase may separate from the walls of a spherical container at zero gravity. Below curve A, the liquid uniformly coats the walls and above curve B the gas phase uniformly coats the walls - from Zenkevich.(14)

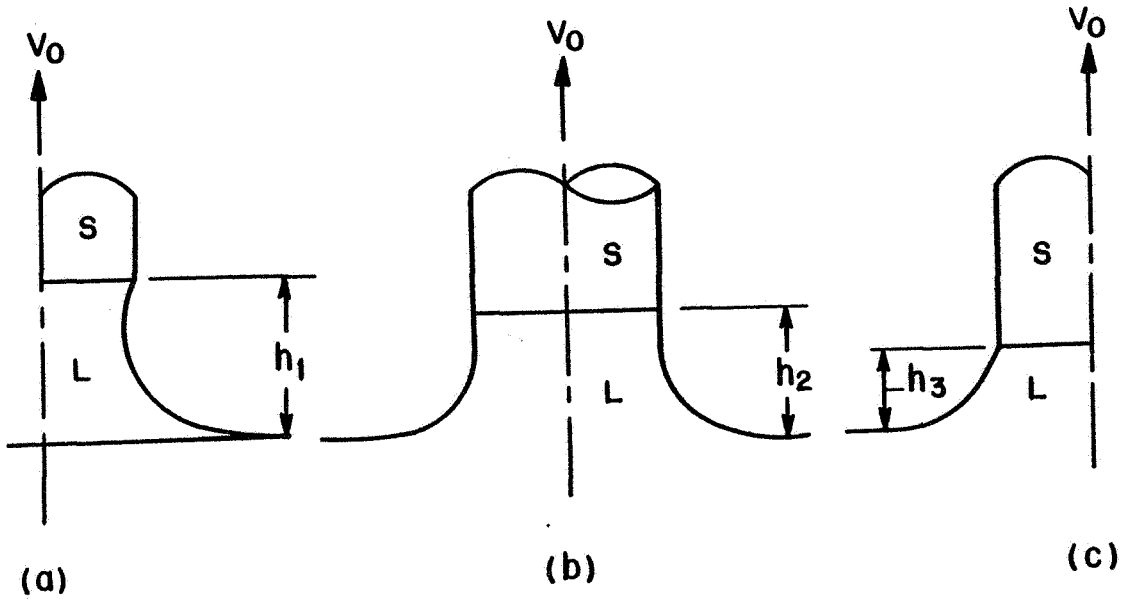

Fig. 5. Menicus configurations important at the crystalmelt interface during Czochralski growth on earth; (a) necking instability, (b) desired configuration, (c) crystal diameter control difficult.

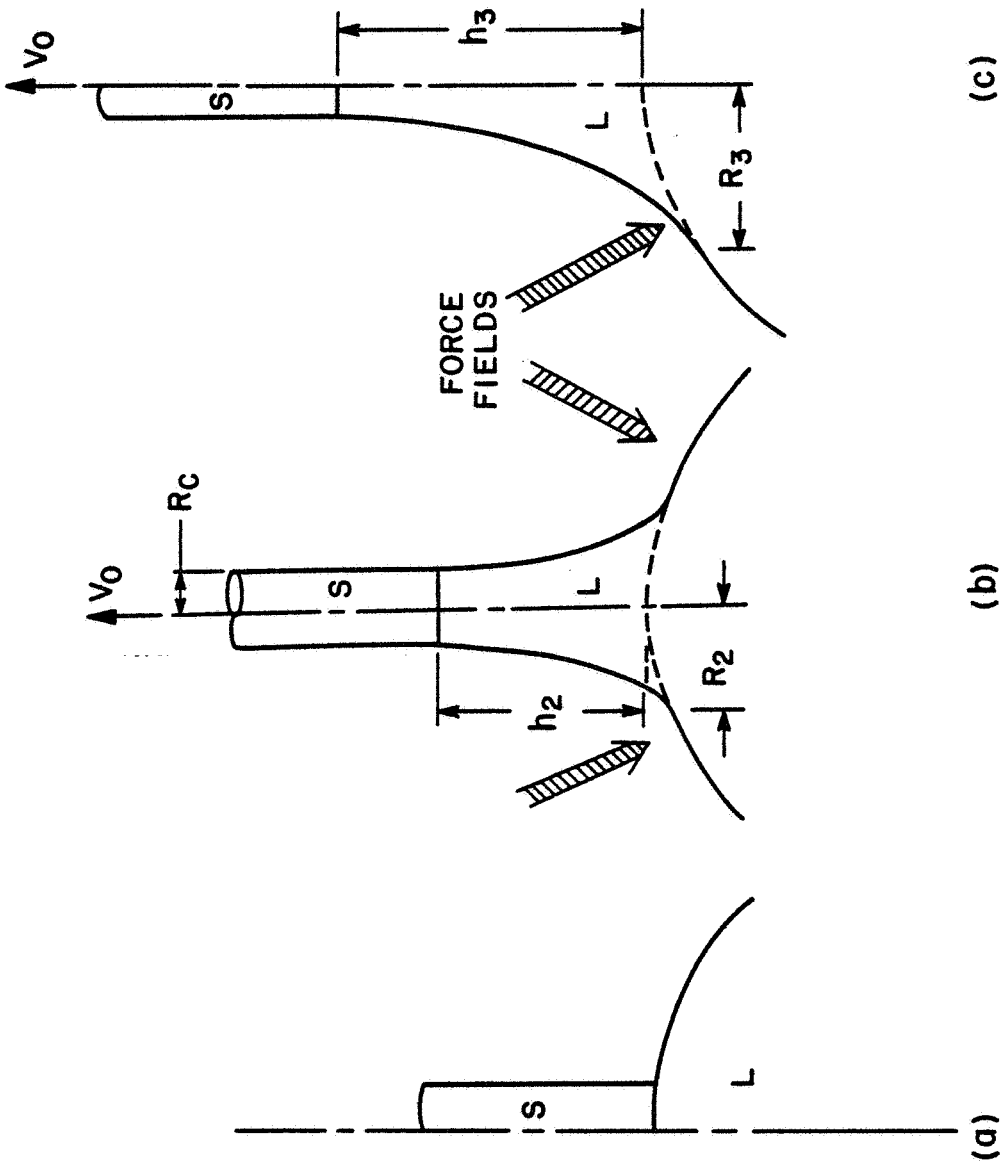

Fig. 6. Menicus configurations for single access liquid drop crystal growth technique of Fig. 2.

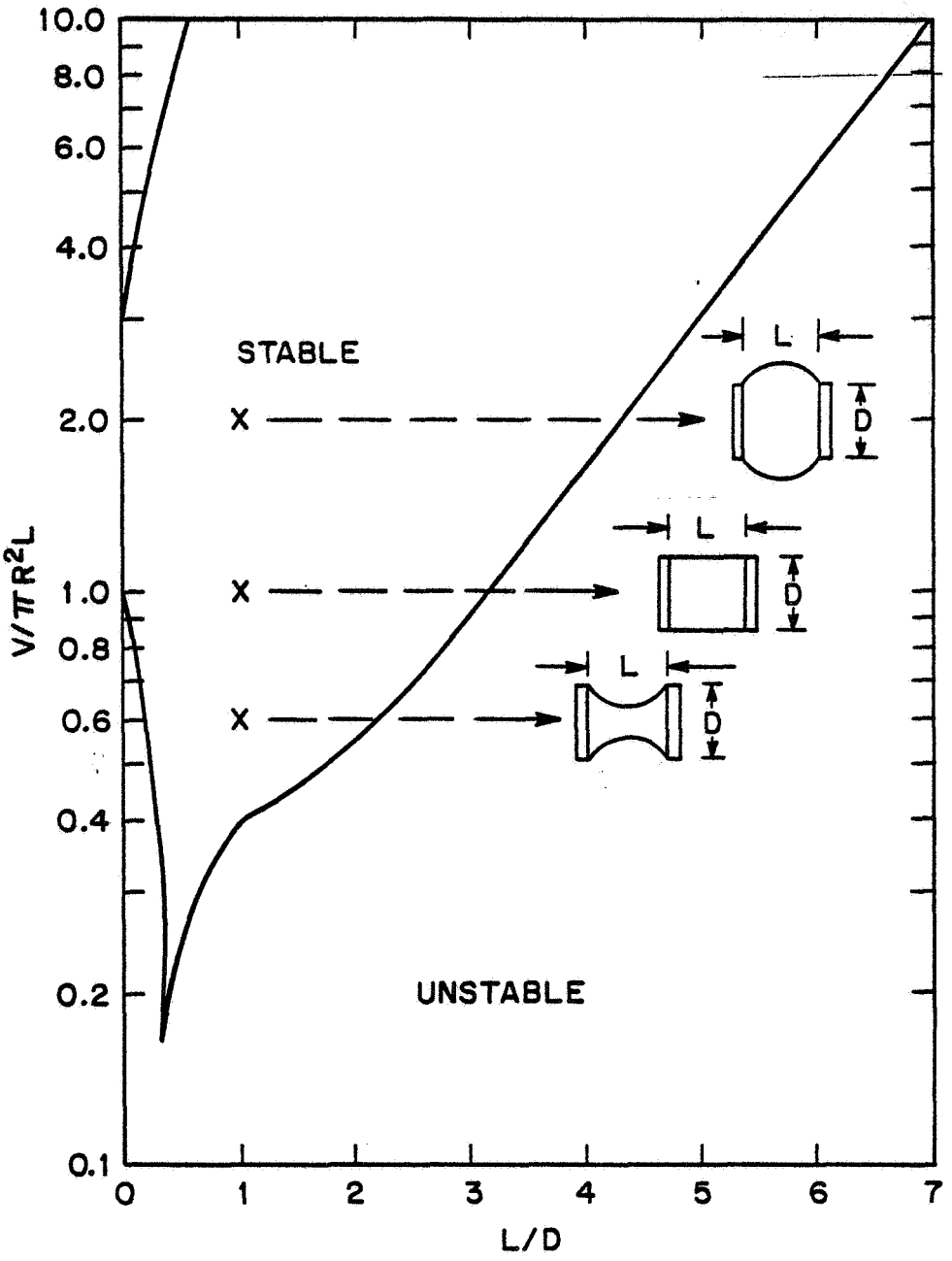

Fig. 7. Stability region of the surface of cylindrical liquid zones of various shapes contained between equal diameter end discs - from Gillette and Dyson.(18)

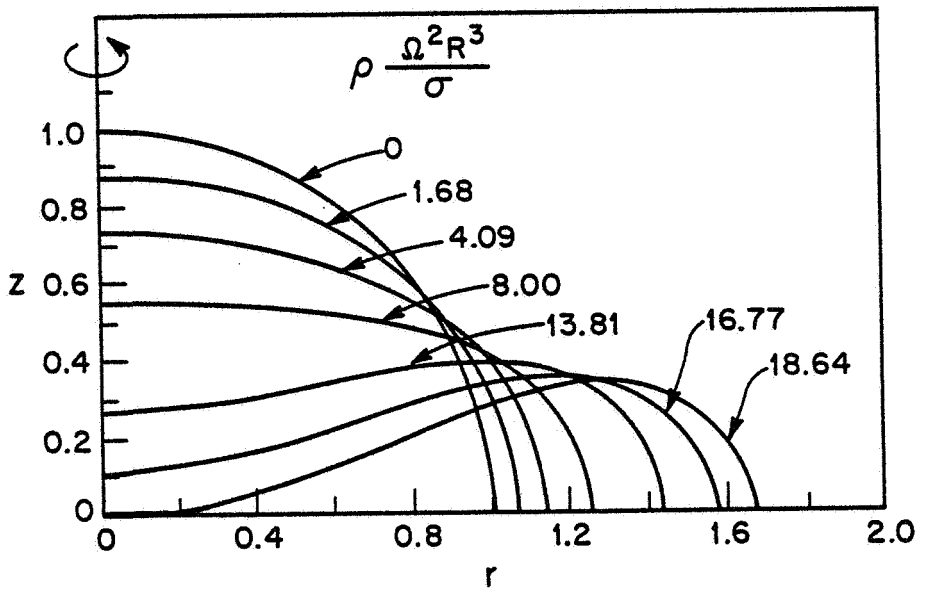

Fig. 8. Calculated shape deformations of an initially spherical liquid drop of radius, R, rotating at increasingly fast rotation rates. Rotation axis is the z-axis and r is the equatorial radius - from Chandrasekhar.

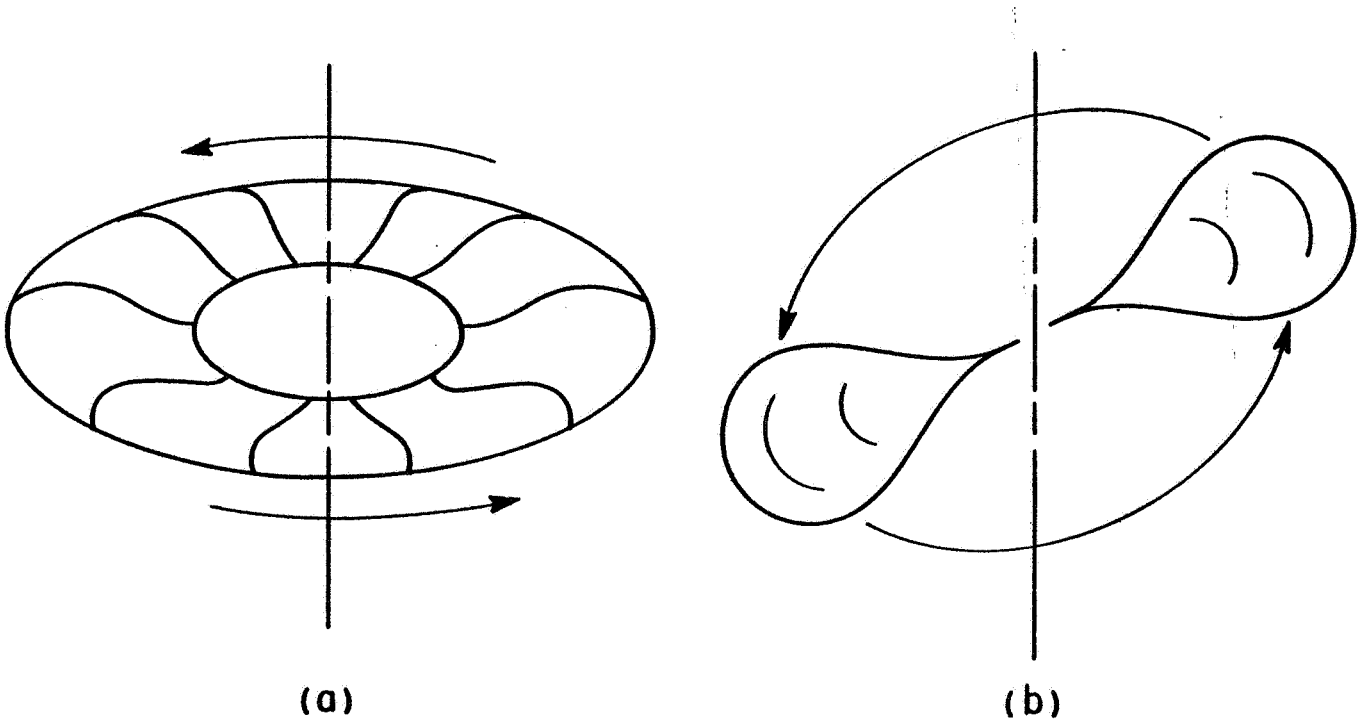

Fig. 9. Unstable shapes of a rotating liquid drop: (a) toroidal instability of Fig. 8, (b) dumb-bell instability observed in Skylab experiments.

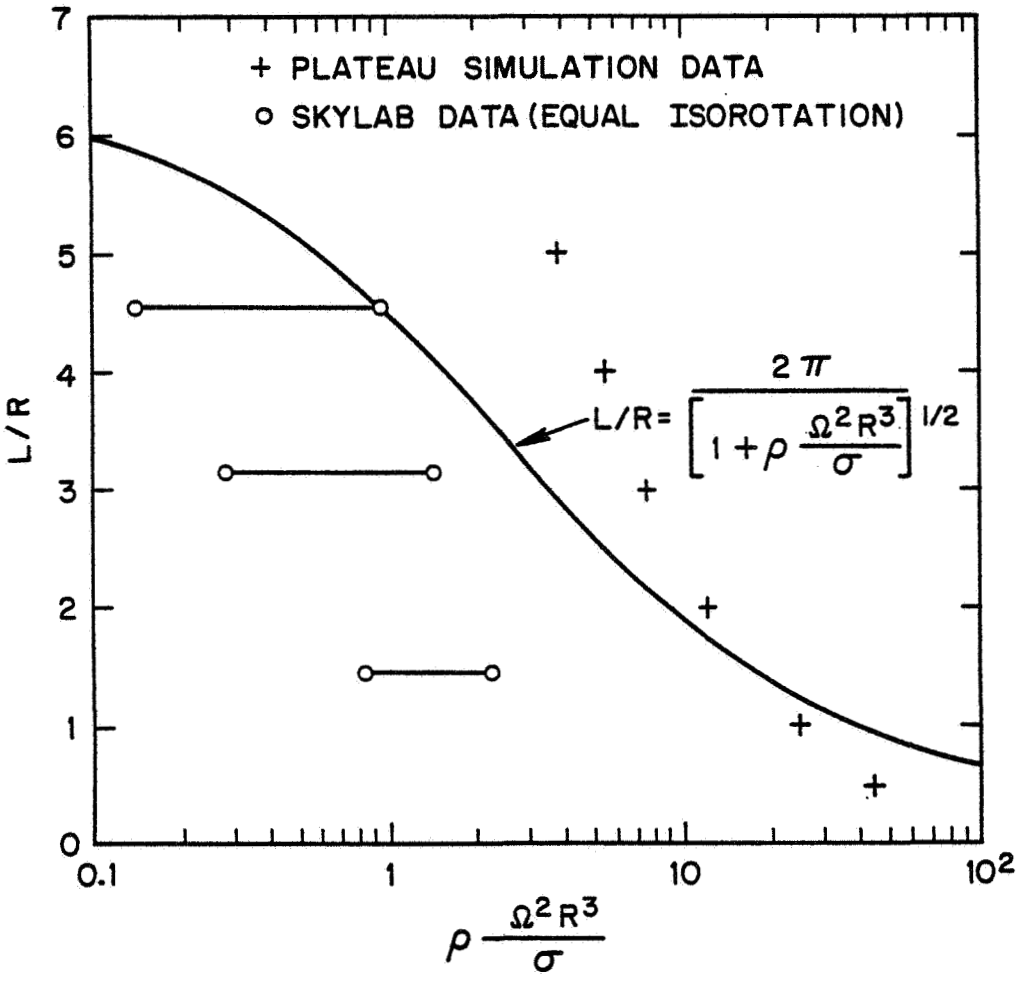

Fig. 10. Comparison of the rotational stability of cylindrical liquid zones in Plateau simulation and Skylab experiments with theory for axisymmetric modes.

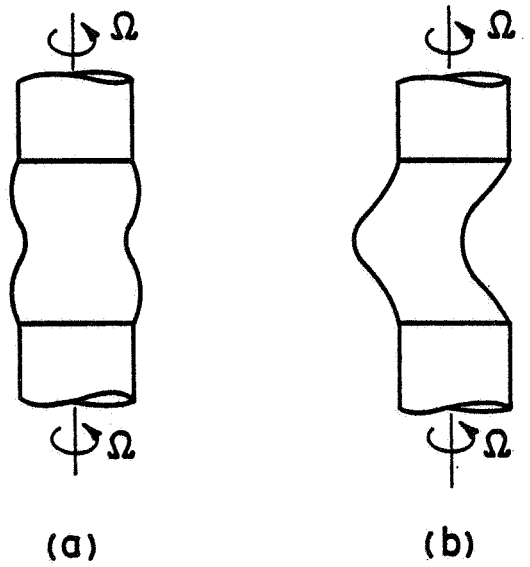

Fig. 11. Forms of rotating liquid zone surfaces: (a) axisymmetric mode observed in presence of highly viscous liquids, (b) nonaxisymmetric C-modes observed for water zones on Skylab.

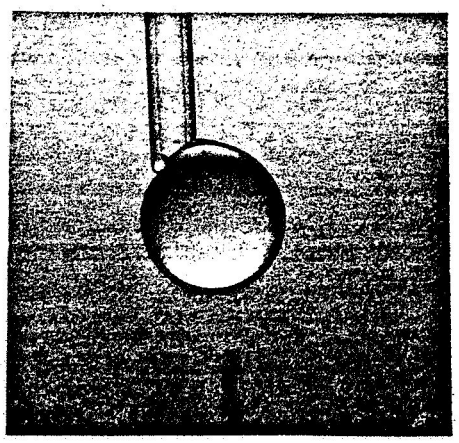

(a)

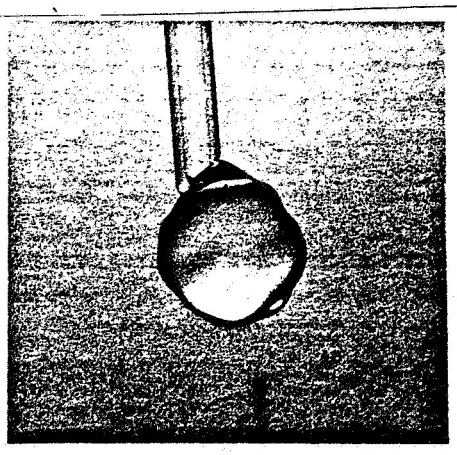

(b)

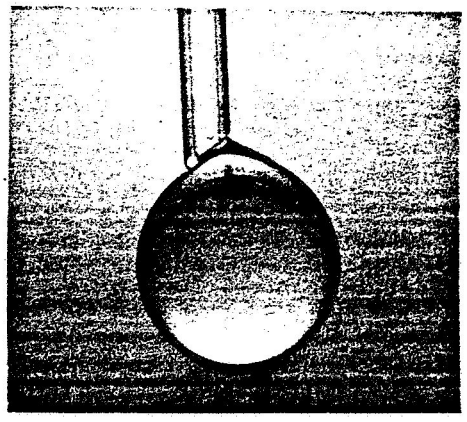

(c)

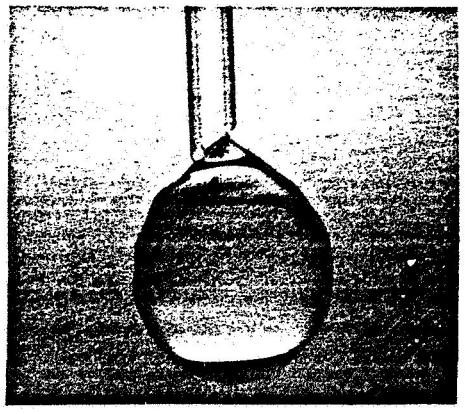

(d)

Fig. 12. Plateau simulation experiments using neutrally buoyant carbon tetrachloride plus benzene solution drops in water. (a) and (c) are static sessile drops, (b) and (d) are drops (a) and (c) respectively under vibrational conditions.

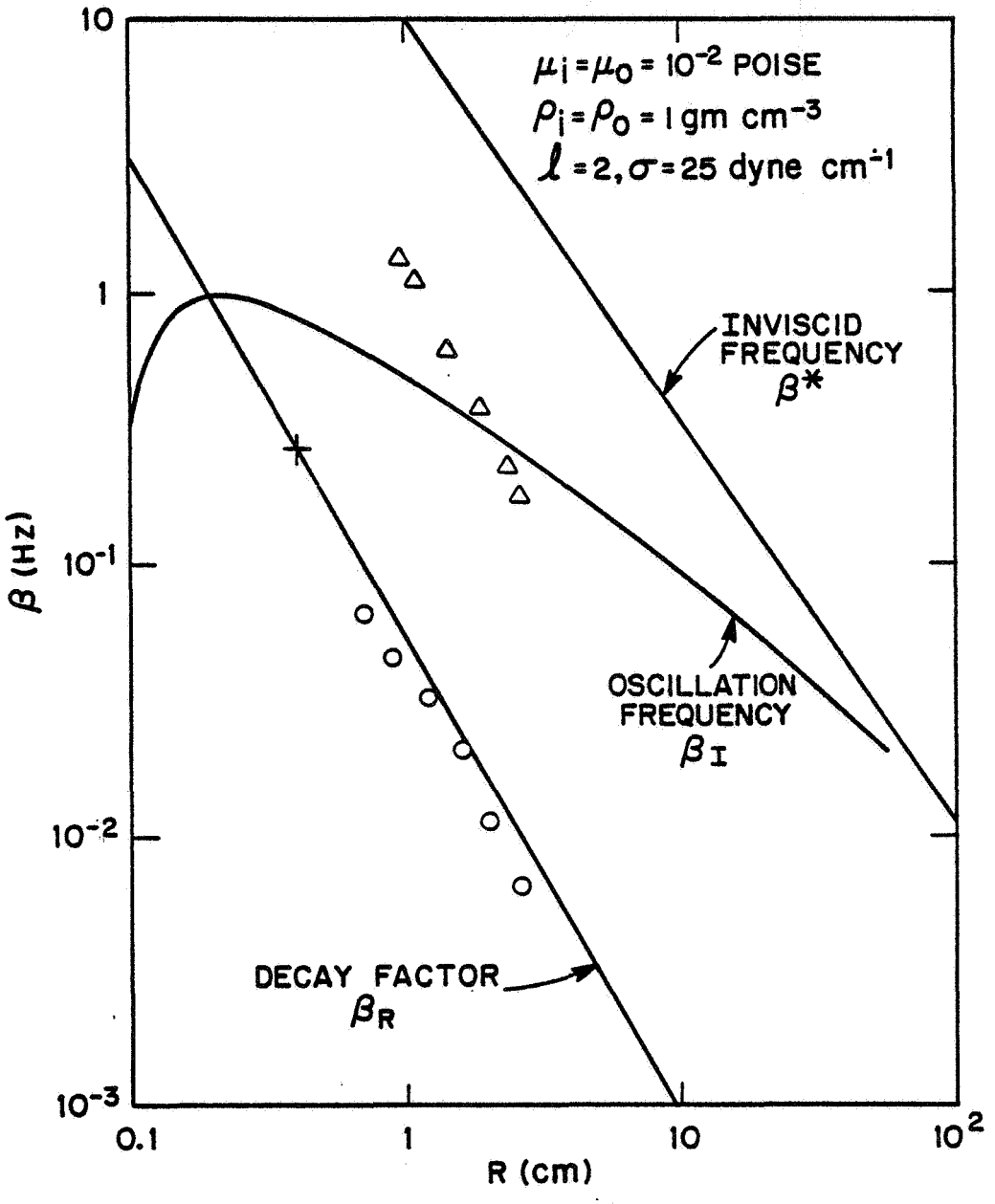

Fig. 13. Oscillation frequencies and decay rates of drops such as those in Fig. 12. Solid curves theoretically determined by Miller and Scriven.[27]

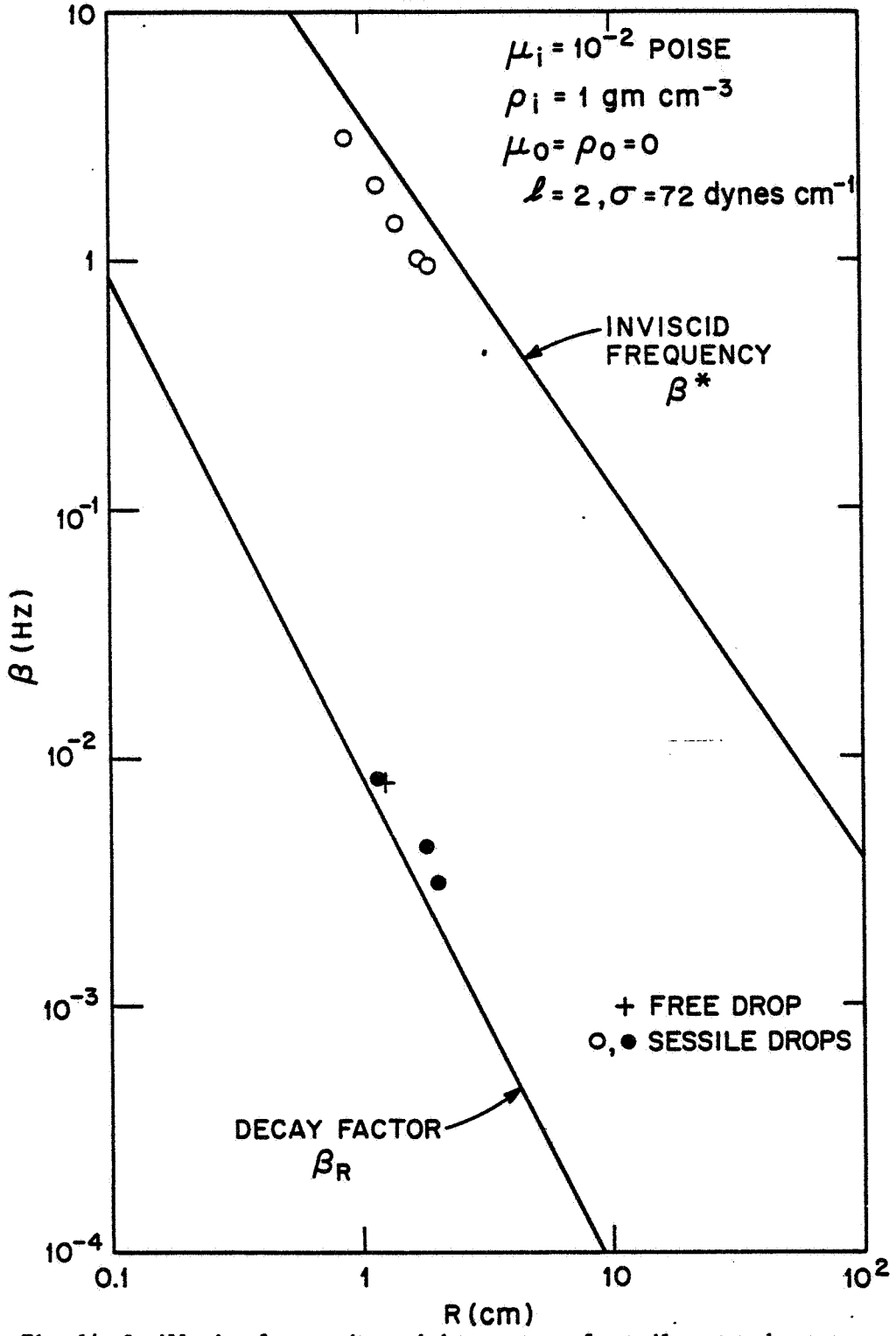

Fig. 14. Oscillation frequencies and decay rates of sessile water drops as measured from Skylab IV video-tape and compared to the theoretical solid curves of Miller and Scriven.(27)

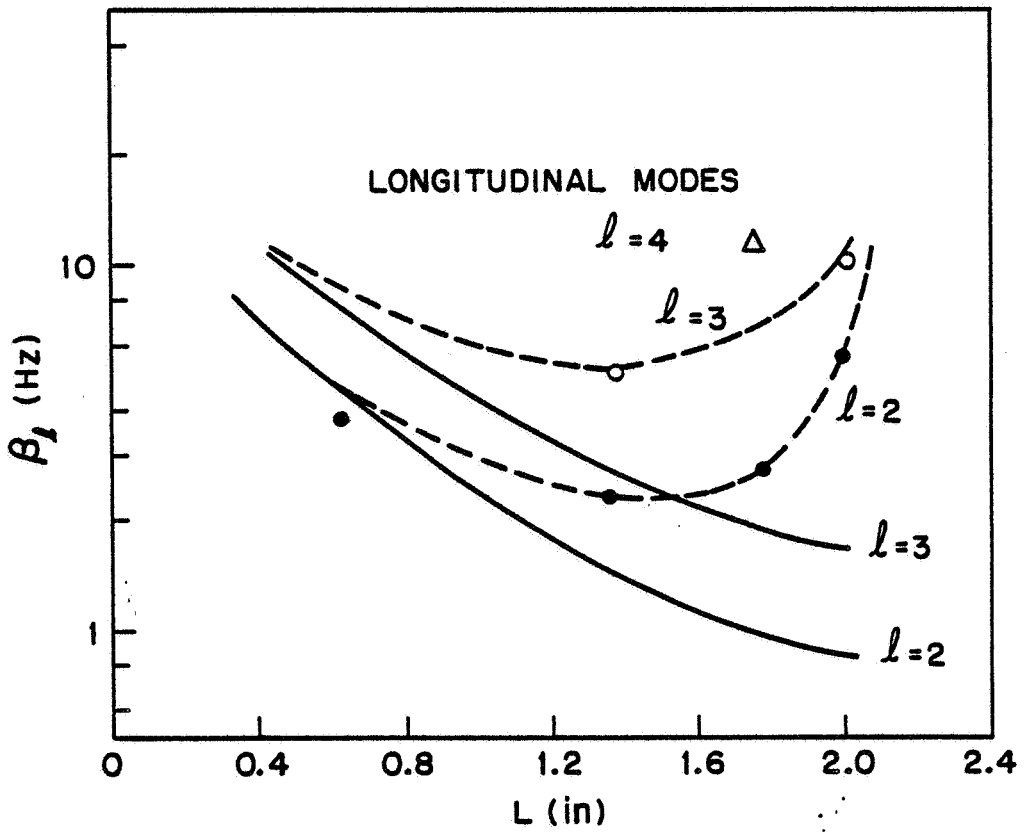

Fig. 15. Longitudinal oscillation frequencies of cylindrical liquid zones as measured from Skylab IV experiments as compared to the theoretical solid curves of Lamb.(26)

D12

THERMOCAPILLARY FLOW IN A CYLINDRICAL LIQUID DROP AT ZERO GRAVITY*

Chong E. Chang and William R. Wilcox
Chemical Engineering and Materials Science Departments
University of Southern California, Los Angeles, California 90007

ABSTRACT

Surface tension driven flow in the floating zone melting geometry was studied by means of computer solution of the differential equations for heat and momentum transfer. At small temperature differences one cell is formed in the top of the zone, and its mirror image in the bottom of the zone. They appear somewhat like vortex rings (smoke rings). As the temperature differences increase, secondary cells form and the flow probably becomes oscillatory. High differences produce turbulence. For silicon, effective heat shields are required to avoid turbulence, and the flow is not appreciably influenced by zone motion or by earth's gravity. The laminar cells do not have a strong influence on the heat transfer with good thermal conductors. Radiant heating of poor thermal conductors may result in oscillatory flow even with small driving forces.

INTRODUCTION

Floating zone melting is used commercially and in research for crystal growth and for purification of high melting materials. The melt does not contact a crucible, as shown schematically in Fig. 1. Heating may be by radiation, by an electron beam, or by induction from a surrounding high frequency coil. The zone is moved through the solid either by moving the heater or by moving the solid rods bordering the zone. There are five sources of convection in a floating zone:

1) When the zone is taken as stationary, there is a flow through the zone generated by melting at one solid-liquid interface and freezing at the other, due to movement of the zone through the solid.

2) Convection due to rotation of the two solid rods. (Slow rotation is sometimes used to maintain a cylindrical zone and growing rod.)

3) With induction heating one obtains electromagnetic stirring, which is difficult to calculate.

4) Buoyancy-driven natural convection due to interaction of a gravitational or accelerational field with density variations in the melt.

5) Surface-tension driven flow due to variations in surface tension along the melt surface.

* Supported by NASA under contract NAS8-29847

The purpose of the calculations described here was to estimate the magnitude of the surface-driven (Marangoni) flow and its influence on heat and mass transfer. Mass transfer influences the degree of purification and the homogeneity of single crystals. Heat transfer influences the perfection of the crystals, the stability of the zone, and sometimes influences the homogeneity as well, through its effect on the freezing interface shape. In order to determine the influence of surface driven flow on zone melting, the partial differential equations for momentum and heat transfer were considered. The momentum equations were expressed in finite difference cylindrical stream-function form, and solved by the Gauss-Seidel iteration method (1). The Newton-Raphson method was used to solve the heat transfer equations, with an over-relaxation parameter of 1.9 for low Prandtl numbers and an underrelaxation for high Prandtl numbers. Solutions were obtained for two situations--a parabolic temperature profile along the melt-vapor surface and for a ring heat source at the center of the zone. The parabolic profile corresponds approximately to radiant heating, and the ring source corresponds to electron beam heating. The mass transfer equation coupled with the computed flow fields were employed to find the impurity concentration fields in the melt at steady state.

The results of the calculations are expressed in dimensionless form and for the physical properties of silicon with a 1 cm x 1 cm zone, as a concrete example. For molten silicon the melting point is 1410°C, the Prandtl number is 0.023, the Schmidt number is about 5, $\rho_f(\partial\gamma/\partial T)/\mu^2$ is 14,000, and the emmissivity is assumed to be 0.3 for both the melt and the solid. Earth's gravitational field and ordinary zone travel rates were found to have negligible influence on the convection for silicon.

RESULTS

Dimensional analysis of the momentum equations produced a parameter characterizing the driving force for surface driven flow, $M = a(T_o-T_m)\rho_f(\partial\gamma/\partial T)/\mu^2$, where a is the radius of the zone, T_o is the temperature of the surface of the melt at the center of the zone, T_m is the interface temperature, ρ_f is the density of the melt, γ is the surface energy or surface temperature, and μ is the viscosity.

Streamlines for a Parabolic Temperature Profile at the Free Melt Surface (Radiation Heating)

For simplicity, a parabolic temperature profile along the melt surface was assumed for our initial calculations. This enabled us to solve the momentum equations without simultaneously solving the heat transfer equations. A parabolic profile, with a maximum at the center, seems reasonable for radiant heating. The dimensionless surface tension parameter M increases as the radius of the zone a and the temperature variation along the melt surface increases. In Figures 2 through 4, the streamlines for parabolic temperature profiles are shown to illustrate the effect of increased values of M (350, 3500 and 7000). Donut-shaped vortex cells were formed. With M = 35 and 350 only two cells are generated, and the centers of the vortices move closer toward the liquid/solid interfaces as M increases. With M = 3500, however, which corresponds to a

condition of a = 0.5 cm and (T_o-T_m) = 0.5°C for silicon,* secondary vortex cells were induced behind the primary vortex, as shown in Figure 3. As the value of M was further increased up to 7000, third and fourth vortices were produced, as shown in Figure 4. These multiple vortices are probably indicative of oscillations and incipient turbulence, which cannot be calculated in a steady state analysis (oscillations are frequently found with free convection in enclosed cavities between laminar and fully turbulent flow). The maximum velocity of the melt for 1 cm diameter silicon with (T_o-T_m) = 1.0°C is calculated to be 2 cm/sec.

Fluid Flow Coupled with Heat Transfer
(Electron Beam Heating)

Electron beam heating is commonly used in floating zone melting and was considered as another heating mode. A ring heat source at the center of the zone was assumed. Rather than specify the power input, the circumferential temperature T_o at the center of the zone was specified for convenience in analysis. The procedure used to solve the coupled heat-momentum transport problem was as follows:

1) The temperature field for conduction was computed by neglecting convective heat transfer.

2) The surface temperature profile from 1) was utilized to calculate the first approximate solution of fluid flow.

3) The temperature field was recalculated using the flow fields from 2).

4) Steps 2) and 3) were repeated until the temperature and the fluid flow fields no longer changed appreciably.

The resulting streamlines with M = 350** are drawn in Figure 5 in which we took values for silicon with the surroundings at the melting point, i.e., the heat shielding about the zone is extremely effective. While this does not correspond exactly with reality, it does show the correct features. Comparing with Figure 2, we see that the vortex centers are shifted nearer to the heat source from the liquid/solid interfaces. This is because the steepest temperature gradient is at the center of the zone. The maximum velocity for silicon was 0.55 cm/sec. Comparing the temperature fields with surface tension driven flow for M = 350 with those for pure conduction, there was no significant change except for a slight one near the center of the zone. This indicates that conduction is much greater than convective heat transfer as would be expected for the small Prandtl number for silicon. The vorticity fields for M = 350 are shown in Figure 6. The maximum vorticity and its location for various conditions are also summarized in Table I.

Influence of Gravity on Flow

In a vertical silicon melt with M = 350 at earth's gravity the flow and

*Without heat shielding, we estimate the temperature difference (T_o-T_m) would be on the order of 10 to 20°C, and the flow would be turbulent.

**For electron beam heating of 1 cm diameter silicon, the Marangoni number Ma is about 1/50 of the value of M. Without heat shielding Ma is estimated to be about 60,000.

temperature fields in the floating zone do not change appreciably from those at zero g.* When the acceleration is increased to ten times the earth's gravity, the lower vortex contracts while the upper one is expanded, particularly at the center of the zone where the flow field is relatively weak. This is shown in Figure 7 and may be compared with Figure 5 at zero g. This means that surface driven flow predominates even on earth for many materials for radiant and electron beam heating. It may even be important when induction heating is employed and may account for some of the compositional inhomogeneities observed.

Influence of Prandtl Number

The Prandtl number was increased from 0.023 to 0.3 and 2.0 by increasing the specific heat, and keeping the viscosity and the thermal conductivity of the melt constant. As the Prandtl number increases, the temperature gradients along the free liquid surface (for fixed T_o-T_m) increase near the heat source and also near the liquid/solid interfaces, but decrease significantly in between. Since the convective heat transfer becomes more significant as a result of increasing the Prandtl number, the isotherms are increasingly distorted from those of pure conduction. This, in turn, causes changes in the flow field. For example, the center of the vortex cell near the liquid/solid interface shifts closer to the interface as the Prandtl number increases, as shown in Figure 8.

Influence of Zone Travel on Hydrodynamics

The effect of zone motion on the flow field was found to be negligible in all of our calculated streamlines for zone travel rates of up to 5 cm/hour in silicon.** However, the effect becomes significant when the zone travel rate becomes comparable with the velocity of surface-driven flow.

The flow field for electron beam heating with M = 35 is taken as a model case in order to show the influence of zone travel on hydrodynamics in the floating zone. The maximum velocity of the melt for M = 35 is 0.07 cm/sec (or 250 cm/hour), and the average velocity is about 70 cm/hour. In Figure 9, the streamlines in floating zone melting of silicon at zero g are shown for a freezing rate of 30 cm/hour. The lower vortex cell floats away from the bottom interface and its size is reduced as the zone travel rate increases.

CONCLUSION

For silicon we have seen that thermocapillary flow is very vigorous, and is turbulent when heat shields are not employed. The buoyancy flow is negligible in comparison. With moderate heat shielding, oscillatory convection is likely, but was not studied here. Zone motion does not have an appreciable effect on the convection unless the temperature gradients along the melt surface are made very small by effective heat shielding. With laminar flow, the convection has only a small influence on heat transfer at small Prandtl number (Pr << 1), but a large influence for Pr > 1.

---

*Only temperature variations were considered.

**A zone travel rate of 5 cm/hour is typical for growth of single crystals, while faster rates are employed for vacuum outgassing and lower rates for zone refining.

REFERENCES

1. B. W. Arden and K. N. Astill, "Numerical Algorithms: Origin and Applications," Addison-Wesley, Reading, Mass. (1970)

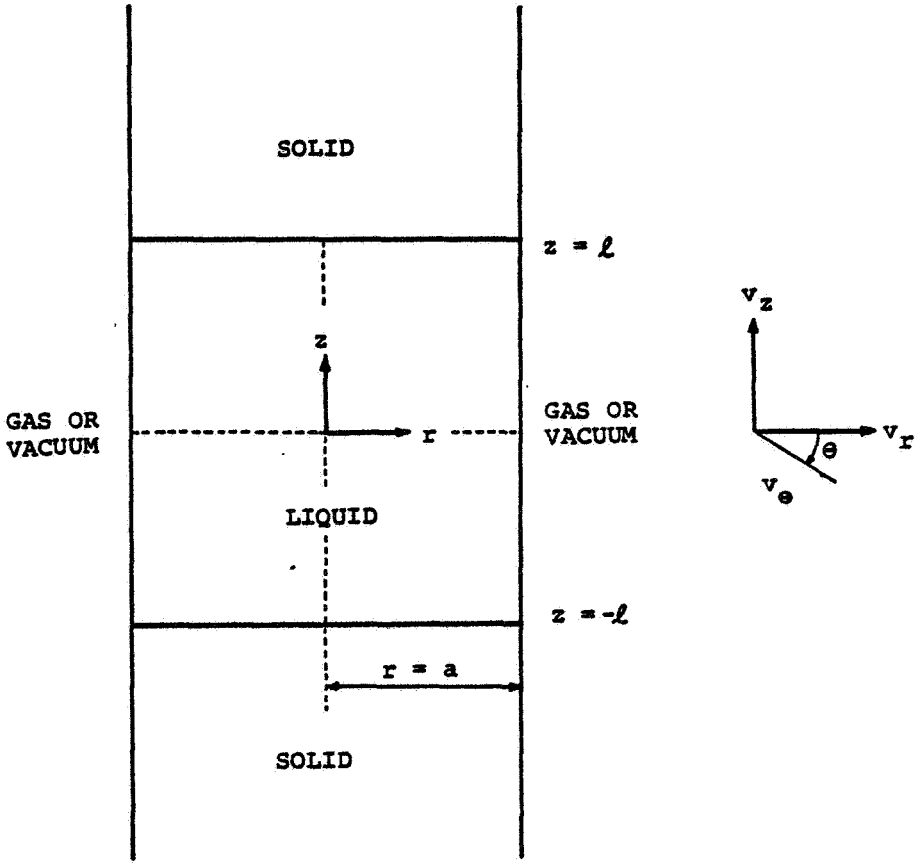

Fig. 1. Idealized diagram of floating zone melting.

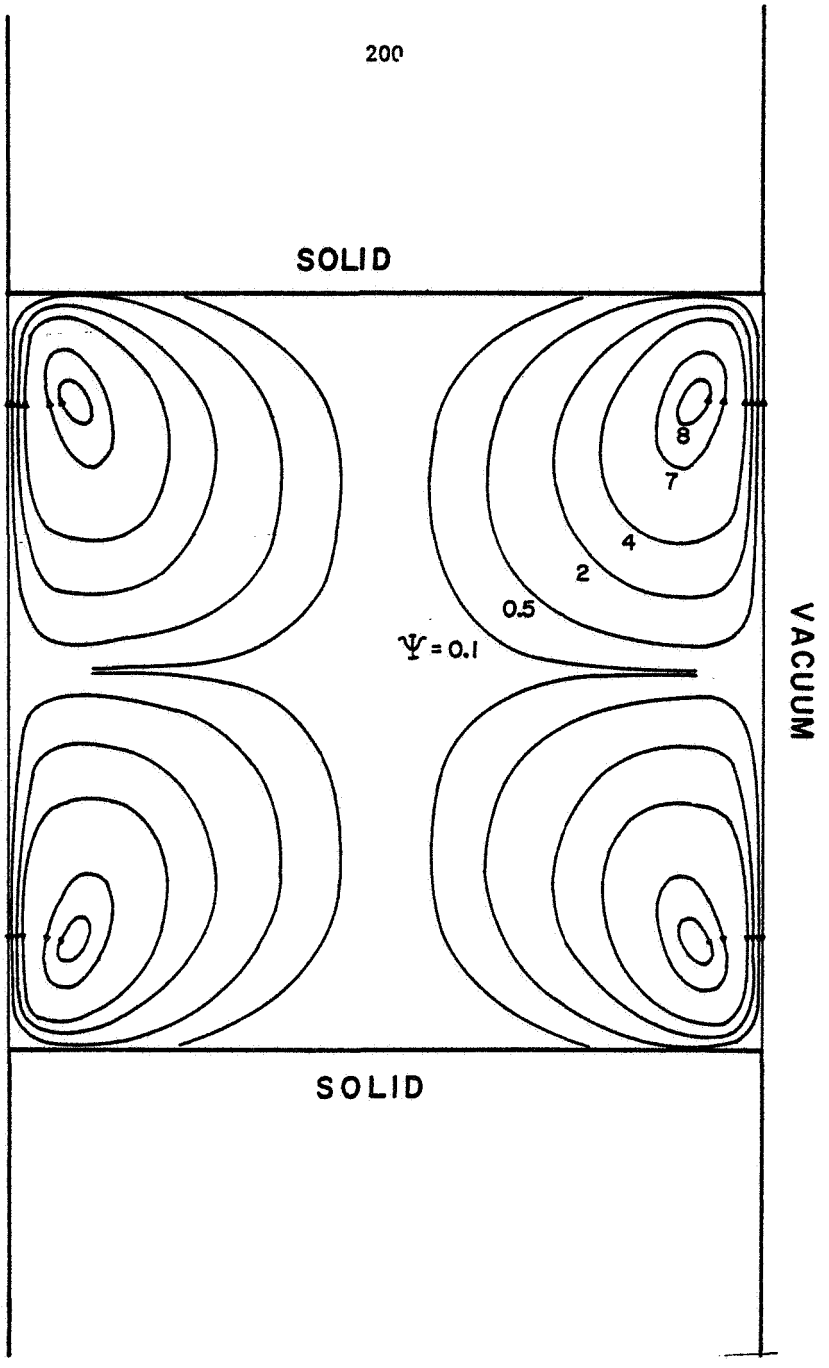

Fig. 2. Computed dimensionless streamlines ψ for surface tension driven flow in a floating zone at zero gravity with a parabolic temperature profile on the free liquid surface with M = 350 and v_c = 0. For silicon with $(T_o - T_m)$ = 0.05°C and a = 0.5 cm.

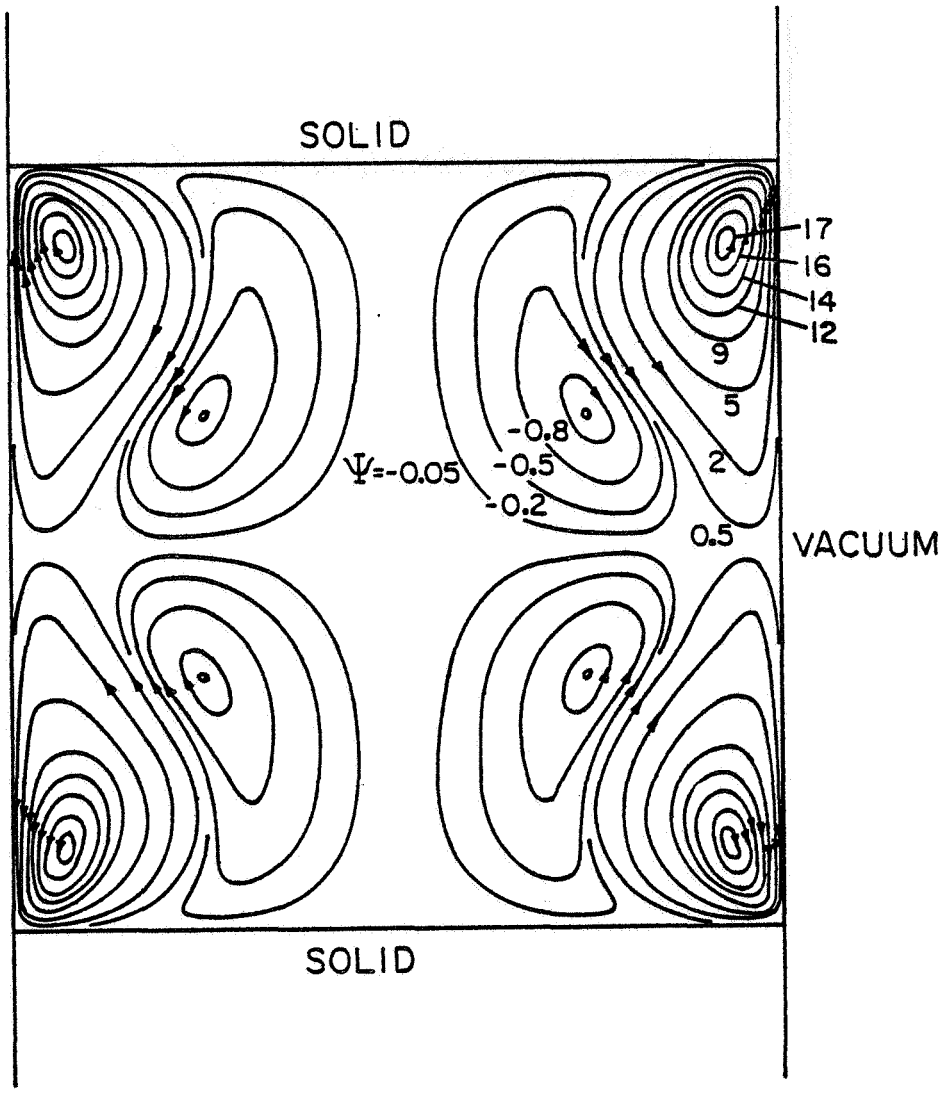

Fig. 3. Computed dimensionless streamlines ψ for surface driven flow in a floating zone at zero gravity with a parabolic temperature profile on the free liquid surface with M = 3500 and $v_c = 0$. Silicon with $(T_o - T_m) = 0.5^oC$ and a = 0.5 cm.

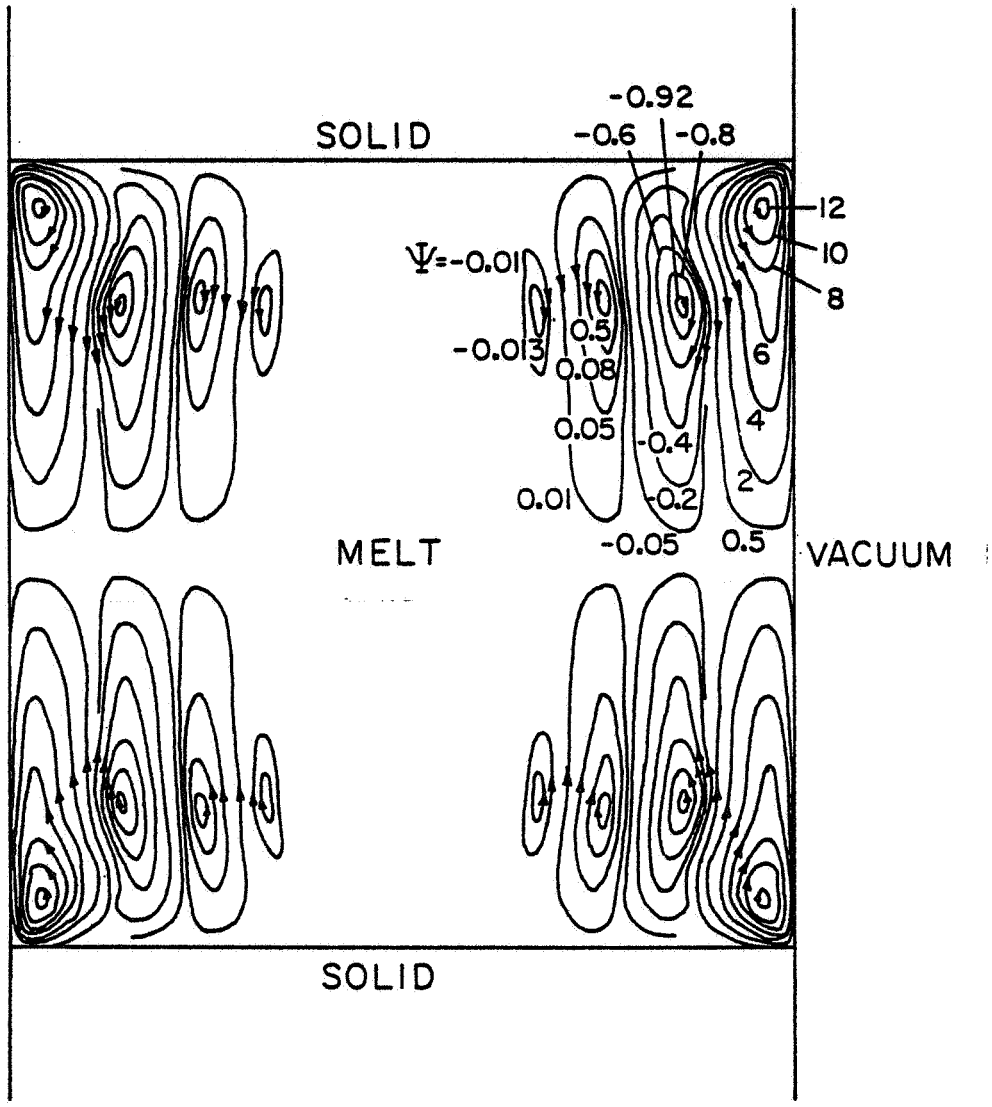

Fig. 4. Computed dimensionless streamlines ψ for surface tension flow in a floating zone at zero gravity with a parabolic temperature profile on the free liquid surface with M = 7000 and v_c = 0. Silicon with (T_o-T_m) = 1.0°C and a = 0.5 cm.

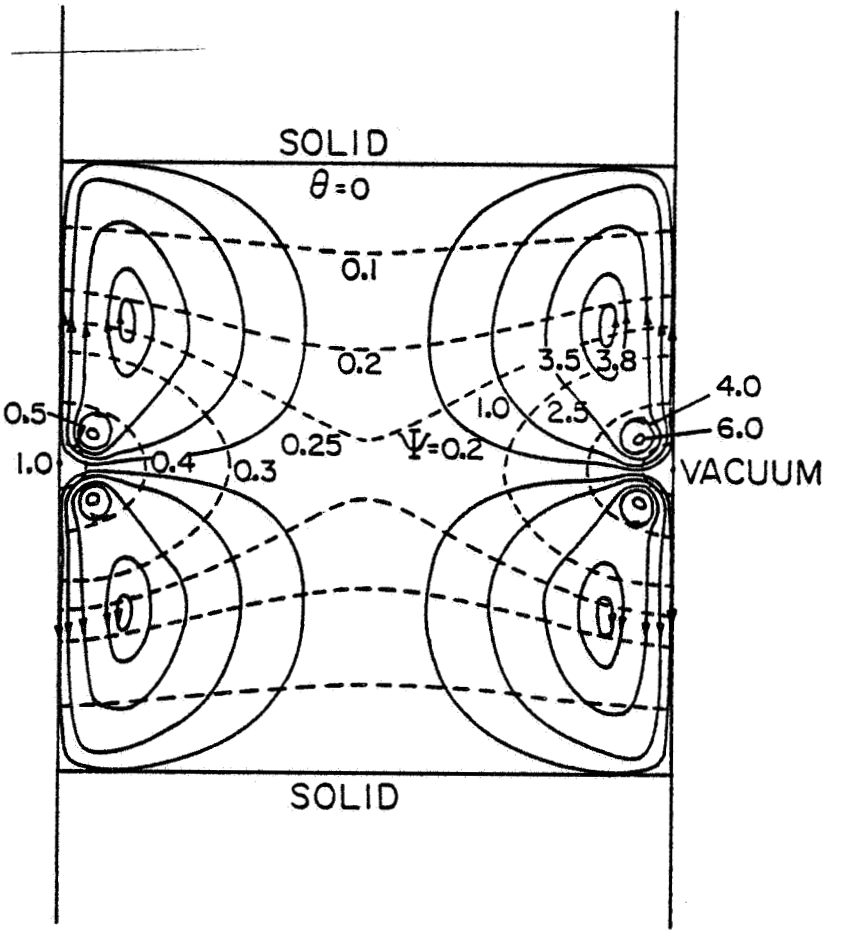

Fig. 5 Isotherms θ and streamlines ψ at zero gravity for electron beam heating of silicon with (T_o-T_m) = 0.05°C, $T_c = T_m$, ε_s = 0.3, a = 0.5 cm, M = 350, Pr = 0.023, v_c = 0.

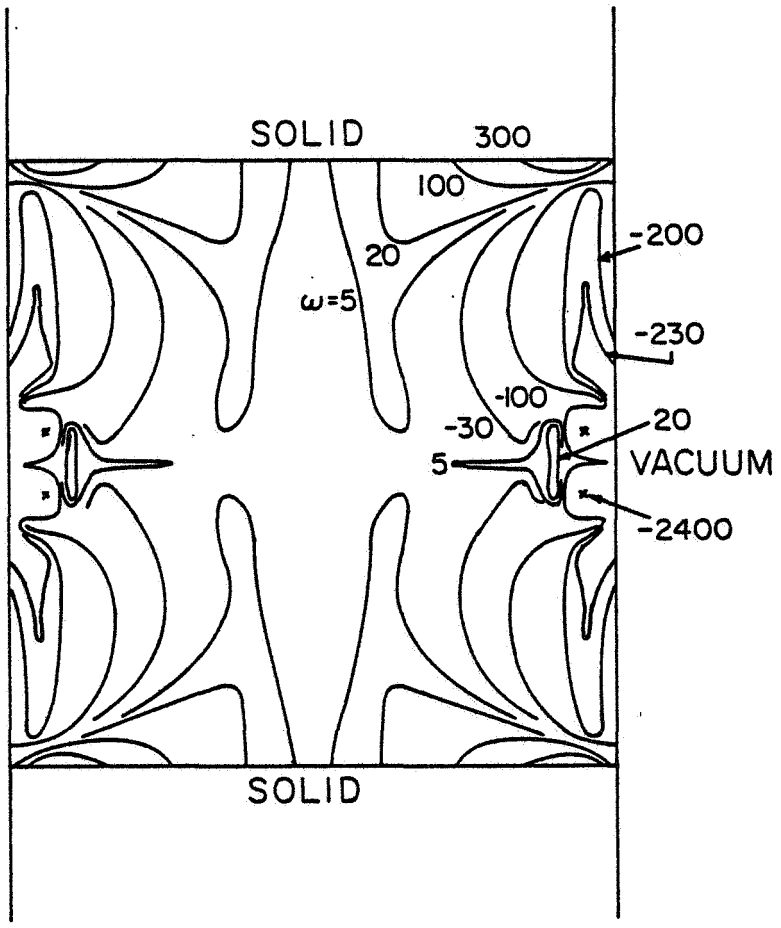

Fig. 6. Dimensionless vorticity field ω corresponding to the streamline field shown in Figure 4.

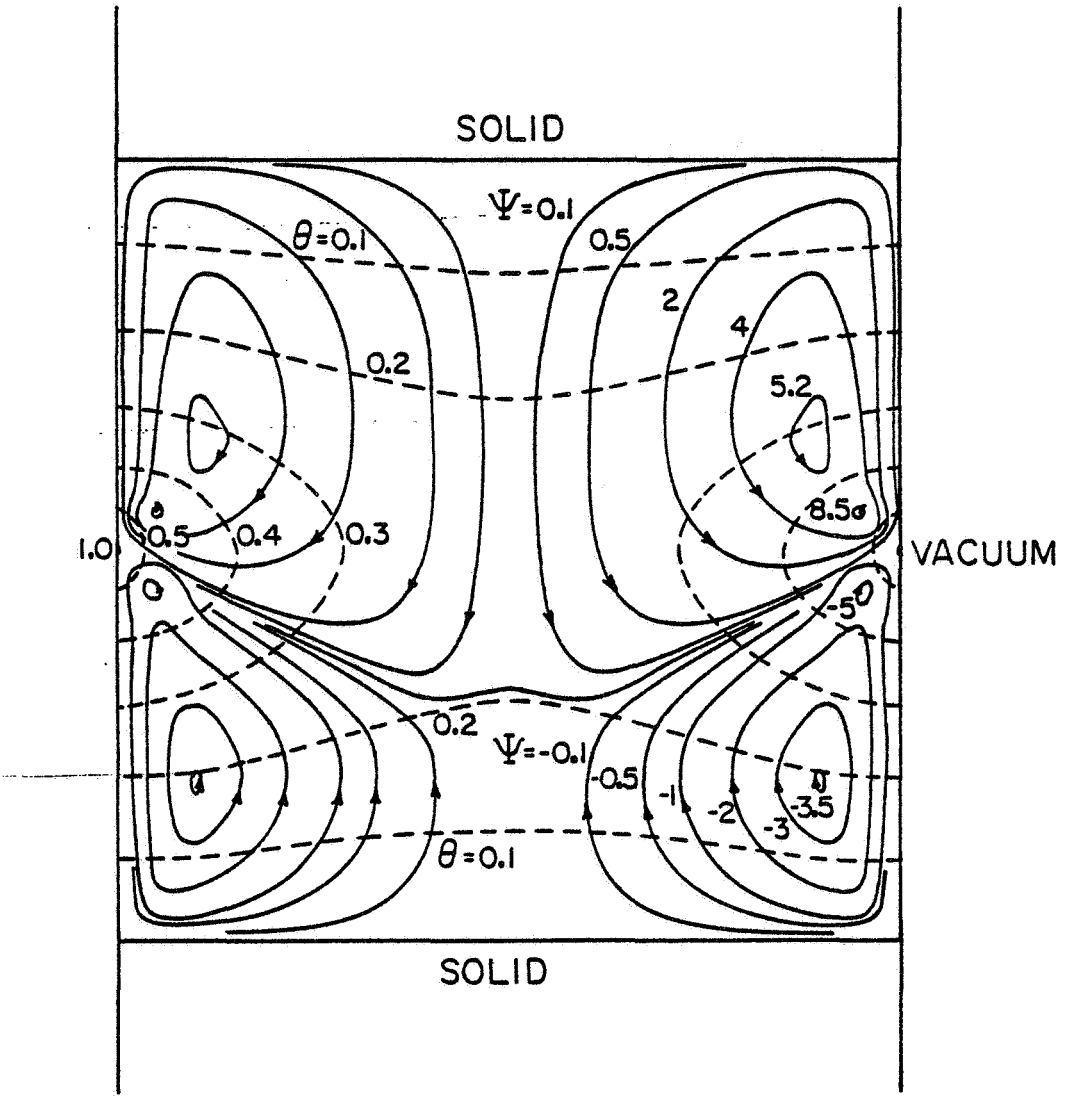

Fig. 7. Streamlines and isotherms for combined surface-driven and buoyancy-driven flow with Gr_h = 775. Other conditions are the same as Figure 4.

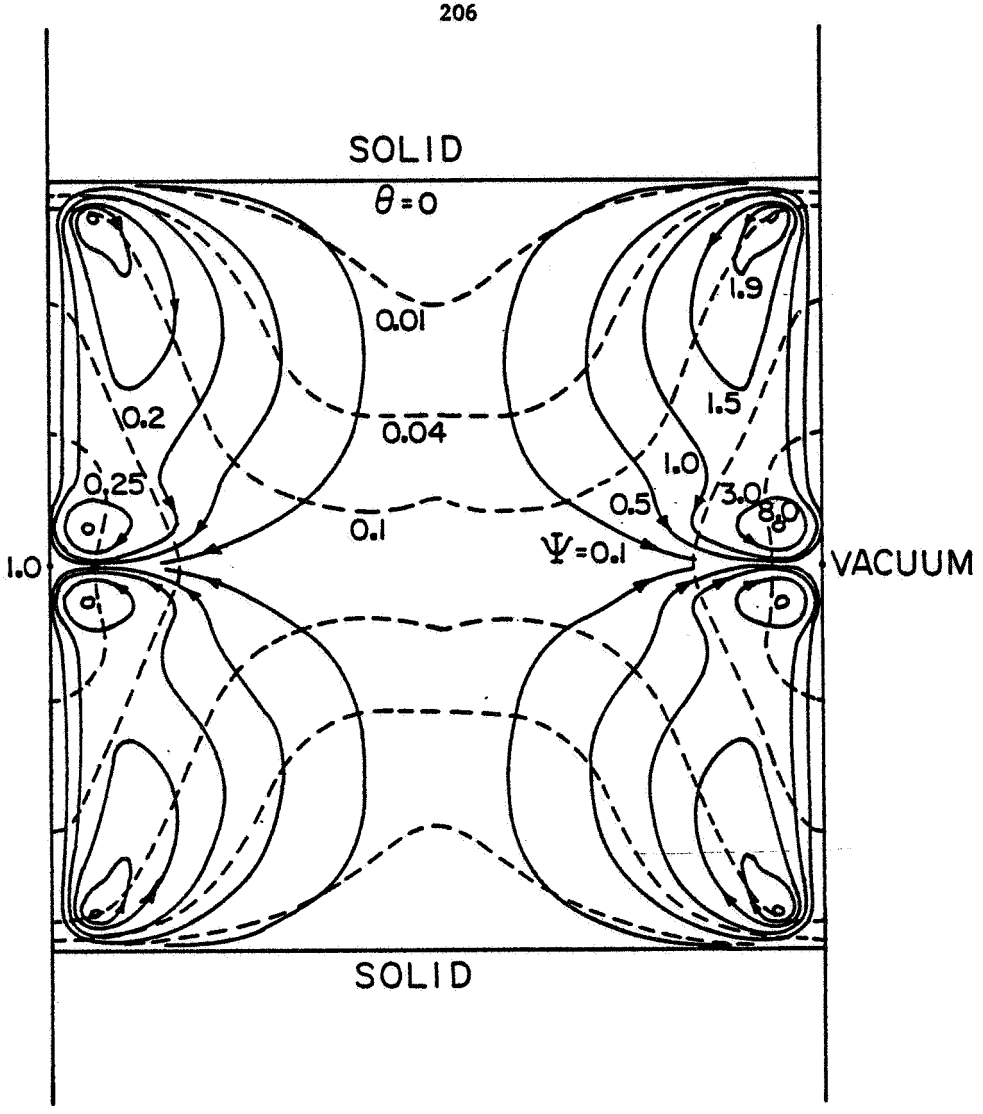

Fig. 8. Isotherms θ and streamlines ψ for the same conditions as in Figure 4, except Pr = 2.

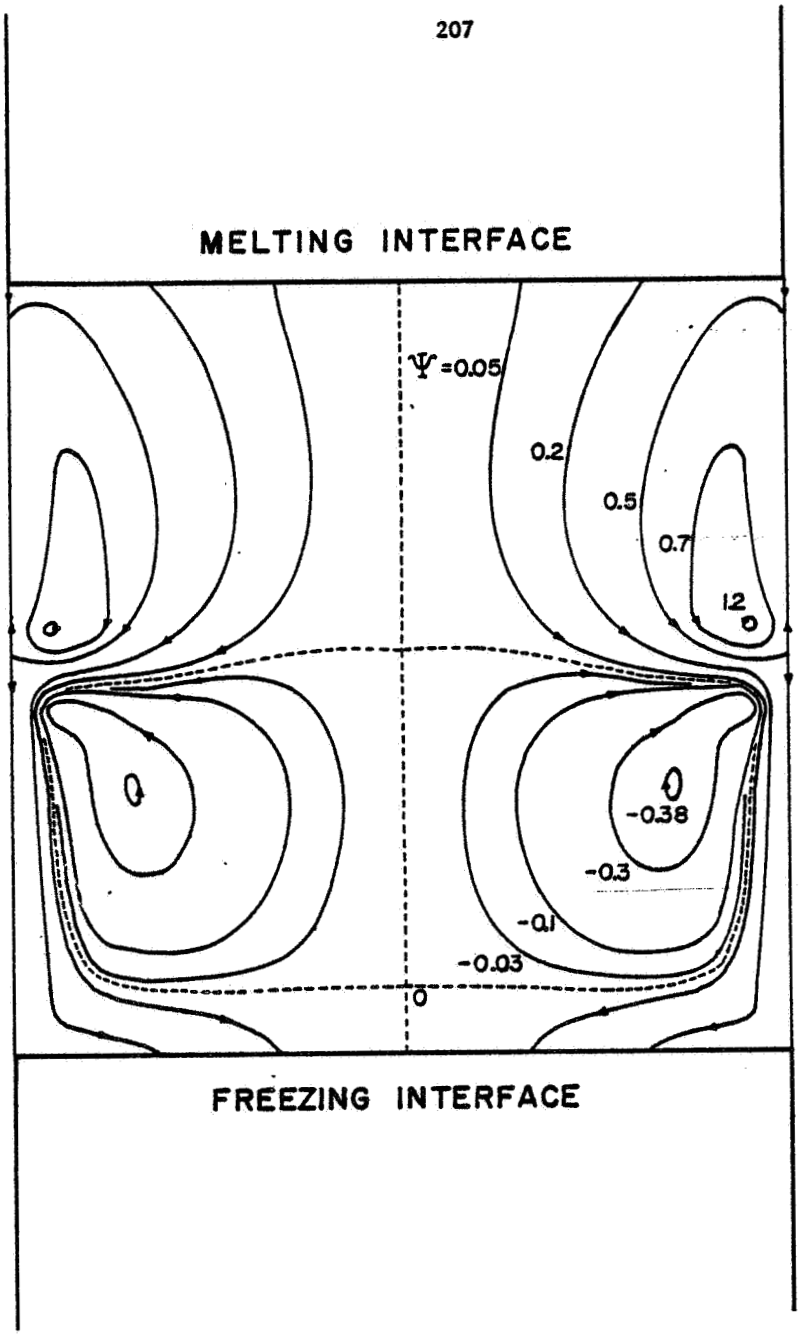

Fig. 9. Streamlines ψ at a zone travel rate of 30 cm/hour with M = 35, Pr = 0.023. For silicon, a = 0.5 cm, (T_o-T_m) = 0.005°C, $T_c = T_m$, ε_s = 0.3.

D13

STEADY THERMOCAPILLARY CONVECTION CELLS IN LIQUID DROPS

Alan L. Dragoo*
Institute for Materials Research, National Bureau of Standards
Washington, D. C. 20234

ABSTRACT

A nominally spherical drop is used as a model for a theoretical analysis of thermocapillary convection and for estimates of convective flow rates in "levitated" melts at zero-g. Since in practice temperature fields and the resulting convective flow can be more complicated than the simple vertical temperature gradient and the single vortex ring, respectively, the convective flow arising from a general steady-state temperature field is analyzed. Expressions for the components of a steady velocity field are obtained by adapting the analytical method of Miller and Scriven. The vortex rings are illustrated by means of typical streamlines for the simpler, more symmetric, temperature fields. The circulation time is introduced as a measure of the rate of circulation in a convection cell and typical values are given for several materials.

INTRODUCTION

When buoyant forces are negligible, such as in a space laboratory, convective flows may still occur in a liquid as the result of gradients in the surface--or interfacial tension. These convective flows are commonly called the Marangoni effect although the Marangoni effect includes both this phenomenon of convection and the phenomenon of the deformation of a free liquid surface (Ref. 1). Among the causes of gradients in the surface tension are gradients in the concentration and in the temperature along the surface of a liquid.

Concentration and temperature gradients may not be completely eliminated in many processes, and in some instances, their presence may be necessary to produce the convection which is desired. The growth of crystals from a melt is a process in which the elimination of convection in the melt is desireable because convection produces non-uniform growth conditions, and, thereby, an increase in the number of dislocations in the crystal. The evaporative purification of a levitated melt is a process in which the opposite result is desired: rapid convection is important here because it increases the rate of purification by replenishing the impurity concentration at the surface and because it tends to maintain an uniform composition throughout the melt.

*Financial support was provided by NASA under contract W-13,475 #1.

The question of how much surface tension driven flows might enhance the rate of purification of a levitated melt at zero-g is the motivation for the work reported here. As a model which will begin to supply part of the answer to this question, we will consider thermocapillary convection--that is, convection resulting from a temperature gradient along the surface (Ref. 2)--in nearly spherical drops. The temperature field at the surface of the drop will be treated in a general way by writing it as an expansion in spherical harmonics. The model will examine one of the convective modes corresponding to one of the terms in the expansion of the surface temperature field. The equations of motion--the Navier-Stokes equations--will be solved within the assumptions of a steady-state and of creeping flow--terms which are nonlinear in the velocity will be ignored. The mathematical analysis will proceed along the lines of the method which Miller and Scriven (3) applied to the oscillations of a fluid droplet although here we will not retain the time-dependence of their problem. The physical boundary conditions will account for both the convective flow and for the deformation of the surface so that both aspects of the Marangoni effect will appear in the problem. The velocity field components which are obtained from the Miller-Scriven analysis will be used to derive the circulation time τ whose inverse characterizes the rate of circulation within a convection cell. An expression for τ will be worked out in detail for convection cells having axial symmetry. Estimates of τ will be given for a variety of materials when the convection pattern is a single, axially symmetric vortex ring. Also, relative circulation times will be calculated for several higher order, axially symmetric convective modes. Illustrations of these convective modes will be given.

THE TEMPERATURE FIELD

The temperature field responsible for the convection is considered to be a general, non-uniform, but steady, field which can be written as:

$$T(r,\theta,\phi) = T_o + \sum_{n=1} \sum_{m=0}^{n} \sum_{\sigma} T^{\sigma}_{mn} \, r^n Y^{\sigma}_{mn}(\theta,\phi) \quad (\sigma = e,o), \tag{1}$$

where,

$$Y^{e}_{mn} = P^{m}_{n}(\cos\theta) \cos m\phi \tag{2a}$$

$$Y^{o}_{mn} = P^{m}_{n}(\cos\theta) \sin m\phi \tag{2b}$$

are spherical harmonics as defined by Morse and Feshbach (4). The function $P^{m}_{n}(\cos\theta)$ is an associated Legendre polynominal. The simple case of a constant vertical temperature gradient through the drop--$Y^{e}_{mn} = P_1(\cos\theta) = \cos\theta$-- is a special case of the solution of Young, Goldstein and Block (5) who derived the velocity field in a bubble rising in a vertical temperature gradient.

SOLUTION OF THE NAVIER-STOKES EQUATIONS

To obtain the velocity field $u(r,\theta,\phi)$ and the hydrodynamic pressure field $p(r,\theta,\phi)$ within a drop of radius R, we solve the linearized Navier-Stokes equations

$$\mu\nabla^2\vec{u} = \nabla p \tag{3a}$$

$$\nabla\cdot\vec{u} = 0, \tag{3b}$$

where μ is the coefficient of viscosity. We impose the requirements

1) of a finite solution at $r = 0$;

2) of the kinematic condition $u_r(R) = 0$, where u_r is the radial component of the velocity; and

3) of the physical boundary conditions which will be examined in the next section.

Since Eqns. (3a,b) are linear, a general solution can be written as a superposition of all the modes. Thus, it is sufficient to find a solution for one of the modes (n,m,σ).

Eqns. (3a,b) can be integrated according to the method of Miller and Scriven. This method integrates (3a,b) in terms of u_r and the radial component of the vorticity, where the vorticity is defined by

$$\vec{\zeta} \equiv \nabla \times \vec{u}. \tag{4}$$

The results of the Miller-Scriven method which satisfy requirements "1" and "2" are

$$u_r(r,\theta,\phi) = -A^{\sigma}_{mn} r^{n-1} (R^2-r^2) Y^{\sigma}_{mn}(\theta,\phi) \tag{5a}$$

$$\zeta_r(r,\theta,\phi) = B^{\sigma}_{mn} r^{n-1} Y^{\sigma}_{mn}(\theta,\phi). \tag{5b}$$

The remaining integration constants A^{σ}_{mn} and B^{σ}_{mn} will be obtained from the physical boundary conditions in the next section.

The velocity components--u_θ and u_ϕ--can be obtained from u_r and ζ_r by a relation due to Sani (6);

$$\vec{u} = \hat{e}_r u_r + [r^2/n(n+1)]\ [\nabla_{II} R u_r - \hat{e}_r \times \nabla_{II} \zeta_r], \tag{6}$$

where $\hat{e}_r$ is the radial unit vector,

$$\nabla_{II} = \nabla - \hat{e}_r \frac{\partial}{\partial r} \tag{7}$$

is the surface gradient operator and R is the operator

$$\frac{1}{r^2} \frac{\partial}{\partial r} r^2. \tag{8}$$

Eqn. (4) and the results for u_r, u_θ, u_ϕ can be used to derived ζ_θ and ζ_ϕ.

The hydrodynamic part $p(r,\theta,\phi)$ of the pressure can be found by taking the divergence of (3a) which yields $\nabla^2 p = 0$.

Thus,
$$p(r,\theta,\phi) = F^{\sigma}_{mn} r^n Y^{\sigma}_{mn}(\theta,\phi). \tag{9}$$

The coefficient F^{σ}_{mn} can also be obtained from (3a) by

$$\vec{r}\cdot\nabla^2\vec{u} = \nabla^2(ru_r) = (r/\mu)(\partial p/\partial r), \tag{10}$$

from which it can be shown that

$$F^{\sigma}_{mn} = 2(2n+3)\mu A^{\sigma}_{mn}/n. \tag{11}$$

PHYSICAL BOUNDARY CONDITIONS

The balance of stresses at the surface requires:

1) that the normal stress on the surface due to the hydrostatic pressure and to the motion of the fluid is balanced by the surface tension; and

2) that the shear stresses due to the variation of the surface tension are balanced by the fluid motion.

The deformation of the surface must be included in these conditions. The deformation is assumed to be small, so that

$$R + \Delta R = R\,[1 + \varepsilon(\theta,\phi)], \tag{12}$$

where ΔR is the displacement of the surface and

$$\varepsilon(\theta,\phi) = E^{\sigma}_{mn} Y^{\sigma}_{mn}(\theta,\phi) \tag{13}$$

is a radial strain. The coefficient E^{σ}_{mn} also must be obtained from the boundary conditions.

The normal stress due to the fluid

$$-p_{rr} = p_o + F^{\sigma}_{mn} R^n Y^{\sigma}_{mn} - 2\mu(\partial u_r/\partial r)\big/_{r+R^*} \tag{14}$$

is balanced by the surface tension produced stress

$$\gamma\left(\frac{1}{R_1} + \frac{1}{R_2}\right), \tag{15}$$

*A simplification of the surface conditions is introduced at this point by neglecting the interfacial dilational elasticity and the interfacial shear elasticity which contribute an interfacial viscosity term to the normal stress equations--see Scriven (7) and Miller and Scriven (5) for discussions of these properties.

where γ is the local value of the surface tension and R_1 and R_2 are the principal radii of curvature. For small deformations of the surface of a spherical drop, Lamb (8) has shown that

$$\frac{1}{R_1} + \frac{1}{R_2} = \frac{1}{R}\left[2 + (n-1)(n+2)\, E^{\sigma}_{mn} Y^{\sigma}_{mn}\right]. \tag{16}$$

The surface tension coefficient is expanded in terms of the mean value γ_o and the temperature coefficient γ_T as

$$\gamma = \gamma_o + \gamma_T [T^{\sigma}_{mn} + L^{\sigma}_{mn} E^{\sigma}_{mn}] R^n Y^{\sigma}_{mn}, \tag{17}$$

where L^{σ}_{mn} is the coefficient obtained in the expansion of $T(R+\Delta R)$ of the deformed surface about the temperature $T(R)$ of the undeformed surface and $T^{\sigma}_{mn} R^n Y^{\sigma}_{mn}$ is the (n,m,σ)-term in the expansion of the surface temperature field.

Setting the hydrostatic pressure $p_o = 2\gamma_o/R$, and considering terms to first order in Y^{σ}_{mn} in the normal stress condition, we obtain the first equation for A^{σ}_{mn} and E^{σ}_{mn},

$$6\mu R^{n+1} A^{\sigma}_{mn}/n = [\gamma_o (n-1)(n+2) + 2\gamma_T L^{\sigma}_{mn} R^n] E^{\sigma}_{mn} = 2\gamma_T T^{\sigma}_{mn} R^n. \tag{18}$$

Instead of solving the shear stress conditions directly, it is more convenient to take the surface divergence and the surface curl of the force on an element of surface. The surface divergence equation is

$$\nabla_{II}^2 \gamma = \mu\left[\frac{\partial}{\partial r}(R u_r) - \nabla_{II}^2 u_r\right]_{r=R}. \tag{19}$$

Eqn. (19) can be simplified since $\nabla_{II}^2 u_r \Big|_{r=R} = 0$. The divergence condition, then, yields a second equation for A^{σ}_{mn} and E^{σ}_{mn},

$$2(2n+1)\mu R^{n+1} A^{\sigma}_{mn}/n - (n+1)\gamma_T L^{\sigma}_{mn} R^n E^{\sigma}_{mn} = (n+1)\gamma_T T^{\sigma}_{mn} R^n. \tag{20}$$

The radial part of the surface curl equation yields the result that $B^{\sigma}_{mn} = 0$, or $\zeta_r = 0$.

Eqns. (18) and (20) can be solved simultaneously for A^{σ}_{mn} and E^{σ}_{mn},

$$A^{\sigma}_{mn} = n(n+1)(n+2)\gamma_o \gamma_T T^{\sigma}_{mn}/2\mu R\, D^{\sigma}_{mn} \tag{21}$$

$$E^{\sigma}_{mn} = \gamma_T T^{\sigma}_{mn} R^n / D^{\sigma}_{mn}, \tag{22}$$

where $D^{\sigma}_{mn} = (2n+1)(n+2)\gamma_o + \gamma_T L^{\sigma}_{mn} R^n$. (23)

THE VELOCITY FIELD AND THE VORTICITY FIELD

Defining a characteristic rate of flow

$$U^{\sigma}_{mn} = -n(n+1)(n+2)\gamma_o\gamma_T T^{\sigma}_{mn} R^n/2\mu D^{\sigma}_{mn}, \tag{24}$$

the components of the velocity $\vec{u}$ can be written as

$$u_r(r,\theta,\phi) = U^{\sigma}_{mn}\tilde{r}^{n-1}(1-\tilde{r}^2)Y^{\sigma}_{mn}(\theta,\phi) \tag{25a}$$

$$u_\theta(r,\theta,\phi) = U^{\sigma}_{mn}(\tilde{r}^{n-1}/n)\left[1-\left(\frac{n+3}{n+1}\right)\tilde{r}^2\right]\cdot(\partial Y^{\sigma}_{mn}/\partial\theta) \tag{25b}$$

$$u_\phi(r,\theta,\phi) = U^{\sigma}_{mn}(\tilde{r}^{n-1}/n)\left[1-\left(\frac{n+3}{n+1}\right)\tilde{r}^2\right](1/\sin\theta)\cdot(\partial Y^{\sigma}_{mn}/\partial\theta), \tag{25c}$$

where $\tilde{r} = r/R$.

Although $\zeta_r = 0$ within the drop, ζ_θ and ζ_ϕ generally do not vanish. Using the definition of the vorticity, Eqn. (4), and Eqns. (25a,b,c),

$$\zeta_\theta = Z^{\sigma}_{mn} r^n (1/\sin\theta)(\partial Y^{\sigma}_{mn}/\partial\phi) \tag{26a}$$

$$\zeta_\phi = -Z^{\sigma}_{mn} r^n (\partial Y^{\sigma}_{mn}/\partial\theta), \tag{26b}$$

where

$$Z^{\sigma}_{mn} = 2(U^{\sigma}_{mn}/R)(2n+3)/n(n+3). \tag{27}$$

The rate of flow, or speed, is

$$v = [u_r^2+u_\theta^2+u_\phi^2]^{1/2}, \tag{28}$$

where in general,

$$u_r = \sum_{n=1}\sum_{m=0}^{n}\sum_{\sigma} u_r(n,m,\sigma) \tag{29a}$$

$$u_\theta = \sum_{n=1}\sum_{m=0}^{n}\sum_{\sigma} u_\theta(n,m,\sigma) \tag{29b}$$

$$u_\phi = \sum_{n=1}\sum_{m=0}^{n}\sum_{\sigma} u\phi(n,m,\sigma). \tag{29c}$$

Thus, the general expression for v can be very complicated. Only expressions for the pure modes will be investigated here.

For the special case of the lowest order mode $(n,m,\sigma) = (1,0,e)$ and where $L^{e}_{01} = 0$, we obtain equations for a levitated drop in a constant vertical temperature gradient. In this case, the temperature in the drop is

$$T = T_o + T_1 R\tilde{r}\cos\theta, \tag{30}$$

which results in the velocity components

$$u_r = -(\gamma_T T_1 R/3\mu)(1-\tilde{r}^2)\cos\theta \tag{31a}$$

$$u_\theta = (\gamma_T T_1 R/3\mu)(1-2\tilde{r}^2)\sin\theta \tag{31b}$$

$$u_\phi = 0.$$

These results can be obtained from the solutions of Young, et. al (5), as mentioned in the Introduction. In addition, we find that

$$E^e_{mn} = \gamma_T T_1 R/9\gamma_o, \tag{32}$$

so that the drop is spherical in the limit $\gamma_T/\gamma_o \to 0$.

SOME CHARACTERISTICS OF AXIALLY SYMMETRIC MODES

For an axially symmetric mode (n,0,e), the expression for the rate of flow, Eqn. (28), is

$$\tilde{v} = (\tilde{r}^{n-1}/n)\left[n^2(1-\tilde{r}^2)^2(P_n)^2+(1-\frac{n+3}{n+1}\tilde{r}^2)^2(P_n^1)^2\right]^{1/2} \tag{33}$$

where $\tilde{v} = v/U^e_{on}$, P_n is the nth order Legendre polynomial and P^1_n is the associated Legendre polynomial of first degree. Eqn. (33) can be used to identify the stagnation points since $\tilde{v} = 0$ at these points.

Within the drop, n rings of stagnation points about the axis of the drop can be readily identified: take $\tilde{r}^2 = (n+1/(n+3)$ and $P_n = 0$; since P_n has n nodes and $0 \le \phi \le 2\pi$, n rings have been identified. On the surface of the drop ($\tilde{r} = 1$), the rate of flow $\tilde{v} = 0$ if $P^1_n = 0$. The associated Legendre polynomial P^1_n has (n+1) nodes, including one at each pole. These two stagnation points at the poles and the (n-1) stagnation rings on the surface coincide with the hot and cold spots of the temperature field and define the boundaries of the convection cells in the drop. If $n > 1$, $v = 0$ when $r = 0$. That is, flow does not occur through the center of the drop when $n > 1$. Finally, we must consider the possibility of other internal stagnation points. That is, are there other points such that

$$n^2(1-\tilde{r}^2)^2(P_n)^2 + (1-\frac{n+3}{n+1}\tilde{r}^2)^2\ (P_n^1)^2 = 0\ ?$$

The answer is no. Since each term is either positive or zero, and since neither $(1-\tilde{r}^2)$ and $(1-(n+3/n+1)\tilde{r}^2)$ nor P_n and P^1_n vanish at identical values of $\tilde{r}$ and $\cos\theta$, respectively, there are no other internal stagnation points.

For an axially symmetric problem, a streamfunction $\psi(\tilde{r},\theta)$ can be obtained from

$$\tilde{u}_r = -\frac{1}{r^2\sin\theta}\ \frac{\partial\psi}{\partial\theta} \tag{34a}$$

$$\tilde{u}_\theta = \frac{1}{\tilde{r}\sin\theta}\ \frac{\partial\psi}{\partial r} \tag{34b}$$

where $\tilde{u}_a = u_a/U^{\sigma}_{mn}$ $(a = r,\theta)$. For the (n,0,e)-mode, the streamfunction is

$$\psi = -r^{n+1}(1-r^2)\ \sin\theta P_n^1(x)/n(n+1), \tag{35}$$

where $x = \cos\theta$. For the mode (1,0,e), the streamfunction is that for Hill's spherical vortex (9). Stagnation points, indicated by "N", and typical streamlines for Hill's spherical vortex are illustrated in Fig. 1 and for the modes n = 2,3,4,5 in Figs. 2-5, respectively. The drops are seen in vertical cross-sections. The model rings lie in planes perpendicular to the axis in each illustration. The straight lines within the circles represent the boundaries of the convection cells, and here $\psi = 0$. The positions of the stagnation points are listed in Table 1 for these five modes.

Table 1. Stagnation "Points" for Axially Symmetric Convection Cells in Nominally Spherical Drops

Mode n	$\tilde{r}$	Interior θ	Type	Surface ($\tilde{r}$ = 1) θ	Type
1	$1/\sqrt{2}$		ring	0°	point
				180°	point
2	0	--	point	0°	point
	$\sqrt{3/5}$	54° 44' 8"	ring	90°	ring
		125° 15' 52"	ring	180°	point
3	0	--	point	0°	point
	$\sqrt{2/3}$	39° 13' 54"	ring	63° 26' 6"	ring
	"	90°	ring	116° 33' 54"	ring
	"	140° 46' 6"	ring	180°	point
4	0	--	point	0°	point
	$\sqrt{5/7}$	30° 33' 20"	ring	49° 6' 24"	ring
	"	70° 7' 28"	ring	90°	ring
	"	109° 52' 32"	ring	130° 53' 36"	ring
	"	149° 26' 40"	ring	180°	point
5	0	--	point	0°	point
	$1/2\sqrt{3}$	25° 1' 2"	ring	40° 5' 17"	ring
	"	57° 25' 14"	ring	73° 25' 38"	ring
	"	90°	ring	106° 34' 22"	ring
	"	122° 34' 46"	ring	139° 54' 43"	ring
	"	154° 58' 58"	ring	180°	point

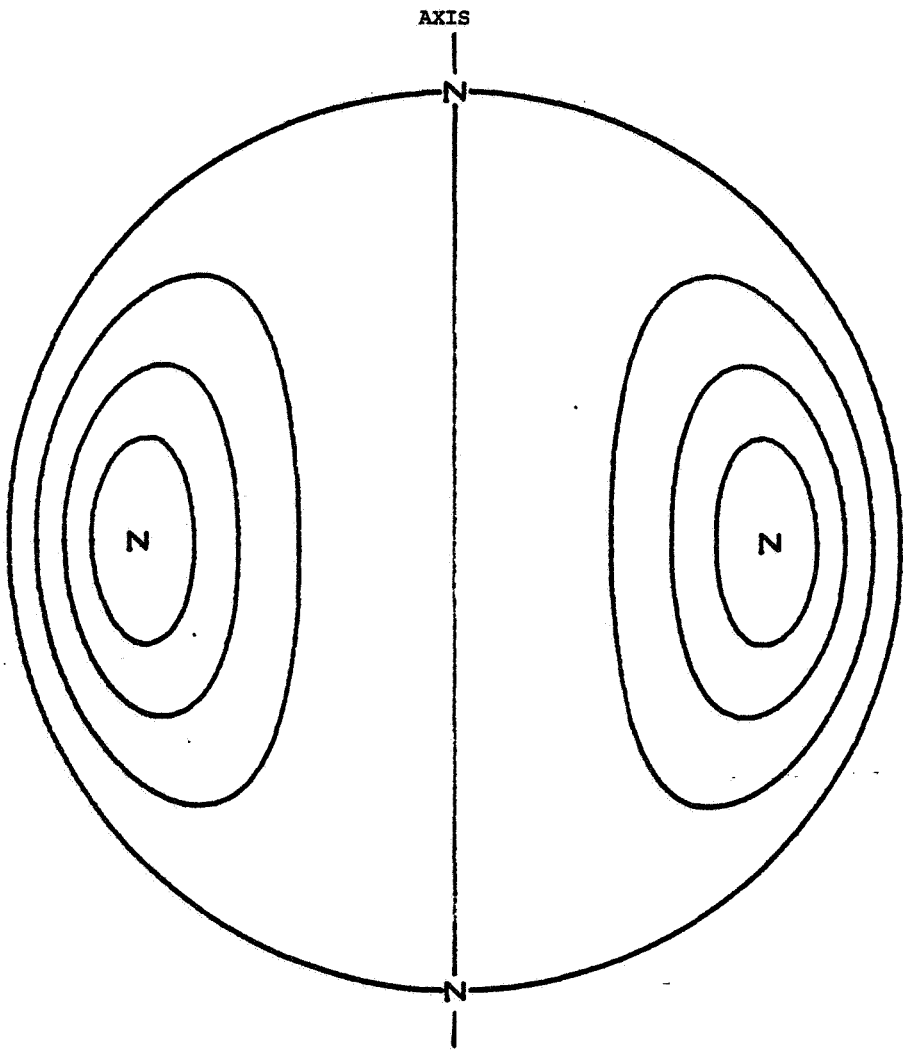

Figure 1. Streamlines and Stagnation Points ("N") for the (1,0,e)-Mode: Hills' Spherical Vortex.

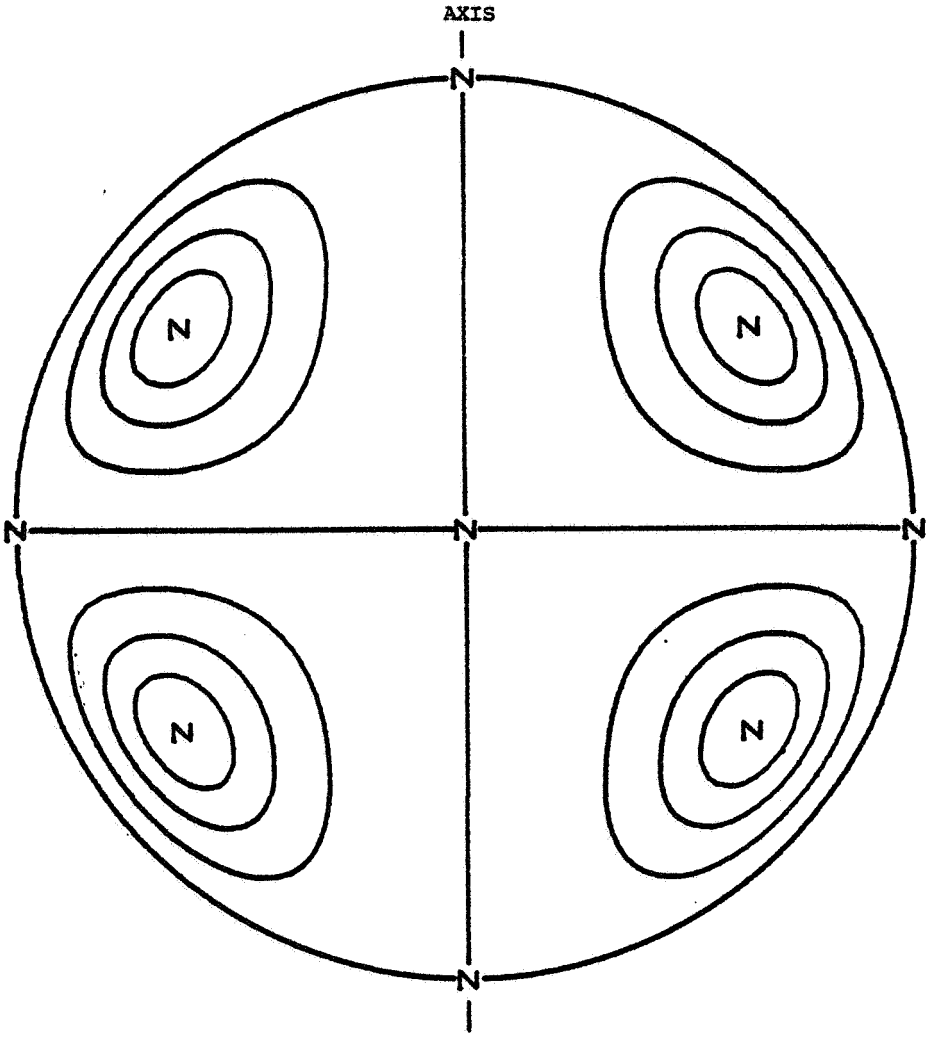

Figure 2. Streamlines and Stagnation Points for the (2,0,e)-Mode

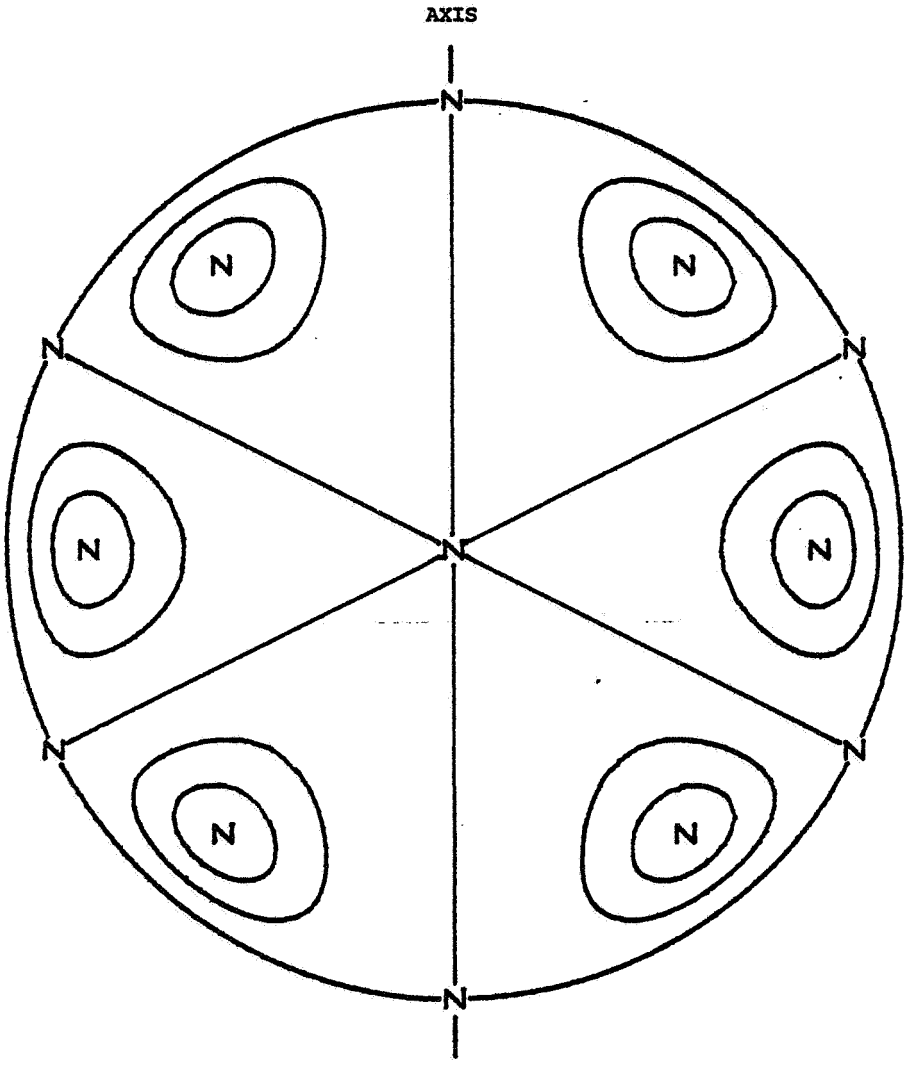

Figure 3. Streamlines and Stagnation Points for the (3,0,e)-Mode

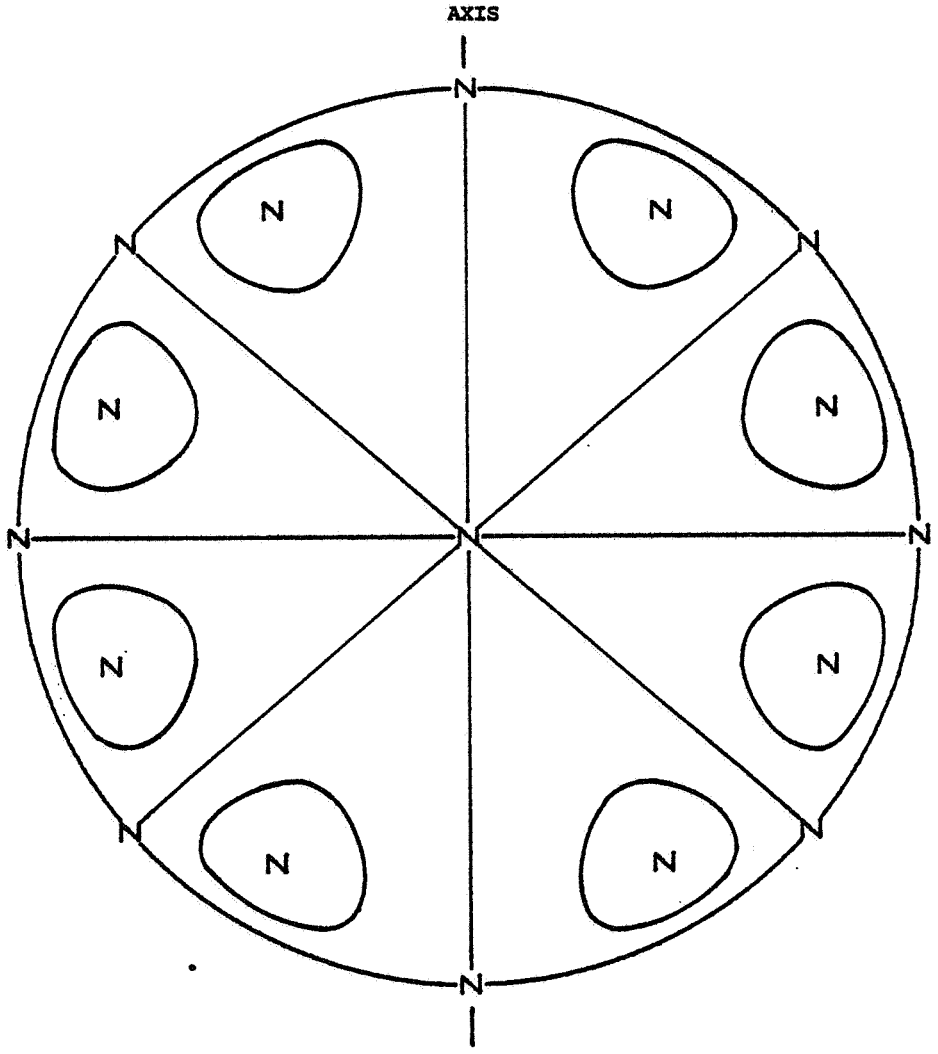

Figure 4. Streamlines and Stagnation Points for the (4, 0, e)-Mode

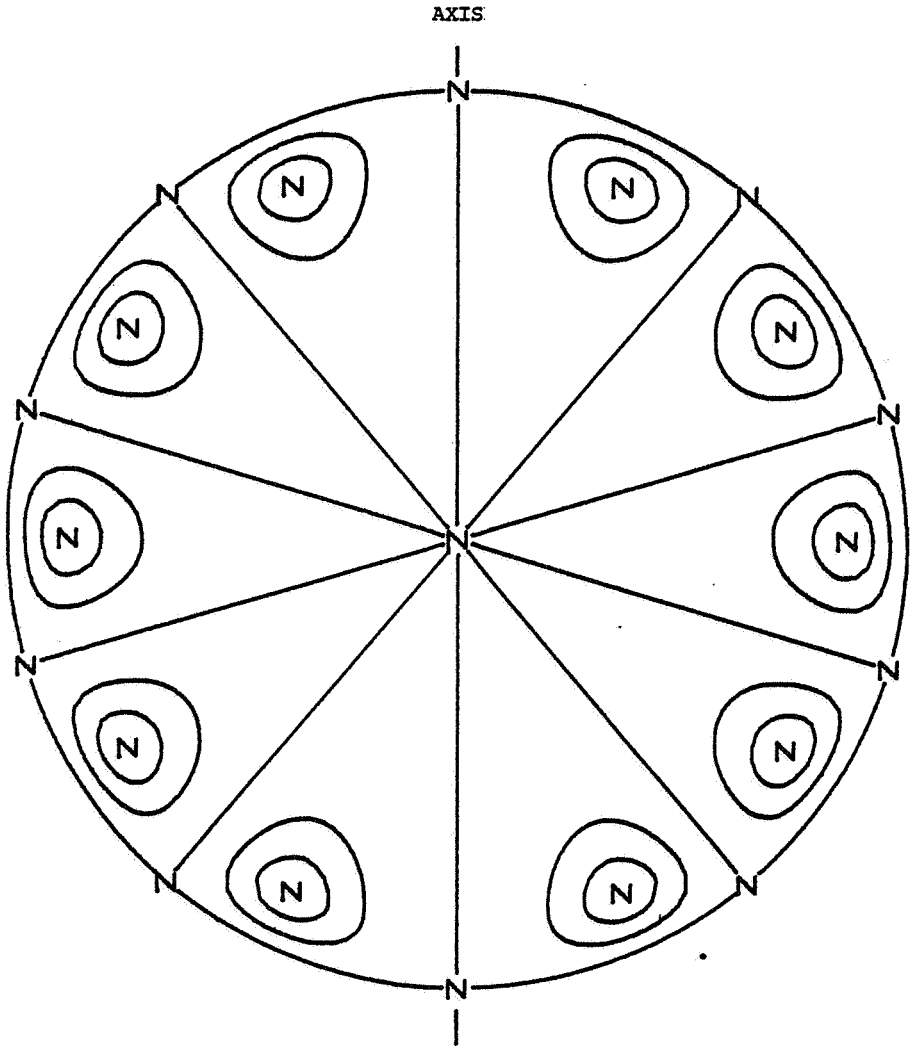

Figure 5. Streamlines and Stagnation Points For the (5,0,e)-Mode

THE CIRCULATION TIME

The circulation time τ will be introduced in this section as a means of characterizing the rate of convective mass transfer from the interior of the convection cell to the vicinity of the surface of the drop. The reciprocal circulation time τ^{-1} is defined by

$$\tau^{-1} = \oint \vec{u}\cdot d\vec{\ell} / \int dS$$
$$= \oint \vec{\zeta}\cdot\vec{n} dS / \int dS, \tag{36}$$

where the circulation integral

$$\oint \vec{u}\cdot d\vec{\ell}$$

is taken around the boundary of the cell formed by the intersection of the cell with a vertical plane containing the axis of the drop, such as any of the cell boundaries shown in Figures 1-5. The second equality follows from Stokes's theorem, where the surface integrals

$$\int \vec{\zeta}\cdot\vec{n} dS \text{ and } \int dS$$

are taken over the region bounded by the circuit of the line integral; $\vec{n}$ is the unit normal vector to the surface and here is equal to $\hat{e}_\phi$. According to Eqn. (36), the reciprocal circulation time is the average vorticity of the cell. The circulation time resembles the period of rotation of a rigid body. Indeed, if the fluid circulated about the vortical center as a rigid body, Eqn. (36) would yield 4π times the frequency of rotation and τ would be the period of the rotation reduced by 4π. Unfortunately, such a simple interpretation of thermocapillary convection cells is not possible, but τ can still be used to characterize the rate of circulation within the cell.

For the axially symmetric mode (n,0,e), the integrals in Eqn. (36) can be performed yielding

$$\tau_{ns} = (n+2)[P_n(x'_s) - P_n(x'_{s+1})]/2Z^e_{on}(\theta'_{s+1} - \theta'_s) \tag{37}$$

for the circulation time for the s-cell, where $1 \leq s \leq n+1$, and x'_s and x'_{s+1} are roots of

$$P^1_n(x) = 0. \tag{38}$$

Cell-s has its vortical center at the stagnation point whose angular position θ_s is given by the root x_s of

$$P_n(x) = 0; \tag{39}$$

θ_s lies within the range whose lower bound is θ'_s and whose upper bound is θ'_{s+1}. The circulation time may be either positive or negative, the sign depending upon the direction of circulation in the cell. Using Eqns. (1), (24) and (27), we can show that, apart from the geometric factor, the circulation time τ_{ns} depends only on the material parameters μ and γ_T and on the temperature gradient at the surface.

The circulation times for the mode n = 1 are given in Tables 2-5 for a variety of liquids. Here, we assume "unit conditions": $L^e_{01} = 0$, and a unit temperature gradient, $T^e_{01} = -1°/cm$. The assumption of unit conditions is indicated for the circulation time by $\tau°$, where the superscript "o" designates unit conditions. Table 2 lists circulation times for some liquids at room temperature; Table 3, for five liquid metals; Table 4, for four molten oxides; and Table 5 for three molten sodium halide salts.

Table 2. Circulation Times* for Some Liquids at Room Temperature (298.15 K)

Material	γ_T mN/K.m**	Viscosity mPa.s**	$\lvert\tau\rvert$, s
Acetone	-0.112 (11)	0.316 (10)	0.0323
DC 200, 20 cs+	-0.062 (5)	19 (5)	3.5
200 cs	-0.065 (5)	193 (5)	34
1000 cs	-0.061 (5)	793 (5)	180
Ethanol	-0.9832 (11)	1.092 (10)	0.150
n-Hexadecane	-0.106 (5)	3.086 (12)	0.334
Krytox 143 AZ++	-0.1 (13)	32.4 (13)	4
Water	-0.1477 (11)	0.8904 (13)	0.06908

*temperature gradient at the poles has a magnitude of 1°/cm.
**1 mN/m = 1 dyn/cm; 1 mPa.s = 1 cp = 10^{-2} dyn.s/cm^2.
+Dow Corning silicone oils of the DC 200 series.
++A perfluoroalkylpolyether.

Table 3. Circulation Times*--Metals

Materials	γ_T mN/K·m	Temp. T_o K	Viscosity mPa.s	$\|\tau\|$,s
Aluminum	-0.356 (10)	930	4.5 (15)	0.14
		1070	2.5	0.08
Copper	-0.06 (10)	1370	4.5 (15)	0.9
		1470	3.9	0.7
Mercury	-0.2049 (11)	290	1.554 (15)	0.0869
		470	1.052	0.0588
Sodium	-0.09833 (14)	470	0.450 (15)	0.00524
		670	0.284	0.00331
Tin	-0.0706 (13)	500	1.97 (13)	0.320
		870	1.05 (13)	0.170

*The temperature gradient at the poles has a magnitude of 1°/cm.

Table 4. Circulation Times*--Oxides

Material	γ_T mN/K·m	Temp. T_o K	Viscosity Pa.s	$\|\tau\|$,s
Al_2O_3	(0.1)+	2400	0.11 (16)	13
		2600	0.062	7
B_2O_3	0.0354 (18)	1410	5.02 (17)	1620
	at 720 K	1670	2.01	651
GeO_2	0.056	1750	12.2 (17)	2500
	at 1390 K	1930	0.787	160
SiO_2	0.031	2280	717 (17)	8×10^5
	at 2000 K	2680	102	1×10^5
		2820	46.4	5×10^4

*Temperature gradient at the poles has a magnitude of 1°/cm.
+Estimated.

Table 5. Circulation Times*--Sodium Halides

Material	γ_T (18) mN/K·m	Temp. T_o K	Viscosity (17) mPa.s	$\|\tau\|$,s
NaCl	-0.0719	1090	1.38	0.220
		1150	1.08	0.172
NaBr	-0.0809	1060	1.28	0.181
		1170	1.00_6	0.142
NaI	-0.129	1030	1.15	0.102
		1100	0.96	0.085

*Temperature gradient at the poles has a magnitude of 1°/cm.

The steady-state temperature gradient is obtained by balancing the conductivie heat flux through the drop against the radiant heat flux away from the drop in the cooler hemisphere. Sufficient heat is applied to the hotter hemisphere to maintain the steady-state gradient. Since the radiant heat flux $\propto T^4$, liquids such as molten metals which have high thermal conductivities will only have steep steady-state gradients at high temperatures. Although copper has the highest thermal conductivity of the liquid metals considered in Table 3, it is the only one of the five metals which is considered at temperatures high enough for a rate of radiant heat loss to be attained which could produce a steady-state gradient of 1°/cm. Thus, the circulation times given for copper in the table are the only ones which are physically attainable under steady-state conditions. For the other metals, the physcially attainable value of τ_1 will be longer than τ_1^o: the attainable steady convective rates will be less than the rates produced by a gradient of 1°/cm.

The long circulation times estimated for the oxides, B_2O_3, GeO_2 and SiO_2 show the importance of the viscosity in determining whether thermocapillary convection can occur in the liquid. For these three oxides, thermocapillary convection is expected to be negligible. However, Al_2O_3 has a lower viscosity than these other three oxides and, thus, a shorter circulation time. Since temperature gradients much larger than 1°/cm can be attained in molten oxides, significant thermocapillary convection might be observed in molten alumina.

The n = 1 mode has been demonstrated on earth by the work of Young, Goldstein and Block (5) who observed the balancing of the thermocapillary and buoyancy forces on small bubbles in a vertical temperature gradient. The low-g of a space laboratory in addition to facilating the levitation of a drop would allow the observation of the higher convective modes, in particular, the n = 2 mode. The circulation could be observed by the movement of a dye or of a radiotracer.

Relative circulation times for the axially symmetric modes n=2,3,4,5 are given in Table 6. These times are calculated relative to the single vortex (n = 1) time τ_1°. The sign of the circulation time for a particular cell indicates the direction of circulation with respect to that in the single vortex drop. Since the convective rate decreases as n increases, the higher modes appear to be less desirable than the n = 1 mode for obtaining rapid purification. However, the convective rates for some of these higher modes still can be large enough for the convective pattern to be studied and for these modes to have some utility for the purification of levitated melts in space.

SUMMARY

Equations describing the convective flow velocities in thermocapillary convection cells in drops have been derived. When the thermal conditions approximate a pure, symmetric mode--that is, when the temperature field can be described by a single Legendre polynomial, the streamlines of the vortex and the positions of the stagnation points in each cell can be calculated. The circulation time, which is the reciprocal of the average vorticity of the cell and which characterizes the rate of circulation, also can be calculated for these high symmetry cells. An estimate of the circulation time for a liquid drop is an indicator of the probable significance of thermocapillary convection in the drop when a temperature gradient is imposed across it.

Table 6. Relative Circulation Times, $\tau_{ns}^\circ/\tau_1^\circ$, for Axially Symmetric Modes with n > 1

Mode n	Cells s	$\tau^\circ_{ns}/\tau_1^{\circ *}$
2	1	3.968
	2	-3.968
3	1	9.981
	2	-7.365
	3	9.981
4	1	19.994
	2	-13.505
	3	13.505
	4	-19.994
5	1	34.960
	2	-22.691
	3	20.647
	4	-22.691
	5	34.960

*τ°_{ns} is the circulation time for the s-cell of the nth mode, τ_1° is the circulation time for mode n = 1; a temperature gradient with a magnitude of 1°/cm is assumed at the poles. The sign indicates the direction of circulation with respect to the n = 1 mode.

REFERENCES

1. L. E. Scriven and G. V. Sternling, Nature 187, 186 (1960).

2. V. G. Levich, Physicochemical Hydrodynamics, Prentice-Hall, Englewood Cliffs, N. J., (1962), Chapters 7 and 8.

3. C. A. Miller and L. E. Scriven, J. Fluid Mech. 32, 417 (1968).

4. P. M. Morse and H. Feshbach, Methods of Theoretical Physics, McGraw-Hill, New York (1953), Chapter 10.

5. N. O. Young, J. S. Goldstein and M. J. Block, J. Fluid Mech. 6, 350 (1959).

6. R. L. Sani, "Convective Instability", Ph.D. Thesis, Department of Chemical Engineering, University of Minnesota, 1963.

7. L. E. Scriven, Chem. Engineering Sci. 12, 98 (1960).

8. H. Lamb, Hydrodynamics, Sixth Ed., Cambridge University Press, London (1932), p. 475.

9. L. M. Milne-Thomson, Theoretical Hydrodynamics, Fifth Ed., Macmillan, New York (1968), Section 19.51.

10. Handbook of Chemistry and Physics, 47th Ed., R. C. Weast, ed. Chemical and Rubber Company, Cleveland, Ohio, (1966).

11. J. J. Jasper, J. Phys. Chem. Ref. Data 1, 841 (1972).

12. R. S. Marvin and D. L. Hogenboom, "Viscosity of Liquids," in the American Institute of Physics Handbook, Third Ed., D. E. Gray, ed., McGraw-Hill, New York (1972).

13. P. G. Grodzka and T. C. Bannister, Sci. 176, 506 (1972).

14. Liquid Metals Handbook, Sodium (NaK) Supplement, C. B. Jackson, ed., U. S. Atomic Energy Commission and the Bureau of Ships, U. S. Department of the Navy, Washington (1955).

15. C. J. Smithells, Metals Reference Book, 4th Ed., Vol. 3 Plenum, New York (1967

16. J. L. Bates, C. E. McNeilly and J. J. Rasmussen, "Properties of Molten Ceramics", Ceramics in Severe Environments, W. W. Kriegel and H. Palmour III, ed., Plenum, New York (1971).

17. G. J. Janz, F. W. Dampier, G. R. Lakshminarayanan, P. K. Lorenz and R. P. T. Tomkins, Molten Salts, Vol. 1, NSRDS-NBS 15, National Bureau of Standards, U. S. Department of Commerce, Washington (1968).

18. G. J. Janz, G. R. Lakshminarayanan, R. P. T. Tomkins, and J. Wong, Molten Salts, Vol. 2, NSRDS-NBS 28.

D14

ANALYSIS OF LIQUID DYNAMICS FOR M551 AND M553 SKYLAB SPACE PROCESSING EXPERIMENTS

M. R. Brashears, S. V. Bourgeois, C. Fan
Lockheed Missiles & Space Company, Inc., Huntsville, Ala. 35807

ABSTRACT

Fluid mechanic analyses were performed for the M551 and M553 materials processing experiments developed by NASA-Marshall Space Flight Center and conducted in the M512 facility aboard the Skylab laboratory by Astronaut Charles Conrad. The M551 Metals Melting experiment consisted of three sample disks with varying thicknesses. An electron beam gun was used to produce a weld seam as well as a molten pool in each specimen which was made to rotate at a controlled speed. The M553 Sphere Forming experiment consisted of 28 nickel specimens of 6.35 mm diameter being cast by utilizing an electron beam as the heat source. After melting, the molten spheres were designed to separate and solidify under a free-float condition in the vacuum chamber.

The beading and spiking phenomena in the M551 experiment are discussed. An analysis of the beading phenomena based on the Kármán vortex shedding theory is presented. A dynamic model of cavity oscillation is discussed to explain the spiking phenomena which were observed in the stainless steel and tantalum samples. The intensity of spiking depends primarily on the vapor pressure and surface tension properties of the material. Spiking may also be affected by the level of gravitational acceleration, however, at low degrees of melt superheat.

Both order-of-magnitude dimensional analysis and thermoconvective instability (perturbation) analysis are applied to the molten metal droplets of the M553 experiment. The controlling physical forces and magnitude of fluid flow are predicted and compared to results exhibited on high-speed photography. Convection thereby ascertained is utilized to analyze expected low-g effects on the attendant solidification processes.

For both experiments, particular emphasis is placed on clarifying the effects of reduced gravity on molten metal flow and solidification.

INTRODUCTION

The M512 facility was flown aboard the Skylab Laboratory to provide the working chamber for numerous scientific experiments including several space processing experiments. The facility included an electron beam heat source operated from 50 to 80 mA at 20 kV aligned in a 40 cm diameter chamber vented directly to outer space. The M551 metals melting and the M553 sphere forming experiments were performed during the June 1973 mission by Astronaut Charles Conrad.

The M551 experiment consisted of three sample disks, each containing three metal specimens of varying thicknesses. These disks were rotated automatically at a controlled speed of 2.5 rpm under an electron beam gun with the gun targeted to produce an electron beam weld seam in

each specimen at a radius of 6 cm. Disk materials included 2219 aluminum, 321 stainless steel and tantalum. During the continuous weld portion of each disk both full and partial penetration of the disk was achieved by having a constant power input with a varying disk thickness. For each disk, the continuous weld was followed by a dwell portion. In the dwell portion of the weld, the disk was stationary, allowing the electron beam to impinge on a thick segment of the disk, thus creating a large molten pool. The electron beam was then cut off to allow the pool to solidify.

The M553 experiment consisted of twenty-eight 6.35 mm diameter spherical specimens cast by utilizing the electron beam heat source. Initially, cylindrical specimens were supported on two wheels (14 specimens on each) by a sting. During melting, spherical drops were formed and subsequently designed to be released from their stings and allowed to solidify while free floating in the vacuum chamber. Specimens consisted of pure nickel, Ni-1% Ag, Ni-30% Cu and Ni-12% Sn.

During the course of the investigation all process phenomena were considered with particular emphasis on the melting and solidification of metals in reduced gravity. Included in these analyses were detailed studies on the fluid dynamics of the molten metal.

For these particular Skylab experiments, the only significant difference between space and earth processing was the lack of gravity. The maximum gravity level experienced during operation of the M551 and M553 experiments aboard Skylab II was 7×10^{-4} g_E (g_E = 9.8 m/sec^2). Other environmental factors which may also differ from earth processing are the vacuum, radiation, electromagnetic and thermal conditions.

Gravity has no direct effect on grain structure or other properties of solidified material. These properties are determined by the crystallization kinetics which are controlled by short-range intermolecular forces; i.e., the temperature and concentration at the fluid-solid interface. Gravity has not been shown to have any significant direct effect on these forces, but can affect solidification indirectly through its direct effect on fluid motion. The three major indirect effects of gravity on solidification are:

- Sedimentation
- Buoyancy-Induced Convection, and
- Hydrostatic Pressure.

These mechanisms are all hydrodynamical in nature. Detailed discussions of the objectives of the study, as well as the results, are available in Refs. 1 through 3.

M551 METALS MELTING EXPERIMENT

- Convection Effects on Solidification

Cross-sectional micrographs of the M551 aluminum disks (Fig. 1) indicate that grain size and orientation differed appreciably between the ground and Skylab samples. Similar trends were exhibited by the stainless steel and tantalum specimens. The ground-based sample consists of large, columnar grains growing normal to the unmelted solid with slight evidence of banding. The Skylab

sample, however, is fine grained and equiaxed. One other significant difference is the negligible width of the chill zone (ultra-fine grained, equiaxed region adjacent to the parent metal) in the ground sample.

Some investigators have attributed these differences to reduced convection during Skylab processing. The accepted principles of crystal growth (Ref.4) however, lead to the opposite conclusion. Many experiments have now shown the strong effect of convection on grain size in cast metals. When this convection is reduced, grain size is larger and columnar structures are much more readily obtained. Convection also appears to play a dominant role in formation of the chill zone as well as in the columnar-equiaxed transition. When convection is absent, no outer chill zone is observed.

One other possibility for the results shown in Fig. 1, besides differences in convection, would be the degree of superheat supplied to the ground and Skylab samples. Superheating results in coarser structures (Ref. 5, p. 6). Thus, the fine grained Skylab structure would indicate less superheat, but its melt zone was 18% greater than the ground sample which indicates higher superheat on Skylab or greater convection on Skylab.

Thus, increased convection during Skylab processing (rather than reduced flow) explains the different microstructures observed in the micrographs, Fig. 1, of the M551 aluminum disk. Preflight analysis predicted an equivalent magnitude of convection between terrestrial and Skylab processing (Refs. 2 and 3). Increased convection aboard Skylab can be explained if the gravity driven and Marangoni convective flow patterns tended to oppose each other on earth. This would leave the unopposed Marangoni convection aboard Skylab to be more vigorous throughout the melt zone. Furthermore, the spiking mechanism is expected to give rise to increased stirring aboard Skylab.

- Beading Phenomenon

During the M551 experiment, motion pictures were taken for each of the three metal disks. The motion pictures taken along with the experiment specimens were then brought back to earth for analysis. Shown in Fig. 2 are photographs taken of the 321 stainless steel after being subjected to electron beam impingement in the flight and ground experiments. For comparison purposes, ground-based tests were also made of the same specimens under similar operating conditions. The photographs taken for the three M551 materials during ground tests are shown in Ref. 6. The most striking phenomenon appearing in these photographs is the "beading" effect which occurs simultaneously with total eb penetration in the stainless steel and tantalum specimens. No beading is exhibited in the aluminum sample, however.

It was hypothesized (Refs. 1 and 3) that the forming of beads after the passage of an electron beam was related to the vortex shedding phenomenon. When a cylinder moves through a fluid above a certain speed, the cylinder sheds behind its wake a periodic pattern of vortices which move alternatively clockwise and counterclockwise. This vortex formation is known as Kármán vortex street. A sketch showing the streamlines of a Kármán vortex street is given in Fig. 3. In this sketch, λ is the wave length or vortex spacing and h is the separation distance between the two rows of vortices.

The shedding frequency, f, i.e., the number of vortices shed per unit time, is dependent upon the density, ρ, and viscosity, μ, of the fluid, the diameter of the cylinder, D, and the velocity, V, with which the cylinder moves relative to the fluid. The interrelationship between these quantities can be correlated in terms of two dimensionless parameters known as Strouhal number, S, and Reynolds number, R, which are defined as

$$S = \frac{f \times D}{V}$$

$$R = \frac{\rho V D}{\mu}.$$

The relationship between S and R was obtained experimentally (Ref.6) for a fluid in large extent.

The wave length of the vortices, λ, is given by

$$\lambda = \frac{V - v}{f} \qquad (1)$$

where v is the velocity of the vortex which decreases with the distance from the cylinder. The magnitude of v is only of the order of 4 to 5% of V at a distance of 10 to 20 diameters downstream of the cylinder. The value of v is even smaller when the flow is confined by side walls. For all practical purposes v can be neglected in Eq. (1).

With the above basic background information, one can compile a list of data regarding the M551 space flight and ground-based experiments in view of the vortex shedding hypothesis. The compiled data are tabulated in Table 1. The manner in which these data are obtained is described as follows.

The two temperatures selected for calculation for each of the three M551 specimens correspond to the melting temperature and predicted maximum temperature (Ref. 1). The Reynolds number was calculated based on the velocity of the electron beam relative to the disk, the focusing diameter of the electron beam, and the density and viscosity of the molten metal. The viscosity of liquid metals depends strongly on temperature. The following equation was used in computing the viscosity of the molten metals

$$\mu = \mu_o e^{E/\Re T} \qquad (2)$$

where μ_o is a reference viscosity, E is the activation energy, $\Re$ is the universal gas constant, and T is the absolute temperature. The values of μ_o and E are different for different materials. For example, for the stainless steel specimen, μ_o and E_o are estimated to be (Ref. 7)

$$\mu_o = 0.37 \quad \text{Centipoise}$$
$$E = 9.9 \quad \text{Kcal/gm-mole-}^{\circ}\text{K}$$

After the Reynolds number was calculated, the Strouhal number was derived from Ref. 6. The shedding frequency can then be computed from the definition of the Strouhal number. The theoretical bead spacing (i.e., wave length)

is calculated from Eq. (1) by neglecting v. The data listed in the last two columns of Table 1 are the average bead spacings obtained by direct measurements from photographs.

It is seen in Table 1 that except for the aluminum specimen for which no beads were observed, the predicted bead spacing based on the vortex shedding theory and the experimentally measured average bead spacing are in good qualitative agreement. Quantitative agreement was not expected since the geometry and boundary conditions of the M551 Metals Melting experiment were not quite the same as those for a long solid cylinder moving in a fluid of large extent.

The theoretically predicted shedding frequency for each of the three specimens is also compared in Table 2 with corresponding experimental results for both space flight and ground-based tests. Again, good qualitative agreement among the data is obtained, except for the aluminum specimen.

It is theorized that surface tension must play an important role in the formation of beads from the vortices of the liquid metal during cooling and solidification. The larger the surface tension, the more easily the beads can be formed. The magnitude of surface tension (σ) for the three M551 materials at their respective melting temperatures are: (1) 321 stainless steel, σ = 1750 dyne/cm; (2) 2219 aluminum, σ = 737 dyne/cm; and (3) tantalum, σ = 2150 dyne/cm.

It is noted that the surface tension of 2219 aluminum is only 30 to 40% of that of the other two materials. Thus, it is quite possible that during the flight and ground tests with the 2219 aluminum specimen, vortices were present but no beads were formed due to insufficient surface tension force.

The above analysis is, of course, qualitative. The motion of the molten metal in the wake of an electron beam is influenced by many factors. In addition to the parameters involved in the definitions of Strouhal and Reynolds numbers, the state of the fluid motion is influenced by the thickness of the disk, confining side walls (between molten and solid metals), free surface and surface tension effects, as well as nonuniform temperature distributions.

In general, the effect of confining side walls is to increase the critical Reynolds number for the onset of vortex shedding. According to Taneda (Ref. 8) when the ratio of the diameter of the cylinder to the distance between the walls is increased from 0 to 0.5*, the critical Reynolds number is increased from 45 to about 80. Shair et al. (Ref. 9) have also conducted experiments showing the effect of confining walls on the stability of the wake behind a circular cylinder. Their results indicated a more pronounced effect than that reported by Taneda. This may also explain the absence of beading in the aluminum specimen, since the calculated minimum Reynolds number for this case is only about 50. It appears, however, that confining wall effects alone do not explain the quantitative differences between the predicted and measured values of λ and f as tabulated in Tables 1 and 2.

---

*The ratio of the diameter of the electron beam to the width of the welding in the M551 experiments is approximately 0.5.

A recent literature search on the subject of vortex shedding revealed little information regarding the effects of the finite length of the cylinder in the low Reynolds number flow region. At high Reynolds numbers (R >1000), a shorter cylinder results in larger vortex spacing (Ref. 10). No information is found at all regarding nonuniform temperature and heat transfer effects on vortex shedding. A detailed analysis of these problems would certainly be very interesting.

- Spiking Phenomenon

A detrimental aspect sometimes inherent in electron beam welding is the phenomenon known as spiking which results in surface ripples and banding in the weld seam microstructure. Many examples of this effect have been documented, especially for partial penetration welds in stainless steel (Ref. 11). This phenomenon is caused by oscillation of the melt.

Several possible evidences of its occurrence during the M551 experiment have appeared in both the aluminum and stainless steel samples. Detailed descriptions of the causes and effects of spiking are given in Refs. 2 and 12.

The spiking frequency can be approximated by (Ref. 12).

$$\omega = \frac{\frac{1}{4}\sqrt{\frac{g}{h}}}{\sqrt{\frac{P_V - 2\sigma/a}{\rho g h}}\ \sqrt{\frac{P_V - 2\sigma/a - \rho g h}{\rho g h}}} \qquad (3)$$

where

ω = spiking frequency
h = maximum depth of penetration
2a = weld width
g = gravity level
P_V = vapor pressure of molten metal
σ = surface tension of molten metal

While the preceding equation should not be expected to generate exact, rigorous results to match actual M551 experimental data, it can be utilized to predict a low gravity variation in the spiking behavior of M551 materials. It can also be utilized to assess the effects on spiking of the degree of superheat. Increasing superheat lessens surface tension and density while increasing vapor pressure. Overall, increasing melt temperature through superheating should increase the spiking frequency. This is illustrated by examining Eq. (1) in the limit as $g \to 0$

$$\omega = \sqrt{\frac{P_V - 2\sigma/a}{4\rho h^2}} \qquad (4)$$

which means that spiking cannot occur below 2027°C for stainless steel. The

surface tension force overcomes any jetting due to vaporization at lower surface temperatures. This is indicated by imaginary numbers in Eq. (4).

The effect of superheat and gravity on spiking frequency for all three M551 materials is shown in Figs. 4, 5 and 6. Physical property data were obtained primarily from Refs. 13, 14 and 15. These results indicate that: (1) spiking frequency varies inversely with gravity, but only above 10^{-2} g; (2) at large superheating, spiking becomes insensitive to microgravity-terrestrial gravity variations; (3) spiking occurs in the stainless steel melt above 600°C superheat (melt temperature, T_M = 1427°C); (4) spiking occurs in aluminum above 1000°C superheat (T_M = 643°C); (5) spiking occurs in the tantalum melt above 1300°C superheat (T_M = 3000°C); (6) Skylab stainless steel samples are most prone to spiking. At minimum degrees of superheating, spiking frequency may be increased by 50% when g-levels of 10^{-4} are attained. This translates to a spike separation distance of 1.1 mm on ground tests versus 0.7 mm on Skylab.

Previous thermal calculations indicate that 600°C of superheat at the melt surface are easily attainable (Ref. 1, p. 26) in the stainless steel specimens, while a superheat of 1000°C for aluminum is also feasible (Ref. 1, p. B-4). It is doubtful that spiking temperatures were achieved in the tantalum specimens (Ref. 1, p. B-14). Thus the ripples on the aluminum and the ripples in the stainless steel microstructure may be caused by spiking.

One additional qualitative assessment can be made for the M551 aluminum specimens, i.e., the apparent disappearance of ripples in the weld region behind the molybdenum film. The molybdenum film has a dimension of 0.5 x 0.5 x 0.0005 inch and was placed on each of the M551 samples in the weld path at a location of 240 degrees. The purpose of placing a molybdenum film on each sample was to analyze fluid motion during melting by micro-sectioning of the weld.

The molybdenum has a lower total vapor pressure and increased surface tension forces (Refs. 14 and 16), thereby decreasing the tendency toward spiking.

- Conclusions

Analyses of both the space flight and ground-based tests of the M551 Metals Melting experiments indicate that:

- Good qualitative agreement was obtained between the measured results of beading frequency and spacing and the predicted values based on the Kármán vortex theory. This tends to support the hypothesis as advanced in Ref. 1 that the beading phenomenon which occurred in the stainless steel and tantalum samples was a Kármán vortex street formation.
- Surface tension and sidewall effects appear to be responsible for the absence of beadings in the 2219 aluminum sample after electron beam impingement.
- Reduced convection in space is definitely not the cause of altered microstructures found in Skylab 2219 aluminum.
- Altered or increased convection can explain the different microstructures exhibited by the Skylab 2219 aluminum specimen; i.e., Skylab convection dominated by surface tension forces whereas ground-based convection controlled by a combination of surface tension and gravity forces.

- Spiking frequency varies inversely with gravity, but only above 10^{-2}g.
- At large superheating, spiking frequency is independent of gravity.
- Stainless steel is the M551 material most prone to spiking, and its spiking frequency may be increased by 50% when g-levels of 10^{-4} are attained.
- Disappearance of surface ripples beyond the molybdenum patch on the ground aluminum samples can be attributed to molybdenum's inherent physical properties which tend to reduce or eliminate spiking.

M553 SPHERE FORMING EXPERIMENT

The fluid dynamics of the M553 experiment is an important factor in determining the quality of the final product. Flow patterns in the molten materials are important because all of the sample materials have low entropies of fusion (Ref. 17). Thus, their solidification (microstructure) is controlled by the rate of heat transfer removal (Ref. 18), which changes with the fluid flow (Refs. 19 and 20). The degree of flow will also determine the amount of mixing attained. Fluid flow can also affect the shape and release of the specimen while it is retained on the ceramic holder.

Application of dimensional analysis (Refs. 21 and 22) to the governing equations for eb melting, coupled with ground-based experiments, enabled prediction of the extent of reduction or increase of motion in the molten metal and/or the change in flow pattern in electron beam melting in space. Possible physical forces which could induce fluid flow in the M553 experiment and their causes include:

- Effective Gravity Force: Resultant force on weld specimen due to earth's gravity and centrifugal and coriolis forces of orbiting spacecraft.
- Lorentz Force: Electromagnetic forces induced by passage of the electron beam current through the specimen.
- Electrostriction: Stresses induced when electrical permittivity changes with density.
- Magnetostriction: Stresses induced when permeability changes with density.
- Electrostatic Force: Caused by presence of excess electrical charge.
- Surface Tension: Tangential stresses at vapor-liquid interfaces can be induced by nonuniform heating or impurities because surface tension depends on temperature and concentration.
- Shrinkage Force: Density differences accompanying phase changes usually cause flow inward to a growing solidification interface.
- Beam Force: Impinging electrons giving up their momentum.

- Thermal Expansion: Dilation and compression of fluids whose density changes appreciably with temperature can induce fluid flow.
- Vibration: Uncontrolled movement due to engine operation, astronaut motion, particle impacts, etc.
- Centrifugal and Coriolis: Generated by disk rotation.
- Vapor Pressure: Evaporating molecules impart momentum which leads to normal stresses at vapor-liquid interface.
- Inertia Forces: Tend to sustain existing motions and resist changes in flow.
- Viscous Forces: Tend to resist driving forces.

The preceding forces, which could influence fluid flow and solidification, appear explicitly in the conservation equations (Ref. 3) which apply to formation of a molten pool by electron beam heating. The controlling forces were previously determined via nondimensional and order-of-magnitude analyses (Ref. 2). The most significant results found are summarized below:

- Vigorous convective stirring occurs in the molten metal for each of the M553 sample materials. This fluid motion was exhibited on high speed motion picture film taken for ground tests and low gravity KC-135 aircraft tests.
- Both gravity and surface tension forces control molten metal flow during M553 ground tests. These natural convection driving forces arise because of severe nonisothermality during heating.
- Surface tension driven convection occurred in Skylab electron beam melting. In the near absence of gravity, the surface tension forces provided an equivalent amount of convection aboard Skylab, but the flow pattern might have been different from those of operations on earth.
- Velocities of 20 cm/sec magnitude were attained 0.1 sec after melting began in the M553 nickel specimen (both for Skylab and ground tests). Fluid flow decayed 60 seconds after melting began. This means that some degree of flow existed upon freezing even for the free-floating M553 spheres.

The effects on fluid motion of surface free charges (excess electrostatic charge) and related electric and magnetic forces at the drop surfaces were also examined. These surface charges are negligible driving forces for fluid motion (Refs. 23 through 25). Furthermore, from the manner in which patches of surface contaminants moved about in the ground films, it is apparent that surface tension driven flows due to concentration gradients may also have been important in this experiment. No reliable data exist, however, on what these impurities are, nor what the value of surface tension gradient with composition is. Thus, the Marangoni effects were limited to thermal differences only in this study.

Application of an earlier analysis of Marangoni thermoconvective stability in drops by Bupara (Ref. 26) yields the same conclusion as to convection in zero gravity. Bupara's study consisted of a steady-state perturbation analysis on

internally heated drops. Thus, his results do not rigorously apply to the rapid heating of the M553 experiment, but allow for an interesting comparison with dimensional analysis. His stability curve (see Fig. B5.1, Ref. 26) indicated a critical Marangoni, Ma_c, of 150. Upon release from the ceramic pedestal, the molten nickel spheres will possess the following properties: R = 0.3175 cm, $d\sigma/dT$ = 0.4 dyne/cm-°C, ρ = 7.77 g/cc, μ = 0.05 g/cm-sec, k = 0.15 cal/cm-sec-°C, C_p = 0.157 cal/g-°C, $\beta = 10^{-4}$/°C and dT/dr = 4450°C/cm (assuming no convection, Ref. 1). Defining Marangoni number as

$$M_a = \frac{-\rho C_p \frac{d\sigma}{dT} \frac{dT}{dr} R^2}{\mu k}$$

one obtains $Ma/Ma_c = 29100/150 = 200$, which indicates vigorous convective stirring. Several seconds after release the temperature gradient reverses and becomes -3.4°C/cm after rapid equilibration (assuming no convection). This gives Ma = -71.

- Conclusions

The primary conclusion of the preceding discussions is that significant flow and stirring in the molten spheres (during and after eb melting) occurred in both terrestrial and space processing as predicted. The magnitude of this convective fluid motion was the same in both environments.

Thus no major differences in microstructure can be expected between terrestrial and Skylab processed M553 spheres due to convection. This conclusion was affirmed by detailed microstructural analyses (Ref. 27).

ACKNOWLEDGEMENT

We sincerely thank Mr. T. C. Bannister, Mr. E. A. Hasemeyer and Mr. R. M. Poorman of NASA-MSFC of which the latter two were principal investigators for these Skylab experiments. We are also grateful to Dr. C. M. Hung, Messrs. S. J. Robertson and R. C. Onyeabo of Lockheed-Huntsville for their consultation and assistance with some of the calculations. This work was supported by Contracts NAS8-27015 and NAS8-28729; we gratefully acknowledge this support.

REFERENCES

1. Brashears, M.R., and S. J. Robertson, "Research Studies on Materials Processing in Space Experiment M512 – Final Report," LMSC-HREC TR D306954, Lockheed Missiles & Space Company, Huntsville, Ala., December 1973.

2. Bourgeois, S. V., "Convection Effects on Skylab Experiments M551 and M553 – Phase C Report," LMSC-HREC TR D306955, Lockheed Missiles & Space Company, Huntsville, Ala., December 1973.

3. Bourgeois, S. V., and M. R. Brashears, "Fluid Dynamics and Kinematics of Molten Metals in the Low Gravity Environment of Skylab," AIAA Paper 74-205, presented at the AIAA 12th Aerospace Sciences Meeting, Washington, D. C., January 1974.

4. Fleming, M. C., Solidification Processing, McGraw-Hill, New York, 1973, pp. 154-155.
5. Kattamis, T. Z., "Nickel-Silver Alloy Evaluation, M553 Sphere Forming Experiment," University of Connecticut, Storrs, 4 December 1973.
6. Roshko, A., "On the Development of Turbulent Wakes from Vortex Wakes," NACA TN 2913, 1953.
7. Beer, S. Z. (Ed.), Physics and Chemistry of Liquid Metals, Marcel-Dekker, Inc., New York, 1972.
8. Taneda, S., "Experimental Investigation of Vortex Streets," J. Phys. Soc. Japan, Vol. 20, 1965, p. 1714.
9. Shair, F. H. et al., "The Effects of Confining Walls on the Stability of the Steady State Wake Behind a Circular Cylinder," J. Fluid Mech., Vol. 17, 1963, p. 546.
10. Papaulios, D., and P. S. Lyondis, "Turbulent Vortex Street and the Entrainment Mechanism of the Turbulent Wake," J. Fluid Mechanics, Vol.67, Part I, 1974, p.11.
11. Konkol, P. J., P. M. Smith, C. F. Willebrand and L. P. Connor, "Parameter Study of Electron-Beam Welding," Welding J., November 1971, p. 772.
12. Tong, H., and Geidt, W. H., "A Dynamic Interpretation of Electron Beam Welding," Welding J., June 1970, pp.259s-266s.
13. Anonymous: Vapor Pressure Data, RCA Review, December 1962, pp. 571-576.
14. Beer, S. Z., Liquid Metals Chemistry and Physics, Marcel-Dekker, Inc., New York, 1972.
15. Metals Handbook, No.8, American Society for Metals, Metals Park, Ohio, Vol. 1, 1973.
16. Taylor, J. W., "Wetting by Liquid Metals," in Solid State Physics and Physical Metallurgy.
17. Laudise, R. A., J. R. Carruthers and K. A. Jackson, "Crystal Growth," in Annual Review of Materials Science, Vol. I, 1971, pp. 253-256.
18. Laudise, R. A., The Growth of Single Crystals, Prentice-Hall, Englewood Cliffs, N. J., 1970, pp. 86-103.
19. Goldak, J. A., G. Burbidge and M. J. Bibby, "Predicting Microstructure from Heat Flow Calculations in Electron Beam Welded Eutectoid Steels," Can.Met. Quart., Vol. 9, 1970, p. 459.
20. Cole, G. S., "Transport Processes and Fluid Flow in Solidification," in Solidification, American Society for Metals, Metals Park, Ohio, 1971, pp. 201-274.
21. Churchill, S. W., and J. D. Hellums, "Dimensional Analysis and Natural Convection," Chem. Engr. Prog. Symp. Ser., Vol. 57, 1964, p.75.
22. Ostrach, S., "Role of Analysis in the Solution of Complex Problems," Third Intl. Heat Trans. Conf., Chicago, August 1966.
23. Melcher, J. R., "Discussions on Electrohydrodynamic Applications in Space Processing," Marshall Space Flight Center, Huntsville, Ala., 11 June 1973.

24. Sozou, C., "On Fluid Motions Induced by An Electromagnetic Field in a Liquid Drop Immersed in a Conducting Fluid," J. Fluid Mech., Vol. 51, 1972, pp. 585-591.

25. Melcher, J. R., and G. I. Taylor, "Electrohydrodynamics: A Review of the Role of Interfacial Shear Stresses," Ann. Rev. Fluid Mech., Vol. 1, 1969, p. 111.

26. Bupara, S. J., "Spontaneous Movements of Small Round Bodies in Viscous Fluids," Ph. D. thesis, University of Minnesota, Minneapolis, November 1964.

27. Bourgeois, S. V., "Solidification Theory for Skylab Experiments M551, M552 and M553 – Summary Report," LMSC-HREC TR D390140, Lockheed Missiles & Space Company, Huntsville, Ala., January 1974.

Table 1 - Comparison of Theoretical and Experimental Bead Spacing

M551 Mtls.	Temp. T (°K)	Reynolds Number R	Strouhal Number S	Shedding Freq. f (Hz)	Theor. Bead Spacing λ (cm)	Flight Bead Spacing λ (cm)	Ground Bead Spacing λ (cm)
321 SS	1700	35	–	–	–	0.356	0.418
	2253	72.5	0.15	1.61	1.0		
2219 Al	916	50	–	–	–	–	–
	2113	171	0.185	1.98	0.81		
Ta	3270	121	0.175	1.88	0.86	1.57	0.94
	3833	181	0.188	2.02	0.80		

Table 2 - Comparison of Theoretical and Experimental Shedding Frequency

M551 Material	Theoretical Shedding Frequency (Hz)	Flight Shedding Frequency (Hz)	Ground Shedding Frequency (Hz)
321 Stainless Steel	1.61	4.52	3.85
2219 Aluminum	1.98	–	–
Tantalum	2.02	1.03	1.71

Ground-Base

Skylab

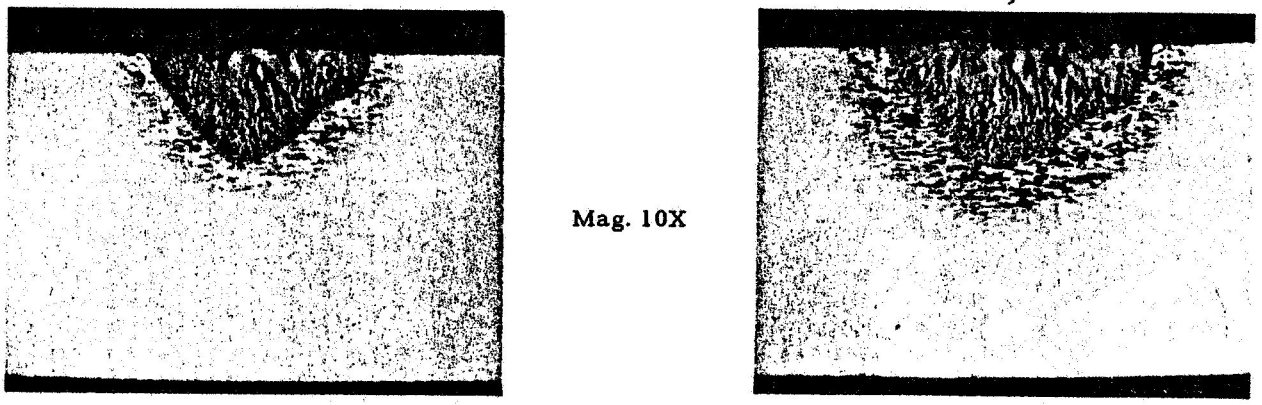

Mag. 10X

Cross Sections Pos. 5

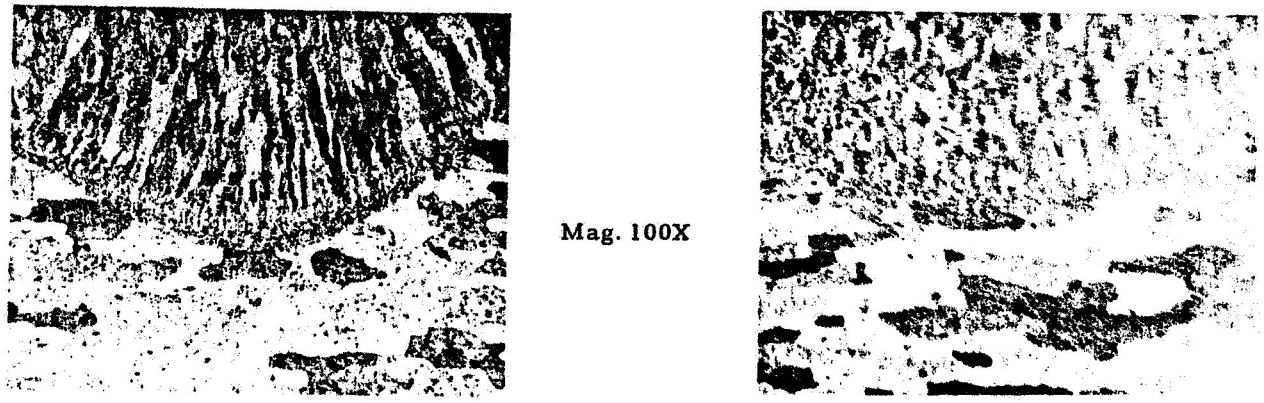

Mag. 100X

Root of Electron Beam Weld Nugget Showing Banding and Columnar Grain Growth

Root of Electron Beam Weld Nugget Showing Fine, Equiaxed Grains

Fig. 1 - Comparison of M551 Ground and Skylab 2219 Aluminum Microstructures

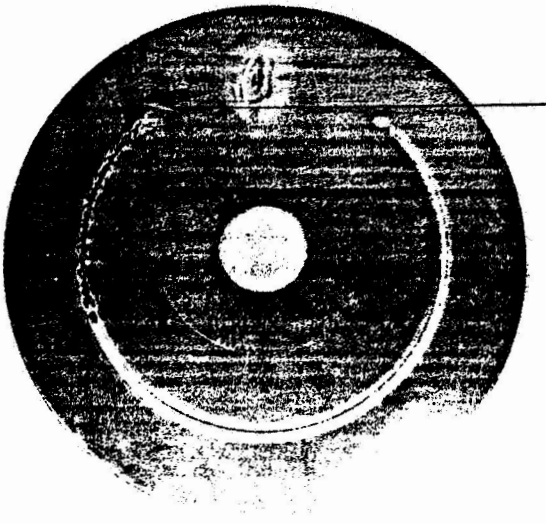

Fig. 2a - Stainless Steel Disk After M551 Flight Tests

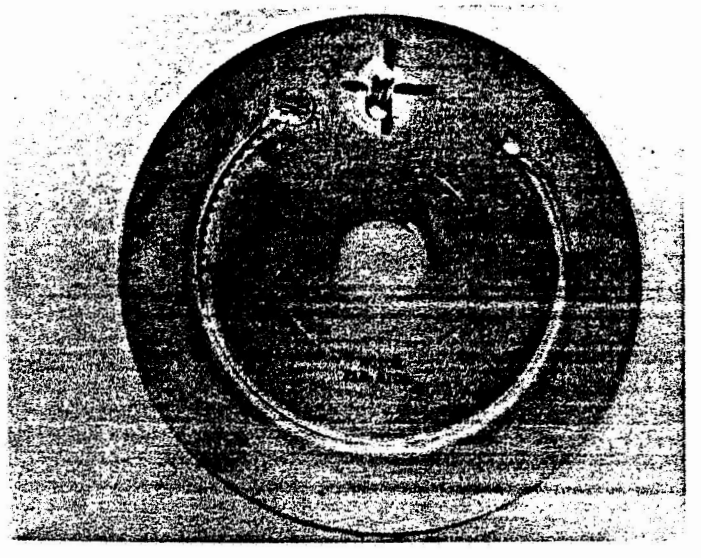

Fig. 2b - Stainless Steel Disk After M551 Ground Tests

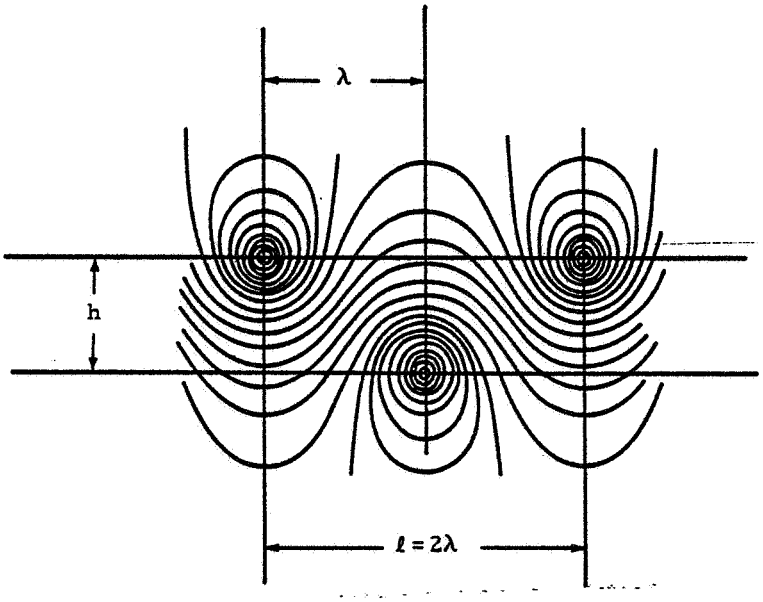

Fig. 3 - Kármán Vortex Street (Diagrammatic); Streamlines Drawn in a System of Coordinates Moving with the Vortex Street

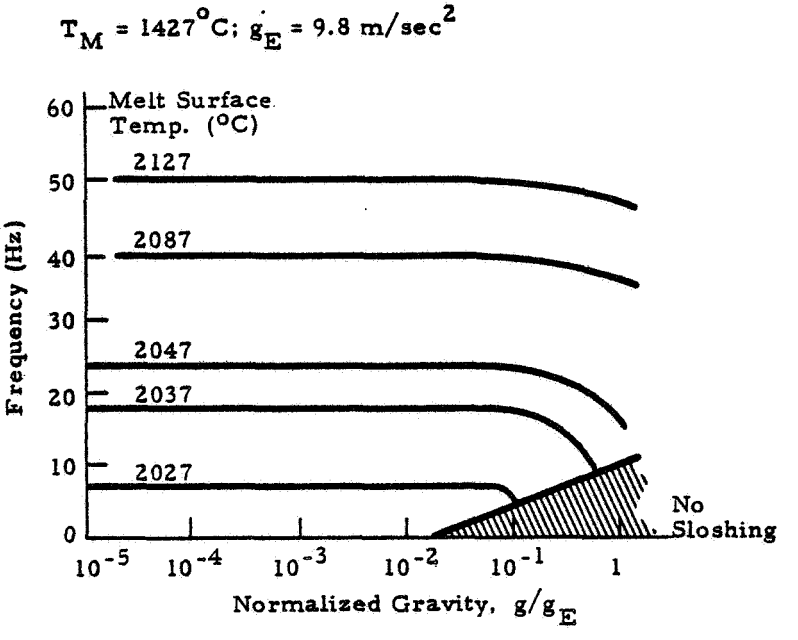

Fig. 4 - Spiking Frequency Graph of Stainless Steel

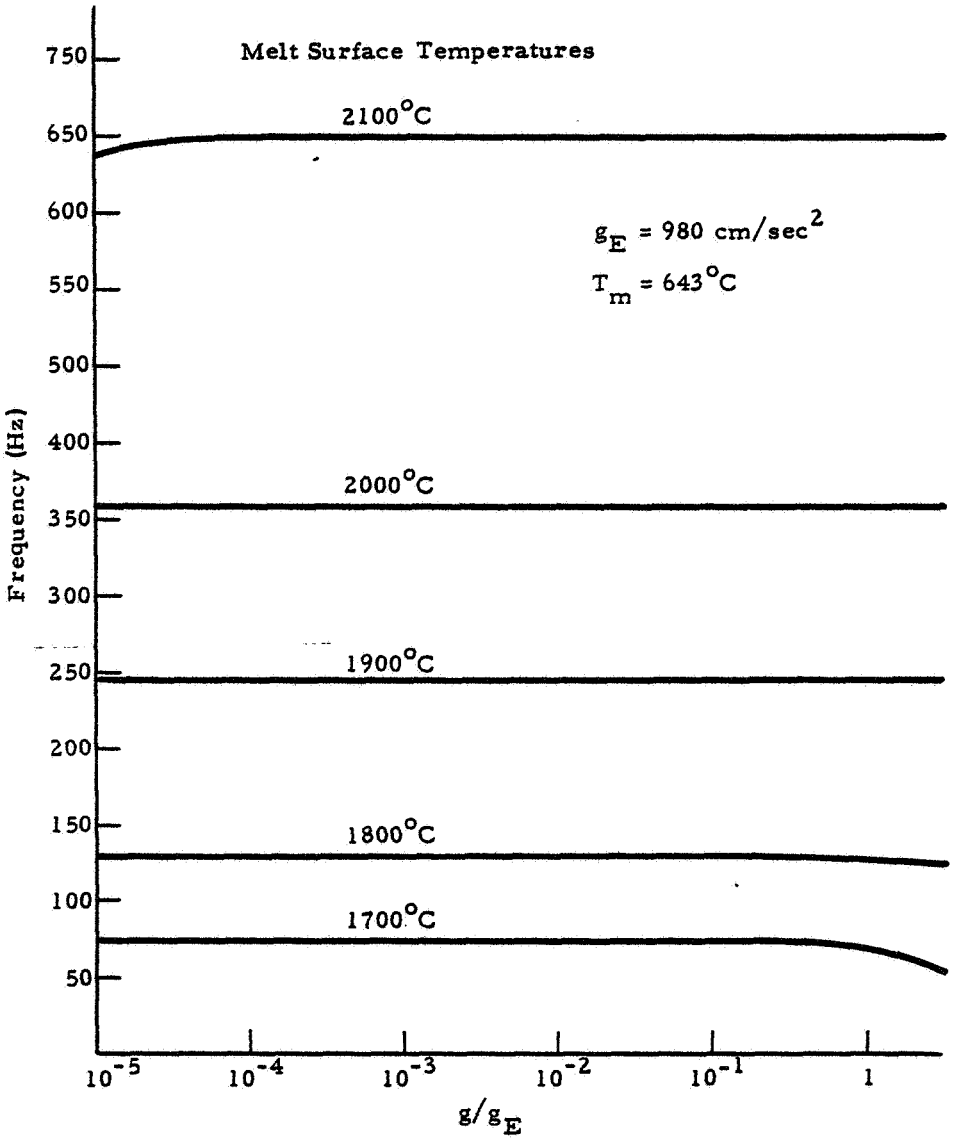

Fig. 5 - Spiking Frequency of Al2219

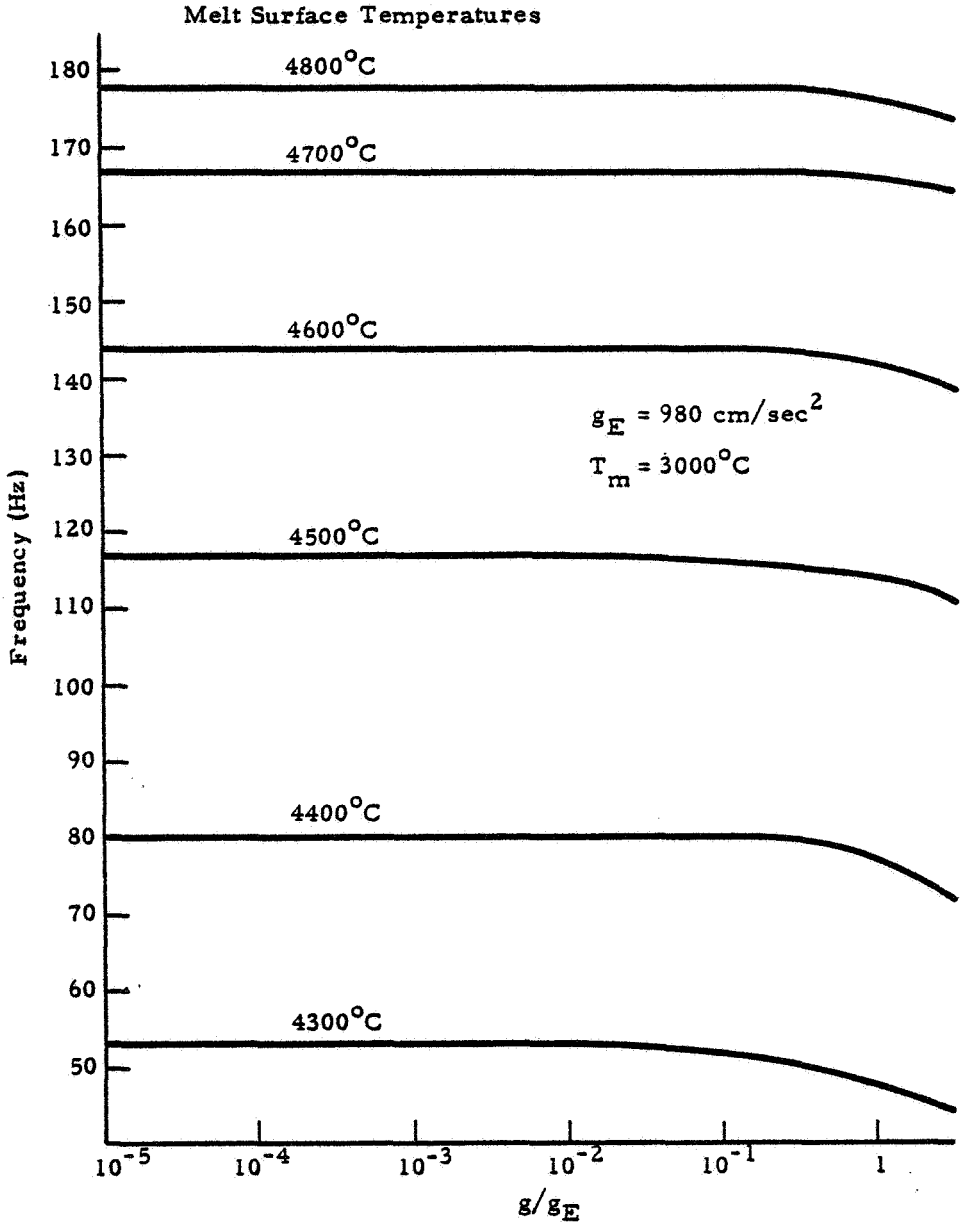

Fig. 6 - Spiking Frequency Graph of Tantalum

D15

EXPERIMENTS WITH ACOUSTICALLY LEVITATED DROPLETS*

Robert E. Apfel

Department of Engineering and Applied Science
Yale University, New Haven, Connecticut

Abstract

The levitation by acoustic means of a droplet of one liquid in an immiscible host liquid provides a means by which a variety of droplet and bubble phenomena can be probed. With the apparatus described below the force due to the buoyancy of the droplet is balanced by a force due to the radiation pressure exerted on the droplet in an acoustic standing wave field established in a cylindrical column of the surrounding liquid. (The acoustic frequency is about 50 kHz.) By proper design the equilibrium of the droplet is stable to any perturbation in the position of the droplet; furthermore, the position in the standing wave field at which the droplet is trapped is independent of the droplet radius, but depends on the density and sound speed of both liquids as well as the acoustic pressure and pressure gradient.

The apparatus consists of a cylindrical glass column containing one liquid which is excited into acoustic resonance by a cylindrical piezoelectric transducer. A heating coil around the column provides the temperature field. A droplet of the sample liquid rising in the host liquid is trapped by acoustical means in a region of uniform temperature. Thus far this technique has been employed in a number of investigations: 1) the theory for droplet motion and droplet levitation in a sound field has been tested and has been found to provide very good predictions for experimental work, 2) the tensile strength (or acoustic cavitation threshold) of greatly superheated droplets of three liquids has been measured as a function of temperature and has been found to be in good agreement with predictions of classical homogeneous nucleation theory, and 3) levitated, superheated droplets have been exploded by a sudden increase in acoustic intensity. Moderately high speed films (about 4000 frames per second) have been taken of the resulting vapor bubble and show some interesting features associated with vapor bubble dynamics.

Experiments planned for the future include 1) radiation-induced cavitation of levitated, superheated droplets, 2) measurements of properties such as density, sound speed, and index of refraction of metastable liquids, 3) observations of the solidifi-

* Work supported in part by the U.S. Office of Naval Research.

cation of supercooled, levitated droplets, and 4) possible investigations of metastability of binary liquid mixtures.

INTRODUCTION

There are many instances in which it is desirable to isolate a sample from a solid container surface. For example, one much discussed application is the levitation of the nuclear fuel for a fusion reactor in order to allow the fuel to be heated to extremely high temperature. Another example is the space processing of materials. Sometimes levitation of the sample in a near vacuum is desirable whereas in other applications a fluid host medium, either gas or liquid, may be necessary. Levitation can be achieved in a number of ways. Zero gravity is the most obvious; for metallic samples magnetic levitation may be used; and fluid flow techniques (e.g. air turbine) or acoustic means have been used for a variety of materials. In this paper we shall confine ourselves to the levitation by acoustic means of droplets of one liquid in an immiscible host liquid.

It has been known for quite sometime that a progressive acoustic wave in a liquid can produce a force due to radiation pressure on an object in the liquid. But it has only been a short time since this fact has been used to practical advantage by many investigators. For instance, the recent use of ultrasonic equipment for diagnosis and therapy in medicine has lead to the need for knowledge of the safe levels of ultrasonic irradiation, and this requires adequate calibration procedures which often involve a measure of the force due to the acoustic radiation pressure on a body.

The analysis of radiation pressure for progressive acoustic waves can be generalized to standing acoustic waves, as will be outlined below. The result of the analysis can be applied to the case of the force on compressible fluid spheres.

If in an experimental situation this force is adjusted to equal the force due to buoyancy,the fluid sphere can be levitated.

Whereas gaseous bubbles are relatively easy to levitate,[1] the situation for liquid droplets is more complex.[2,3] First of all, the sample droplet material must be reasonably immiscible in the surrounding host liquid; second, it will be shown that the droplet material must be more compressible than the host liquid for stable levitation in a real situation; and third, relatively high acoustic pressure amplitudes (ranging from 1 to 15 atmospheres) may be required in order to balance the buoyancy force, implying that techniques for avoiding acoustic cavitation in the sample and host materials must be employed.

If these conditions are met, however, a number of interesting experiments can be performed. These experiments differ from zero gravity experiments in that the position of the levitated droplet is a stable equilibrium point rather than a point of neutral equilibrium. This difference can be an advantage in some situations.

In this paper we shall first review the basic considerations involved in levitating liquid droplets by acoustic means. We shall then discuss 1) experimental apparatus for levitating droplets, 2) some interesting and convenient features of droplet trapping, 3) the use of acoustic levitation in measurements of the tensile strength of liquids,[2,4] 4) the use of acoustic levitation in observing bubble dynamics associated with the explosive vaporization of a superheated droplet, and 5) some proposed experiments involving droplet levitation.

DROPLET LEVITATION

Lord Rayleigh first discussed the force on an object due to an acoustic wave, which he called acoustic radiation pressure, in 1902.[5] Since then much has been written on the subject, some of it conflicting. A lucid discussion of the basic effect can be found in an article entitled "Acoustic Radiation Pressure in a Traveling Plane Wave" by Rooney and Nyborg.[6] An excellant analysis of "The Acoustic Radiation Pressure on a Compressible Sphere" has been written by Yosioka and Kawasima.[7] Below, this analysis will be greatly abbreviated by considering the special case of the acoustic radiation force on a fluid sphere (bubble or drop) that is far more compressible than the host liquid.

Consider a compressible sphere of instantaneous volume $V(t)$. If the acoustic pressure field is described by $P_A(\underline{r},t)$, then the spatial gradient at the position of the sphere is $\nabla P(\underline{r},t)$. The acoustic force, $\underline{F}_A$, on the sphere for our special case is:

$$\underline{F}_A = - \langle V(t) \nabla P_A(\underline{r},t) \rangle_{t \text{ (time average)}} . \qquad (1)$$

If changes in the volume occur more rapidly than heat exchange can take place, then conditions tend toward adiabatic and small changes from the nominal volume of the droplet, V_o, are related to pressure changes by the adiabatic compressibility of the liquid:

$$k_A = - \frac{1}{V_o} \frac{\Delta V}{\Delta P} = \frac{-1}{V_o} \left(\frac{V(t)-V_o}{P_A(\underline{r},t)} \right) . \qquad (2)$$

But, if the liquid is not dispersive in the frequency range of interest, then the adiabatic compressibility is related to the density, ρ^*, and the speed-of-sound, c^*, of the sample liquid by the following relation:

$$k_A = \frac{1}{\rho^* c^{*2}} .$$

We have, therefore,

$$V(t) - V_o = -P_A(\underline{r},t)V_o k_A = -P_A(\underline{r},t)V_o/\rho^* c^{*2}$$

or

$$V(t) = V_o[1 - P_A(\underline{r},t)/\rho^* c^{*2}] .$$

If the time-variation of the pressure field is sinusoidal, we can write

$$P_A(\underline{r},t) = P_A(\underline{r})\sin\omega t;\ \nabla P_A(\underline{r},t) = \nabla P_A(\underline{r}) .\ \sin\omega t .$$

Therefore,

$$\underline{F}_A = -\langle V(t)\nabla P_A(\underline{r},t)\rangle = \frac{-1}{T_P}\int_0^{T_P} V_o\left(1 - \frac{P_A(\underline{r})\sin\omega t}{\rho^* c^{*2}}\right)\nabla P_A(\underline{r})\sin\omega t\, dt .$$

Here, T_P is the acoustic period ($=2\pi/\omega$). The straightforward integration yields

$$\underline{F}_A = + V_o P_A(\underline{r})\cdot\nabla P_A(\underline{r})/2\rho^* c^{*2} .$$

The droplet is also subjected to a buoyancy force:

$$\underline{F}_B = V_o(\rho-\rho^*)\, g\hat{z} ,$$

where ρ is the density of the host liquid, g is the gravitational acceleration, and $\hat{z}$ is the unit vector in the positive axial (z) direction.

In order to levitate a droplet, the z-component of the average acoustic force must be equal in magnitude and directed opposite to the gravitational force; therefore,

$$(\underline{F}_A + \underline{F}_B)_{z \text{ component}} = 0. \tag{3}$$

That is:

$$\frac{V_o P_A(z) \cdot \frac{dP_A(z)}{dz}}{2\rho^* c^{*2}} + V_o(\rho - \rho^*)\, g = 0$$

or

$$-P_A(z)\,\frac{dP_A(z)}{dz} = 2\rho^* c^{*2}(\rho - \rho^*)\, g \equiv K \ . \tag{4}$$

This result is valid if the fluid sphere is far more compressible than its host. More generally, it can be deduced from Reference 7 that for ρ and c equal to the density and sound speed of the host liquid, respectively, and for $\lambda = \rho^*/\rho$ and $\delta = c^*/c$, then

$$-P_A(z)\,\frac{dP_A(z)}{dz} = 2(1-\lambda) g \rho^2 c^2 \Bigg/ \left[\frac{1}{\lambda\delta^2} - \left(\frac{5\lambda-2}{2\lambda+1}\right)\right]$$

For the liquid combinations used in the experiments described below, Eq. 4 has been adequate. It should also be pointed out that in the experimental realization for droplet levitation described in the next section, there is, in addition to an axial pressure variation, a radial pressure distribution which serves to keep the droplet on axis.

APPARATUS FOR DROPLET LEVITATION

The essence of the apparatus used for droplet levitation is shown schematically in Fig. 1. The system is shown with the thermal control (heating wire and thermocouple), but evacuation and filtering apparatus as well as manipulating devices for the probes are deleted in order to leave the diagram uncluttered.

A pyrex glass vessel of the shape shown (30mm o.d. and 9mm o.d. tubes) holds the host liquid. The acoustic driving unit shown is a cylindrical PZT-4 lead zirconate transducer (1.5-in. o.d., 1.25-in. i.d., 1.5-in. length). The composite system, made up of this unit epoxied to the liquid-filled glass tube, resonates in the 50-60 kHz frequency range, corresponding to the (1,0,n) mode of the system, where 1 refers to the first radial mode, 0 refers to axial symmetry, and n is 2, 3, 4, and 5, corresponding to a spatial pressure distribution along the axis that can be

characterized by a wavelength of 2-10 cm. (The axial pressure distribution is not simply sinusoidal because of the irregularities in the shape of the cylinder.) The particular resonance frequency chosen is that for which the acoustic pressure amplitude along the axis of the liquid-filled tube has a maximum in the test region just below the transducer.

The magnitude of the acoustic field can be increased so as to produce a net acoustic force on the test droplet that is equal in magnitude and opposite in direction to the buoyancy force. In other words, the test droplet can be held motionless in the host liquid. By trapping the droplet at a given position, the experimenter can observe its size and can assure that the droplet has time to achieve thermal equilibrium with the immediate surroundings. The thermocouple used in this experiment consists of a ribbon junction which is designed to minimize thermal conduction errors. The acoustic monitoring system is far more complex than the thermocouple. The complexity arises from the difficulty in constructing an acoustic transducing device that has the following properties:

(a) a sufficiently small size in order that it not disturb or detune the acoustic field and so that it has a fairly flat frequency response in the frequency range of interest;

(b) a construction that can withstand temperatures as high as 200C continually, acoustic pressure amplitudes of several bars, and rough treatment; and

(c) a sensitivity that is not affected markedly by small changes in temperature.

Such a probe has been constructed. The essential element is a cylindrical PZT-5 lead zirconate cylinder (nominal dimensions: $\frac{1}{16}$" o.d., 0.0425" i.d., $\frac{1}{16}$" length). A coaxial cable of 0.040" o.d. makes electrical connection with the sensing device in the following way: The inner wire of the coax is looped so that the sensing element can be forced on the loop. A spring-type action keeps the loop in contact with the inner electrode. Some high temperature epoxy can be added to help keep the loop in place. This epoxy also makes a mechanical junction between the coaxial wire and the PZT-5 cylinder. Electrical contact between outer conductors (of coax and sensor) is made with conductive paint. A thin TFE coating protects the probe from the liquid.

SOME INTERESTING AND CONVENIENT FEATURES OF DROPLET LEVITATION

There are some interesting features of droplet levitation that are predicted by Eq. 4 and that have been confirmed using the apparatus described above: (1) Equation 4 is independent of the radius of the droplet. The experimental results complement the results of Crum in confirming this prediction.[3] (2) Equation 4 is also independent of the acoustic frequency. (The above

derivation assumes that percentage changes in the acoustic pressure amplitude are small over distances comparable to the droplet radius.)

These features make calibration of the acoustic probe possible by observing the conditions for droplet levitation. We first assume linearity in two respects: (1) The voltage output of the probe amplifier v_o is proportional to the pressure at the probe position in the liquid. (2) The pressure in the liquid increases linearly with the input voltage to the driving transducer. (This can be assured so long as the electric input impedance to the driver is constant as the voltage is increased. The waveform can also be observed for distortion.)

The first condition can be written

$$P(z) = \alpha v_o(z), \quad dP/dz = \alpha dv_o/dz,$$

$$\alpha = \text{Proportionality Const.} \qquad (5)$$

If the probe amplifier output v_o is β times the actual probe output v_p, then the acoustic probe sensitivity is

$$v_p/P = v_o/\beta P = 1/\beta\alpha. \qquad (6)$$

In logarithmic form, the sensitivity S is just

$$S = 20\log_{10}(v_p/P) = -20\log_{10}\alpha\beta. \qquad (7)$$

The experimental procedure for probe calibration is as follows: with the driver input at v_i, the acoustic field is probed along the axis; the output, as a function of z, is designated $v_o(z)$. The probe is then removed from the liquid.

A droplet of the sample liquid is introduced into the column of the host liquid. When it reaches the test region, the driver input voltage is increased until the droplet is trapped. The input voltage with the droplet trapped at the position z is designated $(v_i)_z$. Assuming linearity, this would correspond to a trapping pressure

$$P(z) = \alpha \left[\frac{(v_i)_z}{v_i} v_o(z) \right] . \qquad (8)$$

[The bracketed term is just what the probe output voltage would be if the probe were at z with the driver voltage, $(v_i)_z$.]

Substituting Eq. 8 (and the derivative of it) into Eq. 4

yields

$$\alpha^2 \left[(v_i)_z / v_i \right]^2 \cdot v_o(z) \cdot \left[-dv_o(z)/dz \right] = K \qquad (9)$$

or

$$\alpha = \frac{v_i}{(v_i)_z} \left\{ \frac{K}{v_o(z) \left[-dv_o(z)/dz \right]} \right\}^{1/2} . \qquad (10)$$

We have included the minus sign with dv_o/dz because this term must be negative if a droplet is to be trapped. Since α, v_i, and K are constant, this relation implies

$$(v_i)_z^2 v_o(z) dv_o(z)/dz = \text{Const}, \qquad (11)$$

where z equals trapping position, $(v_i)_z$ is input voltage when droplet is trapped at z, and $v_o(z)$ is probe output voltage at z when driver input voltage is v_i. As the input voltage is increased, the droplet's position will change and Eq. 11, which is one test of the theory, can be checked. Crum has indirectly confirmed that this prediction is consistent with experiment.[3] Problems of adequate resolution, however, occur in regions in which the pressure gradient is so small that errors in the measurement of $dv_o(z)/dz$ can be large. For practical purposes, therefore, Eq. 11 should be most accurate in regions of maximum pressure gradient. Once α in Eq. 10 is known, the sensitivity of the probe can be calculated using Eq. 7, and Eq. 8 can be used to give the trapping pressure.

We point out, also, that the probe calibration can be circumvented in determining the acoustic pressure at any point on the axis. This is often desirable because the calculation of α assumes that the acoustic field has been probed precisely where the droplet is trapped. Slight probe misalignment would lead to errors in the probe calibration. The following expression for the trapping pressure does not require this precise alignment. Using Eq. 5, we can rewrite Eq. 4 as follows:

$$-P \frac{dP}{dz} = P\alpha \frac{(v_i)_z}{v_i} \cdot \frac{dv_o(z)}{dz} = K,$$

or

$$P(z) = \frac{K}{\alpha} \frac{v_i}{(v_i)_z} \left[- \frac{1}{dv_o(z)/dz} \right] .$$

With Eq. 10 for α, we have

$$P(z) = \left\{ Kv_o(z) \Big/ \left[-\frac{dv_o(z)}{dz} \right] \right\}^{1/2} \qquad (12)$$

Once again, the equation is most accurate at trapping positions for which $dv_o(z)/dz$ is not difficult to measure accurately. In order to find the trapping pressure at a position z' where $dv_o(z)/dz$ is small, we just use the known trapping pressure at z and Eq. 8 to eliminate the proportionality constant, and we solve for P(z'):

$$P(z') = P(z) \frac{v_o(z')(v_i)_{z'}}{v_o(z)(v_i)_z} . \qquad (13)$$

We can summarize the above as follows:

(1) Equations 12 and 13, the formulas for converting voltage measurements to pressure measurements, are based on the assumption that Eq. 4 for the trapping pressures is accurate. The recent work of Crum[3] suggests that results within 10% of the theory are to be expected. The fact that the theory predicts (and experiment confirms) that the trapping pressure is independent of droplet radius, provided that the radius is small compared to an acoustic wavelength, is rather comforting.

(2) Since P(z) in Eq. 12 depends on the ratio $[v_o(z)/(dv_o/dz)]$, the actual magnitude of the probe output does not enter into the prediction of the trapping pressure. (For instance, if the probe is slightly off axis, this ratio will have the same value as that along the axis. The probe must, of course, move vertically.) For probe calibration, however, the actual magnitude of $v_o(z)$ is, of course, important.

Example

The procedure for measuring the conditions that cause droplet levitation is illustrated by the following example. In Fig. 2, two curves are plotted. The upper ordinate scale is the output of the acoustic probe amplifier at a given probe position in the sound field when a constant rms voltage is maintained across the acoustic driving unit. For this particular experiment, the acoustic system resonates in the (1,0,3) mode corresponding to a frequency of about 50 kHz.

Having probed the acoustic and thermal fields, we remove both probes from the liquid. A droplet of sample is introduced into the column of liquid and rises into the test region where it is trapped in the host liquid by appropriately adjusting the input voltage to the acoustic driving unit. The position of the trapped droplet above the pressure maximum and the rms voltage to the

driving unit is then changed, causing the droplet to move to a new equilibrium position closer to the pressure maximum. Input voltage and position are again recorded. This procedure is repeated.

The bottom ordinate in Fig.2 indicates the trapping input voltage versus position for four ether droplets. The host liquid in this case is glycerin.

Observations

One interesting feature of the results is that the data for droplets of different size (ranging from about 0.2-to 2.0-mm diam.) appear to lie on the same curve. This is consistent with the "trapping theory," which predicts the independence of trapping pressure on droplet size, provided that the droplet is small compared to the acoustic wavelength.

According to Eq. 11, the product of $(v_i)_z^2$, $v_o(z)$, and dv_o/dz should be a constant if the theory for droplet trapping is to be trusted. For the region z=4.4-5.0, in which most of the droplet trapping measurements are made, this product varies by less than 10%. The calculated product shows even less variation if the point at z=4.4, where the slope of $v_o(z)$ is more difficult to measure, is not considered.

MEASURING THE TENSILE STRENGTH OF LIQUIDS

Under certain conditions a liquid can sustain large tensile stresses or degrees of superheat without vaporizing. This departure from the vaporization conditions described by the relation between vapor pressure and temperature for a given liquid is a result of the absence of a flat liquid-gas interface in the system under test; that is, vaporization occurs when a vapor cavity forms in the liquid.

This cavity formation, or "cavitation", usually occurs not because of spontaneous breaking apart of neighboring liquid molecules due to fluctuations in the density at the molecular level (homogeneous nucleation) but because of the presence of something foreign to the liquid (heterogeneous nucleation). In the latter of these cases cavitation may occur at a liquid-solid boundary, at a liquid-liquid boundary, at a liquid-solid-gas interface (such as a crevice in an imperfectly wetted container surface or solid impurity suspended in the liquid), or even at a site in the liquid established by impinging radiation (as in bubble chambers).

There were, until recently, no reported measurements of the tensile strength of liquids that came close to the theoretical predictions for the ultimate strength of a liquid as described by homogeneous nucleation theory. The droplet levitation technique,

however, appears to be well suited for such measurements. In an attempt to minimize the chances of heterogeneous nucleation, small, filtered droplets of the sample liquid are immobilized acoustically in an inert host liquid.

The experimental procedure is outlined with the assistance of Fig. 1. An injected droplet of the sample rises in a cylindrical glass column containing the inert host liquid. A heating coil wrapped around the column establishes a positive and stable temperature gradient in the host ("up" positive). The droplet is superheated as it rises and when it reaches the test region it is levitated as described earlier. If the acoustic pressure amplitude is further increased, the droplet will move to a new equilibrium position closer to the acoustic pressure maximum in the standing wave field. This procedure of increasing the acoustic pressure can be continued until at some combination of superheat and acoustic stress, the droplet bursts into its vapor. This can be repeated for different test-region temperatures, thereby allowing the measurement of the trade-off between acoustic stress and superheat as causes of droplet vaporization.

The peak tensile stress experienced by the droplet immediately before vaporization (that is, the peak acoustic pressure amplitude minus the hydrostatic pressure) is plotted against temperature in Fig. 3 for two different liquids: diethyl ether and n-hexane. In both cases the host liquid was glycerin. Also plotted are the results of others who measured the limit of superheat of these liquids under positive pressure using a variety of experimental techniques. The solid lines are the predictions of classical homogeneous nucleation theory.

The experimental results complement each other despite the fact that, for n-hexane, Skripov and Ermakov[8] used a different host liquid than in the present measurements, and the fact that Wismer[9] held his ether samples with capillary tubes rather than in another liquid. These observations strongly suggest that for the liquids tested, nucleation has occurred within the sample and not at the liquid-liquid or liquid-solid interface. The results are also in good agreement with classical homogeneous nucleation theory. Thus, it appears that the droplet levitation scheme has provided a means by which the tensile strength of some liquids may be measured.

VAPOR BUBBLE DYNAMICS ASSOCIATED WITH THE VAPORIZATION OF A SUPERHEATED DROPLET[10]

The dynamics of physical explosions in liquids commands interest in a wide variety of disciplines: Examples of such phenomena are underwater explosions, explosions due to sudden contact of hot or cold liquids (such as Liquid-Natural Gas contacting water, water contacting smelt, and molten metals contacting other liquids), and cavitation explosions (and implosions).

These explosions have been observed directly and also in model systems. In the model systems bubbles have been generated employing methods such as spark-gap discharge[11] and focussed lasers.[12] Here we describe our first attempts at observing photographically the explosion of small superheated droplets of one liquid suspended in an inert host liquid. The size of the droplet and the degree of superheat give us a handle as to the energy associated with the explosion.

Above, we have described a technique for measuring the tensile strength of superheated liquids. When the liquid reaches this ultimate limit, it vaporizes explosively. We have filmed the dynamics of this explosion at moderately high speeds (about 4000 frames per second, fps) with both diffuse and shadow lighting.

The filming has been made relatively easy, because we have taken advantage of droplet levitation and positioned the camera where the droplet will be levitated and exploded. We can, therefore, adjust things so that the vapor bubble resulting from the explosion nearly fills the entire frame.

The explosion is initiated by suddenly increasing the acoustic stress on the levitated droplet. The acoustic stress serves one other useful purpose:

In the absence of the acoustic field the explosive growth of the vapor bubble produced from the initial explosion is followed by the vapor bubble collapse. This collapse process is unstable, with the single vapor bubble shattering into a multitude of smaller bubbles which are propelled, upon rebound, into the host liquid. In the presence of the acoustic field, however, the collapsing bubble is held together by the acoustic field. The tendency of small bubbles to coalesce in an acoustic field is attributed to "Bjerknes" forces.[13] Thus a single vapor bubble results from the explosion. The acoustic field has a frequency about 50-100 times greater than the natural resonance frequency of the resulting vapor bubble and represents, we believe, only a small perturbation, other than its coalescence role, to the dynamics of the initial explosion process.

The Particulars for These Experiments

Ether was the droplet material and glycerin was the host liquid for these observations. The droplets were superheated to approximately 105°C above ether's normal boiling point, or to about 140-141C. At this temperature an acoustic stress of approximately eight bars is required to nucleate the explosion.

The apparatus sketched in Figure 1 was supplemented by a

Fastex 16mm WF3 Camera with a 2 inch lens extension tube. The end of the extension tube was within three inches of the droplet. In this configuration a one millimeter diameter droplet appears on the 16mm film as an image with an approximate dimension (vertical diameter) of 1mm. Because of the cylindrical column, horizontal dimensions are magnified by about 1.6.

When the camera motor is switched on, the film accelerates to 5000 frames per second in less than a second. The film runs for little more than a second. For monitoring the frame rate an oscillator set at 1000 Hz drives a neon bubble in the camera which puts light marks on the film (2000/s, because the neon bulb flashes for positive and negative excursions in voltage). In the sequences shown in Figs. 4 and 5, the time per frame ranged from 0.24 to 0.3 ms (or approximately 3300 to 4000 fps).

Two different lighting schemes were used:

Diffuse Lighting: For the photographs in Fig.4, three 500 watt bulbs in parabolic reflectors surrounded the test region.

Shadow Lighting: For the photographs in Fig. 5, a collimated mercury arc beam was directed through the test region into the lens.

Results

An initial film sequence and radius vs. time graph of a droplet explosion is shown in Fig.4. The explosion process can be summarized as follows: The vapor bubble grows rapidly as a result of the pressure produced inside the cavity during the vaporization of the droplet. It grows past the size at which the pressure inside and outside the cavity are the same, because of the momentum imparted to the host liquid. It then collapses and rebounds several times before the energy associated with the oscillation is completely dissipated. The droplet then moves radially from the center of the tube due to acoustic forces on it.

As the photographs indicate, some of the energy associated with the growing droplet is lost during the collapse as surface instabilities grow.

In Figure 5 using shadow lighting an instability initiated during the collapse of a vapor bubble takes the form of a jet-like protrusion growing rapidly from the main bubble as it rebounds (only part of the main bubble is shown). The approximate velocity of this protrusion is 2m/s. This instability may be analogous to the jets that occur during the violent collapse of a cavitation void in a liquid far below its boiling point. In our case the instability is less violent because of the cushioning

and damping effects of the superheated vapor in the bubble.

The techniques for producing and observing droplet explosions described here may be adaptable to the study of the initial stages of physical explosions in model systems. For a given modeling application, the appropriate choice of test and host liquids is required. (Freon 114 in a host of water is being considered in modeling underwater explosions.)

This scheme should also be easily adaptable to higher speed photography. This would allow us to focus in on the region where the first vapor cavity is nucleated and would give us detailed information about the very important initial stages of growth.

PROPOSED EXPERIMENTS INVOLVING DROPLET TRAPPING

1. Radiation-Induced Cavitation

   A superheated droplet that is levitated in a sound field at acoustic pressures insufficient to cause homogeneous nucleation may explode due to some foreign matter touching the sample or some radiation incident on the sample. By using known radiation sources one should be able to study the temperature and pressure dependence of the threshold of radiation-induced cavitation. Such a study may have implications in the design of a neutron energy spectrometer.

2. The Solidification of Supercooled Droplets

   Using a photographic scheme similar to that described for observing the explosion of superheat droplets, we should be able to observe the solidification of an acoustically levitated supercooled droplet. The information obtained from these films can be compared with the results of the analysis of the retrieved solid pellets in order to shed light on the mechanisms of the nucleation and growth processes involved in solidification.

3. Properties of Metastable Liquids

   Very few properties of metastable liquids have been measured. (e.g. sound speed, index of refraction, density, compressibility, et al.). By probing at and observing the motion of these droplets in a known sound field we should be able to determine the temperature dependence of some of these properties. We, therefore, have the opportunity to increase substantially our knowledge and hopefully our understanding of the liquid state.

REFERENCES

1. A. Eller, "Force on a Bubble in a Standing Acoustic Wave," J. Acoust. Soc. Amer. 43, 170L (1968).

2. R.E. Apfel, "A Novel Technique for Measuring the Strength of Liquids, J. Acoust. Soc. Amer., 49, 145 (1971).

3. L. Crum, "Acoustic Force on a Liquid Droplet in an Acoustic Stationary Wave, 50, 157 (1971).

4. R.E. Apfel, "Tensile Strength of Superheated n-Hexane Droplets," Nature (Physical Science), 233, 119 (1971).

5. Lord Rayleigh, "On the Pressure of Vibrations" Phil. Mag. 3, 338 (1902).

6. J. Rooney and W. Nyborg, "Acoustic Radiation Pressure in a Traveling Plane Wave" Amer. J. Phys. 40, 1825 (1972).

7. K. Yosioka and Y. Kawasima, "Acoustic Radiation Pressure on a Compressible Sphere," Acustica, 5, 167 (1955).

8. V. Skripov and G. Ermakov, "Pressure Dependence of the Limiting Superheat of a Liquid" Russ. J. Phys. Chem. (transl.), 38, 208 (1964).

9. K. Wismer, "The Pressure-Volume Relation of Superheated Liquids," J. Phys. Chem. 26, 301 (1922).

10. R.E. Apfel and J.P. Harbison, "Acoustically Induced Explosions of Superheated Droplets," J. Acoust. Soc. Amer. - in press.

11. See, for example: D.C. Gibson, "The Pulsation Time of Spark Induced Vapor Bubbles," Trans. ASME, Series D, 94, 248 (1972).

12. See, for example: M.P. Felix and A.T. Ellis, "Laser-Induced Liquid Breakdown-a Step-by-Step Account," Appl. Phys. Lett. 19, 484 (1971).

13. V.F.K. Bjerknes, Field of Force (Columbia University Press, New York, 1906).

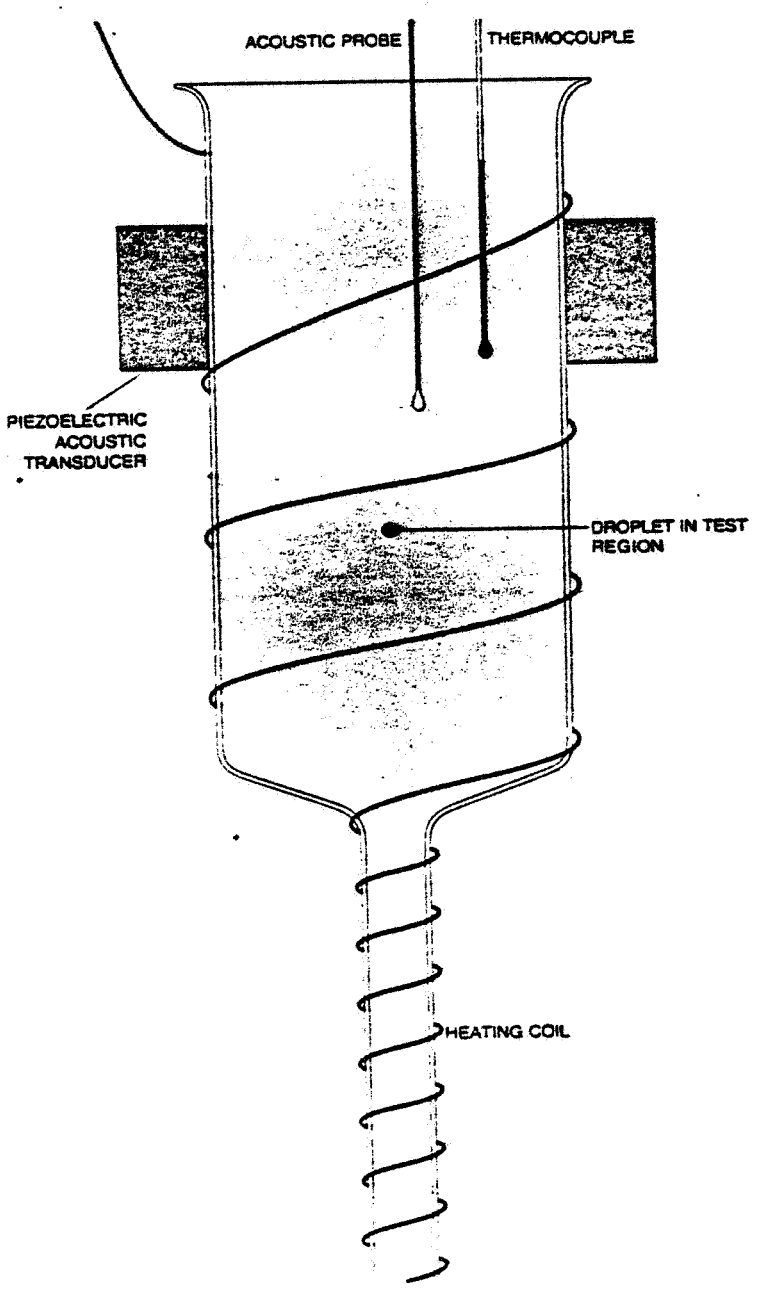

Fig. 1 Acoustic resonator for levitation experiments. Intensity of shaded region is suggestive of acoustic pressure distribution.

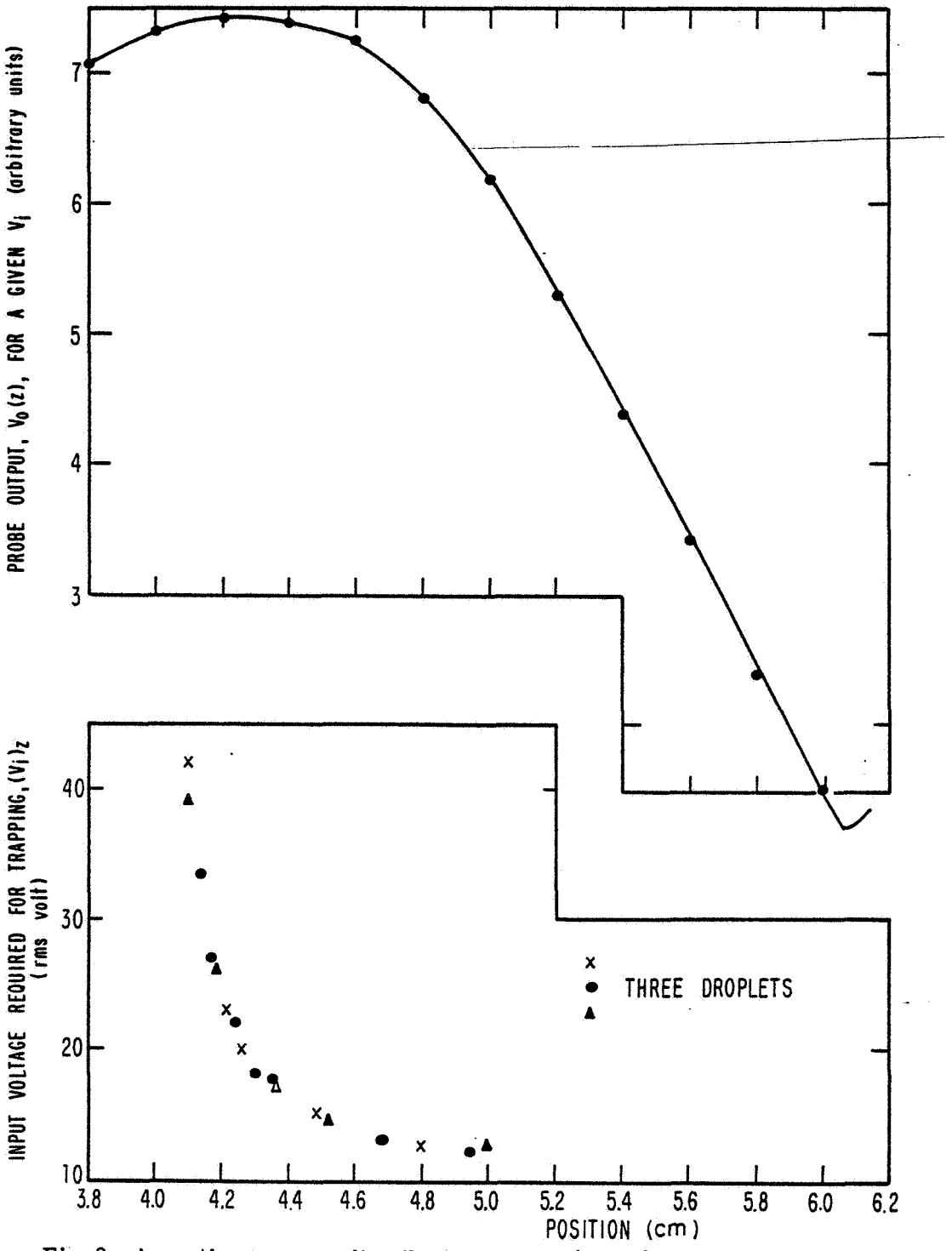

Fig. 2 Acoustic pressure distribution on axis (above) and driver input required to levitate droplets (below).

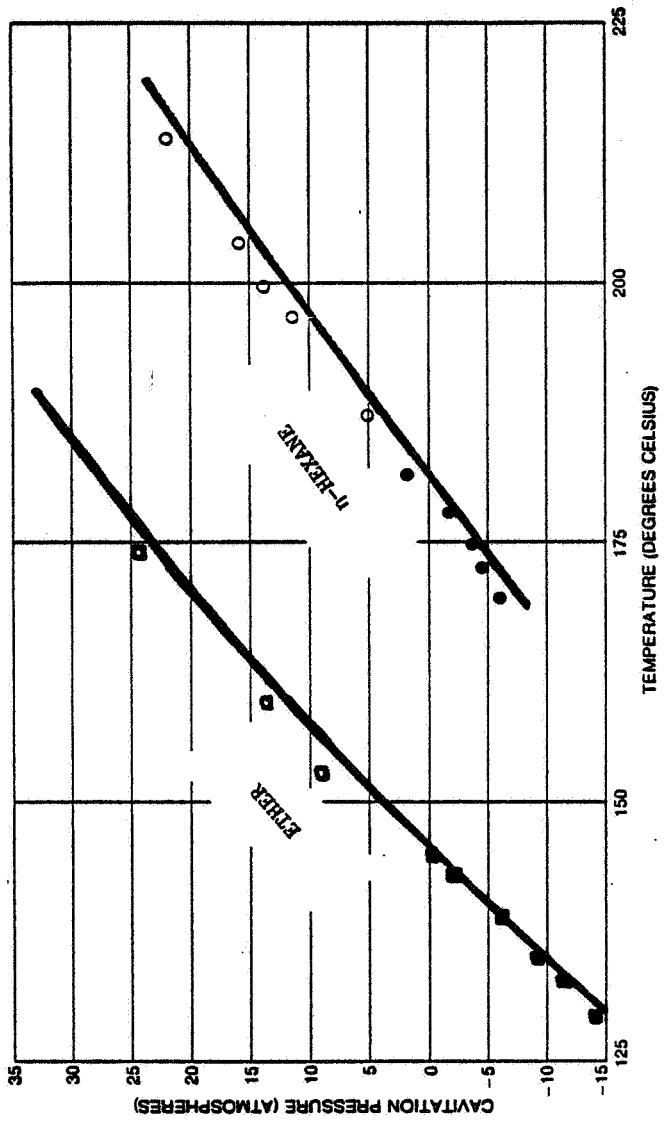

Fig. 3 Tensile strength (at negative pressures) and limiting superheat (at positive pressure) of two liquids.

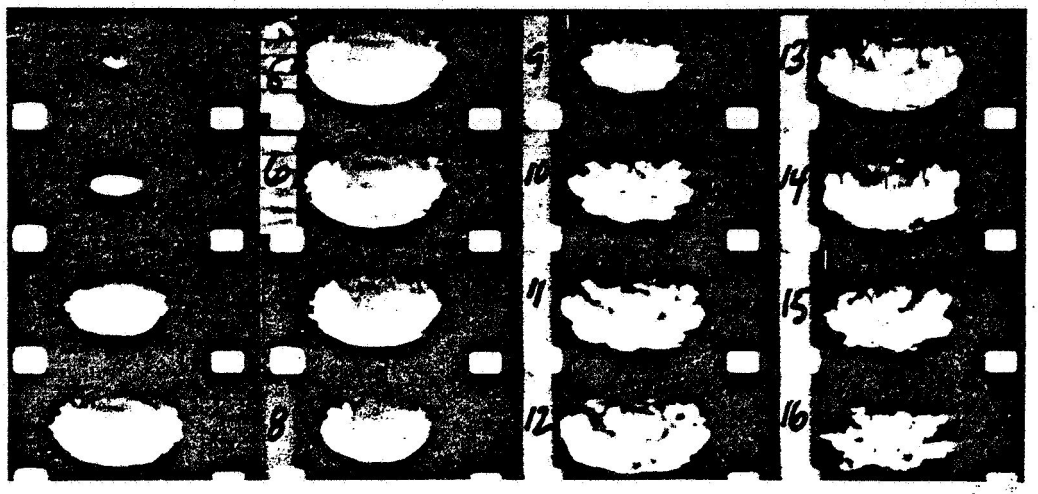

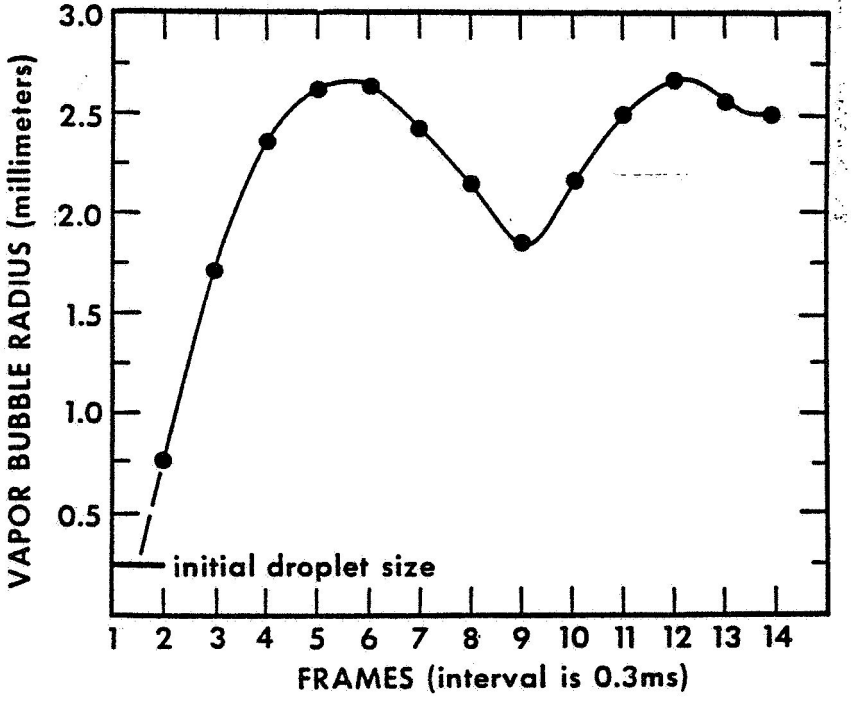

Fig. 4 Droplet explosion and resulting vapor bubble dynamics; Radius vs. time curve for initial sequence.

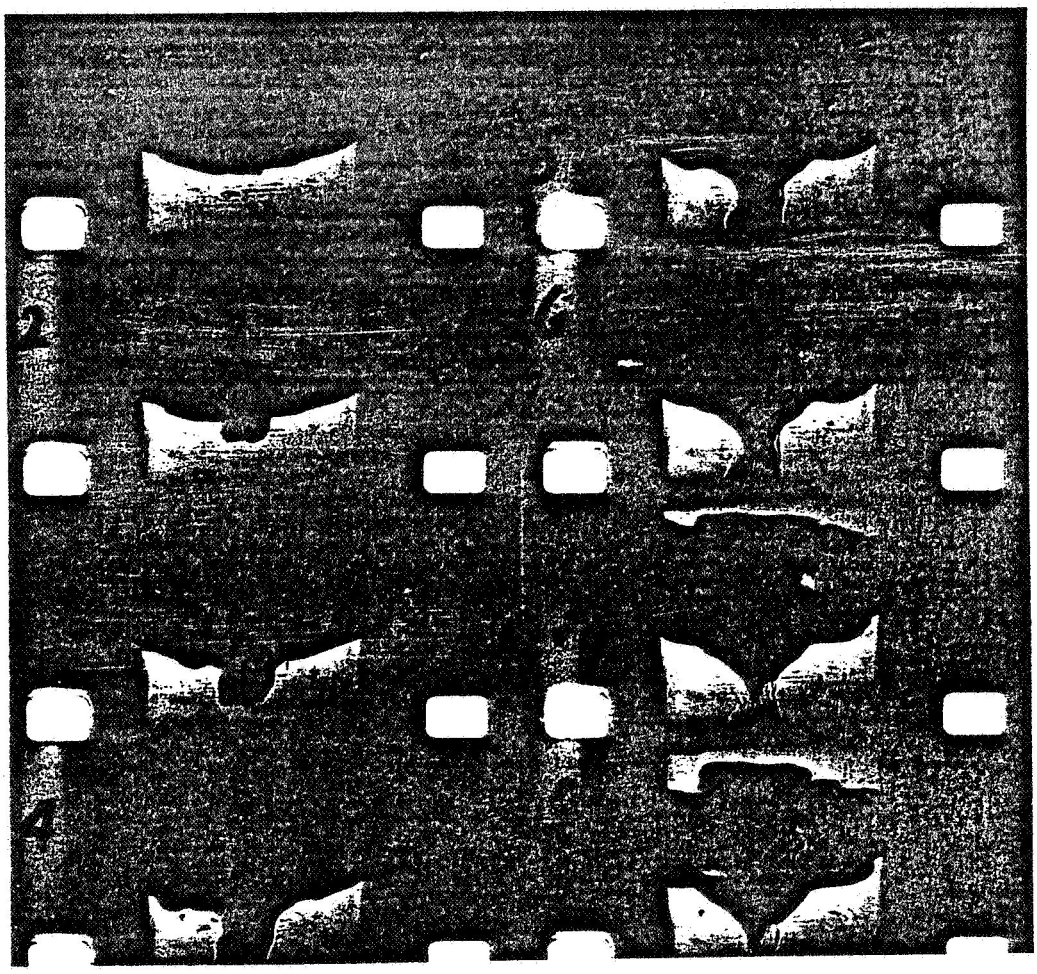

Fig. 5. Instability during oscillation of hot vapor bubble. Only part of bubble is shown.

D16

DROP DYNAMICS IN SPACE

T. G. Wang, M. M. Saffren, D. D. Elleman

Jet Propulsion Laboratory
California Institute of Technology
Pasadena, California

The Jet Propulsion Laboratory (JPL) is planning experiments to be performed in weightlessness to study the dynamics of liquid drops. The liquids will range from superfluid helium through ordinary liquids to molten metals and glasses. These experiments will be carried out in a chamber now being developed at JPL that utilizes the forces and torques produced by acoustic waves excited within the chamber.

Preliminary experiments of short duration (5-20 seconds) are being carried out in the weightless environments provided by NASA drop towers and NASA KC-135 aircraft flown along ballistic trajectories. Experiments are planned which will utilize sounding rockets to provide up to 5 minutes of weightless environment; however, these experiments will eventually require weightlessness of more than 5 minutes duration. None of the current facilities — sounding rockets, drop towers, or KC-135 aircraft — can provide a sustained weightless environment. Ultimately the experiments will be conducted in Spacelab — a manned orbiting laboratory to be flown on the Space Shuttle commencing in 1980. Spaceflight will provide weightlessness over a period of a week or more, allowing truly laboratory-like experiments to be conducted on free liquid drops (and bubbles).

In this paper we first discuss the drop dynamics experiments proposed for Spacelab, and then discuss the acoustic chamber — its operation, and how it is being tested for these and other experiments.

SECTION I

THE DROP ROTATION AND OSCILLATION PHENOMENA (DROP) EXPERIMENT

A. INTRODUCTION

The theory of the dynamics of a free drop has been well studied in the approximation that dynamic quantities deviate linearly from a resting drop. With special exceptions to be discussed below, there is no non-linear theory of the dynamics of a fluid drop. Not only are definitive experiments for the large amplitude behavior of fluid drops lacking but there are few definitive experiments even for linear behavior. This is a consequence of the limitations involved in conducting experiments in an earth laboratory. Among these limitations are insufficient droplet sizes for accurate observation, limited available time for experiments, and perturbing effects due to the method of suspending the droplets.

The proposed drop dynamics experiment will utilize the unique zero-g environment provided by the orbiting space shuttle to investigate the dynamics of a free drop. The results of the proposed experiment will be used to verify existing theory, and to provide the necessary insight for further theoretical development of this subject. The deficiencies of the existing theory, which disregards viscosity, internal flows, virtual mass, and other parameters, are exemplified by the different results of Plateau's system of two immiscible fluids[1] and the Skylab science demonstrations[2]. A more detailed description of these two experiments is given is Section II.

Aside from fundamental interest, a better physical understanding of the behavior of the dynamics of free liquid spheroids is required in many areas of science and technology, as demonstrated by the scope of the program presented at this Colloquium.

B. SCIENTIFIC OBJECTIVES

1. Equilibrium Figures of a Rotating Drop

A rotating fluid in its equilibrium state can sustain no internal flow and so rotates as a rigid body. When subject to gravity and contained in a vessel,

at any angular velocity, the free liquid interface (meniscus) assumes a parabolic shape. When the fluid mass is free, however, the dependence of its shape on angular velocity is far less trivial.

In the proposed Drop Dynamics Module experiments to be performed on the Spacelab mission, the stable equilibrium shape of a rotating drop of fluid will be determined as a function of its angular velocity. Also, the angular velocities at which there is a qualitative change of drop shape (bifurcation points) and the critical angular velocity at which the rotating drop fissions will be determined. A more detailed listing of experiment objectives is given below.

The theory of the equilibrium shapes of rotating fluids began with investigations by Newton[3] on the shape of the rotating earth, and the extensive theory that ensued was that of a free fluid held together by self-gravitation. In a crude attempt to verify this theory, Plateau carried out experiments in 1843 on ordinary rotating fluid drops in a neutral buoyancy tank, although such drops are held together by their surface tension, not by gravitation. His experiments were in rough qualitative agreement with the theory of that time, except for one remarkable difference: one of the stable configurations for a rotating drop was toroidal, not generally thought to be an equilibrium shape for a self-gravitating drop. That it is in fact an equilibrium figure for rotating liquid drops held together by surface tension was not demonstrated until the theory of ordinary rotating liquid drops evolved more than seventy years later when Rayleigh[4] investigated droplets symmetric about the rotation axis (see also Appell[5]). The stability of the simple axisymmetric shapes awaited study by Chandrasekhar[6] and even today the stability of the toroidal and nonaxisymmetric shapes remains virtually unexplored both theoretically and experimentally.

Experimental observation of the behavior of a rotating drop held together by surface tension goes beyond simply testing the existing theory. This theory has in fact been embedded[7] in a grander theory which at one extreme embraces fluid masses held together by their gravity, modelling the stars, and at the other extreme embraces uniformly electrically-charged fluid masses,

modelling atomic nuclei. Consequently, any deviation in the observed behavior of ordinary liquid drops from their predicted behavior would call into question the more all-embracing theory of equilibrium figures of fluid masses. Conversely, if experiments on the equilibrium figures of ordinary drops are in agreement with predictions of theory, this would strongly suggest a unified theory of the dynamics of fluid masses. The observed behavior of ordinary liquid drops would then help to frame the theory of their dynamics and this theory in turn could be extended into the astronomical and nuclear realms. This is one of the ultimate aims of the two proposed sets of experiments. The experiments on rotation and oscillation are precursors to future experiments in which the oscillation of rotating drops will be studied. [Perhaps it is worth interjecting that the experiments are also precursors to ones in which the drops are electrically charged, electrically conducting, dielectric, non-Newtonian, or superfluid; and where external fields are applied (electric, magnetic, electromagnetic, acoustic, or thermal). In addition it is envisaged that multiple drop experiments will be performed in which the interactions of free drops can be observed and these experiments will be based, of course, on what has been previously learned about single drop behavior in externally controlled fields.]

The following discussion presents the current theory of the equilibrium shapes of a rotating fluid drop held together by its surface tension. Rayleigh[4] was the first to calculate the axially symmetric equilibrium shapes. These calculations were extended by Appell[5] who gave a more detailed and elegant description opening the discussion of the dynamics of the change of shape and the stability of these shapes. Chandrasekhar[6] made a definitive study of the stability of the simply connected axisymmetric shapes, and in addition obtained the frequencies of their small amplitude oscillations. Ross[8, 9] reviewed and extended some of the previous work on drops to "bubbles" — fluid drops less dense than the surrounding medium. Gans[10] has examined the small amplitude oscillations about equilibrium shapes of compressible fluids. The equilibrium shape of a drop containing a bubble was discussed by Bauer and Siekmann[11], while Böhme, Johann, and Siekman studied the shape of a rotating dielectric drop in an electric field[12]. Finally, Swiatecki[7, 13], by inserting the theory of the equilibrium shapes of "surface-tension drops" into the more

general theory, was able to give a fairly complete semiquantitative description of the stability of shapes for such drops as a function of their angular momentum, including a discussion of metastable shapes he calls "saddle-point" shapes.

The axisymmetric equilibrium shapes (see Figs. 1 and 2) are conveniently described as a function of the dimensionless angular velocity, Ω , which is the angular velocity measured in units of the fundamental oscillation frequency of the resting drop. [$\Omega = \omega / (8\sigma/\rho a^3)^{1/2}$ where ω is the rotational angular velocity, σ is the surface tension, a is the equatorial radius, and ρ is the density]. When $\Omega < 0.7071$, there are always two equilibrium shapes; the one of lower energy is simply connected, while the other is torus-like. For $\Omega = 0.7070$ there appears an additional "collapsed" shape in which zero thickness at the center yields a "figure-eight" cross section. For $0.7071 < \Omega < 0.73$ there are two torus-like shapes but still two simply-connected shapes. When $\Omega = 0.73$ there is only one torus-like shape[a] but still two simply-connected shapes. The torus-like shapes are lost once $\Omega > 0.073$ and when $\Omega = 0.7540$ there remains only one simply connected shape; this is the greatest angular velocity that an axisymmetric equilibrium shape can have.

The only detailed study of the stability of the equilibrium figures was made by Chandrasekhar[6] but only for the simply connected shapes. He showed that for $\Omega = 0.584$ the drop can deform, without changing its energy, to another shape not having rigid body rotation; thus the original shape is unstable. He presumes that the stable equilibrium shapes become nonaxisymmetric for $\Omega = 0.584$. This presumption is based on an analogy with what is known to occur for a liquid mass held together by self-gravitation. There the stable equilibrium figures are true ellipsoids below a critical angular velocity and triaxial ellipsoids above.

As shown in Fig. 3, at $\Omega = 0.584$ (the bifurcation point), the secular stability passed from the sequence of axisymmetrical shapes to triaxial shapes. Berringer and Knox[14] have calculated that for the "surface-tension" drops the

---

[a] Appell[5] and Ross[8] disagree on the number of toroidal shapes for $\Omega < 0.7071$.

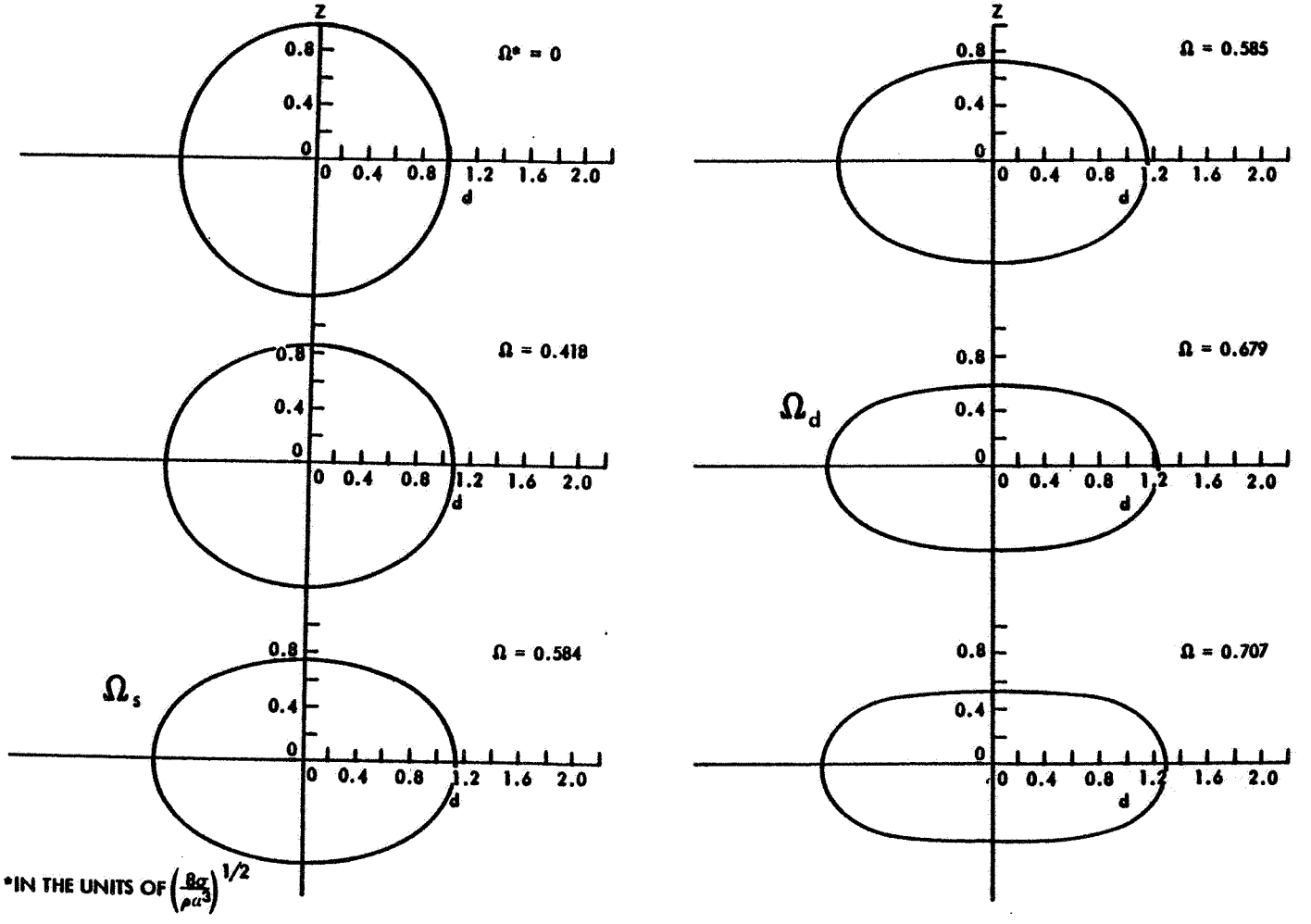

Fig. 1. Axisymmetric Equilibrium Shapes

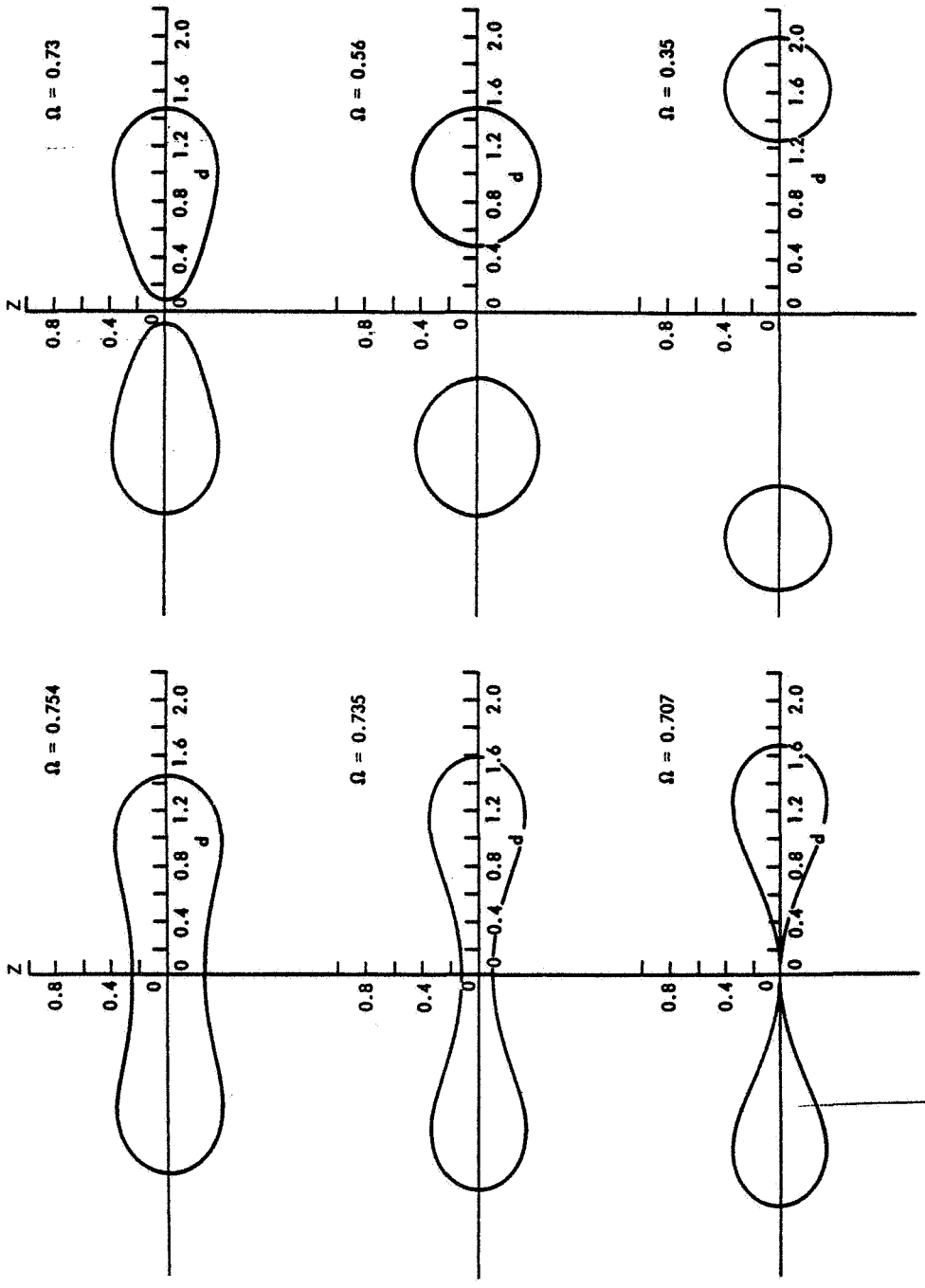

Fig. 2. Axisymmetric Equilibrium Shapes (to Pinch-Off)

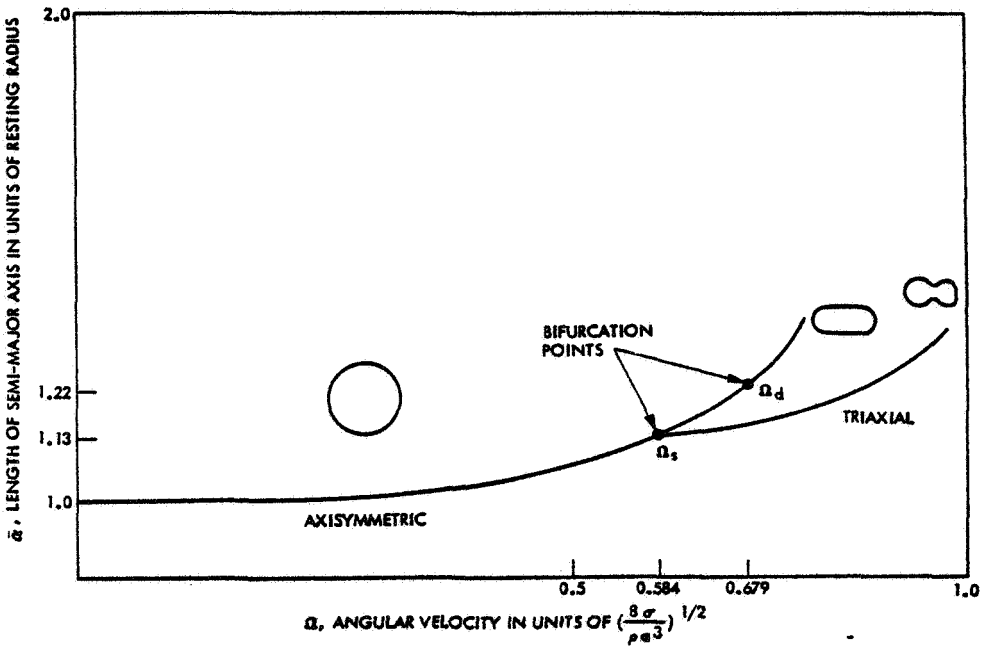

Fig. 3. Illustration of Bifurcation Points

triaxial shapes are not ellipsoids, but the stability of the toroidal shapes has received no definitive treatment. However, the results of Wong[15] on the toroidal shapes of charged liquid drops suggests that these equilibrium shapes may be "saddle-shapes" — shapes stable against deformations that preserve the axial symmetry but unstable against others such as varicose deformation against which fluid jets are unstable (the Rayleigh instability). The triaxial equilibrium saddle-shapes were calculated by Pik-Pichak[16].

The neutral buoyancy experiments of Plateau[1] on the shapes of rotating liquid drops are in qualitative accord with the transition from axisymmetric to triaxial shape as theoretically described by Chandrasekhar[6]. However, Plateau showed that at high angular velocity the drop first rotates nonrigidly and a toroidal shape is then obtained which becomes a rigidly rotating figure, indicating that the toroidal shape is indeed stable. However, this conclusion was called into question by very recent experiments by the authors at JPL which

showed that if the drop is of the less viscous fluid rather than the more viscous as it was in Plateau's original experiment, the toroidal shape is not stable, pinching off as does a liquid jet.

The Skylab experiments on rotating drops[2] yielded the "pinched" triaxial shapes resembling "dog-bones." In one experiment a dog-bone shape fissioned; the reason for this was not clear. The particular dog-bone may actually have been a "saddle-point" shape, or an internal flow or slight oscillation within a stable shape close to the limit of stability may have converted it to a "saddle-shape" when the extra energy was added to the rigid body's fluid motion.

It is very important to note that the Plateau and Skylab experiments yielded different shapes for sufficiently large angular velocity — there was no dog-bone shape demonstrated in the Plateau experiments, nor was there a toroidal shape demonstrated in the Skylab experiments. Similar discrepancies were noted in experiments on cylindrical liquid columns rotating about their axes. Neutral buoyancy experiments carried out by Carruthers[17] showed the instability of such columns always to be axisymmetric, while the Skylab experiment on rotating liquid columns showed the instabilities to be nonaxisymmetric[17]. However, the axisymmetric instabilities were recovered on Skylab once the fluid was made sufficiently viscous.

Plateau's failure to observe the dog-bone may have been due to the effect of "added mass"[b], i.e., in the Plateau experiment a triaxial drop nonaxisymmetric about the rotation axis will entrain adjacent portions of the surrounding liquid (Fig. 4). The consequence of this added mass is to severely modify the pressure drop across the droplet interface. In the limit that the adjacent fluid moves rigidly with the droplet, the pressure drop vanishes. In this extreme, the protions of the droplet that extend into the added fluid will tend to assume a spherical shape to minimize the surface energy. In fact, examination of the shapes obtained by Plateau for rapid rotation do indeed show such "spherical caps" (see Fig. 4).

---

[b] Also know as virtual mass or hydrodynamic mass.

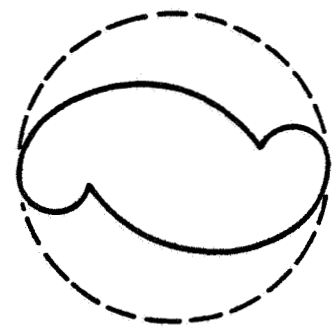

Fig. 4. The solid lines indicate the shape obtained by Plateau. The dotted lines suggest the "boundaries" of the added host liquid

In weightlessness the added mass effect becomes negligible because the ratio of the density of two fluids can be chosen to be three orders of magnitude less than unity.

Thus it appears that viscosity and virtual (added) mass effects strongly limit the validity of neutral buoyancy experiments. In fact, their effects on the flows in rotating fluids may make otherwise stable shapes unstable and vice versa (the "spin-up" effect associated with Ekman boundary layers)[18]. These problems can be studied experimentally only in the true weightlessness afforded by space flight where the viscosity and the density differences of the two liquids can be freely chosen.

2. Large Amplitude Oscillation of a Liquid Drop

In contrast to the problem of a rotating drop, a reasonably complete theoretical formulation of small amplitude dynamics of freely-suspended liquid drops under the influence of surface tension forces has been well developed[19-24]. A rather extensive review of the theoretical work has been given by Chandrasekhar and a large variety of experimental tests have been conducted to verify and support this theoretical work. The experimental procedures fall into three general categories: the liquid drop is suspended in a neutral buoyant media, the drop

is supported by a vertical gas flow, or the drop falls through a gas or vacuum. All of these methods suffer various limitations which have made a detailed quantitative comparison of theory and experiment limited in scope.

At the present time there is no adequate theory for large amplitude oscillations of liquid drops, nor have the criteria for rupture or coalescence of liquid masses and the transition region between the high viscosity and low viscosity regions been developed. However, Foote[25] and Alsonso[26] have simulated with computer calculation the motion of a drop undergoing large amplitude oscillation.

In 1879 Lord Rayleigh conducted one of the first investigations on the behavior of an oscillating liquid drop about its spherical equilibrium shape. He limited his study to the case where the oscillations were axisymmetric and assumed that the internal motions were described by a potential flow field. He did not include viscous effects. The results of Rayleigh's investigations can be expressed by a series of expansion of Legendre polynominals:

$$r = a_0 + \Sigma\ a_n P_n(\cos\theta) \tag{1}$$

where r is the radial coordinate, ρ is the polar angle measured from the pole of the drop and the coefficients a_n are functions of time.

In solving for the a_n's that appear in Equation (1), it is necessary to limit the oscillations to small amplitudes, $a_n << a_0$. It can be shown that if $a_n \cong \cos \omega_n t$ then

$$\omega_n^2 = n(n-1)(n+2)\ \frac{\sigma}{\rho a^3} \tag{2}$$

where σ is the surface tension, ρ is the density of the liquid, and a is the equilibrium spherical radius. It should be noted that n = 0 and n = 1 correspond to rigid body motions. The fundamental mode of oscillation is given by n = 2. The period for the fundamental mode is given by

$$\tau_2 = \pi \sqrt{\frac{\rho a^3}{2\sigma}} \tag{3}$$

For a 2.5-cm diameter water drop where ρ = 1 gm/cm^3 and σ = 75 dyn/cm, the period would be τ_2 = 0.36 sec for the fundamental mode, τ_3 = 0.19 for n = 3 and τ_4 = 0.12 for n = 4.

Foote[25] has carried out rather extensive computer calculations of Rayleigh's equation and has dropped the restriction of the calculations to small amplitudes. The results of Foote's calculations are shown in Fig. 5, for the cases of n = 2, 3 and 4. In all cases the drop is started in motion at time T = 0 in the deformed shape with the internal flows at zero. The time is measured in units of π radians so at T = 1 the drop has gone through one-half of a cycle. Even at large amplitudes the calculated shape of the drop appears to have the approximate shape observed in experiments[25]. A detailed comparison with experimental data[25] is not possible because the quality of the data is limited by the experimental techniques that are now available. It should also be pointed out that the Rayleigh solutions are probably only true for amplitudes corresponding to T from 0.375 to 0.625[25].

In the analysis that has been discussed so far, viscous effects have not been included. Lamb[20] has shown that for small viscosity the only effect on the oscillating spherical drop is the gradual damping of the amplitude of the oscillation. The normal mode frequency is not affected by the viscosity. The decay of the amplitude A can be shown to be given by

$$A = A_0 e^{-\beta_n t} \tag{4}$$

where A_0 is the initial amplitude of the oscillation of the drop and β_n is given by

$$\beta_n = \frac{(n-1)(2n+1)\nu}{a^2} \tag{5}$$

where ν is the kinematic viscosity of the liquid and a is the radius of the drop. For a drop of water 2.5 cm in diameter with ν = 0.014 cm^2/sec oscillating in fundamental mode n = 2 then β = 0.045. Thus a free oscillating drop would decay to 1% of its initial amplitude in 102 sec.

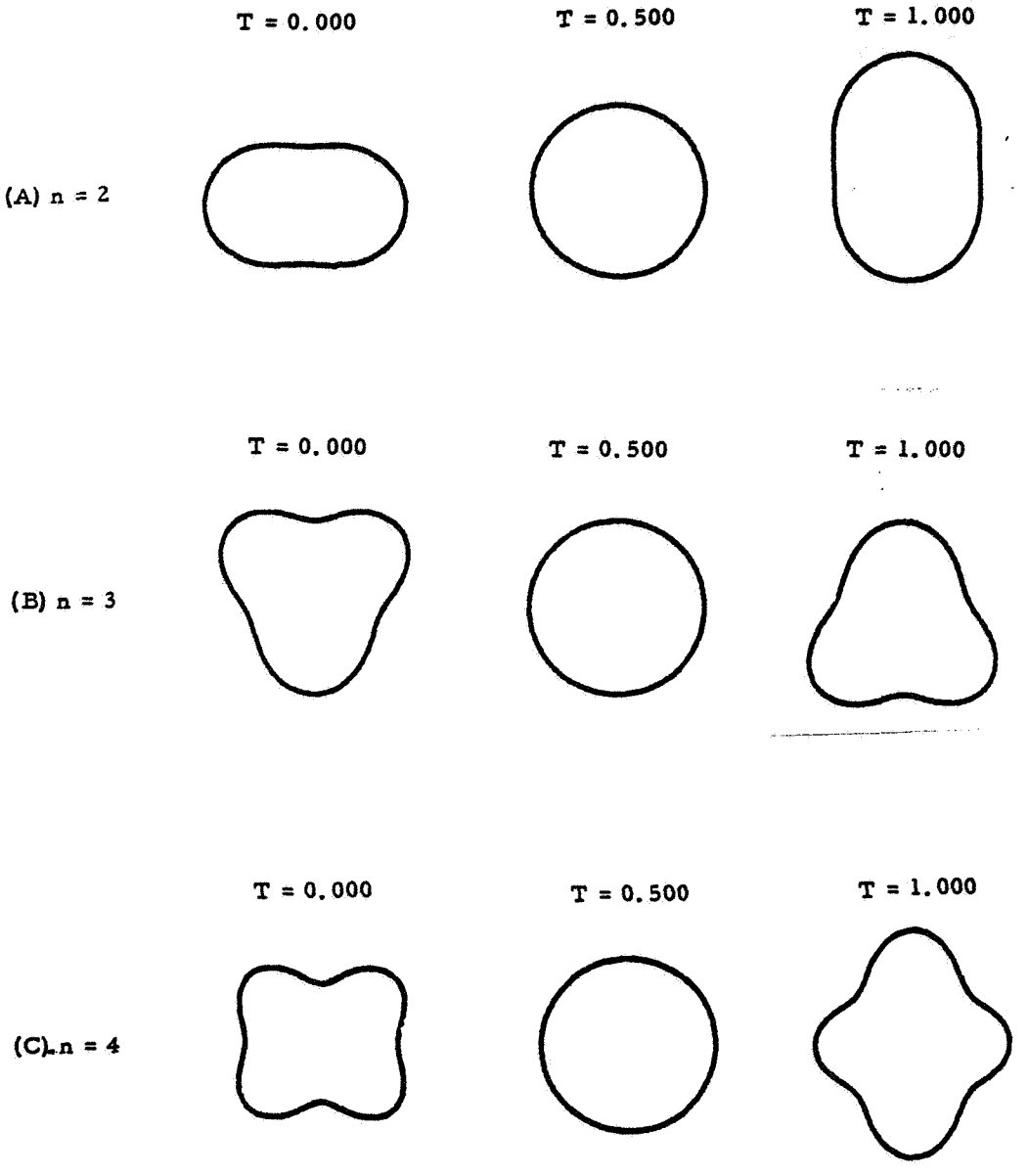

Fig. 5. Fundamental Modes of Oscillation
(The axial ratio is 1.7 at the maximum distortion and the axis of symmetry is vertical)

Chandrasekhar[24] has shown that aperiodically damped motion of the drop is possible for the fundamental mode if $\omega_n a^2/\nu$ is less than 3.69 cm^2/sec. Therefore a drop 0.023 cm in radius or smaller would experience aperiodic motion. Prosperetti[27] has found that a drop that is initially critically damped should have an aperiodic decay for a short time and a damped oscillation motion at a later time. He implies that the effective damping factor first increases and then decreases with time. These predictions have yet to be verified by experiment.

In contrast to the case of small viscosity where ω_n is independent of viscosity, Happel[23] and Chandrasekhar[24] have shown that for a system controlled by gravitational forces as $\nu \to \infty$ the normal mode oscillation can be given by

$$\omega = \omega_n^2 \frac{2n+1}{2(n-1)(2n^2+4n+3)} \frac{a^2}{\nu} \tag{6}$$

where a is the radius of the sphere and ν is the kinematic viscosity.

Foote has noted from his computer calculations that the drop spends more time in the prolate configuration than in the oblate (57% vs 43%). Montgomery[28] has made vertical wind tunnel measurements on drops and has observed a similar behavior. However, it is not clear how much effect the air streaming around the drop has on this unequal distribution of time in the prolate and oblate shapes. At small amplitudes the calculations show that the drop spends an equal amount of time in the two configurations.

Another feature of the computer calculation is that the period of oscillation is not constant with large amplitude oscillations but shows an increase in the period as the amplitude is increased. For a large oscillation in which the axial ratio, γ, and the ratio of major to minor axis is 1.7, the fundamental frequency increases approximately 9% for an ellipsoidal drop. If the calculation is done for a Rayleigh-shaped drop, the predicted increase is about 5%.

Montgomery's[28] experimental work on small drops agrees qualitatively with these computer calculations. The computations show a rather smooth change in the increase of the period with increasing amplitude of the oscillation.

The calculations do not take into account any turbulent flow within the drop which one might expect to find at large amplitude oscillations. This turbulent flow might very well manifest itself as a break in the curve of period vs amplitude as one enters the turbulent flow region.

As the drop oscillations grow to larger amplitudes a point is reached when fission of the drop is possible. A considerable amount of theoretical work on charged drops has been stimulated by nuclear physicists' attempts to model nuclear fission with the behavior of a charged drop. Diehl[29] has calculated the ternary fission for the liquid drop model and has shown that there are two modes of fission, the prolate mode that has axial symmetry and the oblate mode. Alonso[26] has calculated the binary fission case and finds that the neck connecting the two sections becomes very elongated and eventually develops a long thin neck that will not pinch off until it has extended to virtually no width. It has been hypothesized that the pinch-off is actually initiated by a surface fluctuation in the neck. Thompson and Swiatecki conducted a neutral buoyant experiment on polarized drops and observed the thin-necking. In addition, from their data it appeared the drop was attempting fission in the prolate ternary mode.

The liquid drop can undergo another type of oscillation that has received little attention to date. That is the so-called running wave, which for the fundamental frequency is the superposition of fundamental oscillations along the x and y axes $\pi/2$ out of phase with one another. A careful investigation of film taken by the astronauts on Skylab of oscillating drops seems to indicate that this type of oscillation was indeed stimulated. A more detailed investigation of this type of behavior is needed, particularly in the large amplitude regions. One could then determine whether the running wave is still a superimposition of the fundamental modes.

As one can see there has been rather extensive theoretical work carried out on small amplitude oscillation and a considerable number of computer calculations on large amplitude oscillations and fission processes. Unfortunately, the experimental work needed to back up these calculations, even though extensive, has been limited by various experimental constraints.

The experimental techniques used to date fall into four general categories. The first technique is the suspension of a liquid drop in a viscous neutral buoyant medium[30-34]. However, the energy dissipation mechanism for a droplet oscillating within another fluid of appreciable density has been shown by Miller and Scriven[30] to be significantly different from the case in which the second fluid has negligible density. Also, it was pointed out by Park and Crosby[35] that the interfacial tension is modified by the presence of the second medium.

The second technique is the suspension of a liquid droplet in gas currents or electrical fields[28]. Unfortunately, experiments with droplets in air or electrical fields have generally been limited to drop sizes in the millimeter diameter range where it has been difficult to obtain accurate quantitative information for comparison with hydrodynamic theory[35]. In addition, the oscillations in a column of gas supporting the drop may create forced vibrations in the drop[33].

The third technique involves the drops free-falling through a gas or vacuum such as the experiments carried out in the NASA MSFC 400-foot drop tower. These experiments have shown that it is possible to obtain accurate data on shape oscillations of liquid masses deployed in sizes in the centimeter to several centimeter diameter range when the liquids are deployed under carefully controlled conditions with relatively low internal vorticities. Unfortunately, good quantitative resolution in terms of fundamental modes have not been obtained due to the very short (3 second) experiment times available.

Recently, Skylab astronauts have demonstrated the capability of performing drop dynamics experiments in space. Although those experiments were carried out in uncontrolled and unrestrained conditions, the results have already stimulated a great deal of interest both in the scientific community and in the public[2].

This discussion emphasizes the need for a quantitative experiment on oscillation of drops that is free from all the defects mentioned above.

SECTION II

APPARATUS

The photograph in Fig. 6 shows one of the laboratory prototypes of the triaxial acoustical levitation resonance chamber[36] that will be used to position and control large liquid drops in zero-g environments. The chamber itself is nearly cubical with inside dimensions of 11.43 x 11.43 x 12.70 cm, which are the x, y and z faces, respectively. Three acoustic drivers are rigidly fixed to the center of three mutually perpendicular faces of the chamber. During operation of the chamber, each driver excites the lowest-order standing wave along the direction the driver faces.

In a resonant mode, the ambient pressure is maximum at the nodes of the velocity wave and minimum at the antinodes. Consequently there is a tendency for introduced liquids and particles to be driven toward the antinodes where they collect and remain until excitation ceases.

Calculation of the acoustic pressure on the drop is simplified by the fact that the characteristic impedance of the liquid $\rho_\ell c_\ell$ is very much greater than that of the gas, ρc,

$$\frac{\rho_\ell c_\ell \ (\sim 10^5 \text{ cgs})}{\rho c \ (\sim 40 \text{ cgs})} \simeq 10^3, \tag{7}$$

where ρ_ℓ and ρ are the density of liquid and gas, respectively, and c_ℓ and c are the sound velocity of liquid and gas, respectively. Because of this impedence mismatch, the acoustic power in the drop is three orders of magnitude smaller than in the gas and is negligible. This simplifies the expression for the radiation pressure $<\Delta P>$ which is time independent and is given at the boundary by

$$<\Delta P> = \frac{\overline{P^2}}{2\rho c^2} - \frac{1}{2}\rho \ \overline{\bar{U}^2} \tag{8}$$

where P is the excess acoustic pressure, $\bar{U}$ is the gas particle velocity, and the bar over a quantity denotes the time average of the quantity. Equation (8) is the "Bernoulli equation"[36-38] which gives the acoustical perturbation on the ambient pressure from its quiescent value.

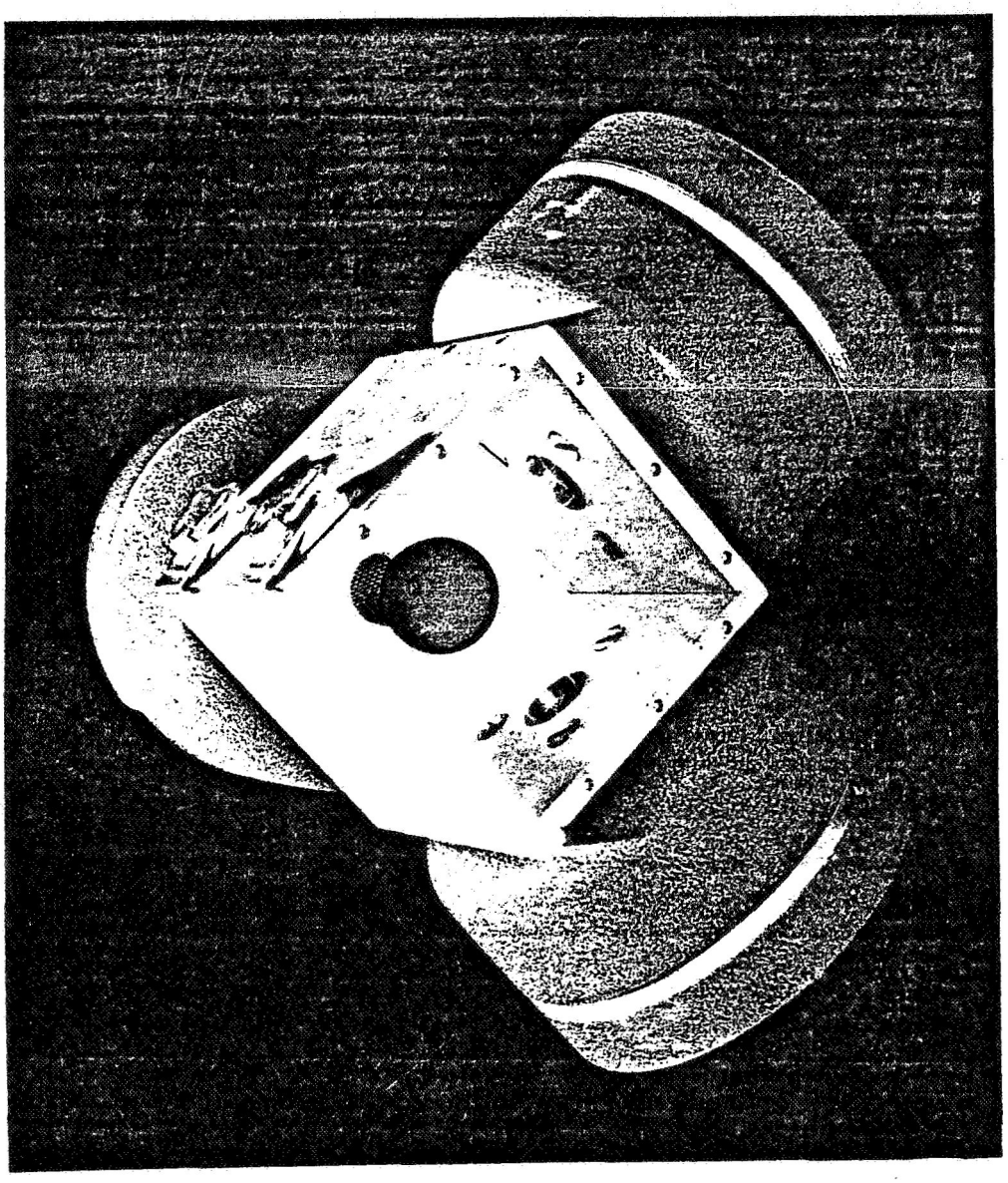

Fig. 6. Acoustic Chamber

The pressure profile in our system can be derived as follows.

The velocity potential ϕ of the wave in the chamber can be expressed as

$$\phi = \phi_x \cos(k_x x) e^{i\omega_x t} + \phi_y \cos(k_y y) e^{i\omega_y t} \tag{9}$$

$$+ \phi_z \cos(k_z z) e^{i\omega_z t}$$

where $\phi_{x,y,z}$ are the complex velocity potential amplitudes of standing waves of frequency $\omega_{x,y,z}$ and wave number $k_{x,y,z}$.

The particle velocity U by definition is

$$\vec{U} = \nabla\phi \tag{10}$$

The pressure is given by

$$P = -\rho\dot{\phi}$$

Fig. 7 shows the resulting expression (Equation 8) for the radiation pressure with only one of the three drivers on ($\phi_x = \phi_y = 0$). The node is a plane ($z = \ell_z/2$), becoming a point when all three are turned on. The profile of Fig. 7 has been verified experimentally.

Because this is a three-dimensional system with independent control on each dimension, it has a great deal of versatility. It can acoustically position a drop, and manipulate a drop once it is positioned; for example, it can induce drop oscillation and/or rotation.

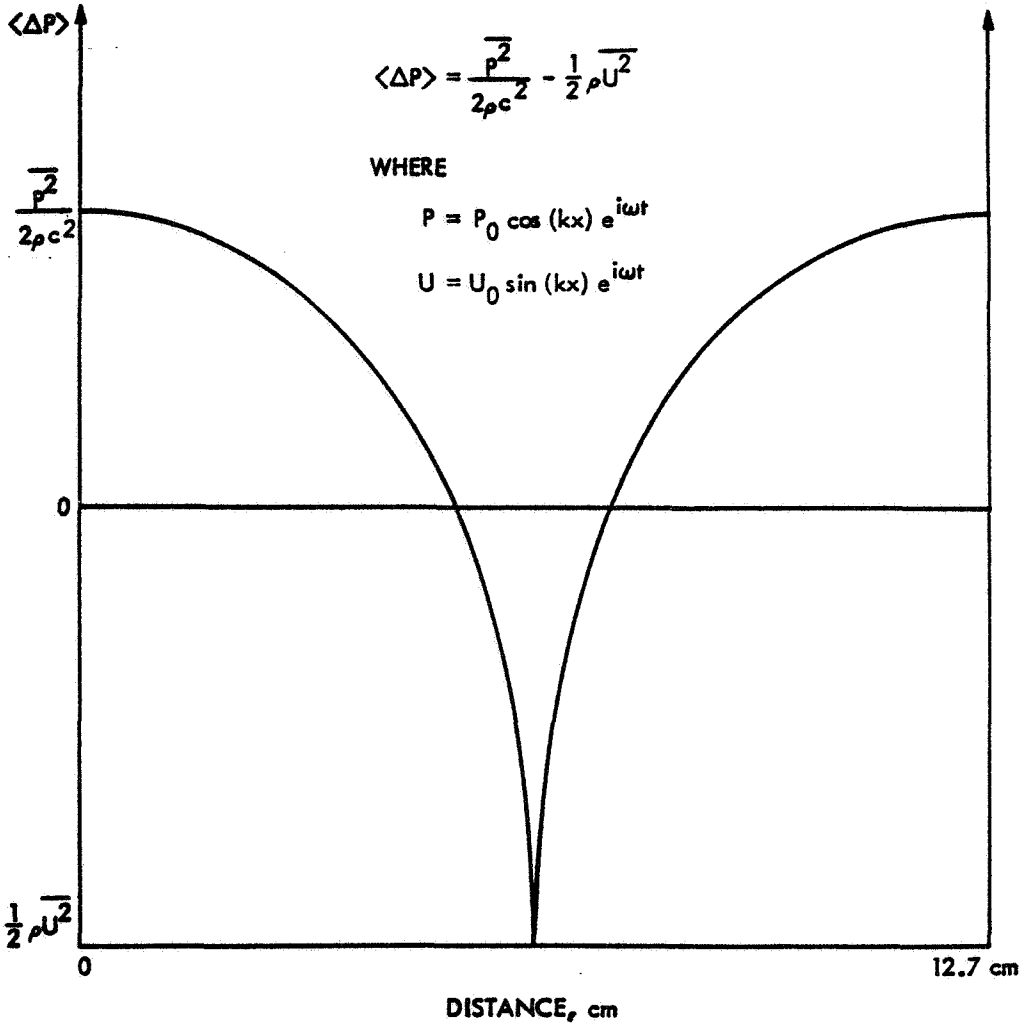

Fig. 7. Theoretical Pressure Profile in the Chamber

SECTION III

OPERATION OF THE CHAMBER

A. ROTATION AND OSCILLATION EXPERIMENTS

In the following discussion, we discuss the operating characteristics of the acoustic chamber necessary to perform rotation and oscillation experiments. Assume that the sample to be studied is a 1.25 cm radius (a) water droplet, the residual acceleration is 10^{-1} cm/sec^2 (10^{-4} g), and the quality factor (Q) (defined as $\omega/2\Delta\omega$) of the acoustic chamber is ~ 25.

a) Newton's equation for the motion of a water drop in an acoustic pressure field is

$$\int \langle \Delta P \rangle \hat{n}_x \, dA = \rho_\ell \cdot 10^{-4} \text{ g} \cdot \frac{4}{3}\pi a^3 \tag{11}$$

In the limit of $ka \ll 1$, this has been calculated by L. V. King[39] to be

$$\frac{P^2}{2\rho c^2} \sin 2kx \cdot 2\pi a^3 \cdot k \cdot \left(\frac{5}{6}\right) = \rho_\ell \cdot \frac{4}{3}\pi a^3 \cdot 10^{-4} \text{g} \tag{12}$$

For a sphere of 2.5-cm diameter, density of 1 gm/cm^3, the corresponding minimum acoustic pressure required to position the drop is

$$P \simeq 10^3 \text{ dyne/cm}^2 \simeq 134 \text{ db} \tag{13}$$

where the decibels (db) are measured against the reference effective pressure (2×10^{-4} dyne/cm^2). For a 50 percent efficient compression driver, less than 0.2 watt of electrical power is needed to provide the required acoustic pressure.

It is worth pointing out that at this acoustic pressure level, the surface tension force (F_s) which acts on the water drop is two orders of magnitude larger than the acoustic force (F_A):

$$\frac{F_s}{F_A} = \frac{\sigma \cdot 2\pi r}{\int \langle \Delta P \rangle \cdot \hat{n}_x \cdot dA} \sim 100 \qquad (14)$$

b) If the amplitude of the above 134 db acoustic wave is modulated at a given frequency ω_o, the drop experiences a modulated force

$$F_o = \int \langle \Delta P \rangle \, n_x \, dA = (\sim 1 \text{ dyne}) \qquad (15)$$

When ω_o matches the normal oscillation modes of the drop given by $\omega_n^2 = n(n-1)(n+2)(\sigma/\rho a^3)$ the amplitude A of the oscillation, assuming potential flow inside the drop, can be as large as

$$|A| = \left| \frac{F_o}{i\omega_o M_\ell \cdot \beta_n} \right| = (\sim 1 \text{ cm}) \qquad (16)$$

where β_n is the damping constant of the nth mode of the drop and M_ℓ is the mass of the drop. Since the drop radius itself is 1.25 cm, this modulation force is sufficient to drive the drop into large amplitude oscillation at least at the fundamental frequency. However, a higher power modulation is required for higher modes due to the increase in damping. That there is in fact sufficient power to do this has been demonstrated in KC-135 flights where the prototype was able to shatter a water drop of 1.25-cm radius in less than one second operating at the fundamental frequency.

c) If the phase between the two orthogonal 134 db waves on the x and y axes is locked with 90° phase shift, this will produce a torque that spins the drop. In the asymptotic limit, the drop will achieve a rotational velocity of 23 rad/sec, exceeding the maximum rotational velocity (10.1 rad/sec) required for this experiment. However, in order to spin up the drop at a constant acceleration, the acoustic power must ramp up as the square root of the rate. The power setting and the rate of increase will have to be determined after the liquid has been selected.

We have demonstrated the rotation capability in our laboratory with a 1.25-cm radius styrofoam ball levitated in a 155 db sound field as presented in Fig. 8. Spinning up of a 1-cm diameter water droplet has also been shown in KC-135 flights.

B. OPERATION OF THE CHAMBER AT EXTREME TEMPERATURES

In future space flights, experiments to be carried out will be extended beyond those on room temperature droplets. These future experiments will require the manipulation and control of liquid helium droplets and of molten metal droplets and glass. In this section we describe laboratory tests of the chamber that demonstrate the feasibility of operation at such temperatures.

a) For the acoustic chamber to operate and function properly between these extreme temperature limits, it must be able to maintain resonance at all times. In fact, the resonant frequencies, f_n, of the chamber are

$$f_n = \frac{nC_o}{2\ell}\sqrt{\frac{T}{273}} \tag{17}$$

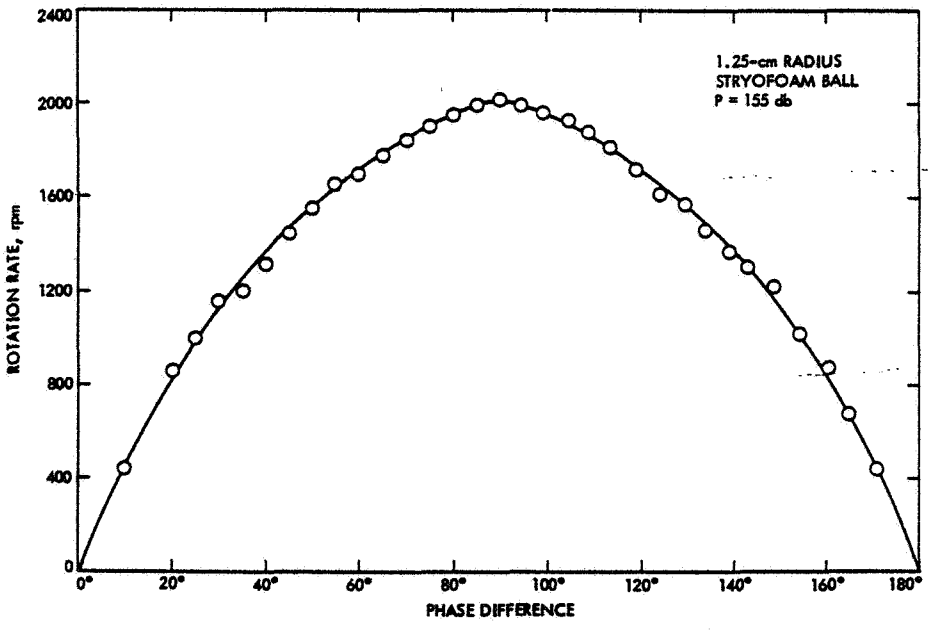

Fig. 8. Rotational Rate as a Function of Phase Difference

where C_o is the velocity of sound at 0°C, ℓ is the physical dimension of the chamber, n is an integer and T is the ambient temperature of the chamber in degrees Kelvin.

An automatic frequency control to maintain resonance despite temperature excursions within the chamber has been developed. The heart of this control is a phase locking loop. The complex displacement X for a system undergoing forced oscillation is

$$X = \frac{-j\, F e^{j\omega t}}{\omega \left[R_m + j\,(\omega m - s/\omega)\right]} \tag{18}$$

where F is the driving force, R is the resistance, m is the mass, and s is the "spring" constant. Without solving the real part of this equation, one can easily see that a resonance occurs where $\omega m = s/\omega$; the complex displacement X lags the driving force by 90°. This is a well known property of acoustical systems. The principle of phase locking is to monitor the driving frequency so that the input signal has 90° phase lead with respect to the acoustical signal inside the chamber at all times.

At the present time we do not have at our disposal acoustical drives that will operate at the high temperatures at which we wish to test the automatic frequency controller. Consequently the variation of high temperatures within the chamber was simulated by mixing helium gas with air to vary in time the resonant frequency in the chamber. The resonant frequencies, f_n, of the chamber are

$$f_n = \frac{nC_o}{2\ell}\sqrt{\rho_o/\rho} \tag{19}$$

where C_o is the velocity of sound in air, ℓ is the physical dimension of the chamber, n is an integer, ρ_o is density of air, and ρ is the density of the air and helium mixture. One can easily see from Equations (17) and (19) that a decrease in the density of the mixture will simulate an increase in the temperature of the chamber. In the test, helium gas was bled into the chamber while a styrofoam ball was being levitated. The purpose of the test is to see how fast the servo loop can track the change in resonant frequency as the "temperature" is varied.

The test was conducted by changing the gas in the chamber from 100% air through intermediate mixtures to a 100% helium composition. This variation in gas density and the resulting change of velocity of sound simulated a change of temperature from 25°C to approximately 2000°C. The fundamental resonance frequency of the chamber thus varied from 1.5 to 4.2 kHz during the simulated temperature rise. The automatic controller was able to vary the driver frequency to match the change in the chamber's resonance frequency, and measurements of the pressure profile in the chamber indicated that the profile maintained its original pattern throughout the test. The most significant portion of the test was the demonstration that the levitated sphere located at the center of the chamber remained at this position throughout the test with no measured motion or oscillation. This indicated that no unwanted oscillation was occurring in the servo system.

b) Another test is the operation of the chamber when the temperature within is highly nonuniform. In a zero-g environment, gravitation-induced convection is absent, leading to inefficient heat transfer from a molten drop positioned in the chamber to the wall. Consequently, the temperature around the droplet can be much higher than at the wall. The questions that we must answer are: (1) Will this extreme temperature gradient affect the sound intensity profile? (2) What will the acoustic wave do to the temperature gradient?

The test apparatus was a glass cylinder 60.76 cm long and 15.78 cm inner diameter. At its upper end a disc heater plate of the same diameter was fitted into the cover. A speaker was mounted in the lower opening. The temperature and sound intensity profile were determined first independently and then simultaneously. The results are shown in Figs. 9 and 10.

Fig. 9, plots the measured acoustic pressure as a function of distance with and without the heater on. It shows that resonance was not perturbed by the temperature gradient. Fig. 10 compares the temperature profiles with and without the speaker on. It shows that the acoustic field slightly improved the heat conductivity of gas without much alteration of the shape of the profile. We conclude from these tests that temperature gradients resulting from molten material being positioned will not affect the positioning capability of the chamber nor will the acoustic field significantly modify temperature gradients which would affect the melting and solidification of the material being positioned.

c) A very convenient method of testing the purity of ultra-pure metals is to measure the resistivity of the metal at low temperatures. The resistivity measurements could be made by using eddy current induction techniques on a levitated sample that would obviate the necessity of placing electrical leads on the sample. Measurements of this type are often conducted at temperatures below 2.0°K.

At the other end of the temperature scale, the determination of the purity of ultra-pure metals requires that the chamber perform at a temperature below 2°K. One of the anticipated uses of the acoustic levitation furnace is the growth of ultra-pure single crystals with a minimum number of crystal defects. It would be convenient to be able to grow the crystal and then make subsequent tests on the crystal in the same chamber. It is felt that this type of handling of the material would greatly reduce inadvertent contamination of the sample and eliminate the possibility of producing defects in the crystal through additional handling when transferring from the furnace to another separate test chamber. The combined

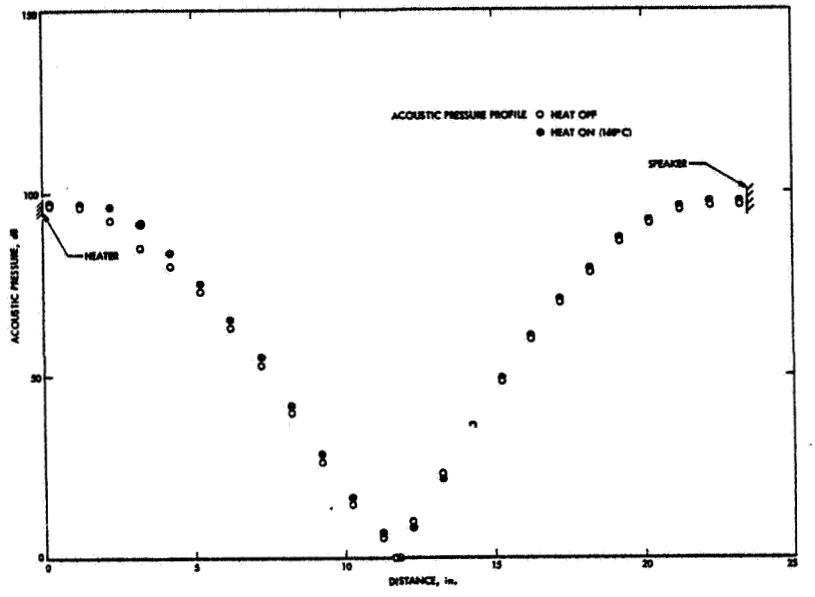

Fig. 9. Acoustic Profile

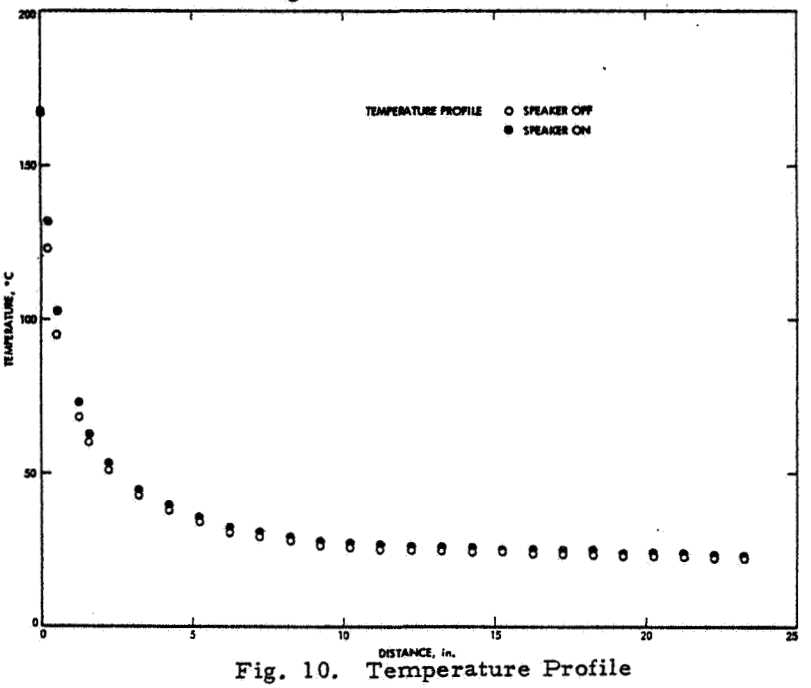

Fig. 10. Temperature Profile

furnace test chamber has the added advantage in that it could reduce the time needed in conducting the purity tests on the samples.

It was therefore decided to conduct exploratory tests on the acoustic levitation chamber at these low temperatures to ascertain any difficulties in operation of the chamber at these reduced temperatures. Preliminary tests were carried out at 1.8°K and the results indicated that the acoustic pattern did not show any significant deviations from room temperature operation.

d) To provide an understanding and engineering design of the flight experiments, it is desirable to study the melting and solidification process under the influence of acoustic fields in an earth laboratory. A high power acoustic chamber that is capable of levitating liquid droplets, glass beads and metal plates in our laboratory has been developed as shown in Figs. 11 and 12.

The capability of the new chamber will be used to make feasibility studies of containerless materials processing in the laboratory, to be carried out with university and industry scientists. Initial tests will be conducted with low-melting organic materials which have the advantages of low density and ease of handling. If these experiments are successful, later tests may be conducted on low-melting metals.

Fig. 11. Acoustically Levitated Water Droplets

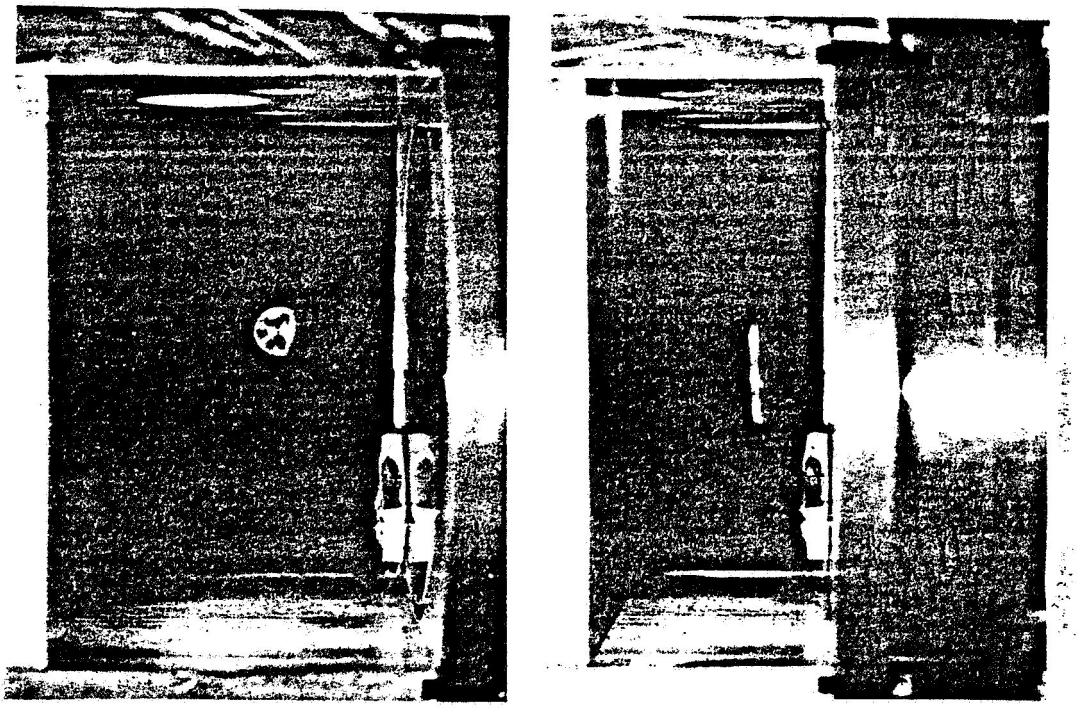

(a) (b)

Fig. 12. Acoustically Levitated Solids: (a) Glass Sphere, (b) Metal Plate

ACKNOWLEDGEMENTS

The authors wish to thank Prof. I. Rudnick (UCLA), Dr. D. J. Collins (JPL), and Dr. P. V. Mason (JPL) for their valuable suggestions, and also Mr. E. E. Olli (JPL) for his excellent help.

V. REFERENCES

1. Plateau, J., Smithsonian Report, 270 (1863).

2. Gibson, E.G., "Skylab Fluid Mechanics Demonstrations," International Colloquium on Drops and Bubbles, Proceedings, (Pasadena, California, August 29-31, 1974) (to be published).

3. Chandrasekhar, S., Ellipsoidal Figures of Equilibrium, Yale University Press, New Haven (1969) (see references).

4. Rayleigh, Lord, "Equilibrium of revolving liquid under capillary forces," Phil. Mag. 28, 161 (1914).

5. Appell, P., Traite de Mecanique Rationelle, Vol. 4, Pt. 1, Chapt. IX, Gauthier-Villars, Paris (1932).

6. Chandrasekhar, S., "The stability of a rotating liquid drop," Proc Roy. Soc. (London), 286, 1 (1965).

7. Cohen, S., Plasil, F., and Swiatecki, W.J., "Equilibrium configurations of rotating charged or gravitating liquid masses with surface tension. II.", Annals of Physics 82, 557 (1974).

8. Ross, D.K., "The shape and energy of a revolving liquid mass held together by surface tension," Australian J. Phys. 21, 823-835 (1968).

9. Ross, D.K., "The stability of a rotating liquid mass held together by surface tension," Australian J. Phys. 21, 837-844 (1968).

10. Gans, R.F., "On the Poincare problem for a compressible medium," Journal of Fluid Mechanics, 62, Pt. 4, 657-675 (1974).

11. Bauer, H.F., and Siekmann, J., Z. Angew. Math. and Phys., 22, 532-542 (1971).

12. Böhme, G., Johann, W., and Siekmann, J., "Note on a Differential Equation of Electrohydrodynamics," Acta Mechanica 20, 303-307, (1974).

13. Swiatecki, W.J., "The Rotating, Charged or Gravitating Liquid Drop, and Problems in Nuclear Physics and Astronomy," International Colloquium on Drops and Bubbles, Proceedings (Pasadena, California, August 29-31, 1974) (to be published).

14. Berringer, R., and Knox, W.J., "Liquid-Drop Nuclear Model with High Angular Momentum,"Phys. Rev. 121, 1195 (1961).

15. Wong, C.Y., "Toroidal and spherical bubble nuclei," Annals of Phys. 77, 279-353 (1973).

16. Pik-Pichak, G.A. (see references given in Swiatecki, references 7 and 13).

17. Carruthers, J., "The Application of Drops and Bubbles to the Science of Space Processing of Materials," International Colloquium on Drops and Bubbles, Proceedings (Pasadena, California, August 29-31, (1974) (to be published).

18. Greenspan, H. P., Theory of Rotating Fluids, Cambridge Univ. Press, Cambridge (1968).

19. Lamb, H., "On the Oscillations of a Viscous Spheroid," Proc. London Math Soc. (1), 13, 51-56 (1881).

20. Lamb, H., Hydrodynamics, 6th ed., Cambridge University Press, 473-639 (1932).

21. Rayleigh, Lord, The Theory of Sound, Dover Publications, New York, 371-375 (1945).

22. Reid, W. H., "The Oscillations of a Viscous Liquid Drop," Quart. Appl. Math, 18, 86-89 (1960).

23. Happel, J., and Brenner, H., Low Reynolds Number Hydrodynamics, Prentice-Hall, 62 (1965).

24. Chandrasekhar, S., Hydrodynamics and Hydromagnetic Stability, Oxford University Press (1961).

25. Foote, G. B., "A theoretical investigation of the dynamics of liquid drops," (Ph. D. thesis), Univ. of Arizona (1971).

26. Alonso, C. T., "The Dynamics of Colliding and Oscillating Drops," International Colloquium on Drops and Bubbles, Proceedings (Pasadena, California, August 29-31, 1974), (to be published).

27. Prosperetti, A., "On the Oscillations of Drops and Bubbles in Viscous Liquids," International Colloquium on Drops and Bubbles, Proceedings (Pasadena, California, August 29-31, 1974), (to be published).

28. Montgomery, D. N., "Collisional phenomena of uncharged water drops in a vertical electric field," (Ph. D. thesis), Univ. of Arizona (1968).

29. Diehl, H., and Greiner, N., "Ternary Fission in the Liquid Drop Model," Phy Letter, 45B, 35 (1973).

30. Miller, C. A. and Scriven, L. E., "The Oscillations of a Fluid Droplet Immersed in Another Fluid," J. Fluid Mech., 32, Part 3, 417-435 (1968).

31. Valentine, R. S., Sather, N. F., and Heideger, W. J., "The Motion of Drops in Viscous Media," Chem Eng Sci. 20, 719-729 (1965).

32. Davis, T. V. and Hagdon, D. A., "An Investigation of Droplet Oscillations During Mass Transfer," Proc. Roy. Soc. A243, 492 (1957).

33. Chomiak, J., "Oscillations of a Viscous Liquid Drop in a Turbulent Gas," Fluid Dynamics Transactions, Vol. 1, The Macmillan Company, New York (1964).

34. Narasinga Rao, E. V. L., et al., "Drop Formation Studies in Liquid-Liquid Systems," Chem Eng Sci, 21, 867-880 (1966).

35. Park, R. W. and Crosby, E. J., "A Device for Producing Controlled Collisions between Pairs of Drops," Chem Eng Sci 20, 39 (1965).

36. Wang, T. G., Saffren, M. M., and Elleman, D. D., "Acoustic Chamber for Weightless Positioning," AIAA paper 74-155 (1974).

37. Landau, L. D., and Lifshitz, E. M., Fluid Mechanics, Pergamon Press (1959).

38. Westervelt, P. J., "Scattering of Sound by Sound with Applications," Finite Amplitude Wave Effects in Fluid, Proceedings of the 1973 Symposium, (Copenhagen) (1973).

39. King, L. V., "On the Acoustic Radiation Pressure on Spheres," Proc. of Roy. Soc. (London), A147, 212-240 (1934).

☆U.S. GOVERNMENT PRINTING OFFICE: 1976 - 685-197/2 Region No. 9-1